ABSTRACT

MION, CHRISTIAN. Investigation of the thermal properties of gallium nitride using the three omega technique. (Under the direction of Dr. J. F. Muth).

Gallium nitride based devices suffer from undesirable heating effects that significantly limit the performance of high electron mobility transistors and laser diodes thereby reducing device lifetime and reliability. An accurate knowledge of the gallium nitride thermal conductivity is crucial to understanding thermal effects.

This work addresses issues related to both the thermal limitations and thermal characterization of gallium nitride alloys and devices. First, theoretical developments concerning the three omega technique applied to a film-on-substrate system are considered when the film-to-substrate thermal conductivity ratio is larger than one. The case of thermal boundary resistance between film and substrate is included. In the case of high thermal conductivity films, it is found that neglecting the presence of thin thermally insulating buffer layer would lead to large uncertainties in extracted film thermal conductivities.

Next, very thick, free standing gallium nitride layers grown by hydride vapor phase epitaxy were precisely measured from 300K to 450K using the three omega method. By comparing the measured values with dislocation density measurements the dependence of the gallium nitride thermal conductivity on dislocation density was obtained and compared with theory. In addition, the thermal conductivity of iron doped semi-insulating gallium nitride was measured to be as high as 230 $W \cdot K^{-1} \cdot m^{-1}$. In this study, a 2mm thick iron doped gallium nitride substrate was measured to have an average dislocation density of 5.10^4 cm^{-2} which represents the present state of the art.

Finally the modeling of the thermal resistance of multifinger AlGaN/GaN HEMTs was examined using the experimentally determined values of the thermal conductivity. Using the three omega method as the starting point, an original accurate closed-form compact expression for the thermal resistance of single and multifinger HEMT device structures was derived. It was found that the thermal

performance of a single finger HEMT composed of homoepitaxial GaN on a GaN substrate is superior to that of single finger GaN HEMT heteroepitaxially grown on silicon carbide.

INVESTIGATION OF THE THERMAL PROPERTIES OF GALLIUM NITRIDE USING THE THREE OMEGA TECHNIQUE

By

CHRISTIAN MION

A dissertation submitted to the Graduate Faculty of

North Carolina State University

in partial fulfillment of the requirements for

the Degree of Doctor of Philosophy

ELECTRICAL ENGINEERING

Raleigh, NC

2005

Approved by:

Dr. Veena Misra	Dr. Douglas Barlage
Dr. John Muth Chair of Advisory Committee	Dr. Mark Johnson

BIOGRAPHY

Christian Mion was born on June 25th 1976 in Bourgoin-Jallieu France while the 2005 French President Jacques Chirac was at the time Prime minister. His city of birth, located about 30 miles south-east from Lyon, is known for its rugby team who qualified for the 2005 semi-final of the national professional championship. Aside from observing the evolution of local professional teams, he received his diploma in microelectronics from the University of Grenoble, France in September 1999. He has been a candidate for the Ph.D degree at North Carolina State University in the ECE department with a specialization in photonics and nanoelectronics. Charming North Carolina has offered a high quality setting for the best conduct of his graduate studies.

ACKNOWLEDGEMENTS

I wish to express my sincere appreciation to my advisor, Dr J. F. Muth not only for his guidance, advice and support but also for offering encouragement and confidence throughout the course of this study. I also would like to express my gratitude and thanks to the director of research and development Drs. Drew Hanser and Edward Preble from Kyma Technologies for providing gallium nitride samples as well as further impetus in the direction of this work. I wish to express my gratitude to Dr. Veena Misra for her support during the early stages of my Ph.D program, gratitude that I wish to extend to Dr. John Hauser and Dr. Richard Kuehn. My special appreciation and thanks also go to advisory committee members Drs. Mark Johnson, Douglas Barlage, and Veena Misra who have been actively supporting my research objectives. I wish to convey my appreciation to Dr. Carlton Osburn for the opportunity he provided for me to work as a teaching assistant.

I am grateful to Dr. Mark Johnson, Yoganand Saripalli, Ji-soo Park, Dr. Robert Davis, and Dr. Jeff Brown for their active collaboration in providing material. This work would not have been possible without help from researchers, faculties, friends, technicians, and students directly or indirectly involved in my graduate studies while at NCSU. More particularly, I would like to thank Joe Matthews for his active collaboration in the laboratory. I would like to acknowledge the role of Patrick Wellenius, Hugh Porter, Ailing Cai, Roy Zang, Heather Lazar, Andy Oberhofer and the numerous other students I interacted with in assisting my research throughout my graduate studies.

TABLE OF CONTENTS

List of Figures ..... **viii**

List of Tables ..... **xii**

Chapter 1 Introduction **1**

1.1 Technological Challenges in Gallium Nitride Devices. 1
1.1.1 Presentation 1
1.1.2 GaN Substrates 4
1.1.3 Gallium Nitride Thermal Conductivity and Heat Transfer Limitations. 5
1.2 Thermal Conduction: Basic Concepts. 9
1.2.1 The Equation of Periodic Heat Conduction. 9
1.2.2 Complement to the Elementary Heat Conduction Equation. 10
1.3 Thermal Conductivity Measurements 11
1.3.1 Presentation of Semiconductor Thermal Conductivity Characterization Techniques 12
1.3.2 Selecting and Developing an Appropriate Technique 14
1.3.3 Gallium Nitride Thermal Conductivity Characterization Techniques. 16
1.4 Objectives 18
1.5 Dissertation Outline 19
1.6 References 21

Chapter 2 The 3ω Method: Principles and Measurements **26**

2.1 The 3ω Technique: Fundamentals. 26
2.1.1 The Heat Source. 27
2.1.2 The Sensor 30
2.1.3 Extracting the Thermal Conductivity: the Slope Method. 31
2.2 Review on the Extension of the 3ω Method 37
2.2.1 Differential Technique 37
2.2.2 Extending the 3ω Method to Multilayer stacks. 42
2.3 Calibration, Experimental Errors and Measurements 47
2.3.1 Experimental set-up 47
2.3.2 Calibration 50
2.3.3 Experimental Results on GaN 53
2.4 References 56

Chapter 3 Determining Film Thermal Properties With the 3ω Method: A Theoretical Consideration **61**

3.1 Overview 61
3.2 Methods of Resolution 65
3.2.1 Multilayer Stack on Substrate with Interfacial Boundary Resistances 68
3.2.2 Numerical Analysis 70
3.3 Thermal Conductivity characterization for low and high K_F/K_S Ratios 72
3.4 Frequency Effects 75
3.5 Thermal Boundary Resistance (TBR) 81
3.5.1 Films with Low Thermal Conductivity 85
3.5.2 General Case 90
3.6 Applicability of the Differential 3ω Method 94
3.7 Conclusion 99
3.8 References 101

Chapter 4 Characterizing the Properties of the Gallium Nitride: Thermal Conductivity 104

4.1 Introduction 104
4.1.1 The Thermal Conductivity of Semiconductors 105
4.1.2 Literature Review 110
4.1.3 Study Outline 113
4.2 Characteristics of Hydride Vapor Phase Epitaxy grown Gallium Nitride 114
4.3 Characterization of HVPE GaN Thermal Conductivity Using the 3ω Method 122
4.3.1 Experimental Details 123
4.3.2 Extracting the Thermal Conductivity 124
4.4 Strong Evidence of the Dependence of Gallium Nitride Thermal Conductivity on Dislocation Density. 133
4.4.1 Dislocations in Gallium Nitride 133
4.4.2 Thermal Conductivity and Dislocation Density 134
4.4.3 Comparison with Previous Theoretical Investigations 137
4.4.4 Effects of Impurities 140
4.4.5 Comparisons Between Gallium Nitride and Diamond 141
4.5 Gallium Nitride Thermal Conductivity Dependence on Temperature 141
4.6 Conclusion 143
4.7 References 147

Chapter 5 The Thermal Resistance of AlGaN/GaN HFET 152

5.1 Overview 152
5.1.1 Self-heating Effects 152
5.1.2 Status in Thermal Modeling. 153
5.2 Trade-off in Thermal Design 155
5.2.1 Definitions 155
5.2.2 Single Finger on Substrate (Long Gate Width) 161
5.2.3 Multifinger on Substrate 162

5.2.4 Multifinger on a Multilayer Film. 166
5.2.5 Small Width Device 168
5.3 Comparative Study between the Thermal resistance of GaN/SiC HEMT and GaN/GaN HEMT. 170
5.3.1 Single Finger 172
5.4 Multifinger 174
5.5 Conclusion 177
5.6 References 178

Chapter 6 Summary and Conclusions 182

6.1 Summary 182
6.1.1 Thin Film Thermal Conductivity Characterization Using the 3ω Method 182
6.1.2 Thermal Conductivity of Gallium Nitride. 183
6.1.3 The Thermal Resistance of HFETs. 185
6.2 Future Directions 186

Appendix A 3-Dimensional Solution of the Thermal Diffusion Equation for Periodic and Time-Independent Adjacent Strip Heat Sources Deposited on a Stratified Medium 188

A.1 Presentation 188
A.2 Resolution in the Two-Dimensional Case 190
A.3 Identical Strip Sources 192
A.4 3-Dimensional Resolution 197
A.5 References 201

Appendix B Solution for Temperature Dependent Thermal Conductivity 203

B.1 Presentation 203
B.2 References 204

Appendix C Estimation of Surface Heat Losses 205

C.1 Presentation 205
C.2 Heat Loss by Radiation 205
C.3 Heat Loss by Conduction 206
C.4 References 207

Appendix D Defect Density Characterization 208

D.1 Introduction 208

D.2 Catholuminescence Prior to Etching (Sample A, B, C, D). 211
D.3 Micrograph Before Etching (Samples C, D). 213
D.4 Micrograph After Etching (Samples A, B, C, D) 213
D.5 AFM After Etching (Sample A, B, C, D) 215
D.6 Sample C 215
D.7 Sample D 217
D.8 Conclusion 219
D.9 References 222

LIST OF FIGURES

Figure 1.1. The Combined Figure of Merit is charted for several semiconductors. 3

Figure 1.2. The thermal conductivity of gallium nitride is low relatively to its competitors used in similar applications.. 6

Figure 1.3. Experimental room temperature thermal conductivity of gallium nitride plotted against time in years..... 7

Figure 1.4 Isothermal representing the thermal waves present in the 3ω method and diffusing into the substrate from the heater..... 16

Figure 2.1. Four point heater: a) of different width and length for effective testing and: b) topview showing the length and width of the structure..... 27

Figure 2.2. The real (in-phase) and imaginary part (out-phase) of the Equations (2.3) and (2.4) were plotted in plain line and dotted line respectively..... 29

Figure 2.3. Typical $V_{3\omega}$ versus lnω curves for a 1mm thick glass slide.. 32

Figure 2.4. The time-dependent temperature oscillations ΔT were simulated by numerical calculation (FEM). 36

Figure 2.5. Schematic of the heat flow for a low thermal conductivity thin film on substrate for $K_F << Ks$ and $d_F < 2b$. 38

Figure 2.6. The third harmonic $V_{3\omega}$ is measured with a lock-in amplifier..... 47

Figure 2.7. Heater resistance versus temperature measurement to deduce the temperature coefficient α_T..... 50

Figure 2.8. Calibration of temperature dependence measurements were performed on a 430um thick sapphire wafer 51

Figure 2.9. The temperature oscillation of the in-phase component as a function of frequency for SiO_2 on silicon substrates 52

Figure 2.10. The temperature oscillation was recorded on GaN films grown on a silicon substrate with an intermediate ~900nm buffer..... 54

Figure 3.1. Film-to-substrate thermal conductivity contrast for a film thermal conductivity of GaN arbitrarily equal to bulk values ~200 $W \cdot K^{-1} \cdot m^{-1}$..... 63

Figure 3.2. Illustration of the governing geometrical and physical parameters 65

Figure 3.3. Cross-sectional schematic of half the structure 71

Figure 3.4. The Equation (3.5) derived at ω=0 is valid for K_F/K_S greater than 1 74

Figure 3.5. The relative error on the apparent thermal conductivity in Figure 3.4 is plotted versus frequency for two K_F/K_S ratios 77

Figure 3.6. For large β_F ratios, the K_{Fy}/K_{1D} ratio derived at ω=0 from Equation (3.5) is plotted in solid line 78

Figure 3.7. Impact of a thermal boundary resistance on the dependence of K_{Fy}/K_{1D} versus K_F/K_S using Equation (3.9) 83

Figure 3.8. Correction factors $F(\beta_F)$, $G(\beta_F)$ on respectively the film thermal resistance and interfacial boundary resistance 86

Figure 3.9. The K_{Fy}/K_{1D} ratio versus β_F for the approximated Equation (3.14) in dashed line and the full solution of Equation (3.9) in solid line 89

Figure 3.10. The factors F and G are plotted against the film-to-substrate thermal conductivity ratio 91

Figure 3.11. The intrinsic sensitivity S_i of the differential 3ω technique defined in Equation (3.22). 96

Figure 4.1. Experimental room temperature thermal conductivity of gallium nitride plotted against time in years 105

Figure 4.2. Fe profile on sample D deduced from Secondary Ion Mass Spectroscopy (SIMS) 115

Figure 4.3. Catholuminescence measurement at 300K for undoped sample A, B, C, and D 118

Figure 4.4. Approximately 350-400 dislocations for sample A a 30um x 30 um. ρ_D=~4.10^7 cm^{-2} 119

Figure 4.5. Approximately 100 to 200 dislocations for sample B over a 30um x 30 um. ρ_D~$1\cdot10^7$-$2\cdot10^7$ cm^{-2} 120

Figure 4.6. Dislocation density measurements on sample C. 79 dislocation densities over a 30x30 um^2 gives a dislocations density of 8.8 10^6 cm^{-2} 120

Figure 4.7. Plane view catholuminescence imaging of the Sample D. 6-7 dislocations over a ~118x90 um^2 area gives a dislocations density of ~5.10^4 cm^{-2} 121

Figure 4.8. UV/VIS transmission measurements at 300K for a) sample C and b) sample D. 121

Figure 4.9. The 3ω temperature oscillation ΔT was normalized to the input power P and recorded versus frequency 125

Figure 4.10. Measured temperature oscillation normalized to power on site A1 (triangle) in the center part of the sample and A2 (square)..... 126

Figure 4.11. 3ω measurements on sample B. 130

Figure 4.12. Thermal conductivity of gallium nitride versus temperature above 300K. 131

Figure 4.13. Dislocation density versus HVPE gallium nitride film thickness 133

Figure 4.14. Thermal conductivity versus dislocation density values..... 135

Figure 4.15. Gallium nitride thermal conductivity versus dislocation density derived from theoretical considerations in Ref. 15..... 137

Figure 5.1. Typical multifinger FET structure 155

Figure 5.2. Channel temperature rise versus dissipated power 157

Figure 5.3. Cross-sectional schematic of simplified HEMT on silicon carbide. 158

Figure 5.4. Simplified multifinger structure considered in this analysis. 160

Figure 5.5. Temperature versus position along a line perpendicular to finger width 163

Figure 5.6. Illustration of the temperature rise produced by a second heater placed adjacent to an initial finger..... 164

Figure 5.7. Thermal resistance of central finger as a function of finger number 165

Figure 5.8. R_{3D} is the thermal resistance averaged over the channel of the central finger half-way between gate extremety widthwise. 169

Figure 5.9. Cross-sectional schematic temperature distribution under the gate. ... 173

Figure 5.10. Cross-sectional view of temperature solution in a half structure of a 8-finger HEMT. 174

Figure A.1. Schematic of parallel wires deposited on a multilayer stack..... 188

Figure A.2. ΔT_{q0} is the average temperature at the $q0^{th}$ heater caused by the presence of all heat sources including the $q0^{th}$ source itself..... 192

Figure A.3. Schematic cross section for an odd number of identical strip sources on a multilayer stack..... 193

Figure A.4. Equation (A.24b) is plotted versus s/b for different β_S ratios..... 196

Figure A.5. Three dimensional Rectangular heat source. 197

Figure A.6. Normalized average temperature versus substrate thickness to heater half-length..... 201

Figure C.1. Metal layer characteristics..... 206

Figure D.1. Catholuminescence spectrum at 300K for sample A, B, C (undoped) and D (iron doped)..... 211

Figure D.2. 30 x 30 um^2 catholuminescence imaging prior to etching for a) Sample A and b) Sample B. The probe current was 10^{-10} A..... 212

Figure D.3 Catholuminescence imaging prior to etching for c) Sample C and d) Sample D. The probe current was 10^{-10} A. 212

Figure D.4. Micrograph of the gallium nitride surface morphology for c) Sample C and d) Sample D..... 213

Figure D.5. Typical micrograph of the surface of sample A after a 15 mn 200 °C phosphoric bath..... 213

Figure D.6. Typical micrograph at the surface of sample B after a 15 mn 200 °C phosphoric bath..... 214

Figure D.7. Micrograph of c) Sample C and d) Sample D after a 30 mn 200 °C phosphoric acid dip (same bath) 214

Figure D.8. Random 50X50 um^2 AFM scans on a) Sample A, b) Sample B, c) Sample C, d) Sample D. 215

Figure D.9. Peculiarity: i) At a boundary on sample C 215

Figure D.10. i) SEM ii) CL imaging at exact same location (10^{-10} A)..... 216

Figure D.11. Comparison between CL (10^{-10} A), SEM, and micrographs taken at the same location on sample D 217

Figure D.12. Enlargement of Figure D.5.28 part (i)..... 217

Figure D.13. i) SEM and ii) CL imaging on semi-insulating sample D after 30mn etching (probe current: 3.10^{-9} A)..... 218

Figure D.14. Dislocation density versus thickness..... 219

LIST OF TABLES

Table 1.1. Physical parameters for various semiconductors including gallium nitride (GaN)..... 2

Table 1.2. The density ρ, the heat capacity Cp, the thermal conductivity κ and the diffusivity α for various non-metallic and two metallic solids..... 9

Table 2.1. Room temperature of various materials measured with the 3ω method and compared with handbook values[16]. 50

Table 4.1. Gallium nitride sample characteristics. U=Undoped. Fe=iron doped. Initial thickness = thickness before polishing..... 114

Table 4.2. Impurity level in Undoped and iron doped gallium nitride..... 116

Table 4.3. Summary of resisitivity, mobility and carrier concentration on sample D measured at room temperature 117

Table 4.4. Thermal conductivity at 300K for samples listed in Table 4.1. 131

Table 5.1. Thermal parameter employed the thermal resistance evaluation of GaN HEMT. R_{buff} is the thermal resistance of the AlN buffer layer..... 170

Table 5.2. Simulated temperature values under the gate. 173

Table 5.3 . Thermal resistance estimation in a 8-finger HEMT 175

Table 5.4. Thermal resistance estimation in a 8-finger HEMT. The gate length is now 5um (b=2.5um) 176

Table D.1. Samples were grown by hydride vapor phase epitaxy 208

Chapter 1 Introduction

1.1 Technological Challenges in Gallium Nitride Devices.

1.1.1 Presentation

The ultimate performance of semiconductor devices has been shown to be theoretically limited by fundamental material parameters. The Combined Figure of Merit (CFOM) shows that wide band gap semiconductors are suitable for high frequency high power applications:

$$\text{CFOM} = \frac{\kappa\varepsilon_0\mu v_s E_B^2}{(\kappa\varepsilon_0\mu v_s E_B^2)_{silicon}} \qquad (1.1)$$

μ is low field mobility, κ is thermal conductivity, v_s is the saturation velocity, ε_0 is the dielectric constant and E_B is the breakdown field. The combined figure of merit is constructed from the Johnson figure of merit[8], the Keyes' figure of merit[10] and the Baliga figure of merit[12]. Table 1.1 includes the fundamental parameters of interest for the semiconductors that are most often used for high power high frequency electronics.

Table 1.1. Physical parameters for various semiconductors including gallium nitride (GaN). The thermal conductivity of gallium nitride is higher than 1.3 $W \cdot cm^{-1} \cdot K^{-1}$ as this study will show.

Properties	Ge	Si	GaAs	6H-SiC	4H-SiC	GaN	Diamond
Band gap (eV)	0.67	1.11	1.43	3.0	3.2	3.45	5.45
Dielectric constant	16	11.9	13.1	9.7	10.1	9	5.5
Breakdown field (V/cm) (doping=cst)	$3 \cdot 10^5$	$3 \cdot 10^5$	$4 \cdot 10^5$	$25 \cdot 10^5$	$22 \cdot 10^5$	$20 \cdot 10^5$	$100 \cdot 10^5$
Saturated velocity (10^7 cm/s)	0.7	1	2	2	2	2.2	2.7
Bulk electron mobility	3900	1350	8500	380	800	1200	2200
Bulk hole mobility (cm^2/V-s)	1900	450	400	95	120	850	850
Thermal conductivity (W/cm·K)	0.6	1.5	0.46	3.5	3.5	1.3<?	22
Melting point (ºC)	938	1420	1240	2830	2830	2500	4000

The CFOM predicts that gallium nitride (GaN) represents a serious competitor against silicon, gallium arsenide and silicon carbide as seen in Figure 1.1.

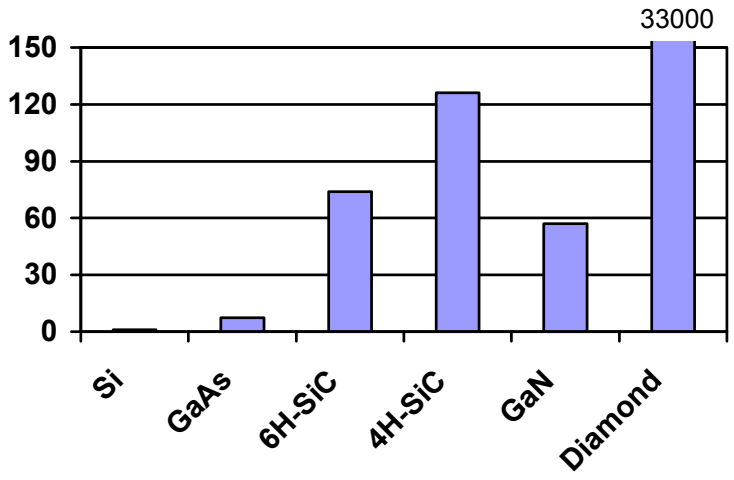

Figure 1.1. The Combined Figure of Merit is charted for several semiconductors showing gallium nitride is suited for high frequency, high power high frequency applications. K=1.3 $W \cdot cm^{-1} \cdot K^{-1}$ for GaN but the CFOM for GaN would be proportionnaly larger with K_{GaN}=2.3 $W \cdot cm^{-1} \cdot K^{-1}$.

Whether in practice gallium nitride will fulfill its expectations depends on solving technological challenges. High power radio frequency devices and high power laser diodes require a thorough understanding of thermal management issues. This is especially true of GaN based devices where undesirable heating effects have been found to significantly limit the performance of AlGaN/GaN HEMT structures[13] and laser diodes[14] reducing lifetime and reliability. Therefore the question of whether improvements in overall III-Nitride device performance in light of thermal management[15] and reliability[16] will lead to success in the marketplace by surpassing the performance of Si, SiGe, GaAs devices and compete effectively with SiC based devices, remains open.

There are at least two acknowledged major technological limitations to GaN applications that represent a source for self heating effects, reduced performance, and poor reliability. They are:

- The lack of native substrate offering a route to the formation of high quality defect-free GaN layers with a reduction in the number of dislocations.
- The poor thermal conductivity characteristics as compared to that of Silicon Carbide.

1.1.2 GaN Substrates

The advantages of having a native GaN substrate have long been understood by the GaN research community. The advent of high quality GaN single crystal substrates would improve the homoepitaxy of GaN epilayer[9], thereby reducing significantly the defect density, mainly dislocation densities[17] as low as ~10^6 cm^{-2}. Laterally Epitaxially Overgrown (LEOG)[9,17] methods typically yield ~10^6-10^7 cm^{-2} dislocations[17] whereas the heteroepitaxy of GaN thin films incorporating a low temperature AlN buffer layer typically gives a dislocation density of 10^{10} cm^{-2} on sapphire[9,17] and silicon carbide[17,18]. A prime commercial incentive in lowering the dislocation density is the increase in blue laser life time in DVD applications[19]. By doping with shallow impurities such as silicon, magnesium, n and p type doping is achieved. With the introduction of deep level impurities such as iron, the formation of semi-insulating substrate is possible[19,20]. Semi-insulating wafers are currently under development[18,21]. The inherent increase of device performance should render GaN based technology more commercially competitive and should hopefully feed back with a further interest in the development of novel III-Nitride based technologies. This should result in increasingly higher device yield, improved resistivity uniformity, lower defect density, larger manufactured active device area, etc.

The major bottleneck in the fabrication of single crystal GaN substrate obtained by standard growth methods from stoichiometric melts is the high vapor pressure of nitrogen at the melting point of gallium nitride[9,17,19,20,22]. Several technologies have been developed to fabricate single crystal GaN substrates[19,20,22]. One of them consists of epitaxially growing GaN by Hydride Vapor Phase Epitaxy (HVPE)[9,19] starting from a sapphire template[9,17]. HVPE permits the achievement of high growth rates in the 100um/hr range compared to MOCVD techniques (~2 um/hr routinely, 10 um/hr at most)[9,23]. The GaN layer is removed from the sapphire substrate by laser lift-off and subsequently polished on both sides to yield a free-standing substrate[9,23]. Numerous variations in HVPE growth techniques have been considered to circumvent the apparition of cracks in a millimeter thick GaN layer.

HVPE grown GaN substrates incorporating a LEOG step have been investigated with yet no dramatic breakthrough[9,17,23].

Another method for the fabrication of true bulk GaN substrate relies on a high nitrogen pressure high temperature solution[24]. In this case, the substrates are virtually free of dislocations (around 100 cm^{-2} and less than 10^4 cm^{-2}) but at the expense of a small substrate area (~1 cm^2) and a high concentration of point defects[4,24]. Bockowski provides a detail explanation of the method[22].

In this work, we will consider the thermal conductivity characterization of state-of-the-art free-standing gallium nitride substrates providing by Kyma Technology located in Raleigh, North Carolina, USA. These crystals are grown by the hydride vapor phase epitaxy method. Other sample, of thin film GaN on Silicon wafers were provided by Nitronex Corporation. These samples were grown by MOCVD on (111) silicon.

1.1.3 Gallium Nitride Thermal Conductivity and Heat Transfer Limitations.

As mentioned in the introduction, for high temperature, high power, high frequency application, the Combined Figure of Merit (CFOM) of semiconductors expressed by Equation (1.1) shows that the thermal conductivity is a criteria for device performance as important as mobility in predicting theoretical limits of device performance beyond device design and material quality. Figure 1.2 illustrates that in comparison to silicon carbide or diamond or even silicon, gallium nitride seems to have a relatively low thermal conductivity.

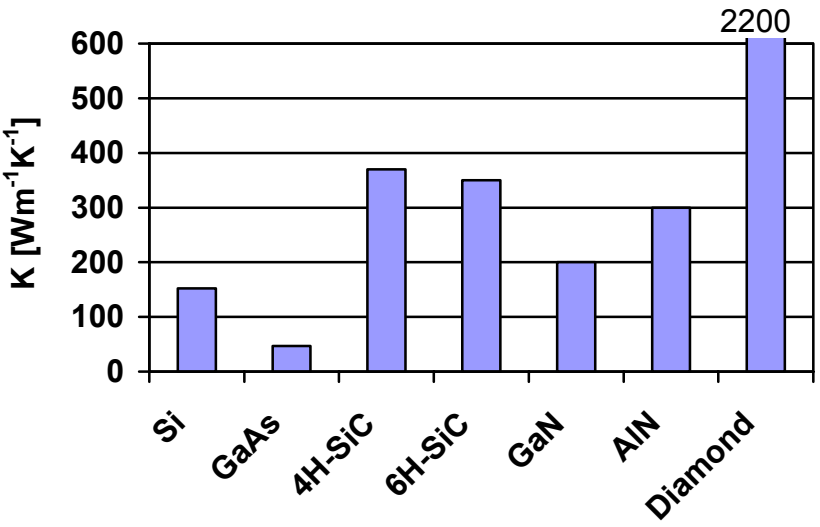

Figure 1.2. The thermal conductivity of gallium nitride is low relatively to its competitors used in similar applications. The gallium nitride thermal conductivity is estimated from Figure 1.3.

The thermal conductivity of gallium nitride is not well characterized as evidenced from Figure 1.3 that plots versus time room temperature thermal conductivity values reported by different research groups.

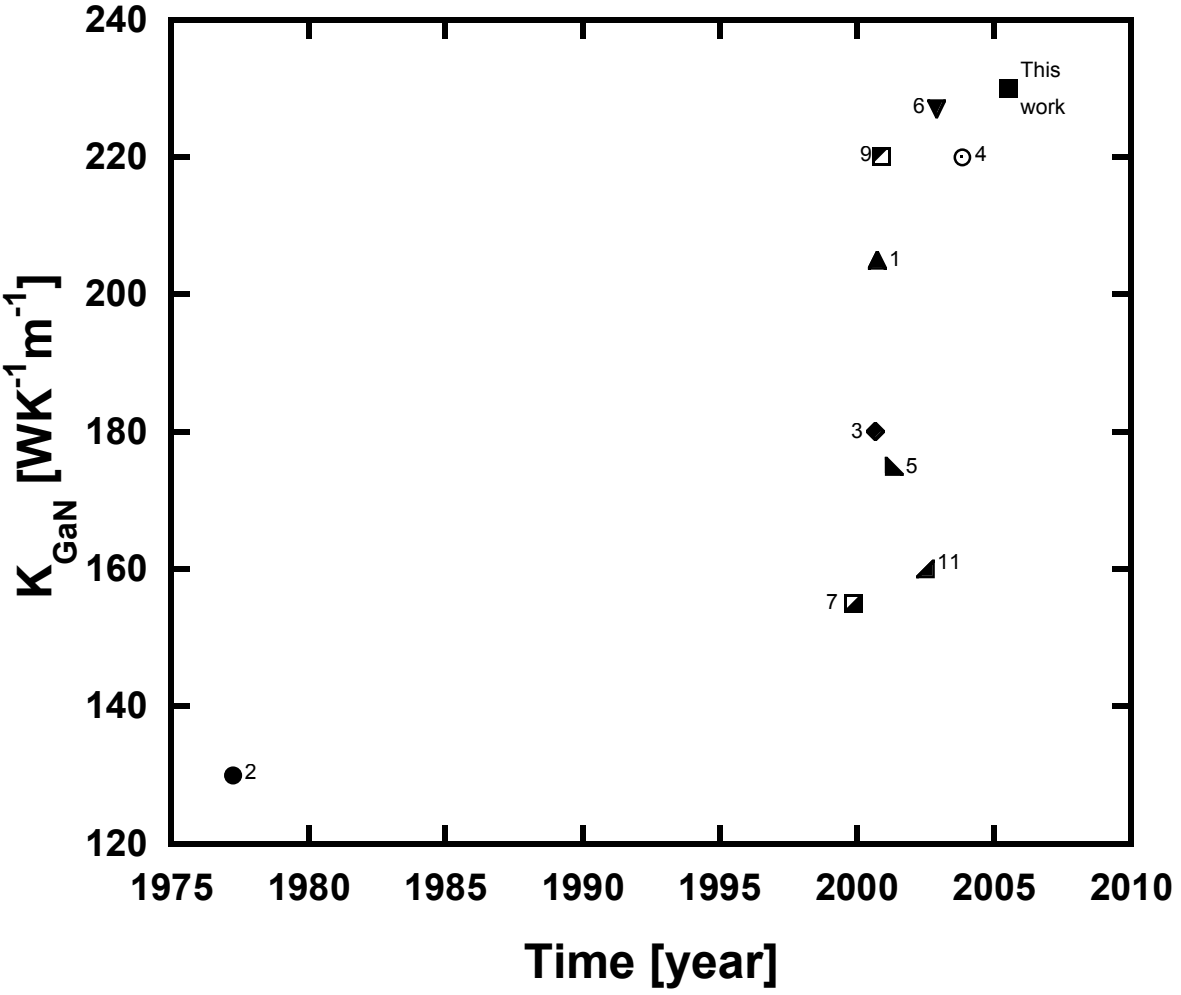

Figure 1.3. Experimental room temperature thermal conductivity of gallium nitride plotted against time in years corresponding to independent research studies. Each data point represents the highest value reported for each reference. The time corresponds to the official date of publication. A broad spread of values can be seen although they tend to be increasingly higher with time.

The first observation is that measured values are widely spread out. Though it seems there would be increasingly higher values reported with time. The differences observed in Figure 1.3 are not well understood except perhaps by the fact that gallium nitride thermal conductivity strongly depends on material quality[5,9]. Yet the precise nature underlying this dependence remains controversial.

In general, the determination of the thermal impedance of GaN based HEMTs and Lasers represents an active focus of research[15,25-28]. Depending on the choice of substrate (SiC, GaN, Si, sapphire, etc), the thermal resistance of HEMT structures

will change considerably. While the substrate can dominate the contribution to the thermal impedance, it remains unclear the precise effects of a multilayer stacks on thermal analysis. One problem is that the fundamental material characteristics of the individual layers are not well known. In contrast with silicon, gallium arsenide or silicon carbide, gallium nitride is grown on non-native substrate including the presence of buffer layers of various thicknesses and material composition. The impact of the buffer layers on heat transfer has been limited to only a few studies[26,27,29]. Chapter 5 will cover the thermal modeling of mulifinger AlGaN/GaN HEMT devices with the gallium nitride thermal parameters measured from Chapter 4. As pointed out in Ref. 27 and Ref. 30, despite the existence of complex thermal models, there is a lack for compact closed-form three-dimensional model that can be employed.

Practically speaking one can grow GaN on a non native substrate, but with high dislocation densities due to lattice mismatch and other problems which will limit the electronic and thermal properties of the resulting material. In ELO grown material, the electronic and thermal properties may be significantly improved, but the void, or masking layers between the good material and the substrate may be limiting. Third alternative would be to grow on native GaN substrates, and hopefully have high quality electronic material, and highly improved thermal conductivities over sapphire. Thus the growth of quasi defect-free GaN thin films would be possible on GaN substrate at the expense of a relatively low thermal conductivity detrimental to thermal management. Therefore the characterization of thermal conductivity is a key study for the development of GaN based technologies.

A review of state-of-the-art GaN thermal conductivity studies related to material quality and microscopic heat transport will be a focus in Chapter 4. It will be shown in detail how the thermal conductivity of GaN has been steadily increasing over the past decade and how further studies are necessary to narrow the origin of this on-going progress. However the focus of this thesis is inherently broader and its scope is addressed in the following introductory sections.

1.2 Thermal Conduction: Basic Concepts

Our main goal in this work is to characterize the thermal conductivity of GaN and conduct thermal analysis. It is therefore important to review the basic principle of macroscopic heat conduction that will support our analysis.

1.2.1 The Equation of Periodic Heat Conduction.

Heat exchange occurs via radiation, convection or conduction. The one-dimensional macroscopic heat conduction equation with no heat source can be derived by expressing the conservation of energy in a continuity equation between the divergence of the heat flux per unit area $\vec{\nabla}\bullet\vec{Q}_A=\vec{\nabla}\bullet\left(-\mathrm{K}\vec{\nabla}T\right)$ and the energy variations of the thermal mass -ρCp ∂T/∂t at a position (x,y,z) in space and is given for an isotropic homogeneous medium by[31]:

$$\rho C_P\frac{\partial T}{\partial t}=\mathrm{K}\frac{\partial^2 T}{\partial x^2}\Leftrightarrow\frac{\partial T}{\partial t}=\frac{\mathrm{K}}{\rho C_P}\frac{\partial^2 T}{\partial x^2}\Leftrightarrow\frac{\partial T}{\partial t}=\alpha\,\Delta T \qquad (1.2)$$

Where ρ is the density in $g\cdot cm^{-3}$ or $kg\cdot m^{-3}$, Cp is the specific heat in $J\cdot kg^{-1}\cdot K^{-1}$, κ is the thermal conductivity in $W\cdot K^{-1}\cdot m^{-1}$, and α=κ/ρCp is the diffusivity in $m^2\cdot s^{-1}$. Typical values for these parameters are given in Table 1.2 for several semiconductors and metallic solids.

Table 1.2. The density ρ, the heat capacity Cp, the thermal conductivity κ and the diffusivity α for various non-metallic and two metallic solids. An arbitrary nature lies on the κ and α of gallium nitride due to partly a lack of experimental data.

Material	ρ [$kg\cdot m^{-3}$]	Cp [$J\cdot kg^{-1}\cdot K^{-1}$]	K [$W\cdot K^{-1}\cdot m^{-1}$]	α [$mm^2\cdot s^{-1}$]
SiO_2	2220	745	1.38	8.3
Sapphire	3970	765	36	12
Silicon	2330	703	150	92
GaN	6150	490	130 < ?	40<?
6H-SiC	3200	640	350	170
Diamond	3500	509	2300	1300
Copper	8920	378	400	120
Aluminum	2700	888	236	98

In time-independent phenomena (static regime), the divergence of the heat flux with zero heat source is zero and the heat equation (1.2) reduces to the Laplace equation $\Delta T=0$ and is governed by the Fourier's law depending on the boundary conditions[31]. In time-dependent phenomena or dynamic regime, the specific heat is non-zero and harmonic analysis can be considered. Considering the temperature to be of the type $\exp(i\omega t)\cdot T(x,y,z)$ in case of periodic phenomena, the heat equation becomes[31]:

$$\Delta T - i\frac{\omega}{\alpha}T = 0 \qquad (1.3)$$

Equation (1.3) can be viewed as an Helmholtz equation with a complex wave vector. This is possible because the heat equation in Equation (1.2) is a parabolic equation (one derivative with respect to time) whereas the Helmholtz equation in electromagnetism derives from an hyperbolic equation (two derivative with respect to time). The solution of the one dimensional equation (1.3) can be expressed on the basis of two vectors[31]: $e^{\sqrt{\frac{i\omega}{\alpha}}x}$ and $e^{\sqrt{-\frac{i\omega}{\alpha}}x}$. The solution includes a damping term and an oscillating term[31] sometimes referred to as "thermal diffusing waves". A typical solution is given in Appendix A. The term $\lambda=(\omega/\alpha)^{-1/2}$ is called the penetration depth[32]. A complete solution necessitates the knowledge of the boundary conditions[31]. If transients are to be included, the initial conditions must be known. Equation (1.3) is inadequate to treat transient problems[31].

1.2.2 Complement to the Elementary Heat Conduction Equation.

The previous introductory section relies on important unstated assumptions that should be examined in the context of this study. In an unhomogeneous medium, the thermal conductivity is a function of spatial coordinate[31]. In our case, a thermal conductivity gradient across the film thickness potentially could take take place usually due to a gradient of material properties. This has been observed in CVD diamond layers grown on silicon substrates[33]. In the case of a gradient of material properties, the heat equation becomes[31]:

$$\rho\, Cp\frac{\partial T}{\partial t} = \vec{\nabla}\bullet\left(\mathrm{K}\vec{\nabla}T\right) \qquad (1.4)$$

The resolution of the heat equation (1.4) in a closed-form becomes extremely complex in most situations, if not impossible to solve analytically. Therefore we have resorted to finite element analysis to extract thermal conductivity measurements and conduct thermal analysis, one of the purposes of Chapter 3.

The second assumption we shall discuss is the dependence of thermal conductivity versus temperature. It is known that the thermal conductivity of solid-state semiconductor is actually a strong function of temperature[34]. The equation (1.2) is no long linear with respect to temperature, and a closed-form solution becomes tedious to extract, if not impossible to formulate[31]. However if the temperature variations are small compared to the gradient of thermal conductivity over the same temperature variations, Equation (1.2) holds true[35]. This approach represents nothing else than a small signal analysis treatment. It is the cornerstone of our experimental method to extract the thermal conductivity and it is discussed in Chapters 2 and 3.

Finally in an anisotropic medium, the thermal conductivity is better described by a tensor. It can be shown that the thermal conductivity in any directions can be described on the basis of three thermal conductivities called principal conductivities similar to the case of ordinary and extraordinary refractive index in anisotropic transparent homogeneous linear optical material[31]. The gallium nitride thermal conductivity varies easily by fifty percent depending on material quality (Figure 1.3). However, in the introductory part of Chapter 4, it will be seen that the isotropy assumption is excellent given the measurement uncertainties (±10%).

1.3 Thermal Conductivity Measurements

Accurate measurements of the fundamental physical properties such as thermal conductivity are crucial inputs into the thermal models used to develop sophisticated devices. Bhandari and Rowe[34] provide a fair and brief presentation of the challenges inherent to thermal conductivity characterization. Heat diffusion is by nature a dissipative process irreversible in time whereas electrical energy can be

transported via fully reversible guided waves with no loss in principle. Moreover unlike in electrical conductivity measurements in which electric current flow losses along the length of the sample can be prevented by suitable electrical isolation, it is very difficult to establish a similar loss-less situation in the measurements of the thermal conductivity. Indeed losses occur via radiation, convection and conduction requiring the presence of radiation shield and thermal insulation such as vacuum. These differences are precisely those that modify the nature of the characterization process and uncertainties in measurements. For large sample (Kg or 100 grams) and bulk materials thermal conductivity measurements are easier than for thin film materials where the thickness of the material may only be a few microns, the area less than a square centimeter and the total mass of the material of interest on the microgram scale.

1.3.1 Presentation of Semiconductor Thermal Conductivity Characterization Techniques

Thermal conductivity measurements can be divided into two groups: static methods and non-steady or dynamic methods[34,36]. All methods involve either the direct measurement of heat which passes through the sample (absolute methods) or the comparison of the amounts of heat flowing through a sample of known thermal conductivity (comparison method). In static methods, measurements are made only after thermal equilibrium has been established. They are generally time-consuming but relatively accurate. The determination of the thermal conductivity often requires the knowledge of the temperature, for instance measured with thermocouples. The heat flux may be determined from the power dissipated by an electrical heater or from a heat flow meter which may consist of a reference material of known thermal conductivity, usually of small size and low thermal conductivity. In a steady-state experiment, the thermal conductivity is deduced from Fourier's law using Equation (1.5) below:

$$k = \frac{Q_A}{\Delta T} \qquad (1.5)$$

The disadvantage with these techniques is that heat losses easily play a dominant role depending on the temperature of measurement and thermal conductivity magnitude and sample size. Several technical variations based on radial heat flow, the presence of guard, or the direct flow in electrically conductive sample are listed in ASTM standards[37-39] and were invented to extend the temperature range of measurements by minimizing heat losses or to accurately characterize specific material with specific thermal conductivity values and sample sizes.

In dynamic methods, thermal gradients are observed as a function of time, enabling measurements to be made relatively quickly and over a wide range of temperatures. However, in dynamic methods, it is usually the thermal diffusivity which is measured. The choice of method is governed initially by the intended temperature range of measurements. Static methods are typically employed at low temperatures and dynamic methods are typically employed at room temperature and above. A couple of dynamic methods have been used extensively and became classical techniques.

In the periodic temperature wave method (Angstrom's method), one end of a long rod-shaped sample is heated periodically. Along the rod, the temperature wave, measured by thermocouples, is attenuated and the thermal conductivity is deduced from the phase information carried by the thermal wave[34]. Transitory or pulse heated methods have also been employed. This is the case of the laser flash technique now widely commercially available. The thermal conductivity is inferred from the temperature decay characteristics measured on the back side of the sample which is heated on the front face by a laser of short pulse duration much smaller than the heat pulse transit time trough the sample[34].

Other miscellaneous methods may rely on the thermoelectric, photoacoustic or pyroelectric effect. For instance, AC calorimetric methods relying on the pyroelectric effects consist of a thin sample in good thermal contact with a pyroelectric crystal with very thin electrodes on both sides. Heat pulses at the surface of the thin sample diffuse to the pyroelectric crystal that produces a charge at the electrodes resulting in voltage drop decays through a load resistor connected

to the electrodes. The thermal property of the thin sample can be deducted form the voltage waveform in time-domain[34].

The photoacoustic effect has also been useful for thin films with low thermal conductivity. In this case, the heat absorbed by the sample heats the atmosphere near the surface of the sample resulting in a change of pressure that can be detected[34]. A variation of this technique is the mirage technique, where a probing laser beam parallel to the sample is deflected by the change in refractive index of the air above the sample when the air above the sample is heated by the incident laser pulse[34]. In all of these techniques the dynamic solution to the heat equation is of interest.

1.3.2 Selecting and Developing an Appropriate Technique

A large number of thermal conductivity characterization techniques has been devised depending on sample size and geometry, material phase, isotropy, homogeneity, thermal conductivity range, temperature range, immunity to heat loss, speed of measurement, accuracy, repeatability, cost, experimental complexity, etc… Numerous classes of techniques have resulted. Experimental uncertainty of new techniques can also be high, so the research community has conducted several round robin studies to validate different characterization techniques. For example, the thermal conductivity determination of diamond is especially challenging because of its high thermal conductivity, unique material geometry and properties[33] and required special technique considerations[33].

Nevertheless if most novel techniques serve a dedicated purpose to form a class of characterization technique, they generally consist of small modifications form preexisting methods. Two chief observations are to be made to assess the suitability of a technique to the characterization of GaN thermal conductivity and analysis of thermal management on GaN based devices. The first observation is that the GaN thermal conductivity is in the same range within an order of magnitude as the thermal conductivity of silicon and silicon carbide at room temperature as evidenced from Figure 1.2 and Figure 1.3. The second observation is that gallium nitride is a solid-state semiconductor often presents in thin films grown on non-native

substrate due to a lack of substrate commercially available. In thin films, gallium nitride is often combined with aluminium nitride (AlN) and aluminium gallium nitride (AlGaN) to form heterostructures[19,20]. A suitable technique would be one that accurately characterize in a simple and cheap manner thin film or small volume of semiconductor gallium nitride or related compound from room temperature to junction temperature.

A few techniques have been recently invented to characterize the thermal conductivity of thin films as the investigation of nanoscale level heat transport applicable to integrated circuit has become increasingly important. Several authors have written thorough review articles on the subject[35,40]. Few key principles are specific to the thermal conductivity measurement of thin films. In this introductory section, thin films refer to thin layers of solid-state material whose thicknesses range from 10nm to 100um[40]. Methods can divide into steady-state or transient, conductivity along layer or conductive normal to layer, contact or non-contact. Uncertainty analysis becomes of greater importance as the film becomes thinner since the substrate and film-to-substrate thermal conductivity contrast contribute to larger uncertainties. A description of normal-to-layer and along-layer characterization techniques are given by Goodson and co-authors[40]. In a 1998 review article[35], Cahill analyses what he considers the most useful approaches for characterizing heat transport in thin film. He distinguished between diffusivity methods, some of which are derived from the Angstrom method, and thermal conductance methods that comprise the 3ω method and the thermoreflectance technique. The former will be described in the next section while the latter is a non contact transient normal-to-layer technique used by Käding at al. in 1994[41].

In the thermal reflectance technique, a temperature decay arises from the high energy laser pulse heating a thin metal layer deposited on the material under study. The decay time constant equals the metal film thickness time the heat capacity divided by the sample conductance. The decay time constant is deduced by measuring the reflectivity of the metal layer using another laser and detector as the metal reflectivity is a weak but measurable function of temperature.

1.3.3 Gallium Nitride Thermal Conductivity Characterization Techniques.

A suitable technique to measure the thermal conductivity of small volume material with thermal properties comparable to those of gallium nitride is the 3ω method introduced by Cahill in 1987[32]. Different terminologies for the 3ω method can be found in the literature such as harmonic joule heating or third harmonic method. This absolute normal-to-layer dynamic technique relies on the diffusion of thermal waves at relatively low frequency, typically ~10Hz to ~10,000Hz, from a heating wire (or microbridge) in contact with the sample but the thermal conductivity is directly measured instead of the diffusivity. An illustration of the technique principle is given in Figure 1.4.

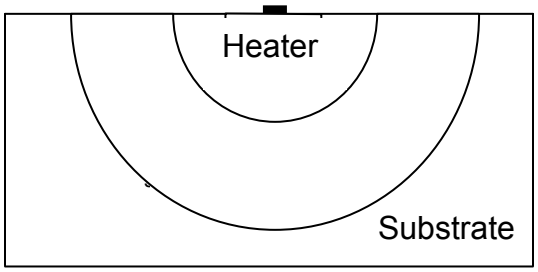

Figure 1.4 Isothermal representing the thermal waves present in the 3ω method and diffusing into the substrate from the heater. The temperature rise at the heater is directly related to the thermal conductivity of the underlying substrate.

This method also presents the advantage to reduce heat losses due to radiation and convection, and becomes particularly suitable for measurements at room temperature and above due to a decreasing diffusivity at higher temperature. The implementation is relatively simple and relatively cheap for solid-state material presenting a reasonable smooth surface. Measurements are usually fast and accurate although sample preparation including lithography can be lengthy[32]. The technique has been widely used for the thermal conductivity determination of SiO_2 and silicon[35]. In this work, the 3ω technique was adopted to characterize the thermal conductivity of gallium nitride structures. An important point of focus in Chapter 3 is that the formalism for the heat diffusion model underlying the 3ω technique is tailored to the analysis of heat transfer and thermal management of typical HEMT and Laser structures.

In the 3ω technique a ~1mm long ~10um wide metal strip is lithographically patterned on the substrate that serves both as a heater and sensor. An ac current with modulation frequency ω is passing through the narrow metal wire. The resulting joule heating generates a heat flux modulated at a frequency 2ω that diffuses into the underlying material under vacuum. Thermal waves oscillate at a frequency 2ω in the specimen and their amplitude is a function of the sample geometry and penetration depth $\lambda = \sqrt{\frac{k}{2\omega\rho C_p}}$ determined from the thermal conductivity k, heat capacity Cp, density ρ and frequency of oscillation ω. The average oscillation temperature over the heater width causes a 2ω modulation of the wire resistance via the non-zero temperature coefficient α_T. A third harmonic, approximately one thousandth the total voltage drop, develops across the wire with virtually no alteration of the heating power. The first harmonic $V_{1\omega}$ taken across a potentiometer in series with the heater is subtracted from the total voltage drop across the heater allowing the in-phase and out phase component of the third harmonic $V_{3\omega}$ to be detected by a lock-in amplifier. Chapter 2 will provide further detailed description of the measurement technique with experimental data.

Several authors have used the 3ω method to study the thermal conductivity of gallium nitride[5,7,42,43]. However, virtually no work has addressed the potential of the 3ω technique to characterize the thermal property when the film-to-substrate thermal conductivity contrast is high, which is likely be the case of GaN/sapphire or GaN/silicon. It is the scope of Chapter 3 to extend the validity of this technique to the case of high thermal conductivity film on low thermal conductivity substrate.

A set of GaN studies[1,3,44] has been conducted using a Scanning Thermal Wave Microscope (SThM) on GaN films thicker than or equal to 2-3 microns regardless of the substrate. Actually this technique is in principle closely related to the 3ω method. It consists of a non-destructive evaluation technique of imaging subsurface structure with high frequency thermal waves from 2kHz to 100kHz typically. The thermal imaging is achieved using a “V” shaped resistive thermal element of curvature radius of 1um incorporated at the end of an atomic force microscope cantilever. Detail experimental descriptions are given in the

literature[35,45]. If high spatial resolution can potentially be achieved with a SThM in some situations compared to most thin film techniques, the thermal conductivity uncertainty depends on a compelled tedious calibration procedure yielding room temperature measurements in the best case. Experimental complexity and cost[46] are other factors limiting its use. Another technique derived from the photothermal effect has been employed to measure the thermal conductivity of gallium nitride although the reported temperature dependence seems somewhat underestimated and controversial[11]. Accurate and reliable low temperature measurements were obtained by Slack[6] and Jeżowski and co-authors[4] using a steady state technique but on bulk GaN materials. On bulk material always, the laser flash technique was employed to measure the thermal diffusivity from 300K to 600K. Hence the thermal conductivity was computed assuming a known heat capacity[9]. In a 1977 pioneer study, Sichel and Pankove[2] measured the thermal conductivity temperature dependence of a 400um thick gallium nitride layer grown on a sapphire substrate with an along-layer steady-state technique. In Chapter 4, a deeper look into the physical properties of the thermal conductivity of gallium nitride will be given.

1.4 Objectives

The main purpose of this work is to characterize the limitation of heat transfer in III-Nitride structures.

Of prime importance is to characterize the thermal conductivity of gallium nitride and relate film property to GaN thermal conductivity in a comprehensive approach. To this effect, measurements will be taken on epi and bulk gallium nitride grown on sapphire and silicon using the 3ω method. Due to the specific property of gallium nitride grown on non-native substrate, the 3ω method was applied with a new set of experimental conditions that require new developments. The heat conduction models must be reviewed and adjusted as gallium nitride presents a high thermal conductivity relative to sapphire, normal-to-layer unhomogeneous material properties, and a layer thickness that varies inaccurately for state-of-the-art samples grown in different conditions.

Of second importance is to investigate the governing parameters important to the thermal design of multifinger HEMT structures. Comparative studies between the thermal performance of AlGaN/GaN HEMT on SiC substrates and AlGaN/GaN HEMT on GaN substrate can be possible provided the thermal properties of gallium nitride are characterized. In order to identify differences of performance from a thermal design viewpoint, it is necessary to analysis the thermal resistance of GaN HEMT by decoupling the effects from the substrate, film layers, finger geometry, buffer layer, etc. For instance, the impact of the presence of an AlN buffer layer between GaN and SiC on the thermal resistance can be readily examined analytically. Expressing the thermal resistance of mutlifinger devices in an accurate but compact expression represents an on-going challenge that must be addressed in this study.

1.5 Dissertation Outline

The remainder of the thesis is organized as follows:

-Chapter 2 provides a detail description of thermal conductivity measurements employing the 3ω method. Routine procedures as well as state-of-the-art development in the field is presented. Calibration measurements are discussed in light of published work. Measurement on thin film GaN grown on silicon and bulk GaN is presented and the conditions for proper data interpretation are discussed.

-Chapter 3 investigates the analytical and numerical modeling of heat conduction to determine the thermal property thin films such as gallium nitride from measurements using the 3ω method. The possibility for the 3ω technique to extract the thermal conductivity is investigated in the case of high thermal conductivity thin film with the presence of interfacial boundary resistance based on analytical work applicable to the case of gallium nitride grown on silicon or sapphire.

-Chapter 4 represents a core study of this thesis. It addresses the factors limiting the thermal conductivity of gallium nitride depending on growth techniques and growth conditions affecting film properties. The effect of dislocation on the GaN thermal conductivity is examined. Chapter 4 shows an empirical dependence of thermal conductivity on dislocation densities in agreement with several theoretical studies. The temperature dependence of the thermal conductivity is discussed. Results on defect density characterization are presented in Appendix D.

-Chapter 5 explores the modeling of the thermal resistance of three dimensional multifinger AlGaN/GaN HEMTs with the gallium nitride thermal parameters taken from Chapter 4. Based on the results of Chapter 3, an original, compact and accurate closed-form expression for the thermal resistance is derived in order to be conveniently and accurately employed for device design. Analytical expressions are properly derived in appendices A, B and C, while the accuracy of the model is compared against simulated results in Chapter 5. The chief purpose of Chapter 5 is the comparative study between thermal performances of heteroepitaxially grown AlGaN/GaN HEMTs on silicon carbide and homoepitaxially grown AlGaN/GaN HEMTs.

-Chapter 6 summarizes the work and proposes future work.

1.6 References

1 D. I. Florescu, V. M. Asnin, F. H. Pollak, A. M. Jones, J. C. Ramer, M. J. Schurman, and I. Ferguson, "Thermal conductivity of fully and partially coalesced lateral epitaxial overgrown GaN/sapphire (0001) by scanning thermal microscopy," *Applied Physics Letters*, vol. 77, pp. 1464, 2000.

2 E. K. Sichel and J. I. Pankove, "Thermal-Conductivity of Gan, 25-360k," *Journal of Physics and Chemistry of Solids*, vol. 38, pp. 330-330, 1977.

3 V. M. Asnin, F. H. Pollak, J. Ramer, M. Schurman, and I. Ferguson, "High spatial resolution thermal conductivity of lateral epitaxial overgrown GaN/sapphire (0001) using a scanning thermal microscope," *Applied Physics Letters*, vol. 75, pp. 1240-1242, 1999.

4 A. Jezowski, B. A. Danilchenko, M. Bockowski, I. Grzegory, S. Krukowski, T. Suski, and T. Paszkiewicz, "Thermal conductivity of GaN crystals in 4.2-300K range," *Solid State Communications*, vol. 128, pp. 69-73, 2003.

5 C. Luo, D. R. Clarke, and J. R. Dryden, "The temperature dependence of the thermal conductivity of single crystal GaN films," *Journal of Electronic Materials*, vol. 30, pp. 138-146, 2001.

6 G. A. Slack, L. J. Schowalter, D. Morelli, and J. A. Freitas Jr., "Some effects of oxygen impurities on AlN and GaN," *BNS 2002, May 18-23 2002*, vol. 246, pp. 287-298, 2002.

7 C. Y. Luo, H. Marchand, D. R. Clarke, and S. P. DenBaars, "Thermal conductivity of lateral epitaxial overgrown GaN films," *Applied Physics Letters*, vol. 75, pp. 4151-4153, 1999.

8 E. O. Johnson, "Physical limitations on frequency and power parameters of transistors," *RCA Review*, vol. 26, pp. 163-177, 1965.

9 R. P. Vaudo, G. R. Brandes, J. S. Flynn, X. Xu, M. F. Chriss, C. S. Christos, D. M. Keogh, and F. D. Tamweber, "Synthesis and properties of HVPE nitride substrates," *Proceedings of International Workshop on Nitride Semiconductors, 24-27 Sept. 2000*, pp. 15-18, 2000.

10 R. W. Keyes, "Figure of merit for IC packaging.," *IEEE Journal of Solid-State Circuits*, vol. SC-13, pp. 265-266, 1978.

11 M. Kamano, M. Haraguchi, T. Niwaki, M. Fukui, M. Kuwahara, T. Okamoto, and T. Mukai, "Temperature dependence of the thermal conductivity and phonon scattering time of a bulk GaN crystal," *Japanese Journal of Applied Physics Part 1-Regular Papers Short Notes & Review Papers*, vol. 41, pp. 5034-5037, 2002.

12 B. J. Baliga, "Power Semiconductor-Device Figure of Merit for High-Frequency Applications," *Ieee Electron Device Letters*, vol. 10, pp. 455-457, 1989.

13 H. Kim, V. Tilak, B. M. Green, H.-y. Cha, J. A. Smart, J. R. Shealy, and L. F. Eastman, "Degradation characteristics of AlGaN-GaN high electron mobility transistors," *Reliability Physics Symposium, 2001. Proceedings. 39th Annual. 2001 IEEE International*, pp. 214-218, 2001.

14 S. Nakamura, "III-V nitride-based blue LDs with modulation-doped strained-layer superlattices," *Compound Semiconductors, 1997 IEEE International Symposium on*, pp. 1-4, 1998.

15 J. Park, C. C. Lee, J.-W. Kim, J.-S. Lee, W. S. Lee, J.-H. Shin, and M. W. Shin, "Thermal analysis of GaN-based HFET devices using the unit thermal profile approach," *Proceedings of the International Conference on Silicon Carbide and Related Materials 2001, Oct 28-Nov 2 2001*, vol. 389-393, pp. 1523-1526, 2002.

16 C. Lee, L. Witkowski, M. Muir, H. Q. Tserng, P. Saunier, H. Wang, J. Yang, and M. A. Khan, "Reliability evaluation of AlGaN/GaN HEMTs grown on SiC substrate," *High Performance Devices, 2002. Proceedings. IEEE Lester Eastman Conference on*, pp. 436-442, 2002.

17 P. Gibart, "Metal organic vapour phase epitaxy of GaN and lateral overgrowth," *Reports on Progress in Physics*, vol. 67, pp. 667-715, 2004.

18 K. K. Chu, P. C. Chao, M. T. Pizzella, R. Actis, D. E. Meharry, K. B. Nichols, R. P. Vaudo, X. Xu, J. S. Flynn, J. Dion, and G. R. Brandes, "9.4-W/mm power density AlGaN-GaN HEMTs on free-standing GaN substrates," *Electron Device Letters, IEEE*, vol. 25, pp. 596-598, 2004.

19 H. Morkoç, *Nitride semiconductors and devices*. Berlin ; New York: Springer, 1999.

20 S. Nakamura, S. J. Pearton, and G. Fasol, *The blue laser diode : the complete story*, 2nd updated and extended ed. ed: Springer, 2000.

21 R. P. Vaudo, X. P. Xu, A. Salant, J. Malcarne, and G. R. Brandes, "Characteristics of semi-insulating, Fe-doped GaN substrates," *Physica Status Solidi a-Applied Research*, vol. 200, pp. 18-21, 2003.

22 M. Bockowski, "Growth and doping of GaN and AlN single crystals under high nitrogen pressure," *Crystal Research and Technology*, vol. 36, pp. 771-787, 2001.

23 G. Martinez-Criado, M. Kuball, M. Benyoucef, A. Sarua, E. Frayssinet, B. Beaumont, P. Gibart, C. R. Miskys, and M. Stutzmann, "Free-standing GaN grown on epitaxial lateral overgrown GaN substrates," *Journal of Crystal Growth*, vol. 255, pp. 277-281, 2003.

24 S. Porowski, "Bulk and homoepitaxial GaN-growth and characterization," *Journal of Crystal Growth*, vol. 189-190, pp. 153-158, 1998.

25 V. O. Turin and A. A. Balandin, "Performance degradation of GaN field-effect transistors due to thermal boundary resistance at GaN/substrate interface," *Electronics Letters*, vol. 40, pp. 81-83, 2004.

26 K. A. Filippov and A. A. Balandin, "The effect of the thermal boundary resistance on self-heating of AlGaN/GaN HFETs," *MRS Internet Journal of Nitride Semiconductor Research*, vol. 8, pp. 8, 2003.

27 A. M. Darwish, A. J. Bayba, and H. A. Hung, "Thermal resistance calculation of AlGaN-GaN devices," *IEEE Transactions on Microwave Theory and Techniques*, vol. 52, pp. 2611-2620, 2004.

28 W. J. Hwang, T. H. Lee, L. Kim, and M. W. Shin, "Determination of junction temperature and thermal resistance in the GaN-based LEDs using direct temperature measurement," *Physica Status Solidi C: Conferences*, vol. 1, pp. 2429-2432, 2004.

29 J. Park, M. W. Shin, and C. C. Lee, "Thermal modeling and measurement of GaN-based HFET devices," *Ieee Electron Device Letters*, vol. 24, pp. 424-426, 2003.

30 A. M. Darwish, A. J. Bayba, and H. A. Hung, "Accurate determination of thermal resistance of FETs," *Ieee Transactions on Microwave Theory and Techniques*, vol. 53, pp. 306-313, 2005.

31 H. S. Carslaw and J. C. Jaeger, *Conduction of heat in solids*, 2nd ed. ed: Clarendon Press ;Oxford University Press, 1986.

32 D. G. Cahill and R. O. Pohl, "Thermal-Conductivity of Amorphous Solids above the Plateau," *Physical Review B*, vol. 35, pp. 4067-4073, 1987.

33 J. E. Graebner, H. Altmann, N. M. Balzaretti, R. Campbell, H. B. Chae, A. Degiovanni, R. Enck, A. Feldman, D. Fournier, J. Fricke, J. S. Goela, K. J. Gray, Y. Q. Gu, I. Hatta, T. M. Hartnett, R. E. Imhof, R. Kato, P. Koidl, P. K. Kuo, T. K. Lee, D. Maillet, B. Remy, J. P. Roger, D. J. Seong, R. P. Tye, H. Verhoeven, E. Worner, J. E. Yehoda, R. Zachai, and B. Zhang, "Report on a second round robin measurement of the thermal conductivity of CVD diamond," *Diamond and Related Materials*, vol. 7, pp. 1589-1604, 1998.

34 C. M. Bhandari and D. M. Rowe, *Thermal conduction in semiconductors*. New York: Wiley, 1988.

35 C. L. Tien, A. Majumdar, and F. M. Gerner, *Microscale energy transport*. Washington, D.C.: Taylor & Francis, 1998.

36 P. R. W. Touloukian Y.S., Ho C. Y., Klemens P. G., "Thermophysical Properties of Matter," *The TPRC Data Series*, vol. 1,2, 1970.

37 ASTM Standard C1113 Test Method.

38 ASTM Standard E1225 Test Method.

39 ASTM Standard C 177 Test Method.

40 K. E. Goodson and M. I. Flik, "Solid layer thermal-conductivity measurement techniques," *Applied Mechanics Reviews*, vol. 47, pp. 101-112, 1994.

41 O. W. Kading, H. Skurk, and K. E. Goodson, "Thermal Conduction in Metallized Silicon-Dioxide Layers on Silicon," *Applied Physics Letters*, vol. 65, pp. 1629-1631, 1994.

42 W. Liu and A. A. Balandin, "Thermal conduction in AlxGa1-xN alloys and thin films," *Journal of Applied Physics*, vol. 97, pp. 1-6, 2005.

43 C. Mion, Y. C. Chang, J. F. Muth, P. Rajagopal, and J. D. Brown, "Thermal conductivity of GaN grown on silicon substrates," *GaN and Related Alloys - 2003, Dec 1-5 2003*, vol. 798, pp. 381-386, 2003.

44 D. I. Florescu, V. A. Asnin, L. G. Mourokh, F. H. Pollak, and R. J. Molnar, "Doping dependence of the thermal conductivity of hydride vapor phase epitaxy grown n-GaN/sapphire (0001) using a scanning thermal microscope," *The 1999 MRS Fall Meeting - Symposium W 'GaN and Related Alloys', Nov 28-Dec 3 1999*, vol. 595, pp. 3-89, 2000.

45 O. Kwon, L. Shi, and A. Majumdar, "Scanning thermal wave microscopy (STWM)," *Journal of Heat Transfer*, vol. 125, pp. 156-163, 2003.

46 ThermoMicroscopes/Park Instruments, 1171 Borregas Avenue, Sunnyvale, CA 94089.

Chapter 2 The 3ω Method: Principles and Measurements

2.1 The 3ω Technique: Fundamentals.

When a sinusoidal current at frequency ω is sourced through a resistor, in addition to a sinusoidal voltage across the resistor at that frequency, a voltage signal at 3 times the source frequency also appears. This was noticed by Corbino in 1911, and is a consequence of the temperature dependence of resistivity. In the early 60's, the third-harmonic signal found practical applications to measure various thermal properties of liquids and solids such as the dynamic heat capacity, the thermophysical properties of thin wires, etc[1,2].

In this thesis, the term "3ω method" will refer to the technique developed in 1987 by Cahill and Pohl[3] , where a thin electrically conductive wire is deposited onto a solid-state specimen whose thermal conductivity needs to be measured. In most thermal conductivity measurement technique, heat is generated at a known rate and temperature is sensed to deduct the thermal conductivity. In the case of the 3ω method, the same wire serves both as a heater and a sensor. There are several significant advantages to the 3ω method. The two most important for this thesis is that it permits thermal conductivity measurements of thin films which would otherwise be very difficult due to their small mass, and since it is an AC technique it is relatively immune to errors from blackbody radiation when performed at elevated temperatures.

2.1.1 The Heat Source.

Let us consider a thin narrow long metal wire deposited onto an isotropic homogeneous semi-infinite dielectric medium in vacuum with no radiation and convection losses. Cahill demonstrates the radiation losses are negligible in the 3ω method over a large range of temperature centered at room temperature[3,4]. An AC current $I_t=I_0\cos(\omega t)$ at angular frequency ω across the heater generates a finite heat flux due to joule heating in the metal line of resistance R_0 dissipating into the material with the power given to first order as :

$$P_t = R_0 I_t^{\,2} = P + P\cos(2\omega t) \geq 0 \text{ where } P = \frac{I_0^{\,2} R_0}{2} \qquad (2.1)$$

R_0 is the resistance of the line for a time independent continuous current. Let us first consider the power component $P_t=P\cdot e^{2i\omega t}$ as a sole source of energy. The heat flux per unit area is $Q_A\cdot e^{2i\omega t}= P_l/(2b)\cdot e^{2i\omega t}$ at the heater-substrate interface where b is the wire half-width and $P_l=P/l$ is the power per unit length, and l the wire length illustrated in Figure 2.1.

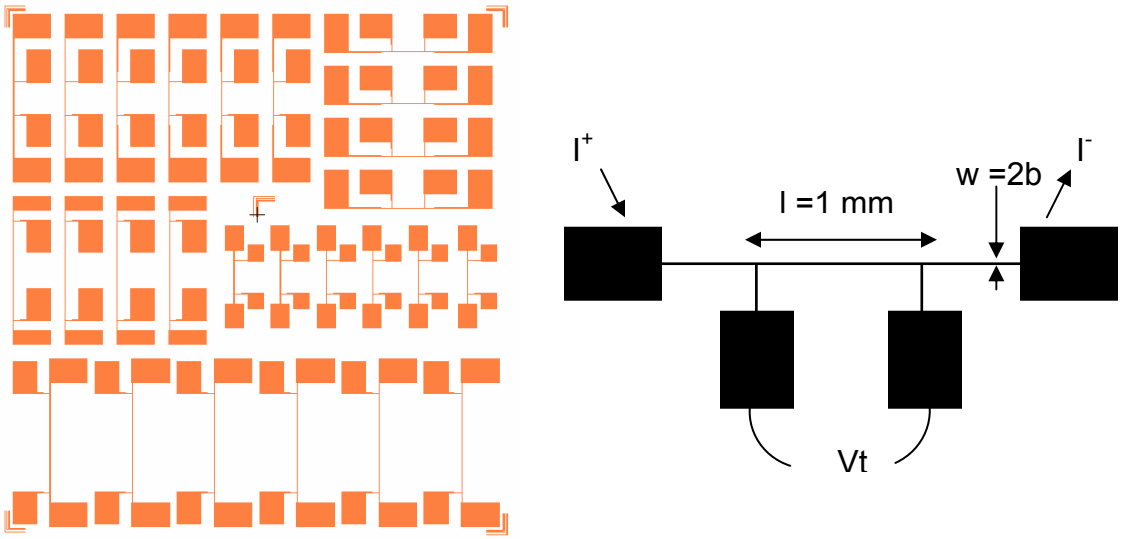

Figure 2.1. Four point heater: a) of different width and length for effective testing and: b) top view showing the length and width of the structure.

In this simplified analysis, any thermal or electrical effects due to the heater are disregarded. The heater only serves as a heat carrier[4]. Thus, a sinusoidal heat

source flux gives raise to a complex temperature oscillation field $T(x,y,z)\cdot e^{2i\omega t}$ in the medium beneath the heater and is a solution of the heat equation[4-7]:

$$\Delta T - i\frac{2\omega}{\alpha}T = 0 \qquad (2.2)$$

The solution of the heat equation depends on the spatial coordinates (x,y,z), the geometry of the line, the thermal conductivity κ_s of the substrate, the penetration depth $\lambda=(\mathbf{2}\omega/\alpha)^{-1/2}$ and the boundary conditions. The heat flux amplitude is zero on the surface of the sample except at the location of the heat source where it varies sinusoidally with time. The temperature oscillations decay with increasing distance from the heat source. In case of a heater with half-width b, the complex temperature oscillation ΔT spatially averaged over the heater width is given as[4]:

$$\Delta T = \frac{1}{2b}\int_{-b}^{+b} T(x, y=0)dx = \frac{P}{\pi d\kappa_s}\int_0^{\infty}\frac{\sin^2(u)}{u^2}\frac{du}{(u^2+iq^2b^2)^{1/2}} \qquad (2.3)$$

Where "q" is the inverse of the penetration depth $\lambda=(\mathbf{2}\omega/\alpha)^{-1/2}$. Solution (2.3) is the relative temperature oscillation about the mean at the heater induced by the periodic heat flux. At vanishingly small frequencies such that $b/\lambda<1$, Solution (2.3) can be approximated as[4,8].

$$\Delta T = \Delta T_{in} + i\Delta T_{out} = \frac{P_l}{\pi\kappa_s}\left(\frac{1}{2}\ln\frac{\alpha}{b^2} + 0.923 - \frac{1}{2}\ln(2\omega) - \frac{i\pi}{4}\right) \qquad (2.4)$$

The accuracy of the approximation can be seen in Figure 2.2 as Equations (2.3) and (2.4) are normalized to $P/(\pi l k_s)$ and plotted against b/λ.

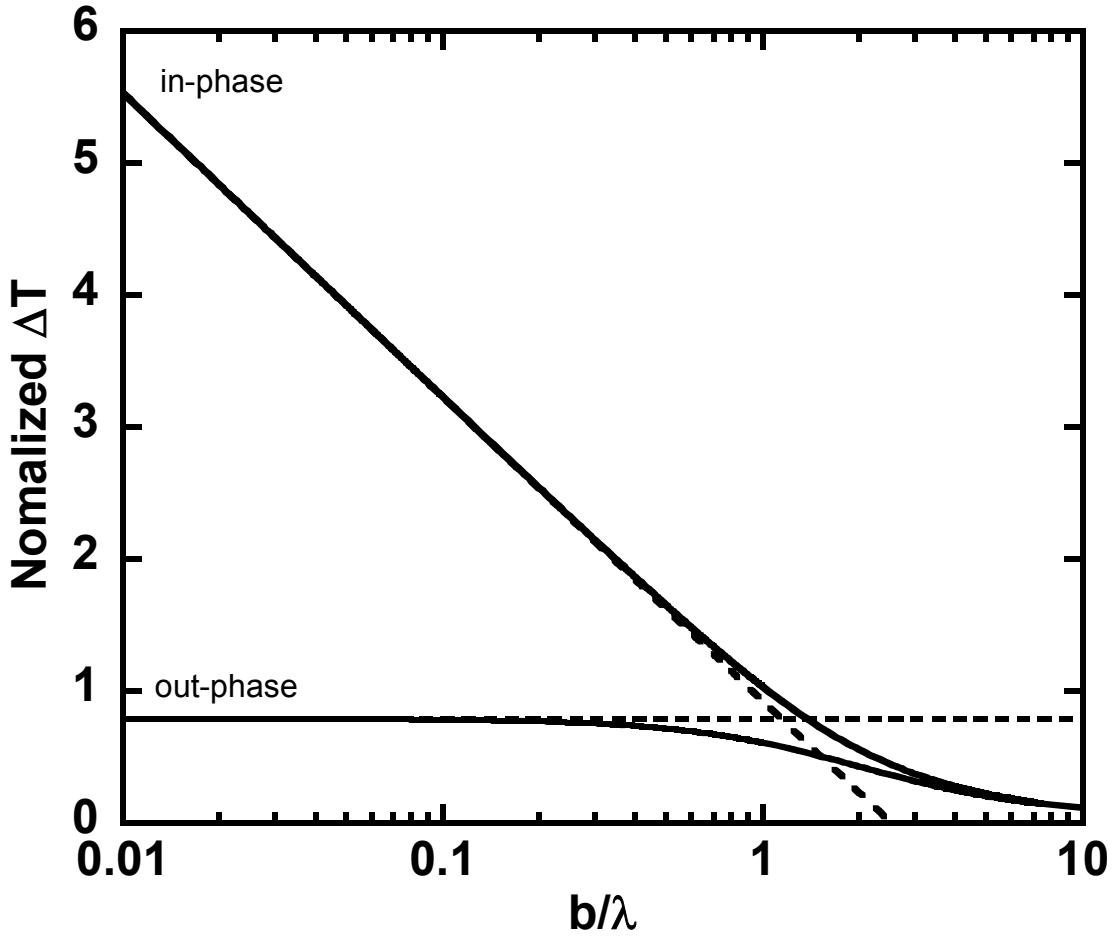

Figure 2.2. The real (in-phase) and imaginary part (out-phase) of the Equations (2.3) and (2.4) were plotted in plain line and dotted line respectively. ΔT was normalized to the pre-factor of Equation (2.3), ie P/(lπks).

The real part of the temperature oscillation ΔT_{in} (in-phase) at the heater is inversely proportional to the thermal conductivity κ_s and proportional to the logarithm of the angular frequency ω[4,8]:

$$\frac{\Delta T_{in}}{P} = \frac{1}{2\pi l \kappa_s} \ln(\omega) + Cst_{not\ \omega} \qquad (2.5)$$

$Cst_{not\ \omega}$ is an expression independent of ω. The derivative of Equation (2.5) with respect to ln(ω) can be derived from the case of an infinite line source with zero width[3]. The heat flux is estimated by computing the joule heating based on electrical

measurements of current and voltage across the wire. The sensing of the temperature oscillations is presented in the following section.

2.1.2 The Sensor

The detection of the complex temperature oscillation amplitude at the heater/substrate interface, can be expressed as:

$$\Delta T(\omega) = \Delta T_{in} + \Delta T_{out} = \Delta T_0(\omega)\exp(i\varphi(\omega)) \qquad (2.6)$$

is performed by sensing the change of resistance ΔR of the metal line with temperature via the non-zero intensive temperature coefficient resistance $\alpha_T=(1/R)(dR/dT)$ of the metal line[1,4,8].

$$\begin{aligned} R_t &= R_0 + \Delta R \\ &= R_0\left[1 + \alpha_T \Delta T_0(\omega)\cos\left(2\omega t + \varphi(\omega)\right)\right] \end{aligned} \qquad (2.7)$$

In other words, the thermometer is defined by the resistance versus temperature relationship. It is desirable to choose a metal line with elevated temperature coefficient inert to oxygen and easy to pattern. Gold represents an appropriate candidate, α_T is typically measured close to $0.003K^{-1}$ at room temperature[2, 7], but is found to be dependent on deposition methods and should be experimentally determined for precision measurements. ΔT_o can be estimated from Equations (2.4) and (2.6) by plugging in typical experimental values: a 10Ω resistance, a 20mA current, b=5μm, a pulsation ω of 500Hz, and typical room temperature physical parameters of either SiO_2, sapphire or silicon. It results a ΔT_o ranging between ~0.1 and ~1K in agreement with measurements[4,8]. This implies that $\Delta R/R_t$ is typically 1/1000 which in turn implies that the 3ω signal will be small in comparison to the voltage at frequency ω. Due to the driving current I(t) through the heater, the voltage V_t across the wire, as a mere function of α_T in first order development, becomes[1,4,8]:

$$V_t = I(t)R(t) = \mathrm{I}_0 \cos(\omega) R_0 \left[1 + \alpha_T \Delta T_0(\omega) \cos(2\omega t + \varphi)\right]$$
$$\approx V_{1\omega} \cos \omega t + \left(V_{1\omega} \frac{\alpha_T \Delta T_0}{2} \right) \cos(3\omega t + \varphi) \quad (2.8)$$

Equation (2.8) indicates the existence of a third harmonic voltage component[1,4,8]:

$$V_{3\omega} = V_{1\omega} \frac{\alpha_T \Delta T_0 \exp(i\varphi)}{2} = V_{1\omega} \frac{\alpha_T (\Delta T_{in} + i\Delta T_{out})}{2} \quad (2.9)$$

The small values of the temperature coefficient α_T and temperature oscillation ΔT account for the $V_{3\omega}$ measured nearly one thousand times lower than the first harmonic voltage $V_{1\omega}$. It also accounts for the negligible dependence of the electrical power in equation (1.1) on α_T (and $V_{3\omega}$). Agreement between theory and experiment shows that the development to first order in α_T represents an excellent approximation[4,7,8]. The total voltage drop V_t is measured on a four-point pad heater while the in-phase $V_{3\omega in}$ and out-phase $V_{3\omega out}$ of the third harmonic are sensed using a lock-in amplifier[7,9]. Provided α_T is known, the in-phase ΔT_{in} and out-phase ΔT_{out} are deduced through relation (2.9)[4,7,8]. Section 2.3 discusses experimental details.

2.1.3 Extracting the Thermal Conductivity: the Slope Method.

It takes two separate independent measurements to extract the thermal conductivity at a given temperature.

- First the output $V_{3\omega}$ from the lock-in is measured against the input angular frequency ω of the generator. In the meantime, electrical parameters $V_{1\omega}$, R_h, P_h are recorded.
- The second measurement is the temperature coefficient α_T. Section 2.3 discusses experimental details.

$\Delta T(\omega)$ is deduced through Equation (2.9). Normalizing $\Delta T(\omega)$ to the electrical power P, the thermal conductivity is deduced by taking the slope of $\Delta T_{in}/P$ versus

ln(ω) using Equation (2.5). Figure 2.3 gives a typical $V_{3\omega}$ versus ln(ω) curve taken on a 1mm thick glass substrate.

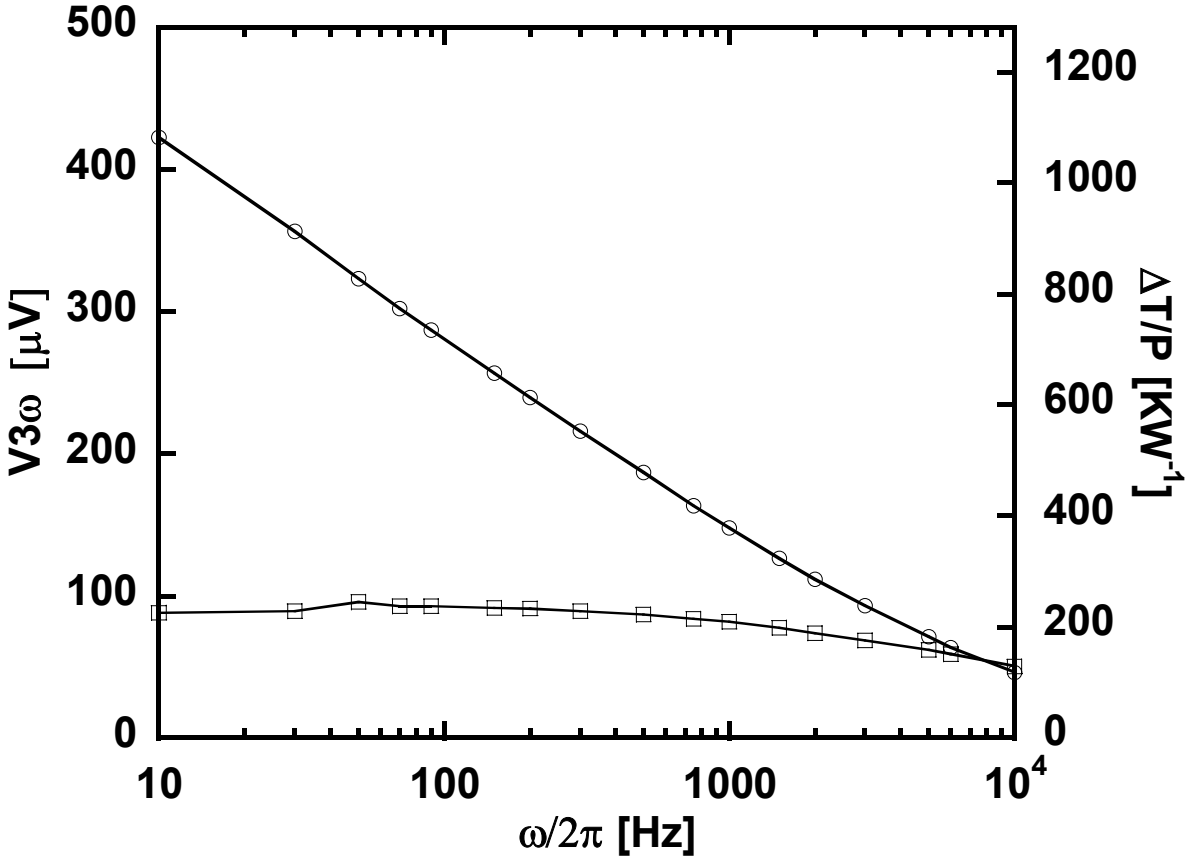

Figure 2.3. Typical $V_{3\omega}$ versus lnω curves for a 1mm thick glass slide. The line with circles represents the in-phase signal while the line with square plots the out-phase signal. From the measurement of the temperature coefficient α_T the ΔT/P was deduced (right vertical axis) . The thermal conductivity was found 1.1 $W \cdot K^{-1} \cdot m^{-1}$ (±10%) from the slope of the in-phase. Handbook[16] value gives 1.1 $W \cdot K^{-1} \cdot m^{-1}$.

Proportional to $V_{3\omega}$ is ΔT/P plotted on the right axis of Figure 2.3. Therefore Figure 2.3 also provides a typical $\Delta T_{in}/P$ versus ln(ω) curve. Deducing the thermal conductivity from the slope of $\Delta T_{in}/P$ versus ln(ω) is a valid approach provided the underlying heat diffusion models and assumptions to Figure 2.3 are faithfully reproducing the experimental conditions.

Several assumptions essential to the derivation of Equation (2.5) are easily invalidated during experiment with an observable impact on data interpretation.

i) First the sample is not infinite. The penetration depth will increase as the frequency decreases up to a point where the penetration depth exceeds the sample thickness: $\lambda/d_s>1$ (d_s sample thickness). A previous study has shown that it actually requires $5\lambda/d_s<1$ to for the Equation (2.5) to be in less than 1% error due to the finite sample thickness[10]. Whereas for $\lambda/d_s\sim1$, it was shown that Equation (2.5) can easily lead to an error of 20% in measured thermal conductivity[10].

ii) Secondly the frequency is not vanishingly small. At high frequencies, the penetration depth becomes comparable to the heater half-width $b\sim\lambda$ and Equation (2.3) must be considered instead of Equation (2.5)[4,8]. In that case, the dependence of ΔT is no longer linear with the thermal conductivity κ via the diffusivity α. At very high frequency, the solution is better approximated by an infinite plane heater (or a plane heater with negligible boundary effects)[1,11]. In that case, the temperature oscillation ΔT is inversely proportional to the effusivity, the product of thermal conductivity and heat capacity.

iii) One may think of considering the high frequency regime to deduce the thermal properties of the substrate[1,11]. Unfortunately, the this is experimentally difficult to implement in practice as several research groups have experimentally shown[10,12] because of a third assumption that limits the validity of the Equation (2.5) before reaching the high frequency regime, that is: the heat capacity of the heater is non-zero and the heater thickness is non-zero[10,12]. In the high frequency regime where the heat is confined in the vicinity of the heater due to a decreasing thermal penetration depth at increasing frequencies ΔT becomes is a strong function of the heater film thickness and heater heat capacity[10,12], this can result in large errors if Equation (1.5) is used.

In practice Equation (2.5) is valid when ω covers approximately the 10Hz-10,000Hz range[7,10]. This satisfies the conditions $b/\lambda<1$, and $\lambda/d_s<1$ (d_s sample thickness) for samples of hundreds of microns thick that have a relatively low thermal conductivity (1 $W\cdot K^{-1}\cdot m^{-1}$) at room temperature. That is why numerous studies employing the 3ω method have been routinely performed on low thermal conductivity (~1 to 10 $W\cdot K^{-1}\cdot m^{-1}$) amorphous dielectric materials. Indeed, it was used extensively by its inventor and other groups to investigate the thermal conductivity of

amorphous glass and other low thermal conductivity bulk solids such as KDP potassium dihydrogen phosphaste crystal (KH2PO4)[8,11], polymethylmethacrylate (PMMA)[3,13], amorphous As_2S_3[3], Ca-K nitrate glass[3], $CdGeAs_2$ glass[14], SiO_2 based glasses[1,3,4] triglycine sulfate[8], etc. Actually by increasing the frequency thereby decreasing the penetration depth, the thermal conductivity of thick films of ~50um of low thermal conductivity SiO_2 film were measured[15].

One can also use the 3ω method to measure the thermal conductivity as a function of temperature. For standard semiconductors, the penetration depth at a given frequency increases drastically as the temperature decreases below room temperature because the diffusivity shots up via an increasing thermal conductivity and decreasing heat capacity[16]. Therefore for a certain range of decreasing temperature below room temperature, the condition $\lambda/d_s<1$ is unlikely to hold depending on the sample thickness. This is not the case of glasses because the thermal conductivity has fairly smooth variations over a large temperature range[3,4,14,15].

Conductive samples such as undoped gallium nitride or silicon must be also be electrically insulating from the heater to preserve the integrity of the four-point electrical measurement. Such an insulation is carried out via the deposition of a ~100nm SiO_2 layer on the substrate prior to heater formation whose impacts on the heat diffusion are unimportant to the method as explained in a next section.

There are a few assumptions that hold true in almost any 3ω method experiments reported up-to-date.

i) First, the dependence of thermal conductivity on temperature can be neglected throughout a 3ω measurement because, as demonstrated in a previous section, the temperature oscillations are very small (less then 1K) for a large set of experimental parameters. Therefore the treatment of the problem is that of a small signal analysis and the cornerstone Equation (2.3) is linear with temperature.

ii) Second, the effects of transients are negligible, which legitimatizes Equation (2.3). The power in Equation (2.1) also presents a time-independent component that establishes a temperature gradient in the sample[9,10], thus allowing the total temperature rise to be positive at anytime, compatible with the principles of

thermodynamic. The temperature at the heater can be summarized as $T_0+\delta T_c+\delta T_{ct}+\Delta T+\delta T_{\omega t}$ where T_0 is the initial equilibrium temperature of the sample before starting the experiment, δT_c is the constant temperature rise due to the time-independent component of the Power P, δT_{ct} is the transient temperature of the constant power, ΔT is the periodic oscillation at 2ω due to the oscillation power at 2ω, and $\delta T_{\omega t}$ is the transient as the frequency varies. The transient times can be estimated from the delay τ for the heat to diffuse within a characteristics length x_c to be determined. In the case of $\delta T_{\omega t}$ in the 3ω method, the author of the present thesis estimates that the heat will be mostly confined within a penetration depth, so that $x_c \sim \lambda$.

$$x_c = \sqrt{\alpha\tau} \Leftrightarrow \tau = \frac{x_c^{\,2}}{\alpha} \Rightarrow \tau = \frac{\lambda^2}{\alpha} = \frac{\alpha/2\omega}{\alpha} = \frac{1}{2\omega} \qquad (2.10)$$

Equation (2.10) states that for ω covering the 10Hz-10,000Hz range, the transient will be in the order of a few hundreds of milliseconds, to perhaps a few seconds at most, which is perfectly in agreement with Figure 2.4 representing elementary time-dependent finite-element simulations.

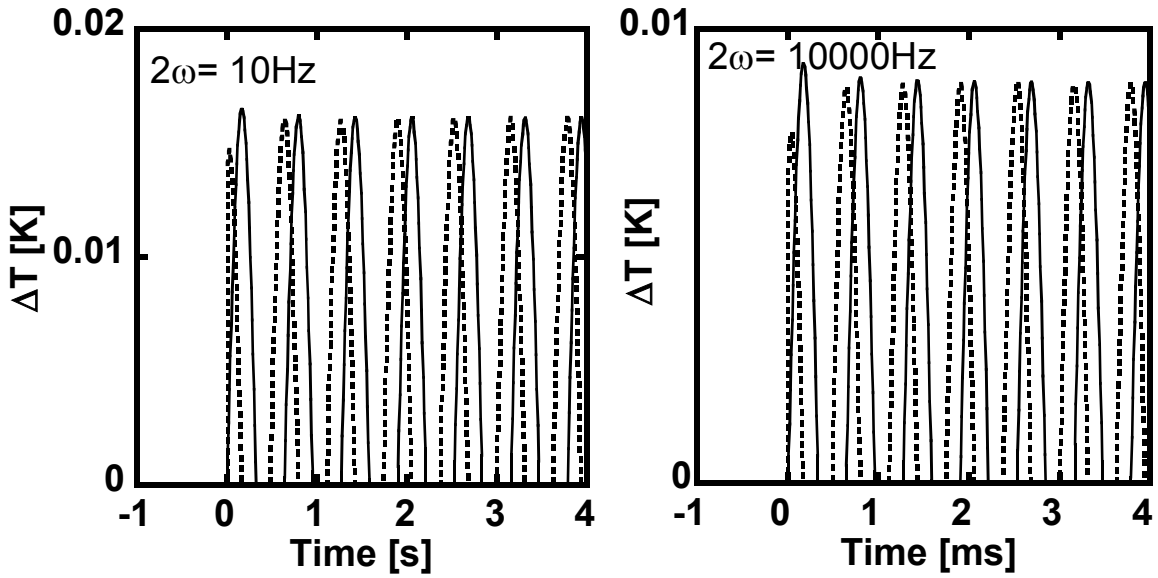

Figure 2.4. The time-dependent temperature oscillations ΔT were simulated by numerical calculation (FEM) on a 5 cm wide by 5cm deep silicon substrate at room temperature starting at t=0 for two frequencies ω=5Hz (left graph) and ω=5000Hz (right graph). For each frequency, two solutions corresponding to different initial conditions of the heat flux were computed: in solid line $Q=10^5\sin(\omega t)$ and in dotted line $Q=10^5\cos(\omega t)$. The heat flux 10^5 $W\cdot m^{-2}$ is typical of experimental values. It can be seen that in either case, the transient vanishes after a few cycles in agreement with Equation (2.10). Note the differences in time scale and amplitude oscillation between the two different situations ω=10Hz and ω=10,000Hz.

Experimentally, the transient term is not observed since small waiting period is used before taking each point. In the case of δT_{ct}, x_c can be matched with the substrate depth. A realistic worst case scenario considering a 5mm thick amorphous material with a thermal diffusivity 10 times lower than that of SiO_2 gives a τ~30s for a δT_{ct}, estimate (3s with 5mm thick SiO_2). δT_{ct} arises only with a change in power of the heater. In the 3ω method, thermal equilibrium is reached quickly and measurement of the third-harmonic is fast. The transient temperature gradient quickly achieves a constant temperature shift in the sample with respect the bath temperature as the system becomes stationary[9]. Thanks to short equilibrium times, accurate control of the temperature of the oven or cryostat for hours is not required for the 3ω method[6].

A final assumption whose validity is usually not questioned is the homogeneity of the sample. In the case of GaN samples, like some diamond samples, the dislocation density can vary significantly with sample thickness. Thus we will include the effect of unhomogeneous material properties in heat models.

2.2 Review on the Extension of the 3ω Method

The methodology presented previously is referred to as the “slope-method”. It is merely a particular case of the overall possibilities the 3ω technique can offer. In case the assumptions underlying Equation (2.5) are not applicable, it does not imply that the thermal conductivity cannot be deduced. On the contrary, it means that more elaborate heat models are needed to account for the experimental conditions and that a proper experimental procedure and experiment planning must be developed to characterize the thermal properties of the desire sample. There are several variations of the 3ω technique, but all have originated based on the same heating and sensing principles previously presented. The differences in the solution of heat equation are just shaped by thermal, electrical and geometrical parameters[15]. Nonetheless, it is important to keep in mind that the 3ω technique becomes particularly powerful and advantageous over other techniques when the slope method, meaning the linearity between $\Delta T(\omega)$, κ, and $\ln(\omega)$, can be verified by experimental condition with a high level of precision. In this thesis the characterization of GaN thermal conductivity will require the development of new methodologies relying on the 3ω method. A review on extensions to the 3ω method presented so far is now given.

2.2.1 Differential Technique

The first extension to the 3ω technique was the measurement of thin film thermal conductivity of dielectric deposited onto a substrate, typically SiO_2 on silicon. In 1994, Cahill *et al.*[17] reported a detail explanation of the methods. In the case of one-dimensional heat flow that occurs in a thin film of low thermal conductivity deposited on a substrate with high thermal conductivity (relative to that of the thin film) the temperature oscillation ΔT_{S+F} averaged over the heater width is the linear sum of the temperature oscillation ΔT_S at the film-substrate interface and the temperature gradient across the film ΔT_F:

$$\Delta T_{F+S} = \Delta T_S + \Delta T_F \quad with\ \Delta T_F = P\frac{k_F d_F}{l2b} \tag{2.11}$$

ΔT_S is the temperature oscillation obeying Equation (2.3), k_F and d_F the film thermal conductivity and film thickness respectively. A cross-sectional schematic of the heat flow in the sample is represented in Figure 2.5.

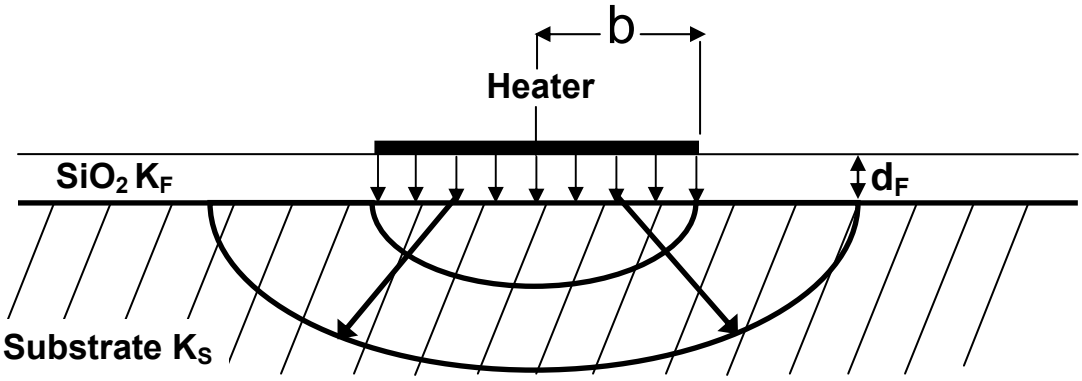

Figure 2.5. Schematic of the heat flow for a low thermal conductivity thin film on substrate for K_F <<Ks and d_F<2b.

Equation (2.11) is valid for $k_F/k_S<<1$ and $d_F/2b<<1$ which matches the condition for one-dimensional heat flow in the film[18]. k_F/k_S represents the film-to-substrate thermal conductivity contrast. Therefore the presence of a film adds a thermal offset to Equation (2.3) independent of frequency. Thus the film thermal conductivity and the substrate thermal conductivity can be determined.

The experimental procedure is as follows. First ΔT_S is measured or calculated versus lnω in the case of a heater deposited on a bare substrate with no film using Equation (2.5) for reference. Then with a heater on a film-on-substrate sample, ΔT_{F+S} is recorded versus lnω. From the difference ΔT_{F+S}-ΔT_S, the thermal offset ΔT_F is deduced and the product $k_F \cdot d_F$ is calculated based on Equation (2.11). By varying the film thickness and repeating the measurement for ΔT_{F+S} for each film thickness, the film thermal conductivity is inferred. Any method based on the difference ΔT_{F+S}-ΔT_S is called the “differential” 3ω technique. Note that it is essential to measure the film thickness and heater half-width with great precision. All in all, the method is

tailored to low-thermal conductivity film with high uniformity that can be precisely measured. The film must be electrically insulating and samples with different film thicknesses must be synthesized. Equation (2.11) provides a solution to measure the thermal conductivity of electrically conductive bulk samples using the slope method via the deposition of an electrically insulating layer, such as 100nm PECVD SiO_2 or Si_2N_3.

The nature of the thermal boundary resistance (TBR) between two materials in intimate contact with a large mismatch of thermal conductivity has been the focus of numerous studies employing the 3ω method. The boundary resistance R_{ab} between one layer of thermal conductivity k_a and another layer of thermal conductivity k_b along one dimension z is defined as:

$$\begin{cases} K_a \dfrac{dT_a}{dz} + R_{ab}^{-1}(T_a - T_b) = 0 \\ K_a \dfrac{dT_a}{dz} = K_b \dfrac{dT_b}{dz} \end{cases} \tag{2.12}$$

From a macroscopic viewpoint, a thermal boundary resistance can be thought as the thermal resistance of a very thin layer of thermal conductivity k_c and thickness d_c sandwiched between two layers with zero heat spreading:

$$R_{ab} = \frac{d_c}{k_c} \tag{2.13}$$

It takes two conditions for Equation (2.13) to complete the definition of a thermal boundary resistance. First the thickness d_C becomes infinitely thin. However the condition that $d_C/k_C=R_{ab}$ remains finite and non-zero must be met. Therefore k_C must go to zero. More precisely, $k_C=d_C/R_{ab}+\varepsilon$ with ε going to zero while d_C vanishes to zero, R_{ab} being a finite and non-zero real. If R_{ab} is zero, then k_C can take any non-zero arbitrary values but this case is trivial. R_{ab} going to infinity sets an adiabatic boundary condition.

A Thermal boundary resistance R_{ab} has standard international units of $K{\cdot}m^2{\cdot}W^{-1}$. In the case of the 3ω technique, the existence of a boundary layer R_{sf} between a film and a substrate adds a thermal resistance to the film resistance in a one-dimensional heat diffusion model. Equation (2.11) must be rewritten as:

$$\Delta T_{F+S} = \Delta T_S + P\frac{d_F}{l2b}\left(\frac{1}{k_F} + \frac{d_F}{R_{SF}}\right)^{-1} \quad (2.14)$$

One can then define an apparent thermal conductivity K_{app} function of film thickness:

$$k_{app} = \left(\frac{1}{k_F} + \frac{d_F}{R_{SF}}\right)^{-1} \quad (2.15)$$

Equation (2.14) is identical to Equation (2.11) if the film thermal conductivity k_F is substituted by the apparent thermal conductivity k_{app} with the same assumptions for Equation (2.14) as for Equation (2.11). Following the same measurement methods, the determination of ΔT_{F+S}-ΔT_S for varying film thicknesses yields the thermal boundary resistance R_{SF} in addition to the film thermal conductivity k_F. An illustration of the method on ~100nm SiO_2 and SiN_x is illustrated by Lee and Cahill[18]. They determined a thermal boundary resistance of R_{sf} ~$2\cdot10^8$ $K\cdot m^2\cdot W^{-1}$ between the SiO_2 film and the silicon substrate at room temperature equivalent to a 20nm SiO_2 layer (SiO_2 has a thermal conductivity of ~1.4 $W\cdot K^{-1}\cdot m^{-1}$)[18]. Thus the measurement of thermal boundary resistance using this methodology becomes a useful concept by which different physical situations can be compared. In general this method has become useful for a wide variety of low-thermal conductivity thin films. For example : α-Si:H[17], sputtered Al_2O_3[19], sputtered Ti_2O_3[19,20], evaporated Ti_2O_3[20], κ-Al_2O_3[21], α-Al_2O_3[21], α-C:H[22], polymers[23], low-permittivity dielectric Xerogel[24], polycrystalline AlN[25], ultra-low permittivity dielectrics[26], SiO_2[7,18,20,27-29], polyimide[29], etc. have all be studied using the differential 3ω technique.

A different body of works, also based on the differential 3ω technique, has addressed the thermal conductivity characterization of superlattices acting as a single film-like structure with an apparent thermal conductivity k_{app} instead of k_F. The observed thermal conductivity reduction in superlattices, whose origin is still the focus of intense research[30-32], is favorable to meet the condition $k_F/k_S<<1$ while $d_F/2b<<1$ is often verified although these assumptions are not always verified so that complex methods were developed to extract the thermal conductivity value. A variety of superlattices were studied, such as: Si-Ge[33,34], $IrSb_3/CoSB_3$[35], Ge quantum dots[36],

$AlAs_xSb_{1-x}$[37], InAs/AlSb[38], Bi_2Te_3/Sb_2Te_3[31], etc… In this case it is important that several remarks be made or reiterated.

i) The measured thermal conductivity of the superlattices represents an apparent thermal conductivity. It implies that, if the characterization of each component of an arbitrary multilayer stack turns to be laborious, it may be instead carried out through an effective thermal conductivity of the complete stack. In the case of superlattices, if they are well defined and atomically smooth one can also attempt to describe the situation by considering the quantum mechanical solution of heat transport by phonons through the superlattice, and tie the low thermal conductivity to more basic principles. In practice this has been difficult, but the ability to make reproducible measurements of the apparent thermal conductivity has been useful.

ii) Electrically isolation of electrically conductive superlattices from the heater is achieved with the presence of an extra cap layer, usually a PECVD SiO_2 layer of assumed known thickness and thermal conductivity value. The temperature drop across the cap layer, most likely SiO_2, is calculated from Equation (2.11) and is subtracted to the temperature oscillation recorded on top of the cap layer/supperlattice/substrate to deduce the superlattice/substrate temperature oscillation. The higher the number of post-processing data steps, the higher the uncertainty becomes. In some papers, it is not clear if the role of the capping layers have been fully characterized.

iii) A few research groups have investigated the anisotropy of the thermal conductivity of strongly anisotropic films including superlattices by varying the heater width and fitting the solution of the heat equation by successive iteration of the thermal conductivity values[10,39-41] or via simplified analytical expressions instead[29]. Errors in the substrate conductivity can also affect the superlattice thermal conductivity uncertainty, which can be reduced by decreasing the k_F/k_S ratio[10], if possible.

2.2.2 Extending the 3ω Method to Multilayer stacks.

In this section, state-of-the-art extensions to the 3ω technique will be introduced. Because GaN and related compounds offer a variety of experimental conditions, a review will be given on the degree of applicability of the differential and slope methods of 3ω technique and the validity of approximations underlying the method. This section will also highlight the degree to which extensions of the 3ω techniques can permit the characterization of planar multi-stack layered structures with arbitrary layer thicknesses and arbitrary thermal parameters.

Borca-Tasciuc *et al.*[10] thoroughly addressed the limitation and accuracy of the 3ω technique for a wide range of sample conditions by examining the temperature oscillation present at the location of the heater deposited on n layers. The substrate is the nth layer, n=1 corresponding to a bare substrate. The j^{th} layer has a thermal conductivity ky_j in the cross-plane, kx_j in the in-plane, a diffusivity αy_i in the cross-plane, and a thickness d_j. The heater is deposited on the top of the sample, that is to say on top of the first layer j=1 and generates thermal waves of frequency 2ω with a power P over a width 2b and length l. The temperature oscillation ΔT averaged over the heater width 2b is given by a recursive relationship[7,10]:

$$\Delta T = \frac{-P}{\pi l k_{y1}} \int_0^{\infty} \frac{1}{A_1 B_1} \frac{\sin^2(bu)}{(bu)^2} du$$

With
$$\begin{cases} A_{j-1} = \dfrac{A_j \dfrac{k_{yj} B_j}{k_{yi-1} B_{i-1}} - \tanh(\varphi_{j-1})}{1 - A_j \dfrac{k_{yj} B_j}{k_{yj-1} B_{j-1}} \tanh(\varphi_{j-1})}, j = 2..n \\ B_j = \left(k_{xyj} u^2 + i \dfrac{2\omega}{\alpha_{yj}} b^2 \right)^{1/2}, \varphi_j = B_j \dfrac{d_j}{b}, k_{xy} = k_x / k_y \\ A_n = -\tanh^p(B_n d_n) \quad p = \begin{vmatrix} 1 \text{ if adiabatic backside} \\ 0 \text{ if semi-infinite backside} \\ -1 \text{ if isothermal backside} \end{vmatrix} \end{cases} \quad (2.16)$$

The coefficient B_j is a function of i, the unity-modulus $\pi/2$-argument imaginary complex number. The coefficient A_n is determined by the boundary condition at the bottom surface of the nth layer, namely the substrate. The parameter p is set to zero for a semi-infinite substrate (A_n=-1), p=-1 for a finite substrate with isothermal bottom boundary, or else p=1 corresponds to an adiabatic bottom boundary. The coefficient A_j is defined only for n≥2 which corresponds to at least one layer on a substrate. The parameter k_{xy} is the ratio of the in-plane to cross-plane thermal conductivity. Note that Equation (2.16) is identical to Equation (2.13) for n=1 for a semi-infinite isotropic substrate corresponding to k_{xy}=1 and p=0 (A_n=-1).

Recursive formulas are typical in the solutions of heat equation for multilayer stacks and take different analytical forms according to the method of resolution[5]. It is well-known that the end-result leads to cumbersome expressions as the number of layers grows beyond unity[5]. Finding an appropriate formalism to express a compact solution oftentimes represents a challenging task unlike the solutions offered by the formalism developed in microwave or optics theory. For instance, Hao analyses the

heat transfer of multilayered microdevices in a time-independent regime[42]. To a certain extent, Hao presents similar treatments with different approaches and analytical expressions[42]. The derivation leading to Equation (2.16) originates in a relative straightforward manner from an original matrix approach based on thermal diffusive waves[6,7] inspired by the formalism describing the phenomenon of optical interferences in strongly absorbing medias. Note that Equation (2.16) above does not include the thermal effects due to the presence of the heater but does account for anisotropy when one principal axe of the thermal conductivity tensor is perpendicular to the film plane or when the off-diagonal component of the thermal conductivity tensor can be neglected. The thermal conductivity and diffusivity parameters are independent of spatial coordinates and temperature. Furthermore notice that Equation (2.16) does not explicitly account for interfacial boundary thermal resistance.

Amongst the multiple analysis presented by Borca-Tasciuc *et al.*[10], two will be briefly highlighted:

i) The applicability of the slope method affected by finite dimensional effects such as the finite substrate thickness.

ii) And the conditions for applicability of the differential 3ω technique for a single film on substrate.

For sake of simplicity and for the most relevant trends to stand out, we will assume in our discussion that the anisotropy factor is sufficiently close to one, ie kx~ky although the factor kxy may appear in analytical expressions. For the case of a quasi-isotropic semi-finite substrate with a line source, the normalized slope is defined as:

$$\text{Normalized slope} = \frac{d\Delta T}{d\ln(\omega)} x \frac{1}{-P/(\pi lks)} = 0.5 \qquad (2.17)$$

Equation (2.17) is in agreement with Equation (2.5). For a finite substrate with adiabatic bottom boundary and a non-zero heater width, It was shown that the Normalized slope can deviate considerably from 0.5. In that case, it may be a strong function of the b/λ, ds/λ , and $\beta_S=d_S/b$ ratios, d_S being the substrate thickness and b the heater half-width. At low frequencies where the penetration depths approach the

substrate thickness, the normalized slope oscillates and can easily be in error by ±20% leading to the same relative error on the thermal conductivity. On the other hand as the heater half-width increases, the error in the normalized slope increases for short penetration depth when at high frequencies. In other words, for all these situations, the extracted thermal conductivity will depend appreciably on the geometrical parameters b, ds and ω. Kim *et al.*[7] provide an illustration. They reported the thermal conductivity measurement on high diffusivity diamond plate by considering a two-layer model. They obtained a slightly better fit to the data with a finite substrate thickness than with an infinite one. Conversely Putnam *et al.*[13] measured the thermal conductivity of low thermal conductivity PMMA (k~0.205 $W \cdot K^{-1} \cdot m^{-1}$) where the condition $b/\lambda<1$ is easily invalidated. The out-of-phase data was then fit to the full numerical solution of the diffusion equation, Equation (2.3).

In the general case of single-film-on-substrate systems with arbitrary film thicknesses and film thermal conductivity, the differential method leads to[10]:

$$\Delta T_{F+S} - \Delta T_S \neq \Delta T_F \quad with\ \Delta T_F = P\frac{k_F d_F}{l2b} \tag{2.18}$$

This is because the heat flow is not necessary one-dimensional depending on the k_F/k_S, d_F/d_S, and d_F/b ratios. Borca-Tasciuc *et al.*[10] examined the ΔT_{F+S}-ΔT_S difference for $k_F<k_S$ considering the following expression:

$$\Delta T_{F+S} - \Delta T_S = \frac{Pd_F}{2blk_{Fy}}\left(1-\frac{k_{Fx}k_{Fy}}{k_s^2}\right)\times \frac{2}{\pi}\int_0^\infty \frac{\sin^2 t}{t^3}\frac{\tanh(t\beta_F)}{\beta_F\left(1+\tanh(t\beta_F)\dfrac{\sqrt{k_{Fx}k_{Fy}}}{k_s}\right)}dt \tag{2.19}$$

The above Equation (2.19) was derived from Equation (2.16) assuming a single film on a semi-infinite substrate with no interfacial boundary resistance at ω=0. One may define an apparent film thermal conductivity expressed as:

$$\frac{k_{Fy}}{kapp} = \left(1 - \frac{k_{Fx}k_{Fy}}{k_s^2}\right) \times \frac{2}{\pi}\int_0^{\infty} \frac{\sin^2 t}{t^3} \frac{\tanh(t\beta_F)}{\beta_F\left(1 + \tanh(t\beta_F)\dfrac{\sqrt{k_{Fx}k_{Fy}}}{k_s}\right)} dt \qquad (2.20)$$

The apparent thermal conductivity is measured in practice instead of the film thermal conductivity k_F. Clearly the ratio $K_{Fy}/K_{app}=1$ cannot be assumed in the general case. However if $K_F/K_S<<1$ and $\beta_F<<1$, then $K_{Fy}/K_{app}=1$ implements a fair approximation and Equation (2.3) is valid. Note the definition of k_{app} through relation (2.20) may not always be of practical interest.

Several extensions to the 3ω method were implemented based on the work presented by Borca-Tasciuc *et al.*[10] and Kim and co-authors[7]. The effects of the thermal capacity and finite thickness of the heater on the temperature oscillations were examined[10,12]. A group of researchers have presented a procedure to extract the heater thickness and heater heat capacity from measurements at high frequency[12]. Borca-Tasciuc *et al.*[10] provide a detail explanation on the methodology employed to back-up the thermal conductivity of anisotropic films, although Goodson *et al.*[29] have characterized anisotropic thin dielectric films with simplified heat model contrasting with Equation (2.16). Another recent study[9] has developed a numerical gradient-based search algorithm with two-dimensional impedance models based on the recursive heat Equation (2.16) to allow up to four degrees of freedom per material layer. From measurements in the high frequency and low frequency range, the thermal conductivity and thermal diffusivity of glass/zeolite and Si/SiO_2 samples are extracted. Note that this work provides an example of the method on low thermal conductivity material, which had been well characterized by the 3ω technique. It is not clear whether the method suffers from adverse thermal effects due to the presence of the heater test element.

2.3 Calibration, Experimental Errors and Measurements

2.3.1 Experimental set-up

As introduced previously, the magnitude of the $V_{3\omega}$ voltage is ~1000 times smaller than the $V_{1\omega}$ voltage. To comply with the finite dynamic range of the lock-in amplifier, the first harmonic $V_{1\omega}$ must be reduced to at least a level comparable to $V_{3\omega}$. The resistance of a potentiometer in series with the heater shown in Figure 2.6 can be nearly matched up with the heater resistance so that the voltage taken across the potentiometer Vp is nearly ~$V_{1\omega}$.

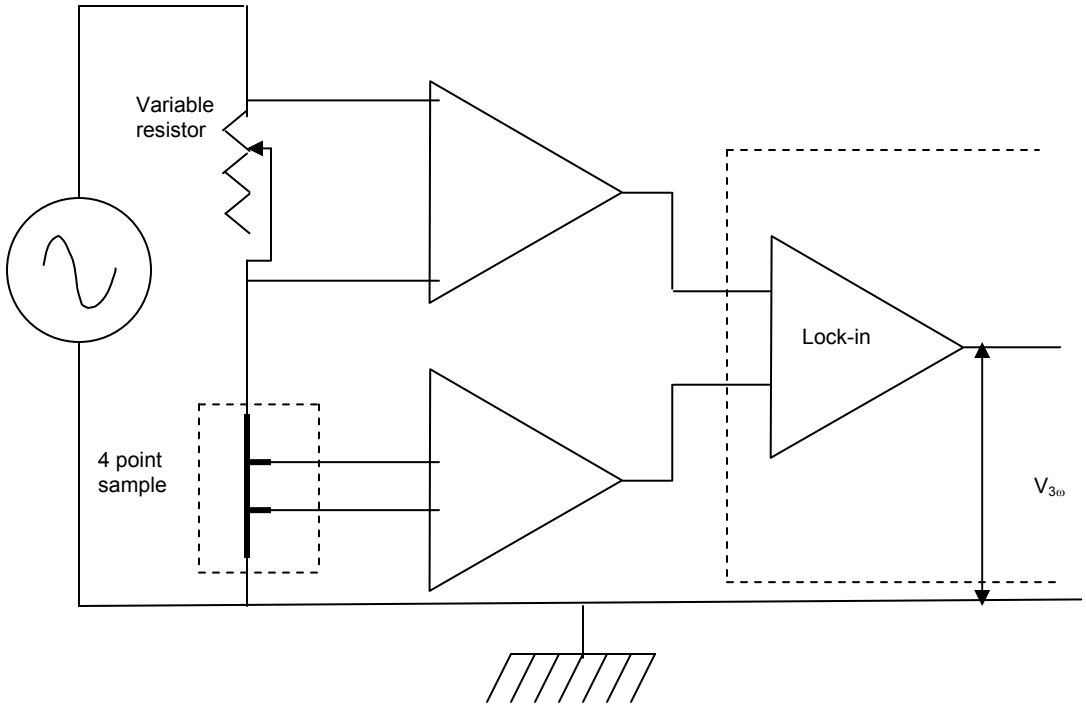

Figure 2.6. The third harmonic $V_{3\omega}$ is measured with a lock-in amplifier.

The subtraction Vp to the voltage across the heater Vt using AD624 differential amplifiers enable the lock-in amplifier to detect the signal amplitude at $V_{3\omega}$ in the frequency domain[7,9] as illustrated in Figure 2.6. The circuit board connects to the lock-in and generator on one side and to the four-point heater on the other sides with coaxial connectors. $V_{3\omega}$ and $V_{1\omega}$ are respectively measured with a lock-in while Vt and Vp can be measured with a 6 digit digital multimeter. Reading $V_{1\omega}$ from

the digital multimeter and assuming $V_{1\omega}$ equals to Vt, gives a very similar value to $V_{1\omega}$ that can be read directly from the lock-in amplifier within less than 1% error. Lock-in techniques provides accurate measurements of the temperature oscillations. A SR830 digital lock-in amplifier and its built-in generator were employed in this experiment. Typical ac voltage applied to the circuit board was ~3 to 4 V_{RMS}. The temperature oscillation in Equation (2.9) is the amplitude of the signal whether the voltage is peak-to-peak or root-mean-square.

The electrical power P dissipated by the wire is calculated from Vt^2/R_h. A reliable manner to measure the resistance of the line source is to place a precision resistor in series and applied the principle of voltage divider. A digital multimeter is used to monitor the voltage across a 1% precision 10Ω resistor during the measurement of V3ω.

1 mm long, 10um wide thin-film four-point heaters, depicted in Figure 2.1 are fabricated with a lift-off process by spinning and patterning reversal photoresist AZ5214E. A 5nm Cr adhesion layer and a 200nm thick gold film are deposited in an ebeam evaporator. The thickness of the gold metal is defined to yield a resistance of ~10-20Ω at 300K.The heater is cautiously released by lift-off in acetone, methanol and DI water. Prior to the lift-off process, the metal heater can be electrically isolated from the underlying conductive sample by depositing a 100nm SiO_2 layer by plasma-enhanced chemical vapor deposition (PECVD). The line width 2b is measured by optical microscope with an accuracy of ±0.5 um.

The sample is mounted on a ~5mm thick gold plated nickel plate (K_{Ni}~90 $W \cdot K^{-1} \cdot m^{-1}$) attached onto a brass chuck (K_{brass}~110 $W \cdot K^{-1} \cdot m^{-1}$) surrounding a heater coil connected to a variable power supply. The chuck can be heated from room temperature to about 300ºC. The temperature is sensed with a type K Chromel Alumel thermocouple mounted on the surface of the chuck embedded in epoxy. Electrical connections to the four-point pad heater are made via probes mounted on micropositioner held to a metal stage. The set-up is enclosed in a shielded aluminum box. The micropositioner probes are connected to the circuit board via BNC cables and BNC connectors.

The additional series potentiometer, resistors and differential amplifier in the circuit might be expected to contribute to spurious third harmonic components. For example, a third harmonic develops across the reference resistor due to temperature dependence of their resistances. While digital amplifiers are designed with third harmonic rejections, the temperature coefficient temperature of potentiometers is nearly 100 to 1000 times lower that of the gold heater. It is important to choose the metal strip with a high temperature coefficient resistance.

The main source of relative errors is the measurement of the temperature coefficient α_T as acknowledged in Ref. 13. Minute differences in resistances must be measured as $\alpha_T \sim 0.003 K^{-1}$ is measured over a 20-30ºC range. α_T is a function of temperature, thereby limiting the temperature range. The temperature monitor has a resolution of 0.1ºC with an accuracy of ±0.5ºC in temperature. The type K thermocouple has an accuracy of 0.4ºC. The temperature at the temperature monitor agreed within less than 0.5ºC with a mercury thermometer at room temperature. It is assumed that the variations of temperature at the top of the sample follow the variation of temperature at the temperature monitor display. While slowly heating or cooling the sample, the temperature is recorded and the voltage at the reference precision resistor and heater are recorded. The temperature resistance is deduced as shown on Figure 2.7. Temperature coefficients may vary with the strain of the metal, impurities, and temperature. Measurements must be taken on each separate heater. Putnam *et al.*[13] provide an illustration of the methodology to improve the precision of the method.

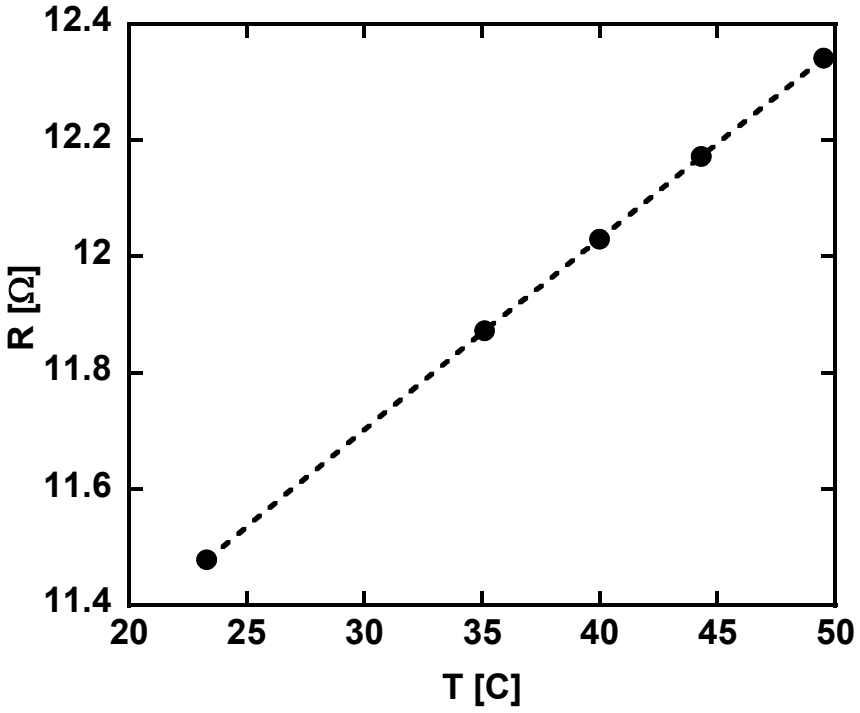

Figure 2.7. Heater resistance versus temperature measurement to deduce the temperature coefficient α_T.

2.3.2 Calibration

Several calibrations were carried out. The first calibration is the measurement of thermal conductivity using the "slope method" on bulk material of known thermal conductivity values as listed in Table 2.1. Bulk samples were used as routine check-up to monitor repeatability and experimental uncertainty drifts.

Table 2.1. Room temperature of various materials measured with the 3ω method and compared with handbook values[16]. The measured value of silicon is slightly lower than the handbook value as expected for doped material and consistent with previous authors.

	Glass	SiO_2	Al_2O_3	Si	6H-SiC
K [$W \cdot K^{-1} \cdot m^{-1}$] (measured)	1.1 ±0.1	1.4 ±0.1	36 ±3	145 ±10	350 ±30
K [$W \cdot K^{-1} \cdot m^{-1}$] Handbook[16]	1.1	1.4	36	152	330-380

Temperature measurements were calibrated using a 430um thick sapphire substrate from 20°C to 280°C. The thermal conductivity values plotted in Figure 2.8

versus temperature were found in good agreement with handbook values from both the in-phase and out-phase.

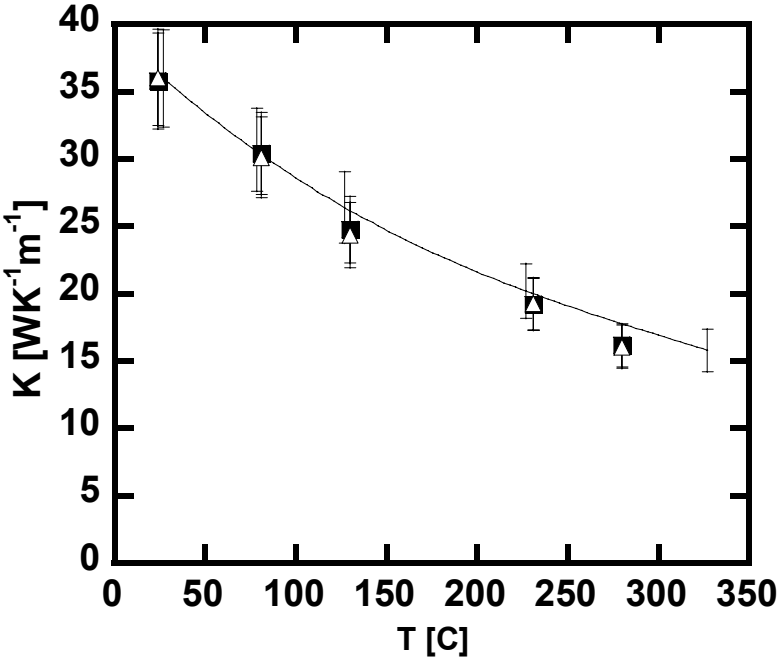

Figure 2.8. Calibration of temperature dependence measurements were performed on a 430um thick sapphire wafer between 20ºC and 280ºC with the thermal conductivity deduced from (■) in-phase and (Δ) out-phase component of $V_{3\omega}$ with ~ 7% relative errors (the out-phase signal can also be used to extract the thermal conductivity, see Equation (2.4)). The values are in good agreement with handbook values shown in solid line. The error made due the finite substrate thickness and finite heater width is less than 1% in the case of sapphire for the range of frequency, heater width, temperature and substrate thickness considered. Note that the observed slight tendency to underestimate the mean thermal conductivity as the temperature increases provide a safe lower bound in the prediction of high GaN thermal conductivity.

Furthermore, we measured the thermal conductivity of thin film PECVD SiO_2 deposited on silicon that were previously measured and reported by Kim, Feldman and Novotny from NIST[7]. The optical SiO_2 thicknesses consisted of 488nm, 101nm, 200nm, and 52.7nm. In these samples, isothermal and heat flux are represented schematically in Figure 2.5. The resulting $\Delta T/P$ versus $\ln(\omega)$ curves are plotted in Figure 2.9. The reference temperature oscillation of the bare silicon substrate was calculated using Equation (2.4). Following the differential method as explained previously, the thermal conductivity of SiO_2 was extracted about ~1.4 $W \cdot K^{-1} \cdot m^{-1}$ and an interfacial resistance of ~$2 \cdot 10^{-8}$ to $4 \cdot 10^{-8}$ $m^2 \cdot W^{-1} \cdot K^{-1}$ was found. From the slope

method, the thermal conductivity of silicon was found ~145 $W \cdot K^{-1} \cdot m^{-1}$depending on the frequency range of extrapolation.

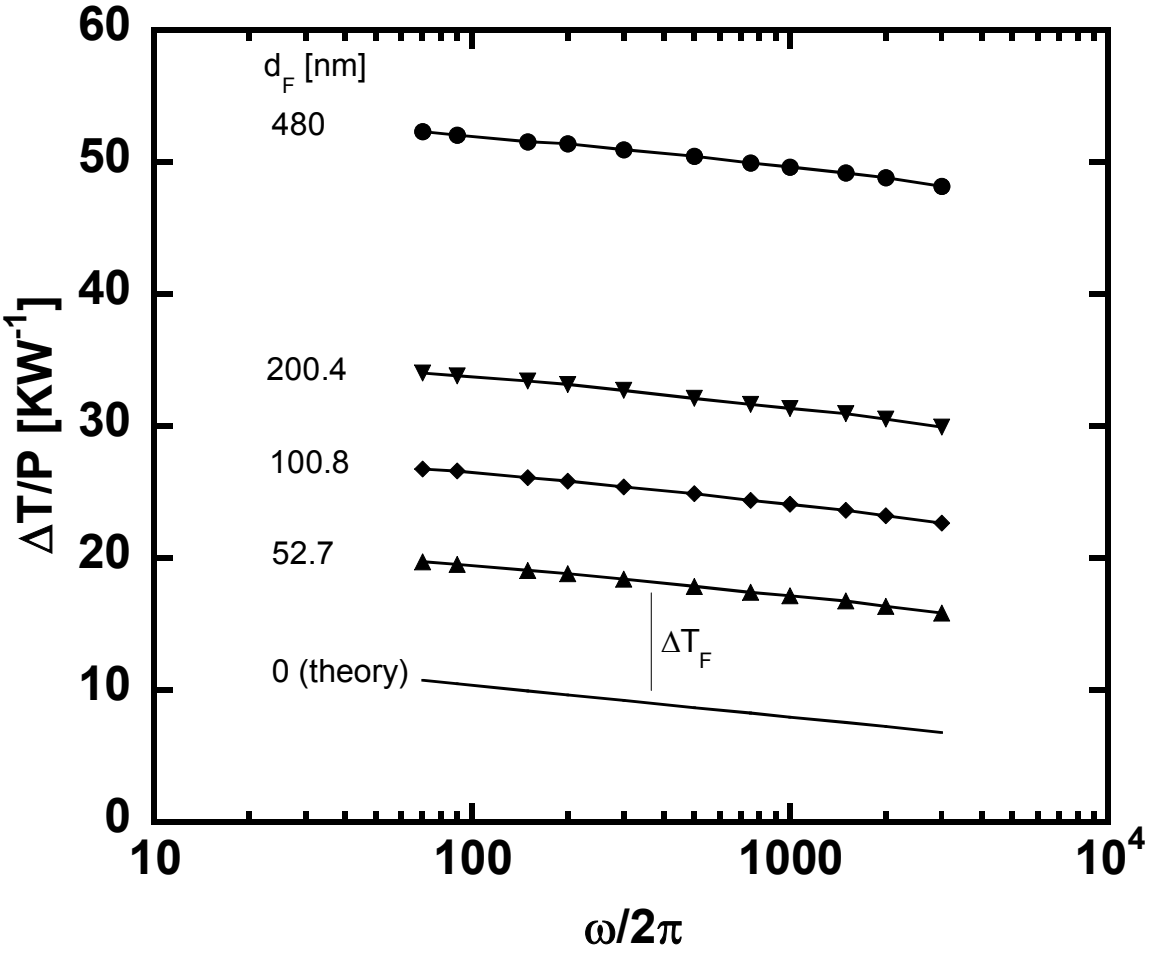

Figure 2.9. The temperature oscillation of the in-phase component as a function of frequency for SiO_2 on silicon substrates of various film thickness d_F . The solid line is calculated based on Equation (2.4) with thermal conductivity of silicon 152 $W \cdot K^{-1} \cdot m^{-1}$. The samples were the same as those used in a reported NIST round robin study[7] except for the heaters.

Our total relative uncertainty is estimated between 5 to 10% with a contribution of 5 to 7% from the temperature coefficient measurement. Note that 5% and often up to 20% inaccuracy is commonly observed in thermal conductivity measurements, several handbooks give a good illustration[16]. Another source of uncertainty resides in the validity of the heat diffusion model to faithfully account for experimental conditions especially for sample in which the penetration depth becomes comparable to the substrate thickness. Putnam *et al*.[13] provide an

illustration of the methodology to improve the precision of the method on a low thermal conductivity material.

2.3.3 Experimental Results on GaN

The 3ω method was applied to a set of GaN films grown on silicon. Beyond qualitative conclusions drawn on the thermal properties of GaN grown-on-silicon, this study raises the question of the ability of the 3ω method to characterize the heat transfer of high thermal conductivity film on low thermal conductivity substrate.

The reference sample (S6) was the buffer(~900nm)/silicon sample with no GaN films. GaN films of 150nm (S2), 325nm (S3), and 700nm (S5) thick were grown on a ~900nm buffer layer previously deposited on the silicon substrate. In addition, two 500nm GaN films (S7) and (S4) grown on silicon in two different reactors were capped with a 30nm AlGaN cap layer. The samples were coated with a 100nm low temperature oxide (LTO) SiO_2 layer. The wafers were placed in the LTO wafer boat in order of their sample label indices from S2 to S7. In addition, three SiO_2 thickness monitor wafers were placed in the LTO wafer boat at regular intervals with a monitor wafer placed in first position in the wafer boat. Following the wire formation, heater widths were optically measured and found to vary less than 1um from one wire to the other. The temperature oscillation was measured on the sample against ln(ω) and the result is depicted in Figure 2.10. It was found that the $\Delta T/P$ decreased with an increasing GaN thickness in contradiction with Equation (2.11).

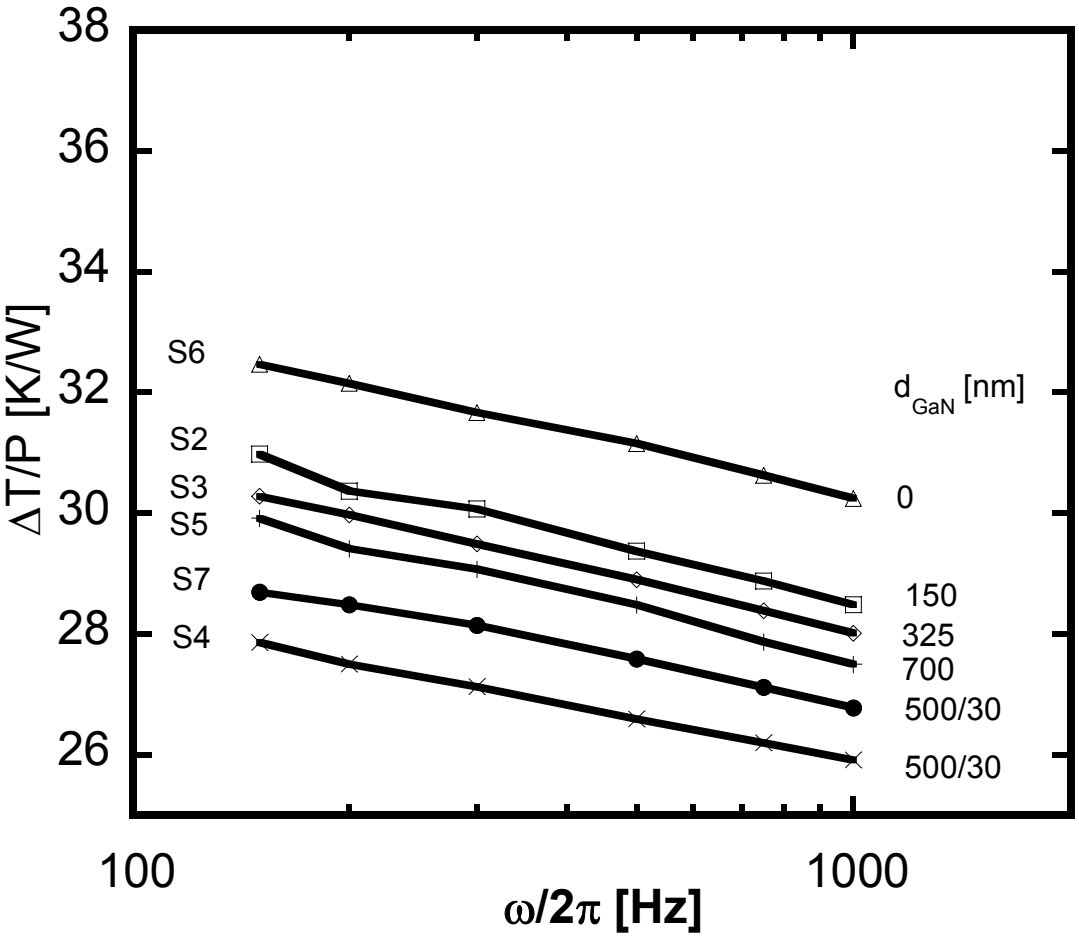

Figure 2.10. The temperature oscillation was recorded on GaN films grown on a silicon substrate with an intermediate ~900nm buffer layer. GaN films were 150, 325, 700nm for respectively sample S2, S3, S5. Sample S6 consists of a buffer layer on silicon while sample S7 and S4 were grown in two different chambers with a 500nm GaN and 30nm AlGaN capping layer. All samples were coated with a 100nm SiO_2 layer. It can be seen that ΔT is decreasing as the GaN thickness increases. The trend is not consistent with the SiO_2 layer thickness variation indicating that the difference in ΔT is due to the film+buffer layers.

Several possibilities are envisioned. First, SiO_2 film thicknesses may decrease monotonically from sample S6 to S4. The SiO_2 thickness does vary slightly and monotonically in the LTO chamber from one extremity to the other across the wafer boat as suggested from optical measurements of the SiO_2 thickness on LTO monitor wafers. However the observed trend in Figure 2.10 does not account for such a SiO_2 thickness variations because the wafers were loaded by ascending sample label indices from S2 to S7, not from S6 to S4. An alternative is that the

barely perceptible ~1um variation in wire width would account for ~10% in the spread of values because the wire width would slightly increase by a few percents from the sample S6 up to the sample S4. It would entail a slight decrease in temperature drop across the oxide layer, resulting in the trend observed in Figure 2.10. However if the latter assumption was the case and if the combinations of GaN layers with buffer layers were highly thermally insulating, $\Delta T/P$ should be increasing with increasing GaN thicknesses, thereby counteracting the steady minute increase in wire width owing to a 6 fold increase in GaN film thickness. Therefore the presence of the GaN/buffer layers may not have any effects on the temperature oscillation compared to the SiO_2 layer. A third possibility is that the gallium nitride thermal conductivity in this study is sufficiently high for the combination of buffer/GaN layers to dissipate the heat more efficiently than the substrate. However it would be required for the gallium nitride/buffer layers to have higher thermal conductivity values than that of the bulk silicon, ie ~145 $W \cdot K^{-1} \cdot m^{-1}$.

The most probable occurrence is that the observed trend in Equation (2.11) is a combination of minute variations in wire widths with relatively good thermal conductance of the nitride multilayer stacks deposited on silicon compared with SiO_2. Therefore one may conclude that the GaN films and buffer layers do not impede significantly to heat transfer, at least not as much as SiO_2. Perhaps more importantly, this study raises the question of the impact of high film-to-substrate thermal conductivity ratios on the 3ω method measurements and analysis. This point will be addressed in Chapter 3.

2.4 References

1 U. G. Jonsson and O. Andersson, "Investigations of the low- and high-frequency response of 3 omega-sensors used in dynamic heat capacity measurements," *Measurement Science & Technology*, vol. 9, pp. 1873-1885, 1998.

2 N. O. Birge and S. R. Nagel, "Wide-Frequency Specific-Heat Spectrometer," *Review of Scientific Instruments*, vol. 58, pp. 1464-1470, 1987.

3 D. G. Cahill and R. O. Pohl, "Thermal-Conductivity of Amorphous Solids above the Plateau," *Physical Review B*, vol. 35, pp. 4067-4073, 1987.

4 D. G. Cahill, "Thermal conductivity measurement from 30 to 750 K: the 3 omega method," *Review of Scientific Instruments*, vol. 61, pp. 802-808, 1990.

5 H. S. Carslaw and J. C. Jaeger, *Conduction of heat in solids*, 2nd ed. ed: Clarendon Press ;Oxford University Press, 1986.

6 A. Feldman, "Algorithm for solutions of the thermal diffusion equation in a stratified medium with a modulated heating source," *High Temperatures-High Pressures*, vol. 31, pp. 293-298, 1999.

7 J. H. Kim, A. Feldman, and D. Novotny, "Application of the three omega thermal conductivity measurement method to a film on a substrate of finite thickness," *Journal of Applied Physics*, vol. 86, pp. 3959-3963, 1999.

8 S.-M. Lee and S.-I. Kwun, "Heat capacity measurement of dielectric solids using a linear surface heater: Application to ferroelectrics," *Review of Scientific Instruments*, vol. 65, pp. 966-970, 1994.

9 B. W. Olson, S. Graham, and K. Chen, "A practical extension of the 3 omega method to multilayer structures," *Review of Scientific Instruments*, vol. 76, 2005.

10 T. Borca-Tasciuc, A. R. Kumar, and G. Chen, "Data reduction in 3 omega method for thin-film thermal conductivity determination," *Review of Scientific Instruments*, vol. 72, pp. 2139-2147, 2001.

11 I. K. Moon, Y. H. Jeong, and S. I. Kwun, "The 3 omega technique for measuring dynamic specific heat and thermal conductivity of a liquid or solid," *Review of Scientific Instruments*, vol. 67, pp. 29-35, 1996.

12 C. E. Raudzis, F. Schatz, and D. Wharam, "Extending the 3 omega method for thin-film analysis to high frequencies," *Journal of Applied Physics*, vol. 93, pp. 6050-6055, 2003.

13 S. A. Putnam, D. G. Cahill, B. J. Ash, and L. S. Schadler, "High-precision thermal conductivity measurements as a probe of polymer/nanoparticle interfaces," *Journal of Applied Physics*, vol. 94, pp. 6785-6788, 2003.

14 D. G. Cahill and R. O. Pohl, "Thermal-Properties of a Tetrahedrally Bonded Amorphous Solid - Cdgeas2," *Physical Review B*, vol. 37, pp. 8773-8780, 1988.

15 D. G. Cahill, H. E. Fischer, T. Klitsner, E. T. Swartz, and R. O. Pohl, "Thermal-Conductivity of Thin-Films - Measurements and Understanding," *Journal of Vacuum Science & Technology a-Vacuum Surfaces and Films*, vol. 7, pp. 1259-1266, 1989.

16 P. R. W. Touloukian Y.S., Ho C. Y., Klemens P. G., "Thermophysical Properties of Matter," *The TPRC Data Series*, vol. 1,2, 1970.

17 D. G. Cahill, M. Katiyar, and J. R. Abelson, "Thermal-Conductivity of Alpha-Sih Thin-Films," *Physical Review B*, vol. 50, pp. 6077-6081, 1994.

18 S.-M. Lee and D. G. Cahill, "Heat transport in thin dielectric films," *Journal of Applied Physics*, vol. 81, pp. 2590-2595, 1997.

19 S. M. Lee, D. G. Cahill, and T. H. Allen, "Thermal-Conductivity of Sputtered Oxide-Films," *Physical Review B*, vol. 52, pp. 253-257, 1995.

20 D. G. Cahill and T. H. Allen, "Thermal-Conductivity of Sputtered and Evaporated SiO_2 and TiO_2 Optical Coatings," *Applied Physics Letters*, vol. 65, pp. 309-311, 1994.

21 D. G. Cahill, S.-M. Lee, and T. I. Selinder, "Thermal conductivity of kappa - Al_2O_3 and α -Al_2O_3 wear-resistant coatings," *Journal of Applied Physics*, vol. 83, pp. 5783-5786, 1998.

22 A. J. Bullen, K. E. O'Hara, D. G. Cahill, O. Monteiro, and A. von Keudell, "Thermal conductivity of amorphous carbon thin films," *Journal of Applied Physics*, vol. 88, pp. 6317-6320, 2000.

23 C. Hu, M. Kiene, and P. S. Ho, "Thermal conductivity and interfacial thermal resistance of polymeric low k films," *Applied Physics Letters*, vol. 79, pp. 4121-4123, 2001.

24 C. Hu, M. Morgen, P. S. Ho, A. Jain, W. N. Gill, J. L. Plawsky, and P. C. Wayner, "Thermal conductivity study of porous low-k dielectric materials," *Applied Physics Letters*, vol. 77, pp. 145-147, 2000.

25 A. Jacquot, B. Lenoir, A. Dauscher, P. Verardi, F. Craciun, M. Stolzer, M. Gartner, and M. Dinescu, "Optical and thermal characterization of AlN thin films deposited by pulsed laser deposition," *Applied Surface Science*, vol. 186, pp. 507-512, 2002.

26 A. Delan, M. Rennau, S. E. Schulz, and T. Gessner, "Thermal conductivity of ultra low-k dielectrics," *Microelectronic Engineering*, vol. 70, pp. 280-284, 2003.

27 T. Yamane, N. Nagai, S. Katayama, and M. Todoki, "Measurement of thermal conductivity of silicon dioxide thin films using a 3 omega method," *Journal of Applied Physics*, vol. 91, pp. 9772-9776, 2002.

28 Y. S. Ju and K. E. Goodson, "Process-dependent thermal transport properties of silicon-dioxide films deposited using low-pressure chemical vapor deposition," *Journal of Applied Physics*, vol. 85, pp. 7130-7134, 1999.

29 Y. S. Ju, K. Kurabayashi, and K. E. Goodson, "Thermal characterization of anisotropic thin dielectric films using harmonic Joule heating," *Thin Solid Films*, vol. 339, pp. 160-164, 1999.

30 G. Chen, T. Zeng, T. Borca-Tasciuc, and D. Song, "Phonon engineering in nanostructures for solid-state energy conversion," *Materials Science and*

Engineering a-Structural Materials Properties Microstructure and Processing, vol. 292, pp. 155-161, 2000.

31 R. Venkatasubramanian, "Lattice thermal conductivity reduction and phonon localizationlike behavior in superlattice structures," *Physical Review B*, vol. 61, pp. 3091-3097, 2000.

32 G. Chen and M. Neagu, "Thermal conductivity and heat transfer in superlattices," *Applied Physics Letters*, vol. 71, pp. 2761-2763, 1997.

33 S. M. Lee, D. G. Cahill, and R. Venkatasubramanian, "Thermal conductivity of Si-Ge superlattices," *Applied Physics Letters*, vol. 70, pp. 2957-2959, 1997.

34 T. Borca-Tasciuc, W. L. Liu, J. L. Liu, T. F. Zeng, D. W. Song, C. D. Moore, G. Chen, K. L. Wang, M. S. Goorsky, T. Radetic, R. Gronsky, T. Koga, and M. S. Dresselhaus, "Thermal conductivity of symmetrically strained Si/Ge superlattices," *Superlattices and Microstructures*, vol. 28, pp. 199-206, 2000.

35 D. W. Song, W. L. Liu, T. Zeng, T. Borca-Tasciuc, G. Chen, J. C. Caylor, and T. D. Sands, "Thermal conductivity of skutterudite thin films and superlattices," *Applied Physics Letters*, vol. 77, pp. 3854-3856, 2000.

36 J. L. Liu, A. Khitun, K. L. Wang, W. L. Liu, G. Chen, Q. H. Xie, and S. G. Thomas, "Cross-plane thermal conductivity of self-assembled Ge quantum dot superlattices," *Physical Review B*, vol. 67, pp. -, 2003.

37 T. Borca-Tasciuc, D. W. Song, J. R. Meyer, I. Vurgaftman, M. J. Yang, B. Z. Nosho, L. J. Whitman, H. Lee, R. U. Martinelli, G. W. Turner, M. J. Manfra, and G. Chen, "Thermal conductivity of $AlAs_{0.07}Sb_{0.93}$ and $Al_{0.9}Ga_{0.1}As_{0.07}Sb_{0.93}$ alloys and $(AlAs)_{(1)}/(AlSb)_{(11)}$ digital-alloy superlattices," *Journal of Applied Physics*, vol. 92, pp. 4994-4998, 2002.

38 T. Borca-Tasciuc, D. Achimov, W. L. Liu, G. Chen, H. W. Ren, C. H. Lin, and S. S. Pei, "Thermal conductivity of InAs/AlSb superlattices," *Microscale Thermophysical Engineering*, vol. 5, pp. 225-231, 2001.

39 B. Yang, W. L. Liu, J. L. Liu, K. L. Wang, and G. Chen, "Measurements of anisotropic thermoelectric properties in superlattices," *Applied Physics Letters*, vol. 81, pp. 3588-3590, 2002.

40 W. L. Liu, T. Borca-Tasciuc, G. Chen, J. L. Liu, and K. L. Wang, "Anisotropic thermal conductivity of Ge quantum-dot and symmetrically strained Si/Ge superlattices," *Journal of Nanoscience and Nanotechnology*, vol. 1, pp. 39-42, 2001.

41 A. R. Kumar, D.-A. Achimov, T. Zeng, and G. Chen, "Thermal conductivity of nanochanneled alumina," *American Society of Mechanical Engineers, Heat Transfer Division, (Publication) HTD*, vol. 366, pp. 393-397, 2000.

42 Q. Hao, "Analytical heat-transfer modeling of multilayered microdevices," *Journal of Micromechanics and Microengineering*, vol. 14, pp. 914-926, 2004.

Chapter 3 Determining Film Thermal Properties With the 3ω Method: A Theoretical Consideration

3.1 Overview

A large number of experimental independent parameters can influence the 3ω method[1-6]. It is important to have a proper heat conduction model of the 3ω method for the accurate determination of film thermal properties. The development of powerful numerical methods have made possible to consider complex models that describe a variety of experimental situations[1-6]. These sophisticated models still require still require a number of independent parameters[5,6]. Both Ref. 5 and Ref. 6 have presented a 3ω extraction technique based on numerical analysis limited to four independent parameters. Therefore even with sophisticated heat conduction models, the nature of the approximations made must be understood and discussed. On the other hand, it is useful to formulate simplified models in order to predict the range of applicability of the 3ω technique by examining the governing parameters for a specific characterization purpose. For example, Borca-Tasciuc *et al.*[1] have presented the principle underlying the thermal conductivity characterization of anisotropic thin films. Lee and Cahill have illustrated the strength of the 3ω method from ultra-simplified heat conduction models applied to low thermal conductivity films to determine the thermal boundary resistance between silicon dioxide and silicon[7].

The 3ω method has been widely considered for the characterization of films and substrates with relatively low thermal conductivity[1,5,7,8]. It has been established rather recently that the film-to-substrate thermal conductivity contrast, K_F/K_S, impacts considerably the validity and applicability of the 3ω method[1]. It turns out that little

work has been conducted on the necessary conditions to make the differential 3ω technique applicable in case where the film thermal conductivity is a few times lower to a few times higher compared to the substrate thermal conductivity.

In this thesis we study the III-nitride thin film systems, where the film-to-substrate thermal conductivity ratio varies dramatically with the substrate. This is largely due to a lack of native gallium nitride substrates being commercially available. Thus in this thesis we explore thin film to substrate thermal conductivity ratios that are extreme compared to what has previously been studied. More precisely, gallium nitride is grown on non-native substrates, most commonly sapphire (36 $W \cdot K^{-1} \cdot m^{-1}$), silicon (150 $W \cdot K^{-1} \cdot m^{-1}$), and silicon carbide (350 $W \cdot K^{-1} \cdot m^{-1}$). Additional substrates for the growth of gallium-nitride thin films have also been employed as listed by Morkoç[9]. Under simplifying assumptions, Figure 3.1 illustrates that the lowest K_F/K_S ratio is obtained for aluminum gallium nitride on silicon carbide while the highest K_F/K_S ratio is observed for gallium nitride on sapphire. Indeed ~500nm thick aluminum gallium nitride layers deposited on sapphire were recently measured with the differential 3ω technique[10]. In this paper, the film thermal conductivity nearly matches the substrate thermal conductivity and the thermal conductivity was claimed to be deduced from sophisticated numerical calculations without any allusion to the conditions of applicability of the 3ω method where the film-to-substrate thermal conductivity ratio is slightly over unity[10,11]. Likewise, reports are scarce on frequency effects in the characterization of films where the thermal conductivity is relatively large compared to that of the substrate.

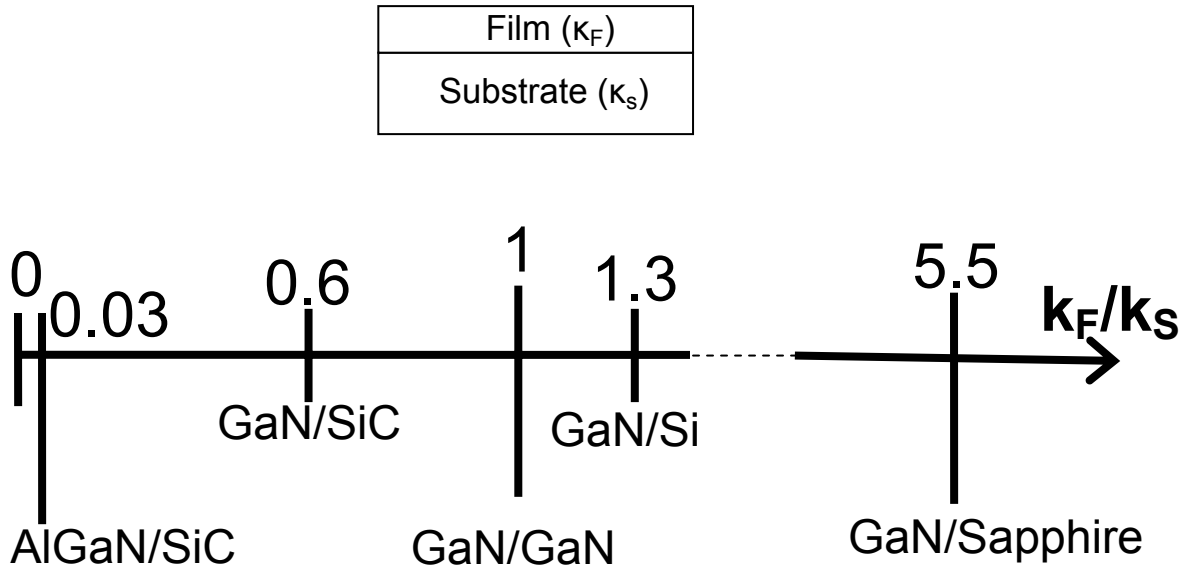

Figure 3.1. Film-to-substrate thermal conductivity ratios. The GaN thermal conductivity is arbitrarily set to an assumed bulk values ~200 $W \cdot K^{-1} \cdot m^{-1}$. Only the most common non-native substrates are considered. Though the GaN thermal conductivity of films may be quite lower, this figures illustrates a broad range of thermal conductivity ratio on various substrates.

While Ref. 6 addresses the 3ω technique at very high frequency, it presents a method to merely extract the thermal property of the metal heater. Indeed Liu *et al.* [4,11] have acknowledged the need to include frequency effects in models governing the 3ω technique for thin film thermal conductivity determination. Furthermore, the existence of an interfacial thermal boundary resistance between a film and a substrate can lead to non-negligible errors in extracted film thermal conductivity as Lee and Cahill have shown[7]. In the general case of an arbitrary K_F/K_S ratio, the role played by an interfacial boundary resistance between a film and a substrate on the 3ω method is not well-documented. Borca-Tasciuc *et al.*[1] have provided a discussion on the role played by an interfacial resistance for a rather arbitrary value of thin film thermal conductivity but corresponding to an interface located between the film and the heater.

In this chapter, the potential of the 3ω method to characterize the thermal conductivity of a single film deposited on a substrate is examined depending on:

i) The film-to-substrate thermal conductivity ratio K_F/K_S larger than unity,

ii) The driving frequency ω, and

iii) The presence of thermal boundary resistance between film and substrate.

The objective of this chapter is to discuss the validity of assumptions in previous reported models, extend the analysis to the situation of high thermal conductivity films and investigate a reliable method to extract the thermal conductivity when $K_F/K_S>1$. Several times in this chapter, an opportunity will be given to the reader to directly compare our results with those presented by Borca-Tasciuc, Kumar, and Chen[1]. In addition to correctly taking into account the impact of thin film to substrate thermal conductivity ratios, an achievement in this chapter is the introduction of a small but new correction term in a routine procedure that extracts the thermal boundary resistance between a thermally insulating film and a substrate.

First the key parameters underlying the heat diffusion models governing the differential 3ω technique will be presented. The solution of the temperature oscillation for a multilayer stack including interfacial boundary resistances will be derived. Throughout this study, finite element simulations were conducted as a means of validating the analytical solutions and exploring the impact of various boundary conditions. In the next section, the data reduction in 3ω thermal conductivity will be studied when the film-to-substrate thermal conductivity ratio is higher than one, but ignoring frequency effects that are studied separately in section 3.4. Next, a detailed analysis of the differential 3ω method that accounts for the presence of interfacial thermal boundary resistance between the film and the substrate is studied. Finally from the results obtained in the previous sections, the condition of applicability of the 3ω method will be addressed. At that point a sensitivity coefficient will be introduced and it will be shown that this new parameter captures the applicability of the 3ω method. The last section will conclude the work in this chapter.

3.2 Methods of Resolution

Figure 3.2 exhibits the geometrical and physical parameters considered in the analysis of the differential 3ω method applied to a single film-on-substrate system, namely the cross-plane K_{Fy} and in-plane K_{Fx} film thermal conductivity, the thermal conductivity of the substrate K_S, the interfacial boundary resistance between the film and the substrate R_{FS}, the film thermal diffusivity α_F, the substrate thermal diffusivity α_S, the film thickness d_F, the substrate thickness d_S, the heater half-width b, and the driving angular frequency ω.

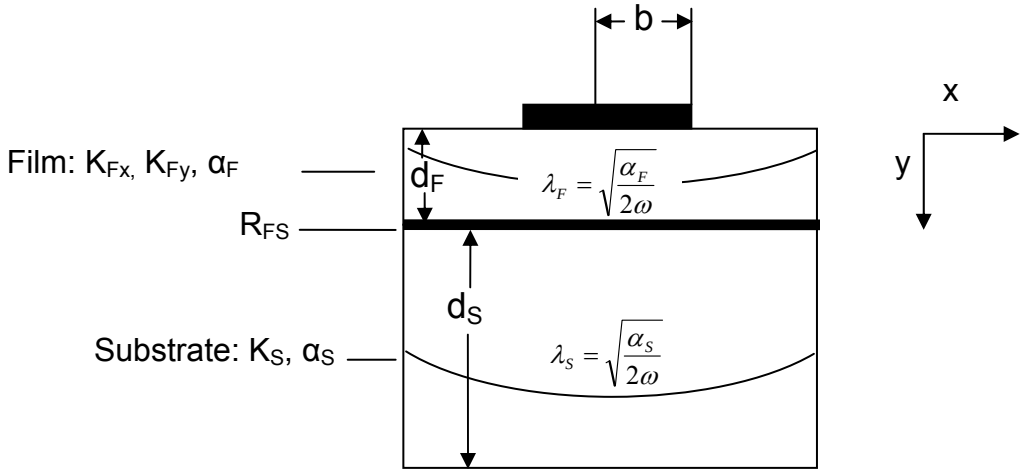

Figure 3.2. Illustration of the governing geometrical and physical parameters considered throughout the 3ω method analysis of a film-on-substrate system. λ is the penetration depth function of the medium, R_{FS} the thermal boundary resistance between film and substrate.

These parameters are naturally lumped into dimensionless parameters during the modeling of the 3ω method in order to express generic solutions. Perhaps the most important dimensionless parameter is the film to substrate thermal conductivity contrast ratio $\frac{K_F}{K_S}$. Throughout this chapter, K_F indicates the geometric average of the cross-plane and in-plane film thermal conductivity: $K_F = \sqrt{K_{Fx} K_{Fy}}$. In the case of isotropic films, K_F matches K_{Fy} equal to K_{Fx}. The mismatch of thermal conductivity (and more generally the mismatch of effusivity) between the film and substrate

introduces heat spreading effects. Another governing dimensionless quantity is the parameter β_F function of the aspect ratio between heater width and film thickness and function of the film anisotropy ratio: $\beta_F = \sqrt{\frac{k_{Fx}}{k_{Fy}}}\frac{d_F}{b}$. In other words, β_F relates to the heat spreading inside the film due to anisotropy and the two-dimensional geometry of a 2b wide heater on a d_F thick film. Note that a β_S ratio could be equally defined for the substrate. The substrate thermal conductivity is taken isotropic throughout this chapter. In the case of an interfacial boundary resistance R_{SF} between a film and a substrate, the associated dimensionless parameter is $\rho_{S(F)} = \frac{R_{SF} k_{S(F)}}{b}$ where ρ_S and ρ_F refer to the dimensionless interfacial resistance defined respectively with the substrate thermal conductivity k_S or the film thermal conductivity k_F. The inverse of the dimensionless interfacial boundary resistance ρ_F relates to the Biot number and β_F values. The frequency can be expressed in a non-dimensional form such as $\sqrt{\frac{2\omega}{\alpha_{S,F}}}b$, $\sqrt{\frac{2\omega}{\alpha_F}}d_F$ where $\alpha_{S,F}$ indicates either the substrate diffusivity α_S or the film diffusivity α_F.

The starting point of our analysis is the real part of ΔT_{F+S}-ΔT_S in a single film-on-substrate system, which defines the difference of temperature oscillation taken between the top of a film-on-substrate system (ΔT_{F+S}) and the top of a bare substrate (ΔT_S). One must bear in mind that ΔT_{F+S}-ΔT_S is not the temperature drop across the film in the general case. Only in a limited number of situations ΔT_{F+S}-ΔT_S approximates the situation of heat flowing one-dimensionally across the film, hence approximating the temperature drop across the film. Proportional to ΔT_{F+S}-ΔT_S is the dimensionless parameter $\frac{K_{Fy}}{K_{1D}}$ as defined rigorously in the previous chapter, where K_{1D} represents the apparent film thermal conductivity function of dimensionless parameters β_F, $\frac{K_F}{K_S}$, ρ_S, etc. The $\frac{K_{Fy}}{K_{1D}}$ ratio is the norm used throughout this chapter to describe the differential 3ω method. Indeed Borca Tasciuc *et al.*[1] have

presented an extensive treatment of the differential 3ω method by considering the $\frac{K_{Fy}}{K_{1D}}$ ratio for anisotropic film thermal conductivities lower than substrate thermal conductivities. In this work, the dimensionless interfacial thermal resistance ρ_S is introduced and the $\frac{K_{Fy}}{K_{1D}}$ ratio is studied for arbitrary film-to-substrate thermal conductivity ratio.

An example of theoretical consideration where dimensionless parameters are defined somewhat similarly has been given by T. Bennett[12]. He has addressed the determination of film thermal properties through harmonic surface heating with a Gaussian laser beam[12]. Aside from heat source geometry, the two main differences between the 3ω method and the Laser method is the heating frequency and the sensitivity of the phase signal to film thermal properties. The 3ω technique can be considered as a low frequency based method as dimensionless frequency parameters are typically lower than 0.1. In the case of laser heating, the dimensionless frequency parameter can equal 1.

Perhaps in a formalism more tightly related to the differential 3ω method, Lambropoulos *et al.*[13] have analytically examined how the presence of interfacial boundary resistance affects the measurement of thin film thermal conductivity from surface heating, although the definition of an effective substrate thermal conductivity was adopted instead of an effective film thermal conductivity corresponding to our case. In the 1992 report of Lambropoulos *et al.*[13], the ratio of the substrate thermal conductivity to the apparent substrate thermal conductivity was investigated as a function of the β_F parameter with the dimensionless interfacial resistance ρ_s as a parameter, and relying on a strict time-independent analysis. The radial symmetry of the time-independent heat source resulted in obscure formulas hindering the emergence of governing parameters in the study. Moreover emphasize was laid on low thermal conductivity dielectric thin films. In this thesis the applicability of the 3ω method is investigated in an illuminating formalism in the case of arbitrary film thermal conductivity with the presence of an interfacial boundary resistance between the film and the substrate.

3.2.1 Multilayer Stack on Substrate with Interfacial Boundary Resistances

To meet our goal, it was first necessary to derive a generic expression for the temperature oscillation amplitude of an infinitely long heater deposited on a multilayer-film-on-substrate system with interfacial boundary resistance between layers. The following derivation was stimulated by the work published by Feldman in 1999[14]. The temperature oscillation amplitude is expressed following a recursive relationship similar to the relationship presented by Borca-Tasciuc and co-authors[1].

$$\Delta T = \frac{P_l}{\pi k_{y1}} \int_0^\infty \frac{M_1}{N_1} \frac{\sin^2 u}{u^2} dt$$

with

$$\begin{cases} M_{j-1} = \dfrac{M_j + N_j \rho_j + \dfrac{k_{yj} N_j}{k_{yj-1} N_{j-1}} \tanh(\varphi_{j-1})}{\dfrac{k_{yj} N_j}{k_{yj-1} N_{j-1}} + (M_j + N_j \rho_j) \tanh(\varphi_{j-1})}, \quad j = 2..n \\ N_j = \left(k_{xyj} u^2 + i \dfrac{2\omega}{\alpha_{yj}} b^2 \right)^{1/2}, \varphi_j = N_j \dfrac{d_j}{b}, k_{xyj} = k_{xj} / k_{yj} \\ \rho_j = \dfrac{R_{j-1\,j}}{b / k_{yj}} \\ M_n = \tanh^p (N_n d_n) \quad p = \begin{vmatrix} 1 & \text{Isothermal backside} \\ 0 & \text{Semi - infinite backside} \\ -1 & \text{Adiabatic backside} \end{vmatrix} \end{cases} \tag{3.1}$$

$R_{i-1,i}$ is the interfacial boundary resistance between the layer j-1 and j. $R_{j-1,j} \geq 0$ while $R_{j,j-1} \leq 0$. Other variables, indices, and constants in Equations (3.1) are defined identically as those in Equation 2.16 from Chapter 2. Indeed Equation (3.1) can be deduced from Equation 2.16 and vice-versa from the following substitution:

$$M_j \rightarrow M_j + k_{yj} \frac{N_j}{b} R_{j-1,j} \tag{3.2}$$

Incidentally Equation (3.1) with $R_{j-1,j}=0$ is now proved to be analytically correct. An hypothetical infinite thermal boundary resistance $R_{j-1,j}$ corresponds mathematically to an adiabatic boundary condition at the bottom of the the j-1th layer. The correctness of Equation (3.1) will now be verified when $R_{j-1,j}$ is non-zero and finite. Starting from Equation (3.1) with $R_{j-1,j}=0$, the idea is to consider at least three layers comprising a j-1th thin intermediate layer with thickness d_{j-1} and thermal conductivity k_{j-1} sandwiched between two films (or between one film and a substrate) to show that the thermal resistance of this thin sandwiched layer is the equivalent of an interfacial boundary resistance. From Equation 2.13 in Chapter 2, the condition must be expressed as d_{j-1} and k_{j-1} vanishing to zero while the ratio d_{j-1}/k_{j-1} remains finite and non-zero for non-trivial solutions.

The verification initiates as follows. From Equation (3.1) and ignoring interfacial thermal boundary resistances, M_{j-2} is expressed as a function of M_j and a lump term that is a function of the j-1th layer parameters expressed by the equation below:

$$M_{j-1}\frac{k_{yj}N_j}{k_{yj-1}N_{j-1}}=\frac{M_j+\dfrac{k_{yj}N_j}{k_{yj-1}N_{j-1}}\tanh\left(\varphi_{j-1}\right)}{\dfrac{k_{yj}N_j}{k_{yj-1}N_{j-1}}+M_j\tanh\left(\varphi_{j-1}\right)}\frac{k_{yj}N_j}{k_{yj-1}N_{j-1}}\approx M_j+k_{yj}N_j\big/b\,\frac{d_{j-1}}{k_{j-1}} \qquad (3.3)$$

The right part of Equation (3.3) was obtained by bringing together the terms d_{j-1}/k_{j-1} in a first order development in d_{j-1}. Noting $R_{j-2,j}=\dfrac{d_{j-1}}{k_{j-1}}$, M_{j-2} becomes:

$$M_{j-2}=\frac{M_j+k_{yj}N_j\big/b\,R_{j-2,j}+\dfrac{k_{yj}N_j}{k_{yj-2}N_{j-2}}\tanh\left(\varphi_{j-2}\right)}{\dfrac{k_{yj}N_j}{k_{yj-2}N_{j-2}}+\left(M_j+k_{yj}N_j\big/b\,R_{j-2,j}\right)\tanh\left(\varphi_{j-2}\right)} \qquad (3.4)$$

By re-indexing the subscript j-2 → j-1 in Equation (3.4), it is confirmed that Equation (3.1) is valid for non-zero $R_{j-1,j}$. Perhaps more importantly, it was established that a single film on substrate system with interfacial boundary R_{FS} corresponds to a three layer system with no interfacial boundary resistance and can

be described solely by Equation 2.16 in Chapter 2 provided no heat spreading in the intermediate layer between the film and substrate.

More recently, in an April 15th 2005 publication a similar relation been recently published but with a different notation and formulation[5]. A numerical method was then developed to deduce the thermal conductivity parameters of a multilayer system[5]. In our work, the effect of film thermal conductivity, thermal boundary resistance, and frequency on the 3ω method is studied in a comprehensive approach.

3.2.2 Numerical Analysis

The solution of the temperature oscillation amplitude corresponding to a heater deposited on a single layer-on-substrate system was carried out with finite element method for the following reasons:

i) To verify analytical models,

ii) To predict a solution when the analytical solution was cumbersome

iii) To explore a solution when an analytical solution could not be formulated in a compact expression.

The resolution of Equation (3.1) in the general case with no approximations requires numerical methods so that numerical calculation is necessary in most cases. Using finite element methods is just one possible numerical method, but has the convenience of providing a visual representation of the physical situation. A commercial package FEMLAB was used to solve the homogeneous linear isotropic time-dependent periodic heat equation. The solution was calculated in the frequency domain with no transients. For a given angular frequency 2ω, the real and imaginary parts of the temperature oscillation averaged over the heater width 2b were directly computed.

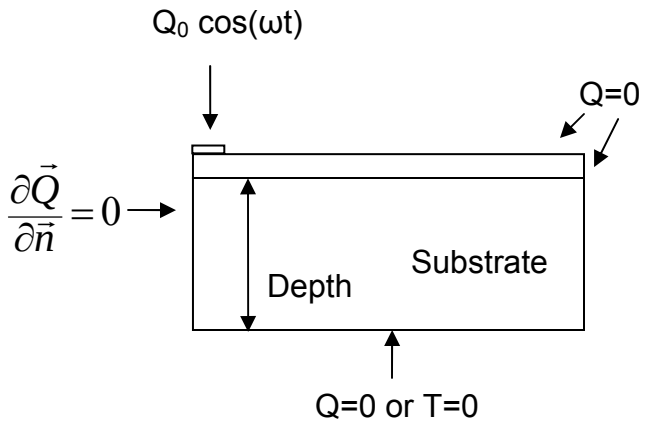

Figure 3.3. Cross-sectional schematic of half the structure with boundary conditions defined for the finite element analysis of the 3ω method in the case of a single film on substrate.

Figure 3.3 shows a typical structure used during finite element analysis. By noting the mirror symmetry of the structure, simulation cost can be reduced by simulating half the life-size structure provided the component of the heat flux vector normal to the surface perpendicular to the heater is set zero, which represents a typical boundary condition. The top surface and edges were taken adiabatic in agreement with assumptions used to derive Equation (3.1). In experimental situations, the heat losses are negligible so that adiabatic conditions represent an adequate approximation. The bottom could be either adiabatic or isothermal. The mesh was carefully refined in the area of strong thermal conductivity and temperature gradients. To check the adverse effect of finite geometry that severally alters the integrity of the finite element method, the boundary conditions were consistently varied from adiabatic to isothermal during simulations. The relative error was lower than 10^{-4} as illustrated in Figure 3.5.

While it is a common practice to simulate the solution of the heat equation to verify analytical results or to gain insights about the governing parameters in a particular situation[1,15], a few studies have relied entirely on finite element method to predict data reduction from simplifying analytical model. Yet the accuracy of the finite element technique has its own limitations. Jacquot *et al.*[16] investigated data reduction in the 3ω method in a time-dependent and computed the amplitude and phase of the temperature oscillation as opposed to the in-phase and out-phase components. Other authors have examined the 3ω method for heat capacity

determination based on accurate finite element simulation in the frequency domain[17].

3.3 Thermal Conductivity characterization for low and high K_F/K_S Ratios.

The difference ΔT_{F+S}-ΔT_S was derived by Borca-Tasciuc *et al.*[1] for a film on a semi-infinite substrate with no interfacial boundary resistance at the limit $\omega \to 0$, the latter condition being consistent as the 3ω method operates at relative low frequencies:

$$\Delta T_{F+S} - \Delta T_S = \frac{P d_F}{2blk_{Fy}} \times \frac{k_{Fy}}{k_{1D}}$$

$$\begin{cases} \dfrac{k_{Fy}}{k_{1D}} = \underbrace{\left(1 - \dfrac{k_F^2}{k_S^2}\right)}_{S_C} \times \underbrace{\dfrac{2}{\pi}\displaystyle\int_0^\infty \frac{\sin^2 u}{u^3} \frac{\tanh(u\beta_F)}{\beta_F\left(1 + \dfrac{k_F}{k_S}\tanh(u\beta_F)\right)} du}_{S_G} \\ k_F = \sqrt{k_{Fx}k_{Fy}}\,,\ \beta_F = \sqrt{\dfrac{k_{Fx}}{k_{Fy}}}\dfrac{d_F}{b} \end{cases} \tag{3.5}$$

K_{1D} is the apparent thermal conductivity of the film corresponding to a virtual situation where the heat would flow in the film following a one-dimensional Fourier's law model with no heat spreading whatsoever. As a result, the film thermal conductivity K_{Fy} will equal the apparent thermal conductivity K_{1D} if and only if the heat physically flows one-dimensionally in the film with no heat spreading of any kind. Therefore the ratio K_{Fy}/ K_{1D} encompasses the effect of heat flow deviating from a one-dimensional time-independent diffusion model. S_C relates to the heat spreading due to the contrast of thermal conductivity between film and substrate. S_G relates to heat spreading due to the effect of a combination of geometrical parameters and thermal conductivity contrast between film and substrate. Therefore S_C is strongly dependent on the K_F/ K_S ratio while S_G is strongly dependent on β_F. At β_F=0, S_G=1. If d_F is zero, β_F=0 and ΔT_{F+S}-ΔT_S=0.

Borca-Tasciuc *et al.*[1] have discussed Equation (3.5) in the limited case of $K_F/K_S<1$. It is Equation (3.5) through the coefficient β_F that provides a simple algorithm to extract thermal conductivity anisotropy. Two points will now be addressed: the validity of Equation (3.5) for $K_F/K_S>1$ and the condition of zero frequency used by Borca-Tasciuc *et al.*[1] to derive Equation (3.5). First it has been briefly checked in this thesis that Equation (3.5) derives from Equation (3.1) with no restriction on the K_F/K_S ratio in the limit of vanishing frequencies. Therefore Equation (3.5) is valid for K_F/K_S ranging from zero to values superior to unity. Second the condition of vanishing frequency must be expressed in a convenient dimensionless form. By looking at Equation (3.1), the term $\sqrt{\frac{2\omega}{\alpha_{S,F}}}b$ introduced earlier vanishes as the frequency vanishes, unless the heater width 2b grows infinitely. Therefore Equation (3.5) is incompatible with the solution corresponding to an infinite heater plane, unlike Equation (3.1) valid for a perfect heater plane.

This can be easily understood since an infinite heater plane is approximated only by the 3ω method at high frequency when the penetration depth is much lower than the heater width. This situation is incompatible with the assumption of zero frequency. Maybe less obvious is that β_F in Equation (3.5) cannot be zero by increasing the heater width infinitely. If the heater width goes to infinity, the condition of vanishing frequency no longer holds, S_C is erroneous and the treatment of the heat equation in that case must be reconsidered. Even more interesting is the case of intermediate heater width range neither too large nor too small, the prediction from Equation (3.5) becoming inaccurate or even erroneous as the heater width grows. In conclusion the heater width 2b must remain relatively small for Equation (3.5) to be accurate. β_F can reach arbitrarily small values via the film thickness d_F or the anisotropy ratio only. In strict terms, it would be preferable to treat experimental 3ω data with no assumptions on the frequency. Actually several contributors of the work presented in Ref. 1 have been extracting the differential 3ω thermal conductivity of thin films by fitting experimental data numerically from complex models making sure to include frequency effects in those models[4,11]. Such a

correction is made maybe because the work presented in Ref. 1 proposes a method to characterize thin film anisotropy by increasing the heater width.

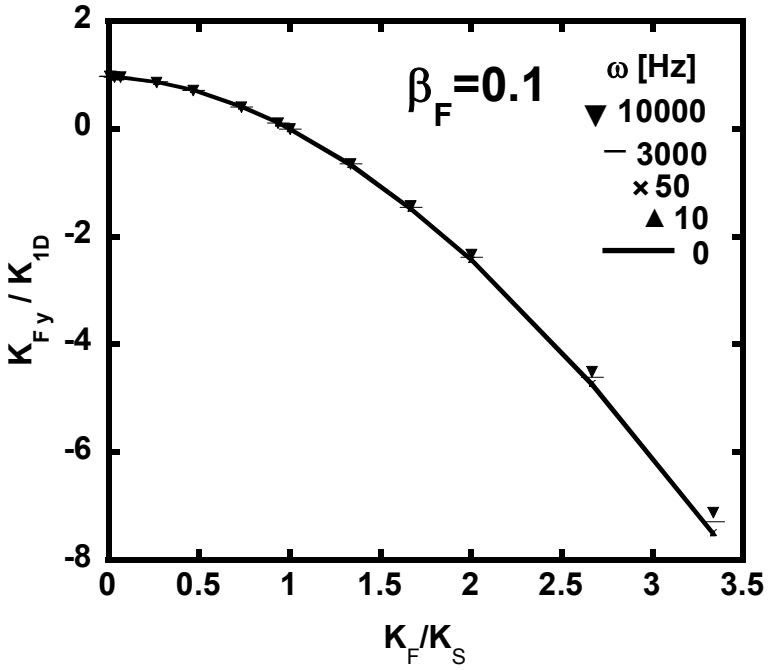

Figure 3.4. The Equation (3.5) derived at ω=0 is valid for K_F/K_S greater than 1. Numerical calculations demonstrate that the solution at ω=0 is an excellent approximation of the complete solution when ω increases from 10Hz to 5000Hz.

Figure 3.4 plots in solid line the K_{Fy}/K_{1D} ratio versus K_F/K_S following Equation (3.5) for β_F=0.1 and an isotropic film. For K_F/K_S<1, conclusions have already been made by Borca-Tasciuc and co-authors[1]. For K_F/K_S>1, the K_{Fy}/K_{1D} ratio is negative indicating that the temperature oscillation on a film on substrate ΔT_{F+S} is smaller than the temperature oscillation ΔT_S with no film.

From Chapter 2, let us visualize a typical ΔT versus ln(ω) plot. The ΔT_{F+S} curve of a film-on-substrate system will decrease as the film thickness increases, which is opposite to the trend for, say SiO_2 on silicon. In the case of gallium nitride on sapphire, the temperature oscillation ΔT_{F+S} may correspond to a negative apparent thermal conductivity K_{1D}. This has shown to be indeed the case[11], which suggests a qualitative characterization methodology. From the knowledge of the substrate thermal conductivity, it is possible to infer a higher or lower bound of the

film thermal conductivity. Therefore by considering gallium nitride grown on various substrates of gradually increasing thermal conductivity value such as sapphire (~36 $W \cdot K^{-1} \cdot m^{-1}$), silicon (~140 $W \cdot K^{-1} \cdot m^{-1}$), and silicon carbide (~350 $W \cdot K^{-1} \cdot m^{-1}$), it is possible to narrow the range of the gallium nitride thin film thermal conductivity values by a qualitative argument. For instance, from our 3ω experiment conducted on gallium nitride-on-silicon samples presented in the previous chapter of this thesis, we concluded that the order of magnitude of thin film gallium nitride thermal conductivity was at least 140 $W \cdot K^{-1} \cdot m^{-1}$, matching the value of silicon thermal conductivity. From the ΔT versus ln(ω) plot in Ref. 10, it is implicitly established that the thermal conductivity of a ~20um thick gallium nitride film deposited on sapphire is at least 40 $W \cdot K^{-1} \cdot m^{-1}$. Indeed Ref. 10 explicitly reports a gallium nitride thermal conductivity value of ~125 $W \cdot K^{-1} \cdot m^{-1}$.

3.4 Frequency Effects

The conclusions drawn in the previous section visualizing ΔT_{F+S} versus ln(ω) plots for $K_F/K_S>1$ were based on Equation (3.5). However the frequency effects on the in-phase thermal offset $\Delta T_{F+S}-\Delta T_S$ due to the presence of the film are not accounted for in Equation (3.5). Recall that ΔT_S is the in-phase temperature oscillation on a bare substrate measured or calculated versus ln(ω). ΔT_{F+S} is the in-phase temperature oscillation on a film-on-substrate system measured versus ln(ω). The thermal offset is the difference $\Delta T_{F+S}-\Delta T_S$ taken over a large range of frequency. The thermal offset $\Delta T_{F+S}-\Delta T_S$ is assumed to be independent of frequencies in most experiments, however it must be a function of frequency according to Equation (3.1). This section discusses the nature and degree of frequency dependence on the thermal offset $\Delta T_{F+S}-\Delta T_S$. This section also emphasizes the impact of geometrical parameters such as heater-half-width b, film thickness d_F, substrate thickness d_S, when the frequency affects the thermal offset $\Delta T_{F+S}-\Delta T_S$.

In this work, a first order development in ω in the real part of the $\Delta T_{F+S}-\Delta T_S$ expression has been attempted using the real part of Equation (3.1) for a single layer on a semi-infinite substrate. Little success was obtained in expressing a meaningful compact expression. Instead deeper insights were obtained from finite

element analysis by calculating the in-phase component of the temperature oscillation on a bare substrate ΔT_S and the temperature oscillation on a film-on-substrate system ΔT_{F+S}. The difference ΔT_{F+S}-ΔT_S was then deduced. The angular frequency ω varied from 10Hz to 10,000Hz and K_F/K_S ranged from nearly zero to about four. It was checked that in the low frequency regime corresponding to large penetration depth, the effects of finite substrate thickness was negligible. The mesh was refined in the high frequency regime where temperature gradient increases. For sake of simplicity, the film thermal conductivity was isotropic, the heat capacity and density of the film and substrate were identical and the heater half-width kept constant at 5um. The K_{Fy}/K_{1D} ratio was deduced from the ΔT_{F+S}-ΔT_S difference using the left part of Equation (3.5) and plotted against the film-to-substrate thermal conductivity contrast K_F/K_S at each angular frequency ω. The influence of ω on ΔT_{F+S}-ΔT_S (or K_{Fy}/K_{1D}) was studied for two cases: for a relatively low β_F of 0.1 by setting the film thickness at 500nm and for a relatively high β_F of 10 by setting the film thickness at 50um.

In the situation of small β_F ($\beta_F=b/d_F=0.1$), Figure 3.4 plots K_{Fy}/K_{1D} as a function of K_F/K_S with the frequency ω as parameter. This situation corresponds to a 10um wide heater and a 500nm thick film typical in most experiments. By comparing the solid line in Figure 3.4 calculated at zero frequency using Equation (3.5) to the marks in Figure 3.4 deduced at several frequencies from finite element analysis, Figure 3.4 shows that the data reduction of K_{Fy}/K_{1D} for increasingly higher frequencies is more severe as the film thermal conductivity increases. More precisely the apparent thermal conductivity K_{1D} deduced from Equation (3.5) is overestimated by less than ~0.1% for K_F/K_S~0.006 to a ~7% for K_F/K_S~3.3 at ω= 10,000 Hz. Figure 3.5 exhibits clear details of the relative error in apparent thermal conductivity K_{1D} due to increasingly higher frequency ω. Note that the saturating trend at 10^{-4} at low frequencies for K_F/K_S~0.006 can be misleading as this relative error also captures the error due to the inherent limitation of the finite element simulation: finite mesh nodes, finite mesh size, finite dimensions, finite numerical errors. Therefore Figure 3.5 provides also an illustration of the accuracy of the finite element method near 10^{-4}.

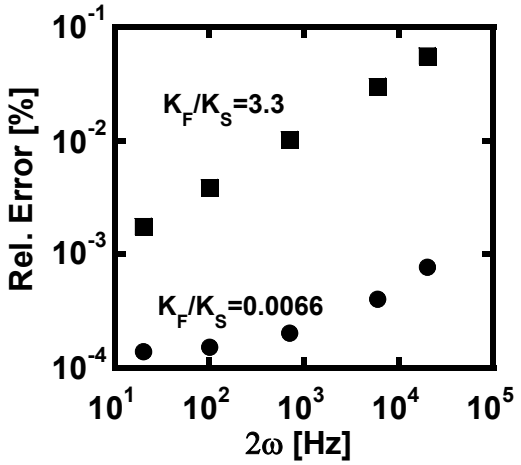

Figure 3.5. The relative error on the apparent thermal conductivity in Figure 3.4 is plotted versus frequency for two K_F/K_S ratios. The solution at ω=0 is about 0.01% accurate for a K_F/K_S~0.066 but is an order of magnitude higher for K_F/K_S~3.3. Therefore the solution at ω=0 is accurate for low thermal conductivity thin film and the importance of frequency grows as the film thermal conductivity increases. This figure also illustrates that the accuracy of the finite element method about 10^{-4}.

The previous analysis was conducted at relatively low film thickness-to-heater width ratio: β_F<<1. Figure 3.6 plots K_{Fy}/K_{1D} versus K_F/K_S in solid line for β_F=10 representing the right part of Equation (3.5) derived in the limit of vanishing frequencies. Keeping β_F=10, dotted lines represent the K_{Fy}/K_{1D} calculated from finite element analysis for a frequency ranging from 10Hz to 10,000Hz. The case of the solid line in Figure 3.6 was discussed previously by Borca-Tasciuc and co-authors[1]. In the limit of vanishing film thermal conductivity, the apparent film thermal conductivity is about 5 times higher than the film thermal conductivity. This is because in the case of large film thickness compare to heater width, the heat will predominantly flow in a two-dimensional fashion, giving more paths for the heat to flow, therefore boosting the apparent thermal conductivity K_{1D} compared to the true film thermal conductivity.

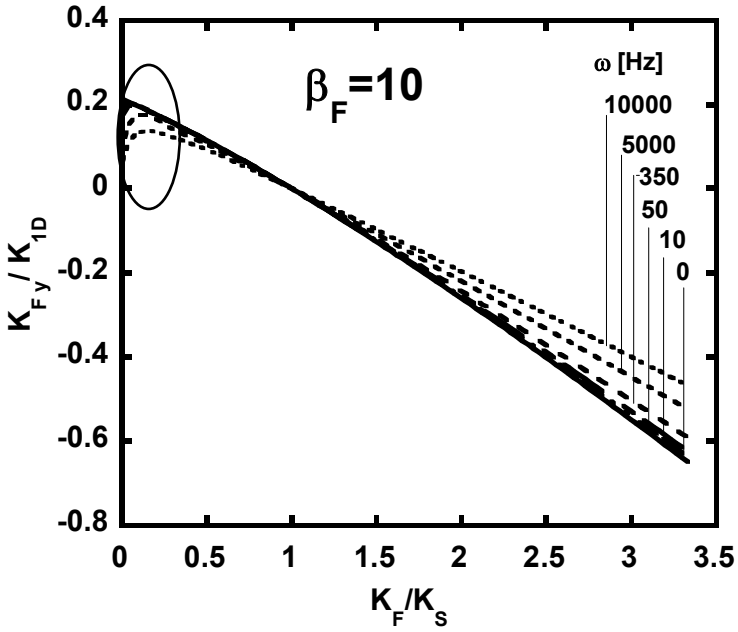

Figure 3.6. For large β_F ratios, the K_{Fy}/K_{1D} ratio derived at ω=0 from Equation (3.5) is plotted in solid line. The solutions from ω=10 Hz to ω= 10,000Hz were calculated using finite element methods in dashed dotted line. The solid line deduced from a two-dimensional model deviates considerably from solutions at non-zero frequency especially for low thermal conductivity films at frequencies ω~ 5000Hz.

However what has not been described in Ref. 1 is that at high β_F=10, the dashed lines are strongly deviating from the solid-line plotting Equation (3.5) due to frequency effects, particularly at low K_F/K_S ratios that has routinely been considered to be a safe area to operate the 3ω method. Such a trend can easily be understood. The penetration depth increases with lower thermal conductivity. For instance, the penetration depth at ω=10,000Hz is ~7um in SiO_2. As a result at low film thermal conductivity, high β_F, and high frequency, the penetration depth is confined in the film. The temperature oscillation ΔT_{F+S} becomes independent of the substrate. ΔT_{F+S} approximating the temperature oscillation of a heater deposited on a free-standing film with isothermal boundary at the bottom of the film. The definition of an apparent substrate thermal conductivity would be perhaps more appropriate than an apparent film thermal conductivity K_{1D} in describing the high frequency regime for thermally insulating films. The normalized frequency $\sqrt{\frac{2\omega}{\alpha_F}}d_F$ is unity for ω=170Hz, so clearly the assumption of zero frequency is invalidated. A 3ω experiment[8] has been

reported on a thick SiO_2 film deposited on aluminum corresponding to a β_F=10 and a K_F/K_S~0.006. The film thermal conductivity was extracted by Cahill *et al.*[8] using the slope method unlike the differential method. This illustrates that the definition of an apparent substrate thermal conductivity would be more appropriate than an apparent film thermal conductivity.

For a film-to-substrate thermal conductivity ratio K_F/K_S higher than one (K_F/K_S>1), the deviation in Figure 3.6 between the zero frequency case in solid line and the non-zero frequency situation in dashed lines is severe but not as serious as for the case of low thermal conductivity films (K_F/K_S<1) because the monotonic nature of the relationship is preserved. It can be seen from Figure 3.6 that in the regime of high film thermal conductivity and intermediate frequencies, K_{Fy}/K_{1D} is linear with K_F/K_S. From finite element simulation at ω=10,000Hz in the case of an isotropic film K_F=K_{Fy}, a simple relationship can be empirically deduced relating the measured K_{1D} to the film thermal conductivity K_F.

$$\begin{cases} \dfrac{1}{K_{Fy}} = \dfrac{1}{K_S} + \dfrac{\theta}{K_{1D}} \\ \theta = 5 \end{cases} \quad \omega = 10{,}000Hz, \beta_F = 10, \frac{K_F}{K_S} > 1 \tag{3.6}$$

Because K_{1D} is directly deduced from 3ω measurement and the substrate thermal conductivity is known, Equation (3.6) suggests a procedure to extract the film thermal conductivity K_{Fy}. To this end, it would be imperative to capture the dependence of Equation (3.6) on additional governing parameters to formulate a reliable thermal conductivity determination method immune to errors. Note that already the relative error on the substrate thermal conductivity is reproduced faithfully in a one-to-one ratio on the film thermal conductivity, which is lower than in the situation of small β_F explored previously.

To gain insight into the nature of Equation (3.6), we calculate K_{Fy}/K_{1D} for an infinite plane heater. By assuming a first order development in frequency, one finds:

$$\frac{K_{Fy}}{K_{1D}} = \left(1 - \frac{K_F}{K_S}\frac{\rho_F C_F}{\rho_S C_{SF}}\right) \bullet \left(1 - d_F \frac{\rho_F C_F}{\sqrt{K_S \rho_S C_S}}\sqrt{\omega}\right) \tag{3.7}$$

The product of thermal conductivity k_F time the heat capacity $\rho_F C_F$ is called the effusivity. From Equation (3.7) and at strictly zero angular frequency (ω=0), the

K_{Fy}/K_{1D} ratio is related to the film-to-substrate effusivity ratio and is linear with the film thermal conductivity K_F. On the other considering large heater width corresponding to β_F~0 in Equation (3.5), the K_{Fy}/K_{1D} ratio becomes equal to the factor S_C proportional to the square of the film-to-substrate thermal conductivity ratio and proportional to the square of the film thermal conductivity K_F. Therefore Equation (3.7) differs significantly in nature from Equation (3.5) at β_F~0. Fortunately neither Equation (3.7) nor Equation (3.5) are valid to describe the 3ω method when the finite heater width is finite at large driving frequency. Nevertheless as the frequency increases, film and substrate penetration depths decrease and the heater becomes closer to approximating an infinite plane source. For $K_F/K_S>1$ ratio and $\rho_F C_F=\rho_S C_S$, the penetration depth in the substrate is smaller than that in the film as opposed to the case $K_F/K_S<1$ previously discussed. Therefore in the case of intermediate frequency range for $K_F/K_S>1$, the situation of an infinite plane heater on a single film-on-substrate system may still adequately desribe parameters governing Equation (3.6) but only over a limited frequency range. Recall for the opposite case $K_F/K_S<1$, the situation at increasingly higher frequency was better described by an infinite plane heater on a bare substrate with no film.

From Equation (3.7), the film thermal conductivity K_{Fy} is deduced as follows:

$$\begin{cases} \dfrac{1}{K_{Fy}} = \dfrac{1}{K_S} + \dfrac{\theta}{K_{1D}} \quad \rho_F C_F = \rho_S C_S \\ \theta = 1 + d_F \sqrt{\dfrac{\omega}{\alpha_S}} \end{cases} \tag{3.8}$$

Equation (3.8) captures the same linear dependence between K_{Fy}, K_S, and K_{1D} as in Equation (3.6). In addition Equation (3.8) captures the qualitative dependence of K_{Fy}/K_{1D} with β_F via d_F and with ω. For instance, from Figure 3.7 when $K_F/K_S>1$, the slope of the dashed curve decreases as the frequency increases. Using the same geometrical and physical parameters as in Equation (3.6), the factor θ was found ~1.5 in Equation (3.8) three to four times lower than in Equation (3.6). One reason for this discrepancy is that the dependence of θ on the film thickness d_F via β_F must be strongly governed by the two dimensional heat spreading. An illustration is provided by the extent to which the trends plotted in Figure 3.4 differ

from those in Figure 3.6 with an associated tenfold increase in β_F. Equation (3.8) accounts purely for frequency effects. Thus it is fair to speculate that the dependence of θ on d_F in Equation (3.8) accounting for Equation (3.6) may be coincidental.

In conclusion, a method relatively immune to errors to extract film thermal conductivity in the case of $K_F/K_S>1$ may be viable for large β_F. In practice it may be necessary to consider relatively thick films of ~20-50um because the wire is often 5-10um wide. Such an extraction procedure should rely on numerical fitting from complex models including frequency effects as no satisfying simplifying analytical models could be determined. Furthermore, for accurate extraction, the presence of interfacial boundary thermal resistance between film and substrate and more importantly the effect of the heater should be included. It is well-known that heater effects become more important as the frequency increases[6]. Incidentally Liu *et al.*[11] measured the thermal conductivity of a 18.5um gallium nitride film on sapphire in a November 2004 report corresponding to a K_F/K_S~3.5 and β_F=7.4 while ω varied between 6000Hz and 60,000Hz. Figure 3.6 and Equation (3.6) nearly describes the method for these range of parameters. Liu *et al.*[11] made sure to encompass frequency effects in their extraction procedure.

3.5 Thermal Boundary Resistance (TBR)

The presence of an interfacial boundary resistance between a film and a substrate alters the thermal conductivity film extraction procedure in the differential method[7]. The essence of the thermal boundary resistance has been the focus of active studies[18]. In the following sections, the impact of the thermal boundary resistance on Equation (3.1) will be examined for a film-on-substrate system with arbitrary values of film-to-substrate thermal conductivity ratio. However as a warning against the many traps that one can encounter in the field, the thermal boundary resistance at a "perfect" interface between distinct materials with a small thermal conductivity mismatch (~10>K_F/K_S>~0.5) may be very low by nature because, in that case, the material dissimilarity may be correspondingly small entailing matched acoustic impedances at the interface[18]. Nevertheless a large thermal boundary

resistance may also originate from the presence of impurities and disorders at an imperfect interface[18]. Even better, it was seen in section 3.2 that a thermal boundary resistance can approximate a very thin thermally insulating layer across which heat flows one-dimensionally. Therefore the presence of a thin buffer layer may be reasonably modeled by a thermal boundary resistance. In light of these considerations and as most film-on-substrate systems imply the formation of a buffer layer at the film-substrate interface, the consideration of thermal boundary resistance in our heat conduction model is readily valuable.

In the limit of vanishing frequency ω=0, and for a semi-infinite substrate, Equation (3.1) applied to a single film-on-substrate system with interfacial boundary resistance leads to:

$$\frac{k_{Fy}}{k_{1D}} = \frac{2}{\pi}\int_0^\infty \frac{\sin^2 u}{u^3}\frac{\left(1-\frac{k_F^2}{k_S^2}-\rho_S u\frac{k_F^2}{k_S^2}\right)\tanh(u\beta_F)+\rho_S u\frac{k_F}{k_S}}{\beta_F\left(1+\left(\frac{k_F}{k_S}+\rho_S u\frac{k_F}{k_S}\right)\tanh(u\beta_F)\right)}du \qquad (3.9)$$

$$with\ \rho_S = \frac{R_{FS}}{b/k_S}$$

Equation (3.9) was derived for arbitrary values of K_F/K_S. The K_{Fy}/K_{1D} ratio follows the same definition as in Equation (3.5). Interestingly an arbitrary nature lies in the choice of the dimensionless boundary resistance ρ_S or ρ_F in Equation (3.5). The boundary resistance R_{FS} introduced in Equation (3.9) breaks the symmetrical role played by K_F and K_S as they cannot both vary while ρ_S or ρ_F stay constant. The same is true for β_F, d_F, and b. It is more likely that the film thermal conductivity will vary with experimental conditions compared to the substrate thermal conductivity. If the film thermal conductivity K_F varies with a parametric substrate thermal conductivity k_S, Equation (3.5) must be formulated through ρ_S. In that case, β_F can freely vary through the film thickness d_F.

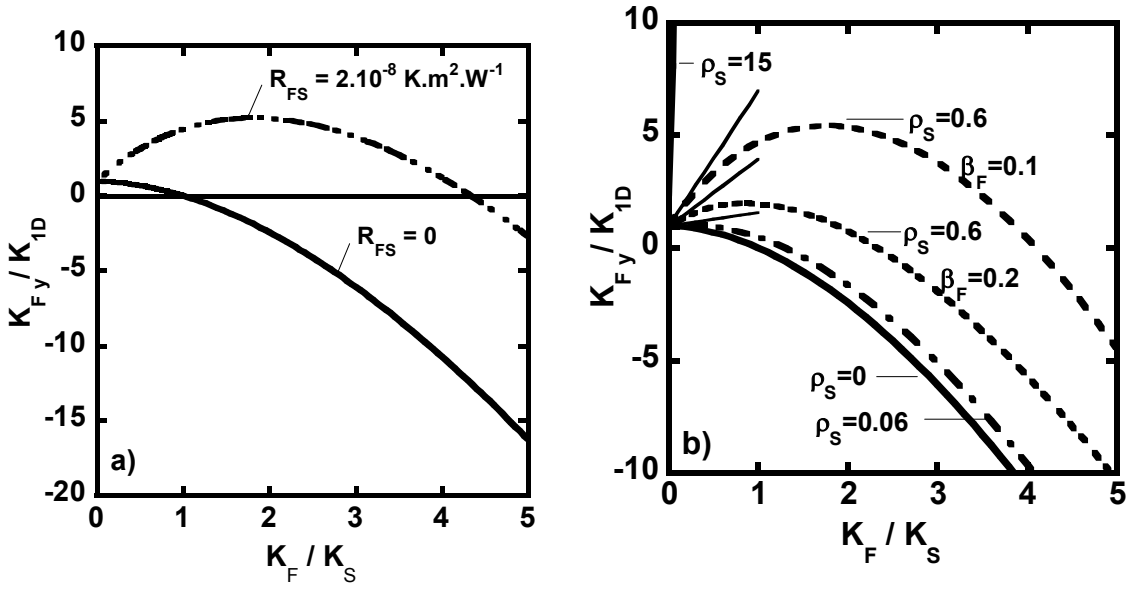

Figure 3.7. Impact of a thermal boundary resistance on the dependence of K_{Fy}/K_{1D} versus K_F/K_S using Equation (3.9): a) $R_{FS}=2\cdot10^{-8}$ $m^2\cdot K\cdot W^{-1}$ and β=0.1 b) Various ρ_S and β_F ratios. ρ_S =0.6 corresponds to $R_{FS}=2\cdot10^{-8}$ $m^2\cdot K\cdot W^{-1}$. The tangents at $K_F=0$ were plotted and represent the well-understood one-dimensional model of heat flow though a single layer with a thermal boundary resistance.

Equation (3.9) is plotted clearly in dotted line against K_F/K_S in the left graph of Figure 3.7a for β_F = 0.1, K_S=150 $W\cdot K^{-1}\cdot m^{-1}$, and for a thermal boundary resistance $R_{FS}=2\cdot10^{8}$ $m^2\cdot K\cdot W^{-1}$ between the film and the substrate. For comparison, the case with zero thermal boundary resistance (R_{FS}=0) between the film and the substrate is shown in solid line in Figure 3.7 and Figure 3.4 as well.

At first sight, the trend represented by the dotted line in Figure 3.7a shows an anomalous behavior compared to the solid line. The presence of a boundary resistance disturbs significantly the case of R_{FS}=0. To further examine the nature of the discrepancy between a zero R_{FS} and a non-zero R_{FS}, Equation (3.9) is plotted in Figure 3.7b with different parameter values of ρ_S and β_F. It can be seen that higher boundary resistance and lower β_F values worsens the deviation from the case of zero boundary resistance.

In the limit of vanishing interfacial boundary resistance, Equation (3.9) must match Equation (3.5). To gain deeper insights into the meaning of the startling trend observed in Figure 3.7, Equation (3.9) is simplified to first order in the following term.

$$\rho_F = \frac{R_{FS}}{b/k_F} = \beta_F \frac{R_{FS}}{R_{Fy}} \langle\langle 1 \qquad (3.10)$$

This condition will hold for a combination of low β_F (thin film, large heater width), low thermal boundary resistance, and relatively high film resistance. With condition (3.10), a simplified expression for Equation (3.9) is derived.

$$\frac{k_{Fy}}{k_{1D}} = \left(1 - \left(\frac{k_F}{k_S}\right)^2\right) \bullet F + \left(\frac{k_F}{k_S}\right) \frac{1}{\beta_F} \frac{R_{FS}}{b/k_S} \bullet G$$

$$\begin{cases} F\left(\beta_F, \dfrac{k_F}{k_S}\right) = \dfrac{2}{\pi} \displaystyle\int_0^\infty \frac{\sin^2 u}{u^3} \frac{\tanh(u\beta_F)}{\beta_F\left(1 + \dfrac{k_F}{k_S}\tanh(u\beta_F)\right)} du \\ G\left(\beta_F \cdot \dfrac{k_F}{k_S}\right) = \dfrac{2}{\pi} \displaystyle\int_0^\infty \frac{\sin^2 u}{u^2} \frac{1 - \tanh^2(u\beta_F)}{\left(1 + \dfrac{k_F}{k_S}\tanh(u\beta_F)\right)^2} du \end{cases} \qquad \beta_F \frac{R_{FS}}{R_{Fy}} \langle\langle 1 \qquad (3.11)$$

Equation (3.11) provides useful insight about the behavior of the differential 3ω technique applied to a single film of arbitrary thermal conductivity value with an interfacial boundary resistance between the film and the substrate. At first sight, the K_{Fy}/K_{1D} ratio is a quadratic function of the K_F/K_S modulated by two obscure coefficients F and G. Equation (3.11) will be examined in more details in a coming section. In the next section 3.5.1, Equation (3.11) is examined in the specific case of low thermal conductivity films. Therefore Figure 3.7 will be first accounted for at low K_F/Ks ratios and at low β_F.

3.5.1 Films with Low Thermal Conductivity

Equation (3.11) can be simplified in the case of low thermal conductivity films, provided the following condition is fulfilled:

$$\frac{K_F}{K_S} \langle\langle 1 \tag{3.12}$$

The quadratic term in Equation (3.11) vanishes and the correction factors F and G simplifies. Recall the definition of the thermal offset in a differential 3ω experiment,

$$\Delta T_{F+S} - \Delta T_S = Q \frac{d_F}{k_{Fy}} \frac{k_{Fy}}{k_{1D}} \; with \; Q = \frac{P}{2bl} \tag{3.13}$$

The measured or apparent film thermal resistance R_{1D} can be expressed as the sum of the film thermal resistance R_{Fy} and the interfacial boundary resistance R_{FS} modulated by the simplified terms $F(\beta_F)$ and $G(\beta_F)$ as follows:

$$R_{1D} = \frac{\Delta T_F}{Q} = R_{Fy} \bullet F(\beta_F) + R_{FS} \bullet G(\beta_F) \quad and \begin{cases} R_{Fy} = \dfrac{d_F}{k_{Fy}} \\ R_{1D} = \dfrac{d_F}{k_{1D}} \end{cases}$$

$$\begin{cases} F(\beta_F) = \dfrac{2}{\pi} \displaystyle\int_0^\infty \frac{\sin^2 u}{u^3} \frac{\tanh(u\beta_F)}{\beta_F} dt \\ G(\beta_F) = \dfrac{2}{\pi} \displaystyle\int_0^\infty \frac{\sin^2 u}{u^2} \left(1 - \tanh^2(u\beta_F)\right) du \end{cases} \tag{3.14}$$

Figure 3.8 plots $F(\beta_F)$ and $G(\beta_F)$ in solid line and illustrates the reason why $F(\beta_F)$ and $G(\beta_F)$ can be considered as correction factors. At $\beta_F \sim 0$ corresponding to a large heater width, $F(\beta_F)$ and $G(\beta_F)$ are equal to unity.

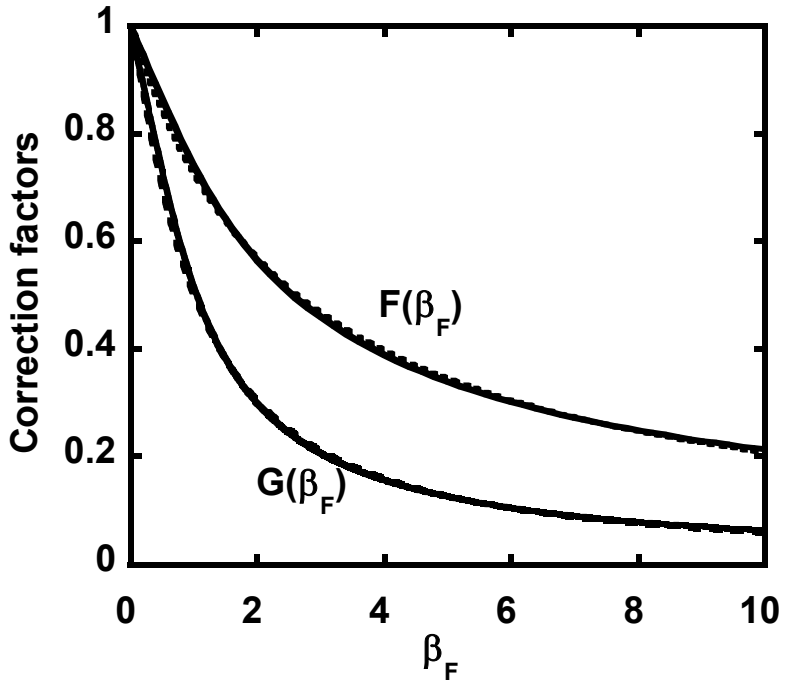

Figure 3.8. Correction factors $F(\beta_F)$, $G(\beta_F)$ for the film thermal resistance and interfacial boundary resistance in the limit of K_F=0. The solid line corresponds to the analytical solution of Equation (3.14) while the dotted line corresponds to the approximate expression (3.16).

It is well known that in the case of an infinitely large heater, the solution is purely one-dimensional. In that case, Equation (3.14) describes nothing else than a one-dimensional Fourier's law, the temperature drop being proportional to the film resistance and inversely proportional to the thermal conductivity via the film thickness:

$$R_{1D} = \frac{\Delta T_F}{Q} = R_{Fy} + R_{FS} \quad with\ Q = \frac{P}{2bl}\ and\ R_{Fy} = \frac{d_F}{k_{Fy}}$$
$$\begin{cases} F(0) = 1 \\ G(0) = 1 \end{cases} \tag{3.15}$$

In Figure 3.8, increasing β_F causes the corrections factors $F(\beta_F)$ and $G(\beta_F)$ to drop, because the heat does not purely diffuse in a one-dimensional pattern. Rather, heat diffuses slightly laterally due to geometrical effects near the edge. The existence of anisotropic film thermal conductivity also results in lateral heat spreading. Therefore the one-dimensional apparent film thermal resistance K_{1D} slightly decreases. Note that β_F cannot be arbitrarily high because the condition

(3.10) must hold. As a result there exists a set of R_{Fy} and R_{FS} values for which the trend represented in Figure 3.8 may not be valid.

$F(\beta_F)$ and $G(\beta_F)$ in Equation (3.14) can be approximated by a simpler formula within less than 5% error for $0<\beta_F<10$.

$$\begin{cases} F(\beta_F) = \dfrac{1}{(1+0.38\beta_F)} \\ G(\beta_F) = \dfrac{1}{(1+\beta_F{}^{1.20})} \end{cases} \tag{3.16}$$

The simplified expressions in Equation (3.16) are plotted in Figure 3.8 in dashed lines. It is the ultra simplified but adequate Equation (3.15) that Lee and Cahill[7] adopted to extract the thermal boundary resistance of SiO_2 on silicon. Equation (3.16) provides a compact formula to correct both the 3ω film thermal conductivity and thermal boundary resistance. For a typical 10um wire width deposited on a 500nm thick film, β_F=0.1, and Equation (3.14) shows that the measured thermal conductivity and thermal boundary resistance assuming a pure one-dimensional model are overestimated by respectively ~3% and ~5%. A systematic error of more than 3% regardless of the sophistication in experimental set-up is introduced when Equation (3.15) is assumed to describe heat flow in the film.

The reader must now draw her or his attention on the fact that the existence of the factor $F(\beta_F)$ in Equation (3.14) has been brought to light by Borca-Tasciuc *et al.*[1], where the limits of one-dimensional heat flow model has been discussed in great details. However what has not been reported in Ref. 1 is the existence of the corrective term $G(\beta_F)$ on the boundary resistance. It is surprising to observe that heat spreading in the film also affects the thermal boundary resistance expression, which is not trivial at first thought. The author of the present thesis is unaware of such a correction reported in a 3ω experiment elsewhere. The similarity between this work and Ref. 1 was important to verify the validity of our approach and the correctness of the derivation. In this thesis, the term $F(\beta_F)$ in Equation (3.14) and (3.16) has been derived with an identical result as the expression introduced and discussed by

Borca-Tasciuc and co-authors. And the correction $G(\beta_F)$ has been derived based on a similar approach as for $F(\beta_F)$.

In Figure 3.8, the correction factor $G(\beta_F)$ on the thermal boundary resistance is more important than the correction $F(\beta_F)$ on the film thermal conductivity. It can be seen that at β_F=0.1, F~97% G~95% while at β_F=1, F~0.73 and G~0.5. However in practice the apparent thermal resistance R_{1D} is dominated by the film thermal resistance R_{Fy} since in various experimental situations the thermal boundary resistance R_{FS} is much lower than the film thermal resistance R_{Fy}, typically R_{Fy}/R_{FS} ~5-10 at least. Therefore the correction brought by G on the apparent thermal resistance R_{1D} is 0.1-0.5% for β_F~0.1. Such a correction is negligible compared to measurement uncertainties. Nevertheless, if measurement precisions and uncertainties were reduced or if the thermal boundary resistance was high, Equation (3.14) depicted in Figure 3.8 should be evidenced. Putnan *et al.*[19] reported an uncertainty of less than 1% on thermal conductivity of bulk material.

In the derivation of Equation (3.14), conditions (3.10) and (3.12) were assumed. It is interesting to note that the condition $d_F/b<1$ has been necessary only for a strict one-dimensional model. To evidence the role played by condition (3.10), Equation (3.14) is plotted versus β_F in solid line in Figure 3.9 whereas Equation (3.9) is plotted in dashed line. In Figure 3.9a, the film thermal resistance is 25 times higher than the boundary resistance and ρ_F~10^{-3}. The difference between Equation (3.9) and Equation (3.14) is not observable for β_F as high as 6. In Figure 3.9b, the film thermal resistance matches the boundary resistance. Equation (3.9) in dashed line differs from Equation (3.14) in solid line, meaning that the condition $\beta_F << R_{FS}/R_{Fy}$ is less applicable. In Figure 3.9b, K_{Fy} is twice K_{1D} at β_F=0 because the apparent thermal resistance is equally shared between the film resistance and the boundary resistance.

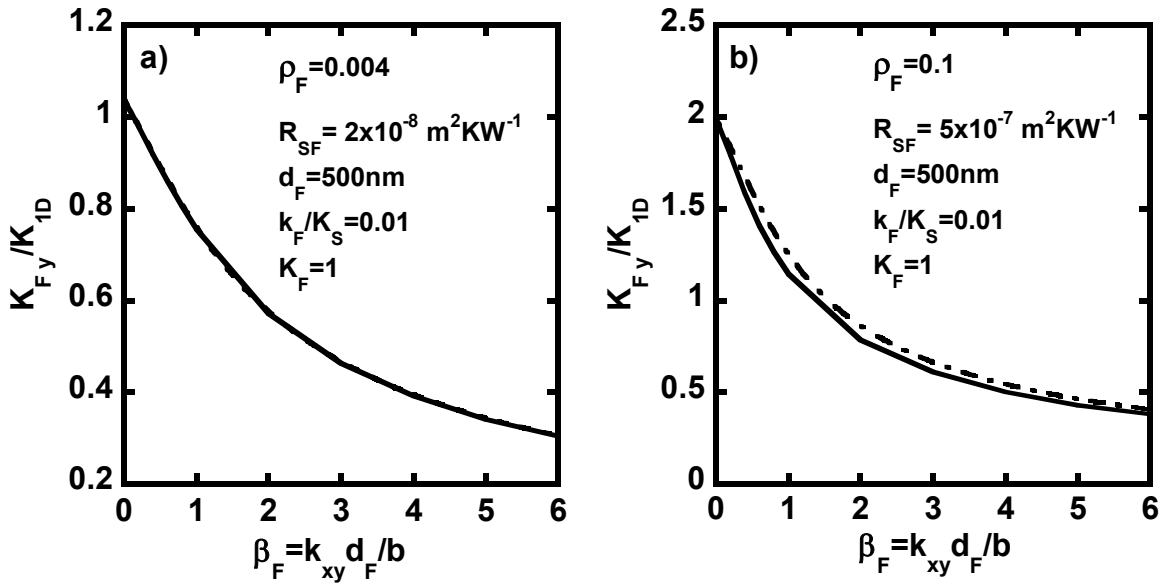

Figure 3.9. The K_{Fy}/K_{1D} ratio versus β_F for the approximated Equation (3.14) in dashed line and the full solution of Equation (3.9) in solid line: a) for a ρ_F=0.004. Note that K_{Fy}/K_{1D} ratio is not unity at β_F=0. b) for a ρ_F=0.1 with a $R_{FS}=5.10^{-7}$ $m^2 \cdot K \cdot W^{-1}$matching the film thermal resistance. As a result, the K_{Fy}/K_{1D} at β_F=0 is twice compared to the left graph a).

Figure 3.7 can now be explained for film thermal conductivity vanishing to zero: $K_F \rightarrow 0$. Equation (3.15) can be rewritten in a first order development as follows:

$$\frac{d_F}{K_{1D}} = \frac{d_F}{K_{Fy}} + R_{FS} \Leftrightarrow R_{1D} = R_{Fy} + R_{FS} \quad (a)$$
$$\frac{K_{Fy}}{K_{1D}} \approx 1 + \left(\frac{R_{FS} K_S}{b}\right) \frac{1}{\beta_F} \frac{K_F}{K_S} \quad (b) \qquad (3.17)$$

Equation (3.17b) gives the slopes in solid line of the dashed curves in Figure 3.7 at K_F/K_S=0 in three cases: i) $R_{FS}=2 \cdot 10^{-9}$ $m^2 \cdot K \cdot W^{-1}$, β=0.1, ii) $R_{FS}=2 \cdot 10^{-8}$ $m^2 \cdot K \cdot W^{-1}$, β=0.1, and iii) $R_{FS}=2 \cdot 10^{-8}$ $m^2 \cdot K \cdot W^{-1}$, β=0.2. Equation (3.17b) illustrates that K_{Fy}/K_{1D} is proportional to the dimensionless thermal boundary resistance ρ_S but inversely proportional to β_F. Therefore the dashed lines in Figure 3.7 depart further from the trend in solid line as the thermal boundary resistance increases. We may now consider the influence of K_F/K_S on the K_{Fy}/K_{1D} ratio with interfacial boundary resistance between the film and the substrate.

3.5.2 General Case

To examine the general situation of a single film with arbitrary thermal conductivity on a substrate with an interfacial boundary resistance, Equation (3.9) was simplified to Equation (3.11), which has been addressed in the previous section in the case of low thermal conductivity films at relatively low β_F. It was found that a correction to the apparent film thermal resistance by a factor function of β_F was necessary in order to deduce an accurate value of the interfacial boundary resistance from differential 3ω measurements. Equation (3.9) as plotted in Figure 3.7 was readily described for K_{Fy} nearly equal to K_{1D} and K_F/K_S near zero.

For a film thermal conductivity varying from almost zero to a few times the substrate thermal conductivity, the trends in Figure 3.7 can be described qualitatively through a few illuminating simplifying formulas stemming from Equation (3.11). The ability to draw enlightening conclusions from Equation (3.11) at a glance is hindered by the relative unappealing form of the factors F and G. It is actually easy to see that the functions F and G are monotonically decreasing with increasing K_F/K_S ratio values. A closer look at Equation (3.11) permits to establish an approximate simplifying formula:

$$\begin{cases} F\left(\dfrac{k_F}{k_S}\right) \sim \dfrac{1}{\left(1+0.38\beta_F + \dfrac{\beta_F}{1+0.8\beta_F}\dfrac{k_F}{k_S}\right)} \\ G\left(\dfrac{k_F}{k_S}\right) \sim \dfrac{1}{\left(1+\beta_F^{1.2} + \left(1.57\beta_F + 3.51\cdot 10^{-3}\right)\dfrac{k_F}{k_S}\right)} \end{cases} \qquad \beta_F \dfrac{R_{FS}}{R_{Fy}} \langle\langle 1 \qquad (3.18)$$

F and G in Equation (3.11) are approximated by less than 3% error by the formulas of Equation (3.18) for $K_F/K_S \leq 4$ and for $\beta_F=0.1$, $\beta_F=0.4$, and $\beta_F=1$. Figure 3.10 illustrates that the factors F and G are monotonically decreasing by 20 to 80% for $0 \leq K_F/K_S \leq 4$. This is contrary to the variations plotted in Figure 3.7. The quantity K_{Fy}/K_{1D} plotted against K_F/K_S in Figure 3.7 is non-monotonic and change of sign for $0 \leq K_F/K_S \leq 4$. Therefore, as in the case of low thermal conductivity film, the terms F and G in Equation (3.11) are not the most important governing parameters and can be viewed as correction terms for $0 \leq K_F/K_S \leq 4$, with however a non-negligible role to

play. Note that Equation (3.18) becomes more accurate as β_F becomes smaller and matches with Equation (3.16) in the limit of vanishing film thermal conductivity.

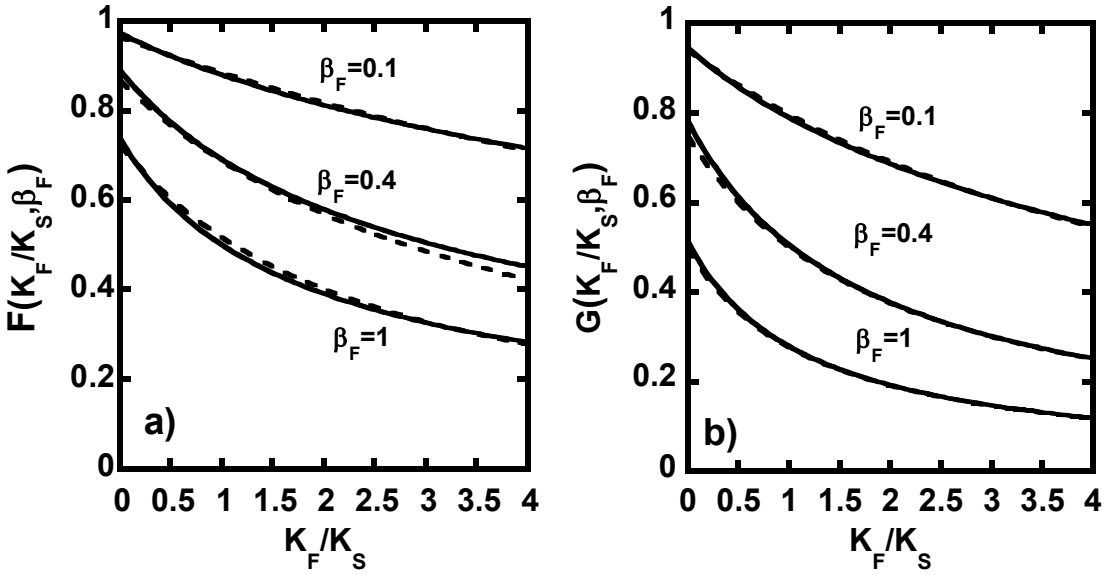

Figure 3.10. The factors F and G are plotted against the film-to-substrate thermal conductivity ratio from Equation (3.11) in solid lines and from the approximated expression of Equation (3.18) in dotted lines for three values of β_F: 0.1, 0.4, and 1. The dotted lines and solid lines describe a trend qualitatively similar in nature.

The governing terms in Equation (3.11) stand out If one disregards the factor F and G by setting G=F=1, which represents a crude but acceptable approximation in a qualitative analysis of Figure 3.7. The Equation (3.19) here below represents a cornerstone relation:

$$(a)\ \frac{k_{Fy}}{k_{1D}} = 1 + \left(\frac{k_F}{k_S}\right)\frac{1}{\beta_F}\frac{R_{FS}}{b/k_S} - \left(\frac{k_F}{k_S}\right)^2 \qquad (3.19)$$

$$(b)\ R_{1D} = R_{Fy} + R_{FS} - R_{SPRC} \quad with \quad F = G = 1$$

Equation (3.19b) derives from Equation (3.19a) by multiplying with the film thermal resistance $R_{Fy} = d_F/k_{Fy}$. In light of Equation (3.19a), Figure 3.7 can be readily accounted for. Equation (3.19a) is parabolic with respect to the film-to-substrate thermal conductivity ratio K_F/K_S and qualitatively describes Figure 3.7. The quadratic nature of K_{Fy}/K_{1D} with respect to K_F/K_S is more acute with higher boundary resistance R_{FS} and lower β_F ratios. Note that the presence of a thermal boundary

resistance is of prime importance to account for the differences between Figure 3.4 and Figure 3.7. At R_{FS}=0, Equation (3.19a) corresponds to derivation introduced by Borca-Tasciuc and co-authors. As a non-zero R_{FS} is introduced, a term proportional to K_F/K_S appears in Equation (3.19a). As the thermal boundary resistance R_{FS} increases, the condition expressed by Equation (3.10) may not hold and Equation (3.19a) may be predominantly linear with K_F/K_S. The case of outrageously high thermal boundary resistance is illustrated in Figure 3.7b with a dashed curve almost merged with the vertical axis corresponding to a thermal boundary resistance $R_{FS}=5\cdot10^{-7}$ $m^2\cdot K\cdot W^{-1}$ and ρ_S=15. One can now see that the approximation F=G=1 is well justified to conduct a qualitative treatment of Equation (3.11) through Figure 3.7.

The expression of Equation (3.19a) is well suited to capture the parameters governing Equation (3.11) plotted in Figure 3.7. However it may not lead to a very eloquent description of the physical situation. A lyric and prosaic discussion may easily initiate from Equation (3.19b). The apparent thermal resistance R_{1D} experimentally measured is the sum of the film thermal resistance R_{Fy} plus the thermal boundary resistance R_{FS} as expected, but must be subtracted by a spreading resistance R_{SPRC} related to the contrast of the film-to-substrate thermal conductivity. The expression for the spreading resistance due to the contrast of thermal conductivity is given by:

$$R_{SPRC} = R_{Fy}\left(\frac{k_F}{k_S}\right)^2 \tag{3.20}$$

In the case of a film thermal conductivity matching the substrate thermal conductivity ($K_F=K_S$) with R_{SF}=0, the apparent thermal conductivity of the film R_{1D} is zero because increasing the film thickness corresponds to increasing the substrate thickness with no alterations on the temperature distribution inside the sample whatsoever. When $K_F=K_S$, the heat in the film-on-substrate, or more simply in the substrate, flows radially from the heat source approximating a δ-line source applicable in our case of vanishing frequency. Departure of the film thermal conductivity K_F from the substrate thermal conductivity K_S results in modifications of the heat spreading configuration in the film and the substrate compared to the situation where the heat spreads radially. For a window of film thermal conductivity

near the substrate thermal conductivity, the δ-line source approximation remains accurate even if the heat spreads is no longer purely radial. This variation in heat spreading is inherent to the existence of film-to-substrate mismatch, not to the film-to-heater aspect ratio. Consequently the true film thermal resistance R_{Fy} in the expression of R_{1D} must be counterbalanced by a term R_{SPRC} that accounts not only for differences in heat spreading in the film but also in the substrate as compared to the situation when $K_F=K_S$. The term R_{SPRC} captures a relative change in heat spreading in the film and the substrate caused by the presence of the film. R_{SPRC} does not capture the absolute heat spreading in the film. The sign of the apparent thermal resistance R_{1D} will be positive ($K_F<K_S$) if heat spreading reduces from the situation when $K_F=K_S$ and negative ($K_F>K_S$) if the heat spreading is more severe compared to the case $K_F=K_S$. Recall that in the case of low thermal conductivity, the heat spreading in the film is predominantly described by the factors F and G, not by R_{SPRC} provided frequency effects are neglected.

Interestingly the thermal boundary resistance is not affected by R_{SPSC} but only by the term F and G provided condition (3.10) is satisfied. When the film thermal conductivity matches the substrate thermal conductivity $K_F=K_S$, the apparent thermal resistance is approximately equal to the thermal boundary resistance R_{FS}.

To extract the film thermal properties from the apparent thermal conductivity k_{1D} directly measured in the 3ω technique, an accurate and precise treatment of the heat conduction model is necessary. It was shown here that no simple formulas can be adopted. The G and F terms in Equation (3.11) are by no means negligible in a quantitative analysis as illustrated in Figure 3.10, save for the situation of films with low thermal conductivity. Perhaps shown below is the simplest possible expression of k_{1D} accounting for a thermal boundary resistance between the film and substrate and for a film-to-substrate thermal conductivity ratio exceeding unity.

$$\frac{1}{k_{1D}}=\frac{F\left(\beta_F,\frac{k_F}{k_S}\right)}{k_{Fy}}-\frac{k_F}{k_S^2}k_{Fxy}F\left(\beta_F,\frac{k_F}{k}\right)+\frac{R_{FS}}{d_F}G\left(\beta_F,\frac{k_F}{k}\right) \tag{3.21}$$

An accurate and systematic determination of film thermal properties will therefore require the development of adequate numerical methods as no simple

approximation can be made unless large errors are made. Besides, Equation (3.21) is already a mere simplification because it was derived under condition (3.10) and it neglects frequency effects. Due to finite substrate depth, it may be more accurate to apply the 3ω method to an intermediate range of frequency. In Section 3.4, no illuminating formulas were expressed to describe the differential 3ω method due to frequency effects. In that case, numerical resolution may be applied directly to a single layer on substrate using the complex Equation (3.1), which does even not account for the presence of the heater on the film. To illustrate the difficulty in applying the 3ω method in the general situation, it is worth noting that several authors are routinely using powerful numerical methods to extract the thermal conductivity in complex situations. Film thermal properties have been extracted from numerical analysis considering the influence of the heater[1,6], frequency effects[4-6,11], film anisotropy[1], and non-negligible film-to-substrate thermal conductivity contrast[1,4,11].

3.6 Applicability of the Differential 3ω Method

Before considering an experimental scheme to characterize the thermal conductivity of a single film on substrate, a model governing the 3ω method must be defined. It is now widely accepted that the 3ω method is a strong and complex function of a wide range of electrical, geometrical and physical parameters in the general case[1,4-6,11]. Assumptions must be made and it is important to identify the range of applicability of the differential 3ω method. The purpose of this section is to discuss the range of experimental parameters permitting an accurate and systematic 3ω characterization of a film-on-substrate system. It will be assumed an interfacial boundary resistance between the film and the substrate and arbitrary values of K_F/K_S ratios.

The applicability of the 3ω method depends on

i) The sensitivity of geometrical, electrical and thermal parameters on the experimental temperature oscillation.

ii) The source and impact of errors on the experimental temperature oscillation.

We first examine the difference ΔT_{F+S}-ΔT_S relative to the substrate temperature oscillation ΔT_S in the case of a single layer-on-substrate system with interfacial boundary resistance. From Equation (3.11) and (3.18), we define the intrinsic sensitivity S_i of the 3ω method as follows:

$$S_i = \frac{\Delta T_{F+S} - \Delta T_S}{\Delta T_S} = \varepsilon F \beta_F \left(\frac{k_S}{k_F} - \frac{k_F}{k_S} \right) + \varepsilon G \left(\frac{R_{FS}}{b/k_S} \right)$$

$$\begin{cases} \varepsilon \approx 0.3, \beta_F = \sqrt{\dfrac{k_{Fx}}{k_{Fy}}} \dfrac{d_F}{b} \\ F = \dfrac{1}{\left(1 + 0.38\beta_F + \dfrac{\beta_F}{1 + 0.8\beta_F} \dfrac{k_F}{k_S} \right)} \\ G = \dfrac{1}{\left(1 + \beta_F^{1.2} + \left(1.57\beta_F + 3.51 \cdot 10^{-3} \right) \dfrac{k_F}{k_S} \right)} \end{cases} \tag{3.22}$$

If the measurement error is 5% due for instance error in temperature coefficient or in substrate bottom boundary conditions, the sensitivity S_i may be arbitrarily required to be at least twice as high.

$$|S_i| \rangle 0.1 \tag{3.23}$$

The absolute value of the sensitivity coefficient derived in (3.22) is plotted against the film-to-substrate thermal conductivity ratio K_F/K_S in Figure 3.11. To confirm the validity of our approach, we may now reformulate a few conclusions drawn either in this thesis or elsewhere.

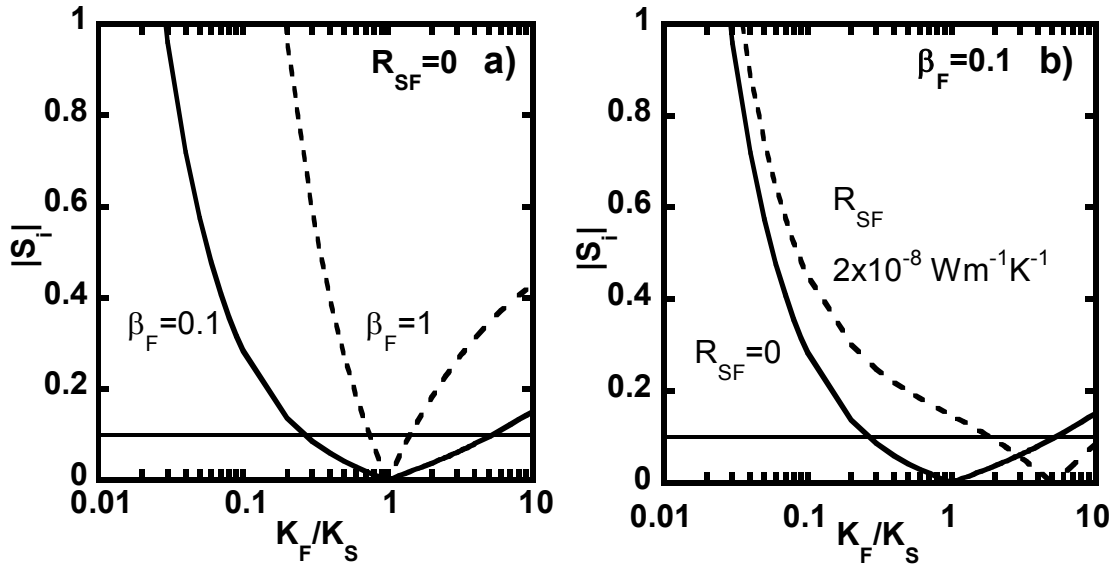

Figure 3.11. The absolute value of the intrinsic sensitivity S_i of the differential 3ω technique defined in Equation (3.22) is plotted versus the film-to-substrate thermal conductivity ratio in two cases: a) for a zero thermal boundary resistance with β_F=0.1 in solid line and β_F=1 in dashed line b) for a constant β_F=0.1 and a varying thermal boundary resistance R_{SF}. The horizontal solid line represents an arbitrary minimum sensitivity for the 3ω technique to be reliably applicable.

It is easy to see in Figure 3.11a that the film thermal conductivity has almost no impact on the differential 3ω method for a film thermal conductivity nearly matched with the film thermal conductivity K_F=K_S. On the other hand, in the low thermal conductivity regime K_F<<1, the sensitivity increases proportionally with the film-to-substrate thermal conductivity ratio. The sensitivity coefficient confirms that the differential 3ω method is adequate for the characterization of single film-on-substrate system with large film-to-substrate thermal conductivity mismatch. From Equation (3.22), the sensitivity increases with higher β_F values. Figure 3.11a plots the sensitivity for two cases: β_F=0.1 in solid line and β_F=1 in dashed line. Clearly the sensitivity increases between the case in dashed line and solid line. At β_F=0.1, the sensitivity of the technique is lower than 10% for 0.3<K_F/K_S<6. Therefore the differential 3ω technique is poorly reliable if applied to characterize a film thermal conductivity a few times lower to a few times higher than the substrate thermal conductivity. Nevertheless, the K_F/K_S window over which the differential technique becomes applicable widens by increasing the β_F ratio via thicker films: it is well

known that thick films have tendency to increase the sensitivity of thin film thermal conductivity characterization methods.

For low film thermal conductivity, the factor S_i depends on the anisotropy factor via the factor F because the product of β_F/K_F is proportional to $1/K_{Fy}$ and becomes independent of K_{Fx}. Therefore higher sensitivity will be achieved when the out-of-plane thermal conductivity K_{Fy} becomes higher than the in-plane thermal conductivity K_{Fx}. Furthermore the technique is more sensitive to the anisotropy factor as the heater width decreases. Indeed T. Borca-tasciuc *et al.*[1] have described a method to extract the anisotropy factor of low thermal conductivity films by varying the heater width. However the technique is not as sensitive with the anisotropy factor as on film thickness, heater width or film thermal conductivity. For instance, at $\beta_F=1$, a decrease of anisotropy by a factor 2 gives a mere 10% increase in sensitivity. Conversely at high film thermal conductivity, the product of β_F/K_F becomes proportional to $1/K_{Fx}$ and becomes independent of K_{Fy}. However the situation is unfortunately not reversed compared with the case of low film thermal conductivity. If the factor S_i is still dependent on the anisotropy factor via the factor F, this time F drops which makes the technique poorly reliable to measure the anisotropy at high film thermal conductivity. It is fortunate that at low thermal conductivity, the technique will be rather sensitive to the anisotropy factor. At high thermal conductivity, the technique is unlikely to be adequate to measure the anisotropy factor. The success of the method in Ref. 1 relies partly on the fact that the 3ω technique is rather sensitive to the anisotropy ratio for low thermal conductivity films, making it a reliable technique. Note that 3ω technique is not suitable for the diffusivity measurement as long as the assumption of zero frequency holds.

The latter conclusions are drawn assuming no thermal boundary resistance between the film and the substrate, no frequency effects and no heater effects. Section 3.4 has shown that frequency effects were small for small β_F values. The influence of the heater[6] is minute when the dimensionless frequency is less than 0.1. The effect of the boundary resistance can be seen in Figure 3.11b where the sensitivity factor is plotted against K_F/K_S for a constant $\beta_F=0.1$. The differential technique becomes adequate in the case of low thermal conductivity films but less

applicable in the regime of high thermal conductivity films. In Figure 3.11b, the sensitivity is equally shared between the film thermal conductivity and the thermal boundary resistance for K_F/K_S~0.2. Beyond K_F/K_S>0.2, the 3ω method is mainly sensitive to the thermal boundary resistance. Neglecting the thermal boundary resistance can lead to large errors in thermal conductivity extraction. Equation (3.22) shows that the relative sensitivity on the thermal boundary resistance can be reduced only by increasing the film thickness or the anisotropy factor. The presence of an interfacial boundary resistance becomes detrimental to the characterization of film thermal conductivity when K_F/K_S>1. To measure the film thermal conductivity more accurately, the sensitivity on the boundary resistance can be reduced by increasing the layer thickness, increasing the heater width and considering a relatively low thermal conductivity substrate. If the thermal conductivity of the 18.5um thick gallium nitride in Ref. 10 was extracted neglecting the presence of a thin 100nm buffer layer, then the value of the thermal conductivity would be underestimated. From that perspective, the extracted value of 125 $W \cdot K^{-1} \cdot m^{-1}$ would represent a lower bound for the thermal conductivity of gallium nitride.

The definition of the sensitivity factor may suggest a clear methodology in sample preparation to extract three unknowns namely the film thermal conductivity, the thermal boundary resistance, and the anisotropy factor (via β_F). From Equation (3.22), the operator has only control on the wire width 2b and film thickness d_F (via β_F) as it is difficult to control the thermal conductivity of the substrate in practice.

Assume a small film-to-substrate thermal conductivity ratio, say K_F/K_S ~5%, a thermal boundary resistance $R_{SF}=2.10^{-8} m^2 \cdot K \cdot W^{-1}$ and a substrate thermal conductivity k_S=150 $W \cdot K^{-1} \cdot m^{-1}$ (silicon). From Equation (3.22), measurement of the anisotropy factor is preferentially done for thick films (~1um) and relative small heater width by varying the heater width or film thickness. It may be easier in practice to vary the heater width.

Conversely measurements of thermal boundary resistance are carried out at low film thickness (~100nm) and large heater width by varying film thickness. As a reminder, increasing the heater width is in contradiction with approximation of zero frequency. In case the film-to-substrate thermal conductivity ratio increases, Figure

3.11 suggests that neither the film thermal conductivity nor the thermal boundary resistance may be negligible, unless the film thickness increases. At low β_F, both heater width and film thickness would need to be varied. Varying multiple parameters represent an additional hurdle to the characterization of film thermal conductivity.

Oftentimes, a 100nm insulating layer, typically SiO_2, is deposited on the film-on-substrate system prior to heater formation if the underlying material is electrically conductive. The insulating layer introduces a thermal offset ΔT_{IS} purely dependent on the heater width, the film thickness d_{IS} and the insulating layer thermal conductivity k_{IS}. Partly because the method is differential, the quantity ΔT_{F+S}-ΔT_S will depend on differences in film thickness and heater width between two distinct samples. This observation is not relying on error analysis. Simply the heat conduction theory assumes a unique value of heater width and film thickness for both samples. As seen before, the sensitivity coefficient is high for low thermal conductivity films. In that the case, it is expected that the technique be sensitive to variations in heater width or insulating film thickness d_{IS} from one sample to another. One could define an extrinsic sensitivity that would encompass differences in film thickness and heater width between two different samples. The technique becomes error prone as the variations in film thickness d_{IS} and heater width variations. That situation becomes worse as measurement errors are introduced.

3.7 Conclusion

In this chapter, the applicability of the 3ω method in the case of relatively elevated film thermal conductivity was examined for a single film-on-substrate system. Gallium nitride-on-substrate provides an adequate example of sample having film-to-substrate thermal conductivity ratios below or above unity. The presence of an interfacial boundary resistance was included in the heat conduction model. The role played by the frequency on the extracted thermal conductivity was studied. Each parameter, namely the film thermal conductivity via the K_F/K_S ratio, the thermal boundary resistance, and the driving frequency were studied separately. In Section 3.5.2, the role of the film-to-substrate thermal conductivity contrast and the

thermal boundary resistance were included simultaneously in the heat conduction model under the assumption of low frequency. Several simplifications were made and their accuracy was discussed.

The novelty throughout the chapter lies in the discussion on thermal boundary resistance. The situation of a thermal boundary resistance between a film and a substrate corresponds to the case of a three-layer problem with no heat spreading in the layer between the substrate and the top layer, which may be applicable to the case of gallium nitride-on-substrate system with thin buffer layers. Therefore we generalize in an elegant formalism the treatment of the 3ω method to a thee-layer system under the condition of one-dimensional heat flow in the intermediate layer. Predicting an adequate experiment is facilitated by examining the sensitivity coefficient introduced. The analysis turns to be complicated as the number of parameter increases.

Theory shows the 3ω interfacial resistance must be corrected by a small factor in the case of low thermal conductivity films. As the film thermal conductivity increases, the film thickness must increase to characterize the film thermal conductivity more successfully. It was established that influence of frequency was small for small film thickness-to-heater width aspect ratio. In the case of a β_F=10, good agreement between numerical simulations and the model derived form the assumption of plane heater was found.

3.8 References

1 T. Borca-Tasciuc, A. R. Kumar, and G. Chen, "Data reduction in 3 omega method for thin-film thermal conductivity determination," *Review of Scientific Instruments*, vol. 72, pp. 2139-2147, 2001.

2 G. Chen, S. Q. Zhou, D.-Y. Yao, C. J. Kim, X. Y. Zheng, Z. L. Liu, K. L. Wang, X. Sun, and M. S. Dresselhaus, "Heat conduction in alloy-based superlattices," *Proceedings of the 1998 17th International Conference on Thermoelectrics, ICT, May 24-28 1998*, pp. 202-205, 1998.

3 J. H. Kim, A. Feldman, and D. Novotny, "Application of the three omega thermal conductivity measurement method to a film on a substrate of finite thickness," *Journal of Applied Physics*, vol. 86, pp. 3959-3963, 1999.

4 J. L. Liu, A. Khitun, K. L. Wang, W. L. Liu, G. Chen, Q. H. Xie, and S. G. Thomas, "Cross-plane thermal conductivity of self-assembled Ge quantum dot superlattices," *Physical Review B*, vol. 67, pp. -, 2003.

5 B. W. Olson, S. Graham, and K. Chen, "A practical extension of the 3 omega method to multilayer structures," *Review of Scientific Instruments*, vol. 76, 2005.

6 C. E. Raudzis, F. Schatz, and D. Wharam, "Extending the 3 omega method for thin-film analysis to high frequencies," *Journal of Applied Physics*, vol. 93, pp. 6050-6055, 2003.

7 S.-M. Lee and D. G. Cahill, "Heat transport in thin dielectric films," *Journal of Applied Physics*, vol. 81, pp. 2590-2595, 1997.

8 D. G. Cahill, H. E. Fischer, T. Klitsner, E. T. Swartz, and R. O. Pohl, "Thermal-Conductivity of Thin-Films - Measurements and Understanding," *Journal of Vacuum Science & Technology a-Vacuum Surfaces and Films*, vol. 7, pp. 1259-1266, 1989.

9 H. Morkoç, *Nitride semiconductors and devices*. Berlin ; New York: Springer, 1999.

10 W. L. Liu and A. A. Balandin, "Temperature dependence of thermal conductivity of AlxGa1-xN thin films measured by the differential 3 omega technique," *Applied Physics Letters*, vol. 85, pp. 5230-5232, 2004.

11 W. Liu and A. A. Balandin, "Thermal conduction in AlxGa1-xN alloys and thin films," *Journal of Applied Physics*, vol. 97, pp. 1-6, 2005.

12 T. D. Bennett, "Determining anisotropic film thermal properties through harmonic surface heating with a Gaussian laser beam: A theoretical consideration," *Journal of Heat Transfer*, vol. 126, pp. 305-311, 2004.

13 J. C. Lambropoulos, S. D. Jacobs, S. J. Burns, and L. Shaw-Klein, "Effects of anisotropy, interfacial thermal resistance, microstructure, and film thickness on the thermal conductivity of dielectric thin films," *Winter Annual Meeting of the American Society of Mechanical Engineers, Nov 8-13 1992*, vol. 227, pp. 37-49, 1992.

14 A. Feldman, "Algorithm for solutions of the thermal diffusion equation in a stratified medium with a modulated heating source," *High Temperatures-High Pressures*, vol. 31, pp. 293-298, 1999.

15 Y. S. Ju, K. Kurabayashi, and K. E. Goodson, "Thermal characterization of anisotropic thin dielectric films using harmonic Joule heating," *Thin Solid Films*, vol. 339, pp. 160-164, 1999.

16 A. Jacquot, B. Lenoir, A. Dauscher, M. Stolzer, and J. Meusel, "Numerical simulation of the 3 omega method for measuring the thermal conductivity," *Journal of Applied Physics*, vol. 91, pp. 4733-4738, 2002.

17 U. G. Jonsson and O. Andersson, "Investigations of the low- and high-frequency response of 3 omega-sensors used in dynamic heat capacity measurements," *Measurement Science & Technology*, vol. 9, pp. 1873-1885, 1998.

18 D. G. Cahill, W. K. Ford, K. E. Goodson, G. D. Mahan, A. Majumdar, H. J. Maris, R. Merlin, and S. R. Phillpot, "Nanoscale thermal transport," *Journal of Applied Physics*, vol. 93, pp. 793-818, 2003.

19 S. A. Putnam, D. G. Cahill, B. J. Ash, and L. S. Schadler, "High-precision thermal conductivity measurements as a probe of polymer/nanoparticle interfaces," *Journal of Applied Physics*, vol. 94, pp. 6785-6788, 2003.

Chapter 4 Characterizing the Properties of the Gallium Nitride: Thermal Conductivity

4.1 Introduction

In this chapter, the thermal conductivity of relatively thick gallium nitride grown by Hydride Vapor Phase Epitaxy (HVPE) is characterized using the 3ω method in an attempt to identify the key factors limiting the gallium nitride thermal conductivity. One major result of this thesis is that a precise dependence of the gallium nitride thermal conductivity on dislocation density was clearly evidenced in this work in contrast with previous reports. It is important to note in our experimental approach that the thermal conductivity measurements were taken prior to material characterization. But before getting to more details, it is necessary to introduce two key background elements: the very basics of thermal conductivity theory and the research status in the field of gallium nitride thermal conductivity. Afterwards, the body of the study will be presented starting with a description of sample characteristics and characterization methodology. Thermal conductivity experimental data will be interpreted depending on sample thickness and material inhomogeneity, and compared with finite element simulation analysis. Next a section will discuss the dependence of gallium nitride thermal conductivity mostly on dislocation density, point defects, and temperature in light of experimental results and previous reported works. The last section will underline the major advances made throughout this study.

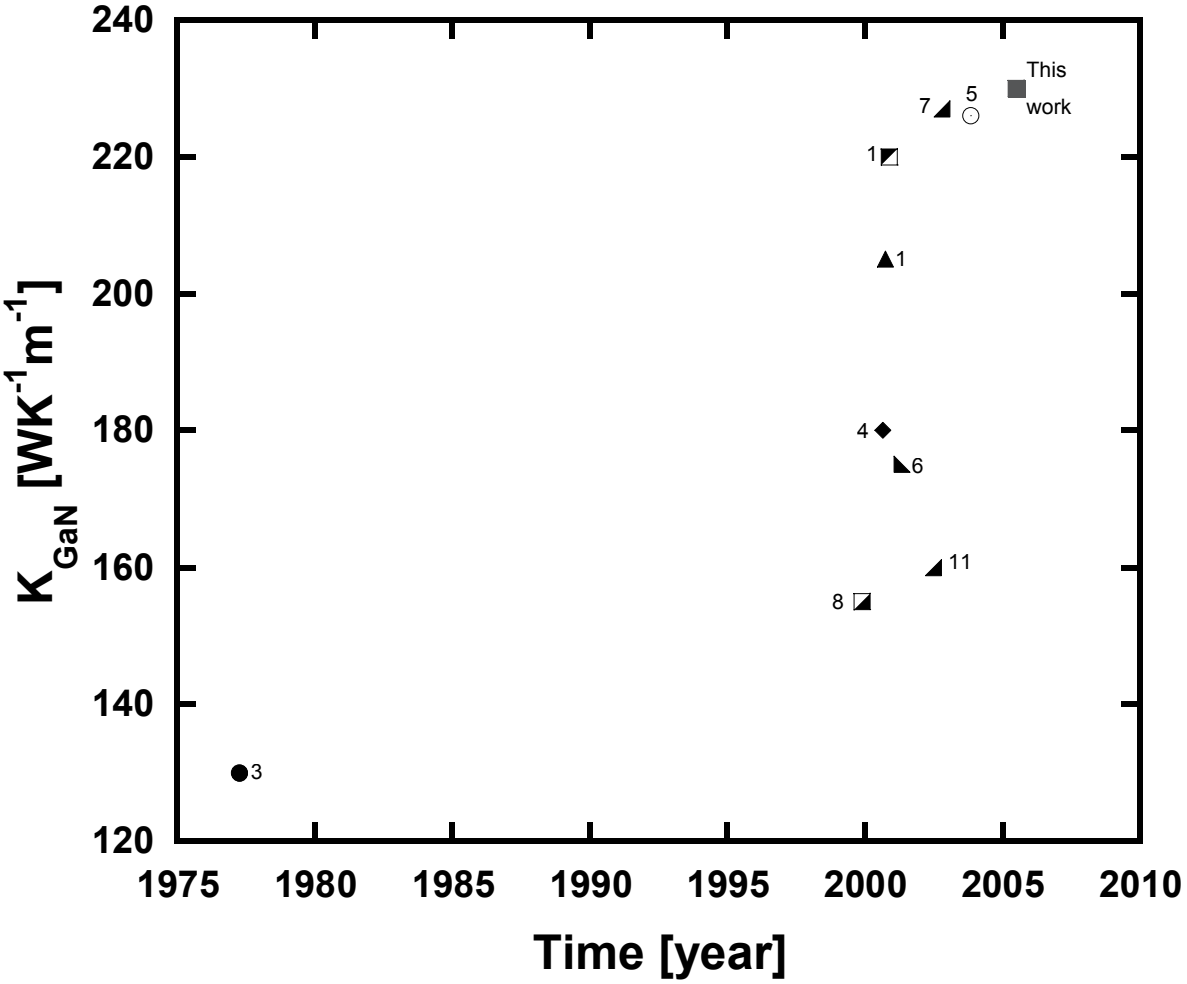

Figure 4.1. Experimental room temperature thermal conductivity of gallium nitride plotted against time in years corresponding to independent research studies. Each data point represents the highest value reported in each reference. The time corresponds to the official date of publication. A broad spread of values can be seen although they tend to be increasingly higher with time.

4.1.1 The Thermal Conductivity of Semiconductors

Heat in solids may be conducted through a variety of carriers[12]: electrons, phonons (lattice waves), magnons (spin waves), photons, possibly excitons[13], etc. In semimetals, the principal carrier are electrons and phonons, leading to an overall thermal conductivity $k=k_e+k_g$ where k_e is the electronic component and k_g the lattice component[12]. In metals, the electronic thermal conductivity dominates[12-14] whereas in semiconductors such as gallium nitride, the thermal conductivity is completely dominated by the lattice thermal conductivity except perhaps in a limited number of

cases[12-14]. For instance Ref. 9 experimentally determined that the electronic thermal conductivity in gallium nitride is ke~0.15 $W \cdot K^{-1} \cdot m^{-1}$ which is three orders of magnitude lower than typical experimental gallium nitride thermal conductivity values depicted in Figure 4.1. In practice, it is difficult to evidence the electronic thermal conductivity of semiconductor even at very high doping level and high temperature[13,14]. Nevertheless it is important to bear in mind that electrons may play an appreciable role in limiting the lattice thermal conductivity through interactions with phonons[13,14]. As a consequence of thermal conductivity dependence on lattice characteristics, any disturbance on lattice waves and crystal structure will directly affect the thermal conductivity value. Material quality is therefore of prime importance in the determination of semiconductor thermal conductivity. This is especially true of gallium nitride[2,15]. Furthermore, the heat is dominantly carried by acoustic phonons because of high group velocity. Therefore the dispersion relation of acoustic phonons is generally of utmost importance in the determination of thermal conductivity although optical phonons can alter the thermal conductivity by scattering with acoustic phonons[14].

The thermal conductivity of a “perfect” defect-free semiconductor is limited by crystal anharmonicity or phonon-phonon interaction. In that case the thermal conductivity is referred to as the intrinsic thermal conductivity and represents the highest value achievable. The theory of crystal anharmonicity that accounts for thermal expansion introduces the Grüneisen parameter γ (or anharmonicity parameter) often present in thermal conductivity studies.

A bulk of work, best summarized in Ref. 13 and 16, has shown that the magnitude of room temperature thermal conductivity of non-metallic solids such as lithium fluoride, diamond, silicon, gallium nitride, silicon carbide,etc can be predicted by a semi-empirical relation of the type[12-14,16,17]:

$$k \sim A \frac{\overline{M} \delta \theta_D^3}{\gamma^2} \qquad (4.1)$$

A is a constant, Θ_D is the Debye temperature, $\overline{M}$ is the average mass of an atom in the crystal, δ^3 is the average volume occupied by one atom of the crystal,

and γ is the Grüneisen constant. Because of a lack of experimental data in γ values thirty-two years ago, Slack determined in 1973 a best fit empirical value for A/γ^2 = $8.77.10^{-3}$ $W/g{\cdot}cm^2{\cdot}K^4$ for a series of 15 crystals at room temperature[7,17]. Equation (4.5) becomes more exact to describe the high temperature ($T>\Theta_D$) thermal conductivity of face-centered-cubic crystals having one atom per primitive crystallographic unit cell. In that case, A=B/T where T is the temperature and B is a constant. From Equation (4.5), it is easy to see that the four rules for selecting a nonmetallic crystal with high thermal conductivity are:

(1) a low atomic mass (high Θ_D),

(2) a strong interatomic bonding (high Θ_D),

(3) a simple crystal structure (low number of atom per primitive unit cell),

(4) a low anharmonicity (low γ).

Diamond is a good example of nonmetallic material optimizing the relation (1.5)[17]. The Debye temperature plays a major role in predicting the intrinsic thermal conductivity[12,17]. Unfortunately the Debye temperature is oftentimes theoretically determined and is not precisely known in the case of gallium nitride. There is a large discrepancy of reported values partly because of an associated disparity in gallium nitride elastic constants. A few theoretical studies have estimated the room temperature GaN thermal conductivity. Deriving an expression very similar in nature to Equation (1.5), Witek[18] estimated a room temperature thermal conductivity ~410 $W{\cdot}K^{-1}{\cdot}m^{-1}$ using the heat capacity corresponding to a Debye temperature Θ_D~830K. Recently Slack *et al.*[7] have determined 227 $W{\cdot}K^{-1}{\cdot}m^{-1}$ calculating Θ_D~650K from elastic constant values reported by other authors. Actually Slack estimated 170 $W{\cdot}K^{-1}{\cdot}m^{-1}$ in a 1973 report assuming a Θ_D~600K despite limited knowledge of the gallium nitride physical constants[17]. Ref. 15 and 19 established intermediate values at 370 $W{\cdot}K^{-1}{\cdot}m^{-1}$ and 344 $W{\cdot}K^{-1}{\cdot}m^{-1}$ adopting respectively Θ_D~1058K and ~830K. It is worth noting that Jeżowski *et al.*[5] determined experimentally Θ_D~400K from thermal conductivity data fit at room temperature and confirmed the Debye temperature thus obtained from calculations based on elastic constant reported in the literature. It follows that theoretical values of gallium nitride may simply not provide an accurate

insight on the highest thermal conductivity value achievable. Rather it may indicate a rough range of higher bound of thermal conductivity values probably lying somewhere between 170 $W \cdot K^{-1} \cdot m^{-1}$ and 410 $W \cdot K^{-1} \cdot m^{-1}$.

Apart from phonon-phonon interaction, other important phonon-scattering mechanisms arise in a crystal due to phonon scattering from lattice disorders, crystal boundaries or interaction with electrons. The phonon mean free path is directly related to the phonon scattering constant time when the Boltzmann equation is solved through a relaxation time approach. The total phonon relaxation time τ_T is related to each individual relaxation processes of time constant τ_i through the relation[13-15]:

$$\frac{1}{\tau_T} = \sum_i \frac{1}{\tau_i} \tag{4.2}$$

For point imperfections, phonon scattering may be caused by the difference in mass and size because of variations in force constant between the impurity and the host atom in the lattice. It the impact of mass impurity inhomogeneity on the phonon spectrum is obvious, the difference in size entails a misfit strain field in the vicinity of the impurity that modifies the force constant through anharmonicity in the lattice. The scattering time constant associated with point defect scattering in the case of a single substitutional impurity can be shown to be inversely proportional[13,14,17] to Γ.

$$\Gamma = f\left[\left(\frac{\Delta M}{M}\right)^2 + 40\left(\frac{\Delta\delta}{\delta}\right)^2\right] \tag{4.3}$$

f is the fractional concentration of the impurity atom of mass M. ΔM is the mass difference between impurity and host atom, Δδ is the local lattice mismatch and δ is the cube root of atomic volume of the impurity in its own lattice. Equation (4.3) illustrates that mass defects and strain defects can be responsible for thermal conductivity limitations. To quantitatively treat the case of several impurities in compound material, the expression for Γ differs form Equation (4.3) by minor corrections[7].

Fluctuations in mass-difference throughout the crystal can cause additional thermal resistance[13,14]. In particular, the existence of isotopes in the constituent

element will limit the thermal conductivity value, not only because of inherent random mass defects but also due to lattice distortion and change in effective force constant resulting from quantum effects[14]. In the case of gallium nitride, Witek determined an intrinsic thermal conductivity value of 410 $W \cdot K^{-1} \cdot m^{-1}$ and he assigned lattice defects as the main cause of measured thermal conductivity being lower than theoretical value[18]. Later, Berman shed more light on the correctness of Witek's statements by estimating the isotopic thermal resistance from a hypothetical "Zimman limit" of the gallium nitride thermal conductivity at 300K[20]. The isotopic thermal resistivity was found about twenty times lower than the experimental gallium nitride resistivity of ~$8.3 \cdot 10^{-3}$ $K \cdot m \cdot W^{-1}$. Berman explained that the effects of the large concentration, 38.5% of the isotope ^{71}Ga in the gallium is offset by the small relative mass difference ($\Delta M/M$), while the isotope ^{15}N represents only 0.38% in nitrogen isotopic impurities. Slack *et al.*[7] corrected their experimental room temperature thermal conductivity values for isotopic using a similar expression as Equation (4.3) to find that thermal conductivity increased from 227 $W \cdot K^{-1} \cdot m^{-1}$ to 251 $W \cdot K^{-1} \cdot m^{-1}$. The resulting isotopic thermal resistivity was in good agreement with Berman's determination. Fluctuations in mass difference and the presence of strain are also an important factor to describe the thermal conductivity of alloys such as $Al_xGa_{1-x}N$ [2,13,14]. Moreover it is important to note that thermal conductivity limitations may occur via lattice disorders other than point defects such as dislocations. Berman provides an extensive review on the modeling of phonon scattering by dislocations[14].

Phonons can also be scattered by electrons or holes in bound states or in free carrier state[13,14]. The precise effect of free carrier scattering may be difficult to experimentally determine in semiconductors as an increase of electron concentration from higher impurity concentration can be responsible for additional phonon scattering[15]. Separating the effect between carrier and impurity scattering may be attempted with experiment conducted in the presence of a magnetic field or over a large range of temperature[13,14]. At low temperature the thermal conductivity is sensitive to impurity scattering[13]. Boundary scattering is preponderant at very low temperature and the thermal conductivity is proportional to the cube of the temperature and the diameter of the crystal[13,14]. In the high temperature regime,

phonon-phonon scattering dominates via three-phonon Umklapp processes[13,14]. The thermal conductivity approximates the intrinsic thermal conductivity and is inversely proportional to the temperature. The inverse temperature dependence becomes increasingly accurate as the temperature exceeds the Debye temperature[12-14,16,17]. Somewhere between the high temperature regime and the low temperature regime described above, the thermal conductivity peaks, usually at a temperature well below 300K for almost all standard semiconductors[13]. Therefore the room temperature thermal conductivity provides a fortunate benchmark reference between different semiconductors. Note that the thermal conductivity properties of highly disordered material such as amorphous materials or alloyed materials is drastically different compared with the thermal conductivity properties of semiconductors covered previously[13].

Most single crystal semiconductors such as germanium, silicon, gallium arsenide, etc present negligible thermal conductivity anisotropy[13]. The degree of thermal conductivity anisotropy can be inferred from a few characteristics of the lattice. Considering equation (1.5), anisotropic properties are expressed through the Debye temperature function of the sound velocity and through the Grüneisen parameter. Slack *et al.*[7] illustrate that the average c-plane and a-plane sound velocity differ by less than 1% whereas the anisotropy in the Grüneisen parameter was measured to zero[7]. Hence Slack *et al.*[7] estimate the gallium nitride thermal conductivity anisotropy is less than 1% at 300K.

4.1.2 Literature Review

The first report on the gallium nitride thermal conductivity was given by Sichel and Pankove in 1977[3]. In this pioneer study, the temperature dependence of a 400um thick gallium nitride layer grown by HVPE on a r-plane sapphire substrate was measured using an along-layer steady state technique. A room temperature thermal conductivity of 130 $W \cdot K^{-1} \cdot m^{-1}$ was found. In this thesis, it is observed from the published data that the temperature dependence of the thermal conductivity is strongly related to material quality. Luo *et al.*[8] measured the thermal conductivity of laterally epitaxially overgrown (LEOG) gallium nitride using a third harmonic method

and found a lower bound of 155 $W \cdot K^{-1} \cdot m^{-1}$. The 3ω slope method was employed again to measure the thermal conductivity temperature dependence of four specimens consisting of three HVPE grown gallium nitride samples and one LEOG gallium nitride sample[6]. The highest value at room temperature was ~165 $W \cdot K^{-1} \cdot m^{-1}$ on the HVPE grown gallium nitride sample having a dislocation density of ~10^8 cm^{-2} measured from atomic force microscopy. The carrier concentration was $5 \cdot 10^{18}$ cm^{-3} according to the authors[6]. The latter study raised several concerns about the report of Asnin *et al.*[4] published in 1999. In this work, the thermal conductivity was measured 170-180 $W \cdot K^{-1} \cdot m^{-1}$ at room temperature using a scanning thermal microscope. The same team joined up by Florescu and Jones reported exactly a year later with the same scanning thermal microscope technique a room temperature gallium nitride thermal conductivity reaching 210 $W \cdot K^{-1} \cdot m^{-1}$ on the overgrown regions of partially coalesced LEOG samples where the dislocation density was the lowest[1]. In between the LEOG stripes where the dislocation density is the highest, the thermal conductivity was measured 100 to 120 $W \cdot K^{-1} \cdot m^{-1}$, pointing out that the reduction in thermal conductivity was correlated to a high dislocation density. In parallel, Florescu *et al.*[9] studied the thermal conductivity limitations of HVPE grown GaN/sapphire (0001) samples as a function of both carrier concentration varying from $8 \cdot 10^{16}$ cm^{-3} to $8 \cdot 10^{18}$ cm^{-3} and sample thickness varying from 0.8um to 74um. Beyond the relation established between increasing film thickness and increasing thermal conductivity values, this study laid the emphasis on the observed linear decrease in thermal conductivity with the logarithmic of the concentration. More specifically, a twofold reduction in thermal conductivity was found for every decade increase in the carrier density measured by hall effect and raman spectroscopy. Soon after, Florescu and Pollak discussed the effect of grain boundaries combined to dislocations in HVPE gallium nitride samples in an attempt to account for the limitations of gallium nitride thermal conductivity[21]. In the meantime a room temperature thermal conductivity of 220 $W \cdot K^{-1} \cdot m^{-1}$ was reported on bulk gallium nitride from Vaudo and co-authors[10]. In a 2002 theoretical study based on a relaxation time approach, Zou *et al.*[15] have shown that the observed decrease of thermal conductivity with increasing electronic concentration from Ref. 9

can be readily ascribed to the presence of impurities. In other words, the impurities Si, O, C known as main donors in gallium nitride can be proved to be the sole source of scattering centers and account for the observed trend in Ref. 9 minimizing the role of electron-phonon interaction in thermal conductivity limitations[15]. Moreover In the same theoretical report, it was shown that the thermal conductivity can be limited by dislocations provided their density is higher than 10^{10} cm^{-2} which represents a high value in contradiction with Ref. 1 discussed earlier[15,19]. The same authors as in Ref. 21 but this time joined up with Lee, Ming, and Ramer established an empirical correlation between MOCVD grown gallium nitride thermal conductivity values and photoluminescence signal, surface roughness, dislocation density, and X-ray diffraction measurements.

Slack *et al.*[7] reported the thermal conductivity dependence of HVPE grown gallium nitride and found a value of 227 $W \cdot K^{-1} \cdot m^{-1}$. Intriguingly, the gallium nitride thermal conductivity limitation was ascribed to the presence of oxygen in gallium nitride by drawing a parallel with results obtained in the field of aluminium nitride. Further controversy is introduced with the report of a research group located in Japan where the thermal conductivity is measured from 110K to 370K on a 122um thick free-standing HVPE grown gallium nitride sample[11]. It is found a room temperature thermal conductivity of approximately 160 $W \cdot K^{-1} \cdot m^{-1}$ with a temperature dependence nearly identical to that reported by Sichel and Pankove in 1977 but in large contradiction with the temperature dependence reported by Slack and co-authors[7]. More recently, thermal conductivity measurement was performed on gallium nitride material almost free of dislocation grown by a unique method at high temperature and high pressure causing a high oxygen content in gallium nitride ($>10^{20}$ cm^{-3})[5]. It was found a room temperature thermal conductivity of 226 $W \cdot K^{-1} \cdot m^{-1}$ with a temperature dependence in good agreement with Ref. 7 although the measurements were taken down to 4.2K, probably representing the lowest thermal conductivity temperature measurement ever reported on gallium nitride[5]. However the thermal conductivity was found minimum with lowest electron concentration, which at first sight seems to contradict the predictions made in Ref. 15, except that in the high temperature high pressure growth method, high electrical resistivity

material is obtained by introducing compensating Mg impurities. Considering this, agreement with Zou *et al.*[15] is restored. Given the high concentration of oxygen in their high temperature high pressure grown bulk gallium nitride, the authors proposed that the presence of oxygen could be responsible for the observed thermal conductivity limitations[5]. Finally, very recently theoretical development based on a relaxation time approach[2] was found to give reasonable numbers for the experimental thermal conductivity temperature dependence of gallium nitride grown by high temperature high pressure of Ref. 5.

4.1.3 Study Outline

This present study investigates the thermal conductivity characteristics of undoped and iron doped HVPE gallium nitride. Using the 3ω slope method from 300K to 450K, thermal conductivity measurements were carried out on samples of various thicknesses ranging from hundreds of microns to a few millimeters. It is found that the thermal conductivity is strongly dependent on material quality and more precisely on dislocation density above 10^7 cm^{-2}. The highest room temperature thermal conductivity value is found on a semi-insulating iron sample to be ~230 $W \cdot K^{-1} \cdot m^{-1}$. The thermal conductivity was deduced by carefully accounting for sample finite thickness and material inhomogeneity using analytical model and finite element analysis. From our work and in conjunction with previous work on undoped gallium nitride, the dependence of thermal conductivity on dislocation density is specified. The effect of semi-insulating impurity on thermal conductivity such as iron is discussed. The temperature dependence of gallium nitride thermal conductivity above room temperature is examined. It is reemphasized once again that the thermal conductivity measurements were taken prior to any material characterization. It was the thermal conductivity measurements that were suggestive of the relevant sample characterizations to be carried out. However for sake of clarity, results on material characterization are presented first followed by thermal conductivity data.

4.2 Characteristics of Hydride Vapor Phase Epitaxy grown Gallium Nitride

Four gallium nitride samples were grown on c-plane sapphire with different thicknesses by KYMA Technology, Inc employing the Hydride Vapor Phase Epitaxy Method (HVPE) introduced in Chapter 1. Sample characteristics are summarized in Table 4.1.

Table 4.1. Gallium nitride sample characteristics. U=undoped. Fe=iron doped. Initial thickness = thickness before polishing. Dislocation densities were measured by catholuminescence (see Appendix D)

Sample ID	Doping	GaN layer	As-grown Thickness [um]	Final Thickness [um]	Resistivity [Ω·cm]	Dislocations at surface [cm^{-2}]
A	U	epi	~250	200 ±70	1-20	$4 \cdot 10^{7}$
B	U	bulk	~700	370 ±20	1-20	$1.5 \cdot 10^{7}$
C	U	bulk	1700	1400 ±50	1-20	$8.8 \cdot 10^{6}$
D	Fe	bulk	2000	2000 ±50	$2 \cdot 10^{8}$	$5 \cdot 10^{4}$

Sample A, B, C, and D were grown following the HVPE process resulting in gallium nitride thicknesses of ~250um for A, ~700um for B, ~1700um for C, and ~2000um for D. Sample B, C, and D were subsequently lifted-off from the sapphire wafer by KYMA Technology, Inc. Therefore Sample B, C, and D represent free-standing gallium nitride materials and are referred to as “bulk” material in Table 4.1. On the contrary, sample A is a thick epitaxial gallium layer on sapphire throughout the study. Sample B was polished on both side equally resulting in a final ~370um thick bulk material. Sample A was polished in the center but the edges were almost untouched because of dramatic wafer bow. The final thickness was ~200um. Sample C front side was left as-grown with hillocks while 300um of gallium nitride material were removed on the backside. Finally Sample D was unpolished

presenting an as-grown front surface. Micrograph of sample C and D surface can be found in Appendix D. As-grown surface samples are thought to have the highest thermal conductivity values. Indeed in diamond thermal conductivity studies, better results were obtained on as-grown surface samples[22], the top surface layer being the less defective part of diamond sample.

Sample A, B, and C were undoped while sample D was in-situ iron doped. Impurity levels were measured with Secondary Ion Mass Spectroscopy (SIMS) measurements. Figure 4.2 below provides an example of iron profile in sample D.

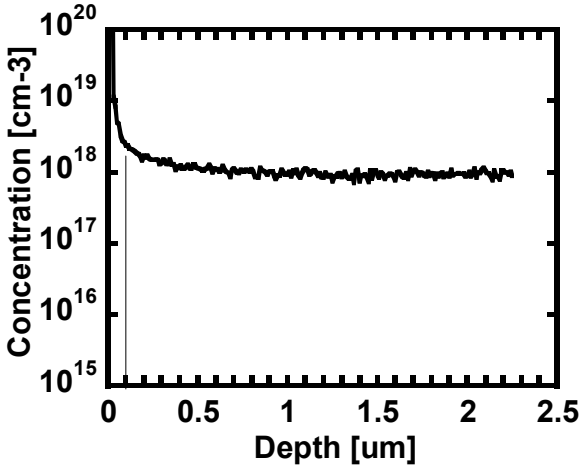

Figure 4.2. Fe profile on sample D deduced from Secondary Ion Mass Spectroscopy (SIMS) using an oxygen beam. The vertical line roughly indicates the depth at which SIMS becomes reliable.

In Figure 4.2, the profile below a depth of 20nm corresponds to the gold coating whereas the detected Fe concentration in the next 70nm below the surface sample is sensitive to the presence of surface contamination and variation in sputtering yield. All in all, the impurity concentration becomes reliable for depth superior to 100nm indicated by the solid line in Figure 4.2. The iron concentration determined by SIMS measurements confirmed the targeted in-situ doping of 10^{18} cm^{-3}. On iron doped material, the concentration of Fe^{3+} was determined from Electron Paramagnetic Resonance (EPR) at 50K by M.E. Zvanut from the University of Alabama at Birmingham. Impurities concentrations are summarized in Table 4.2.

Table 4.2. Impurity level in undoped and iron doped gallium nitride. All were deduced from SIMS measurements except Fe^{3+} deduced from EPR at 50K.

Sample Type	Undoped (A, B, C)				Fe :GaN (D)	
Impurities	H	C	Si	O	Fe	Fe^{3+}
Level [cm^{-3}]	$4 \cdot 10^{17}$	10^{17}	$3 \cdot 10^{16}$	10^{17}	10^{18}	10^{18}

The measured concentration of Fe^{3+} matches the Fe concentration from SIMS measurements which suggests that irons are electrically active and dominantly substitionnal on gallium sites. EPR measurement is suggestive of the semi-insulating nature of sample D and confirmed the targeted iron concentration of 10^{18} cm^{-3} during growth in addition to SIMS measurements. The EPR donor signal at 4K on undoped samples was $5 \cdot 10^{16}$ cm^{-3}. The achievable carrier concentration at 300K is in good agreement with the concentration of dominant persuasive donor namely oxygen, and silicon[23,24] as listed in Table 4.2. Recall that iron is introduced in gallium nitride to render the material semi-insulating by compensating unintentionally incorporated donor impurities. In other work, Iron impurities has been shown to form a deep acceptor level located ~0.34 eV below the conduction band[25].

The electrical resistivity of iron doped gallium nitride has been determined at $2 \cdot 10^{8}$ Ω·cm from conventional hall effects by William C. Mitchel from AFRL/MLPS labs.

Table 4.3. Summary of resisitivity, mobility and carrier concentration on sample D measured at room temperature by William C. Mitchel from AFRL/MLPS labs.

Resistivity Ω·cm	Mobility $cm^2/V.s$	Carrier concentration cm^{-3}	Type
$2 \cdot 10^{-8}$	330 ± 30	$\sim 10^8$	N

Table 4.3 demonstrates that iron-doped sample D is semi-insulating (SI), in agreement with observations made from electron paramagnetic resonance measurements (EPR) associated with SIMS profiles. In Table 4.3, the resistivity as well as carrier concentration is typical of semi-insulating semiconductor. Typically the resistivity is higher than 10^7 Ω·cm in SI-GaAs, SI-InP, SI-SiC, etc. From four-point measurements, the electrical resistivity of undoped gallium nitride material was measured between 1 and 20 Ω·cm. Taking a free carrier concentration estimated at $5 \cdot 10^{16}$ cm^{-3} (EPR) and a mobility of 300 $cm^2 \cdot V^{-1} \cdot s^{-1}$ (hall effect), the resistivity can be roughly estimated ~0.5 Ω·cm whose order of magnitude is in close agreement with measured values.

Catholuminescence of sample A, B, C and D was studied at 300K.

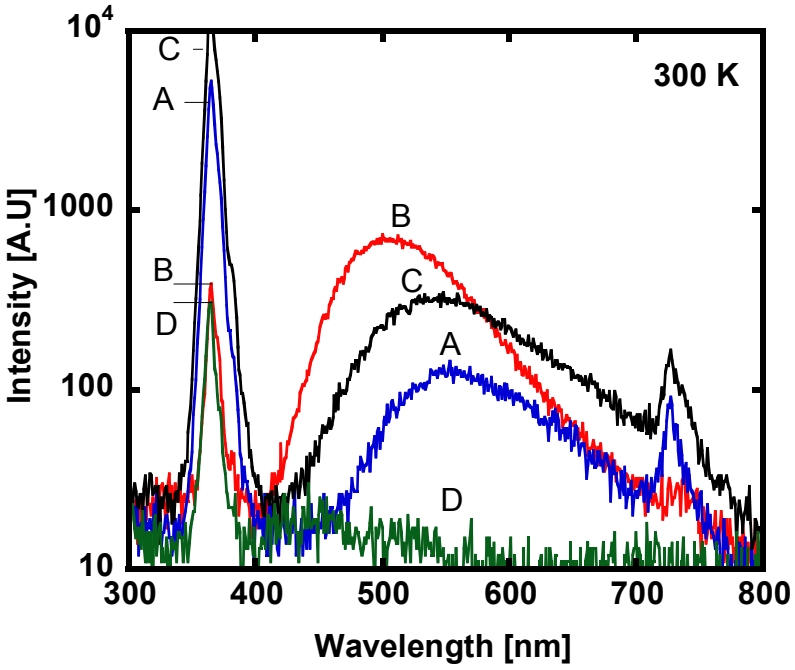

Figure 4.3. Catholuminescence measurement at 300K for undoped sample A, B, C, and D. The probe current was 10^{-10} A for samples A, B, C and $3 \cdot 10^{-9}$ for sample D. The peak at 730nm is the second order diffraction of the band edge emission.

Two features stand out in Figure 4.3: the intensity of the band edge emission at 365nm and the intensity and location in energy of the defect peak near 550nm. The lower band edge emission for sample D compared to sample C could be due to the high concentration of 10^{18} cm^{-3} deep acceptor irons inhibiting the formation of electron-hole pairs (typically 10^{18} cm^{-3} generated pairs in CL experiment for typical beam current of 10^{-10} A[26]). It is interesting to note that the 500nm defect peak is absent for sample D or lies within the noise level. The yellow luminescence commonly observed in gallium nitride thin film and reproduced for sample A, B, and C is tentatively ascribed by several authors to originate from the interaction between oxygen and gallium vacancies[7,26]. The concentration of gallium vacancies[7] can typically lie between 10^{16} and 10^{18} cm^{-3}. In that case it is not impossible that the presence of a content of 10^{18} cm^{-3} iron occupying gallium sites[27] could modify the equilibrium concentration of gallium vacancies, thus reducing the intensity of the yellow peak emission. Those comments are pure speculations and further state-of-the-art research would need to be addressed to investigate the nature of the iron

impurity in gallium nitride notably with low temperature photoluminescence experiment.

More relevant to our study is the characterization of dislocation density at sample surface from catholuminescence imaging and etch pits count deduced from AFM scans and Nomarski micrographs. For further details on defect characterization of sample A, B, C and D, the reader is referred to Appendix D where the defect density is clearly shown to decrease with the as-grown GaN thickness listed in Table 4.1. Appendix D establishes that the catholuminescence technique gives the most accurate dislocation density values in this study. Four catholuminescence images are shown below for respectively sample A, B, C, and D.

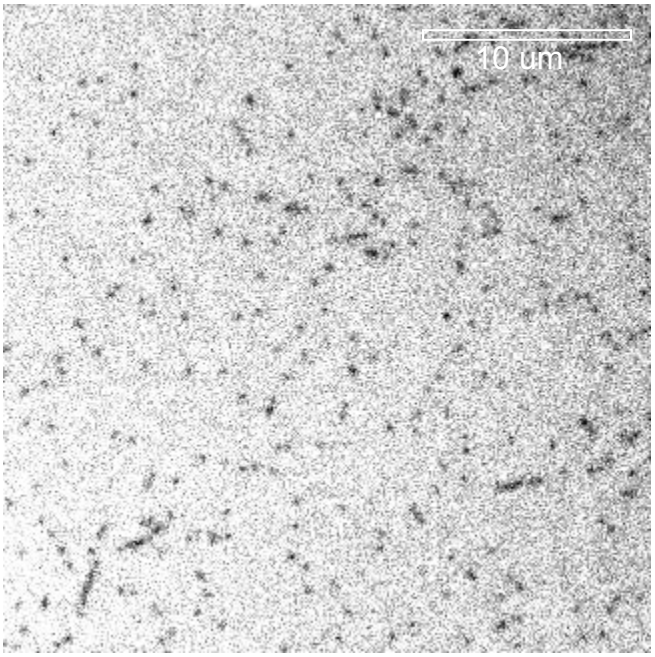

Figure 4.4. Approximately 350-400 dislocations for sample A (30um x 30 um). ρ_D=~4·10^7 cm^{-2}.

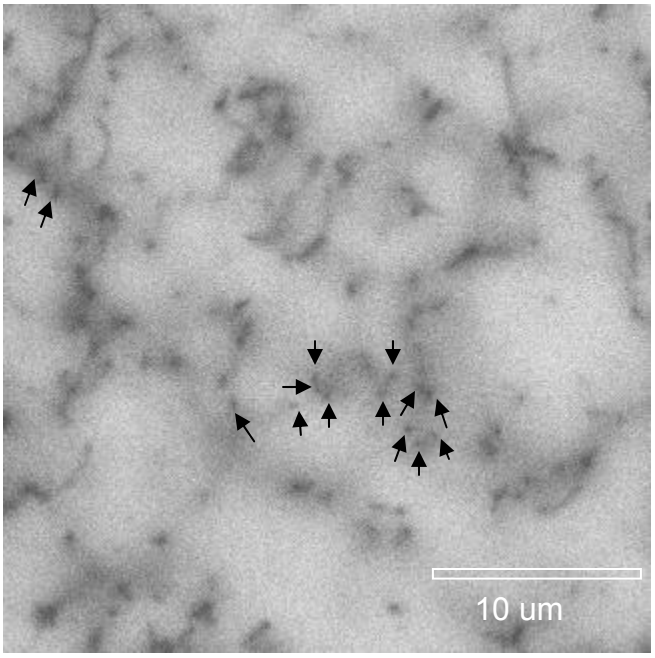

Figure 4.5. Approximately 100 to 200 dislocations for sample B (30um x 30 um). ρ_D~$1 \cdot 10^7$ to $2 \cdot 10^7$ cm^{-2}. Dark spots seem difficult to count but are not impossible to count as the arrows indicate. Dark spots are surrounded by dark blur that are not counted as dislocations. The dislocation density is clearly higher for sample C and higher for sample B for the area considered.

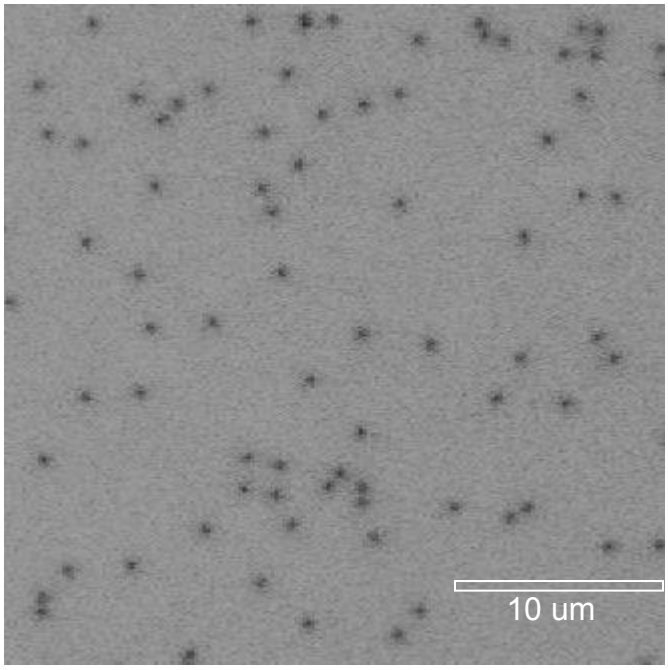

Figure 4.6. Dislocation density measurements on sample C. 79 dislocation densities over a 30x30 um^2 gives a dislocations density of $8.8 \cdot 10^6$ cm^{-2}.

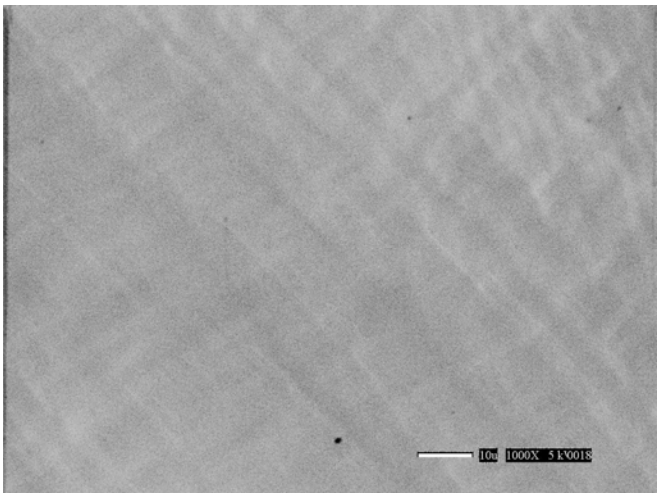

Figure 4.7. Plane view catholuminescence imaging of the Sample D. 6-7 dislocations over a ~118x90 um^2 area gives a dislocations density of ~5·10^4 cm^{-2}. Appendix D presents further results that better justifies the average value of 5·10^4 cm^{-2} as accurate for the dislocation density of sample D.

Dislocation density measurements are covered in-depth in Appendix D and will not be repeated here. Rather more attention are now being brought to the two Figures below that show transmission measurement at 300K on sample C and D in the ultra-violet and visible region of the spectrum (UV-VIS).

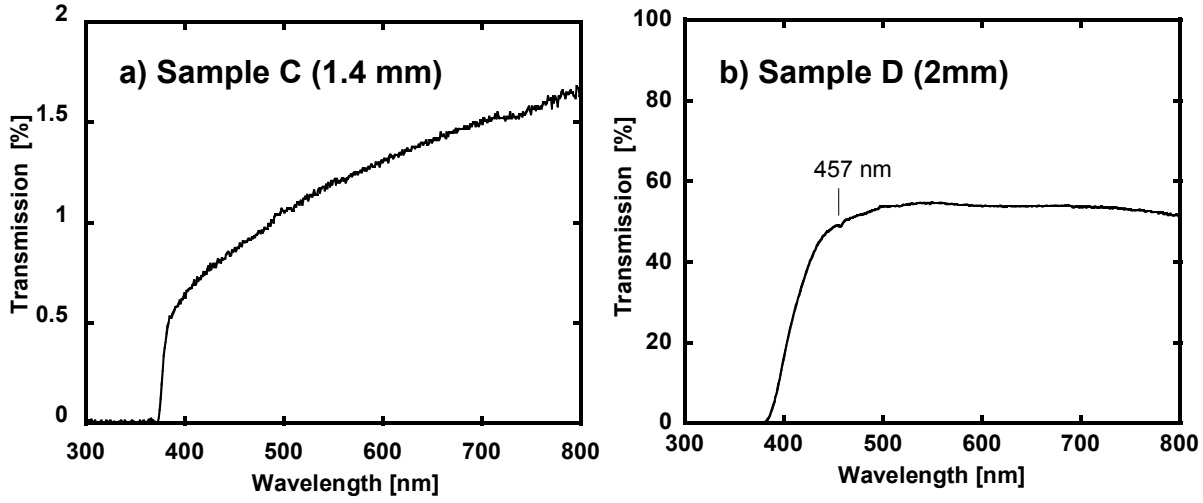

Figure 4.8. UV-VIS transmission measurements at 300K for a) sample C and b) sample D. Note the scale of the transmission: ~1% for 1.4 mm thick sample C (opaque) and ~55% (transparent) for sample D despite a thickness of 2mm and rough surfaces. The kink at 457nm for sample D has been reproduced over several transmission measurements taken at various scan speed in different sample positions and dates. This kink has also been reported in Ref. 25.

It is important to note that samples C and D are unpolished and thick (~mm). They consequently present a rough surface that can increase light scattering at the surface and can artificially reduce the level of transmission, the latter reduction can be exacerbated by absorption due to thickness effects especially near band edge where absorption varies dramatically[7]. Nevertheless, Figure 4.8a shows that sample C is highly absorbing. However the band edge fall-off is sharp for sample C. It is not clear what exact role a 10^{18} cm^{-3} concentration of deep acceptor Fe present in sample D would play in transmission measurements. Figure 4.8b shows that sample D is at least semi-transparent. From naked human eyes sensitive to the 550nm wavelength strongly emitted by the sun, sample D looks indeed transparent and colorless while sample C looks brownish and opaque. Interestingly a kink in the spectrum of sample D in Figure 4.8b was repeatedly observed at 457nm over several measurements taken at various scan speeds with different sample positions at different dates. Although there is presently no explanation accounting for the 457nm kink, other works have similarly reported a dip at 457nm in transmission data of lightly doped Fe:GaN with a concentration of Fe equal to or lower than the oxygen background concentration[25].

4.3 Characterization of HVPE GaN Thermal Conductivity Using the 3ω Method

First thermal conductivity measurement of gallium nitride samples at room temperature will be examined. In the 3ω technique, two assumptions may not systematically hold.

i) The sample thickness may not always be considered infinite but finite depending on the penetration depth.

ii) The thermal conductivity may not always be assumed constant with thickness but function of thickness instead.

Despite an extensive literature search, no reports have been found on the applicability of the 3ω technique in the situation of inhomogeneous materials, unlike photoacoustic or photothermal techniques[28-34]. Therefore, to account for finite

thickness effects and the presence of a thermal conductivity gradient in gallium nitride substrate, accurate 3ω data analysis will be interpreted through finite element simulations.

Finally, temperature dependent measurements will be presented. The linear slope method was found to be valid for measurements at T>370K given the decrease in thermal conductivity and penetration depth in the temperature range considered. It will be seen that the thermal conductivity of gallium nitride range around 200 $W \cdot K^{-1} \cdot m^{-1}$ at room temperature and that, most importantly, it is monotonically decreasing with thickness.

4.3.1 Experimental Details

The thermal conductivity was measured using the 3ω slope method. An exhaustive presentation of the 3ω slope method was given in Chapter 2. Nevertheless a few basic elements must be briefly outlined to grasp the correctness and relevance of future experimental interpretations. First, sample preparation proceeds as follows. Prior to heater formation, a 100nm PECVD oxide is deposited on the gallium nitride sample to electrically isolate the heater from the gallium layer. The SiO_2 thickness was monitored by ellipsometry on a silicon monitor sample. Next 5nm Cr/ 200nm Au is deposited by e-beam, lithographically defined and released by lift-off procedure. The nominal heater length was 1mm long while the heater nominal width was 10um or 8um in different locations on the mask. It is worth noting that severe wire width shrinkage was observed during the lithography step as a result of rough surface on sample C (hillocks) or non-uniform thickness in sample D. Further experimental details are found in Chapter 2. Heater width is measured by optical microscopy.

Under the approximation of an infinitely long line source located on an homogeneous semi-infinite isolating substrate of thermal conductivity k_s and diffusivity D, the temperature oscillation ΔT averaged over the heater of width 2b delivering an electrical input power per unit length P_l is related to the third harmonic $V_{3\omega}$ as follows:

$$\frac{2V_{3\omega}}{\alpha_T V_{1\omega}} = \Delta T = \frac{P_l}{\pi \kappa_s}\left(\frac{1}{2}\ln\frac{D}{b^2} + 0.923 - \frac{1}{2}\ln(2\omega) - \frac{i\pi}{4}\right) + \Delta T_{OX} \qquad (4.4)$$

By taking the slope of the third harmonic $V_{3\omega}$ versus the driving frequency ω, the thermal conductivity is inferred. The PECVD SiO_2 layer adds a frequency independent component ΔT_{OX} leaving the temperature oscillation versus frequency slope unchanged for two reasons. First the oxide penetration depth is much higher than the oxide thickness at the frequency of operation. Second the film to substrate thermal conductivity ratio will be less than 1%. Again, the 3ω slope method consists of extracting the substrate thermal conductivity from the slope of the temperature oscillation versus lnω based on Equation (4.4). The discussion in Chapter 2 on experimental details including calibration and measurement errors will not be reproduced here.

4.3.2 Extracting the Thermal Conductivity

Sample C and D (300K)

The temperature oscillation normalized to power, $\Delta T/P$ is plotted versus frequency ω for sample C and D in Figure 4.9.

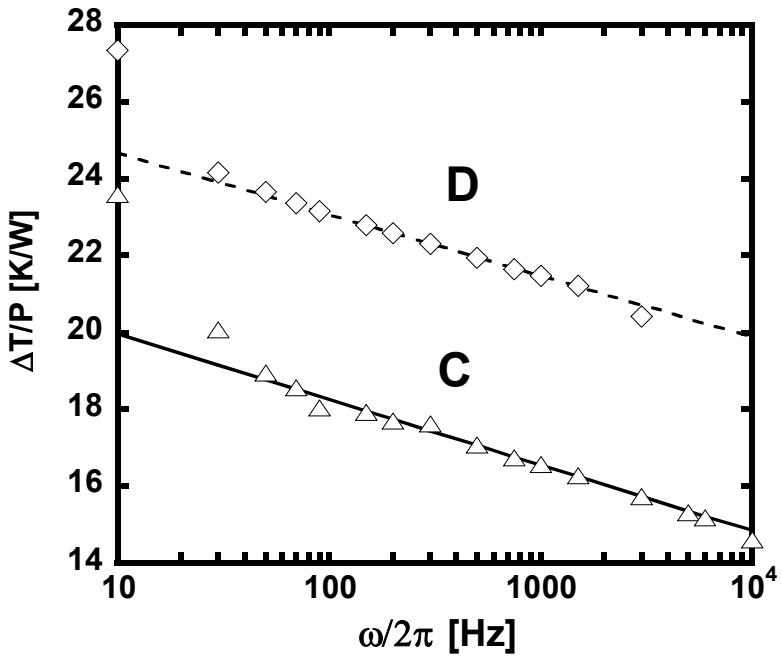

Figure 4.9. The 3ω temperature oscillation ΔT was normalized to the input power P and recorded versus frequency at room temperature for sample C and D listed in Table 4.1.

The thermal conductivity was deduced by taking the slope of the temperature oscillation using Equation (4.4) for ω/2π ranging between 150 Hz and 1500 Hz. A room temperature thermal conductivity of 230 $W \cdot K^{-1} \cdot m^{-1}$ and 215 $W \cdot K^{-1} \cdot m^{-1}$ was determined for respectively the iron doped 2mm thick sample D and the undoped 1.4 mm thick sample C. The temperature oscillation is higher for the sample D than for sample C due to narrower wire width associated with the as-grown surface roughness and tilted surface. The wire width was ~5um on sample D and ~7um on sample C.

In the low frequency range (ω/2π<70Hz), the temperature oscillation versus lnω departs from the linear extrapolation. As the frequency increases, the penetration depth λ increases becoming in most cases comparable to the substrate thickness d_S. This effect is not taken into account in Equation (4.4) where the substrate thickness is assumed to be infinite. At low frequency, the temperature oscillation is highly dependent on the bottom boundary condition and on the substrate thickness[35]. The frequency upper bound of linear extraction is limited by the finite heater width and finite wire heat capacity. Therefore, as with most 3ω

measurements relying on the slope method, the frequency range of linear extraction is restricted in practice from about 150Hz to 3000Hz for consistency between samples of different thickness.

Sample A (300K)

Measurements were taken in two different locations on the ~ 200um gallium nitride epi sample (labeled A in Table 4.1). Figure 4.10 shows the 3ω temperature oscillations recorded on a site labeled A2 near the sample edge and another site A1 in the center part of the polished area where the gallium nitride layer is probably thinner. Recall that sample A consists of thick gallium nitride layer on top of a sapphire substrate.

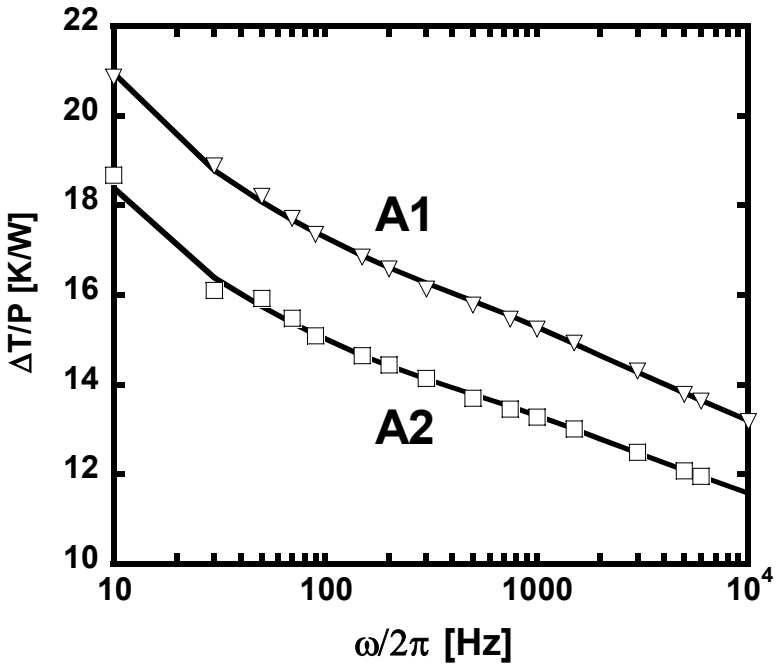

Figure 4.10. Measured temperature oscillation normalized to power on site A1 (triangle) in the center part of the sample and A2 (square) closer to the sample edge. The solid line represents the calculated temperature oscillations from finite element.

The first observation is that the experimental data, plotted in triangle and square for respectively A1 and A2 in Figure 4.10, departs from a linear trend throughout the frequency range, expect perhaps for frequencies over 5000Hz. Estimating the diffusivity from previous measured thermal conductivity value with the heat capacity and density values from Table 1.3 in Chapter 1, the order of

magnitude of penetration depth is expressed in gallium nitride as $\lambda \sim 6 \cdot 10^3 \cdot \omega^{-1/2}$ um. At $\omega/2\pi$=100Hz, λ~600um exceeds the gallium nitride thickness of sample A and at 1000Hz the penetration depth is ~190um corresponding to a substrate thickness-to-penetration depth ratio $\lambda/d_S \sim 1$ for sample A. The validity of applicability of the 3ω slope method relying on Equation (4.4) has been discussed at length in Ref. 35. Implicitly it is assumed in Equation (4.4) that the sample thickness is infinite and the heater width is negligible compared to the penetration depth. If the 3ω method is operated in a frequency regime where the penetration depth is comparable to the substrate thickness or the heater width ($\lambda \sim d_S$ or λ~b), the substrate thermal conductivity deduced from a linear fit of the temperature oscillation versus lnω data will be in large error (20%)[35]. For qualitative consideration, an in-depth treatment is necessary. In the case of a finite sample with adiabatic boundary, Equation (4.4) must be replaced by Equation (4.5) below:

$$\Delta T = \frac{P_l}{\pi k_S} \int_0^\infty \frac{1}{\tanh\left(\sqrt{t^2 + iqb}\,\frac{d_s}{b}\right)\sqrt{t^2 + iqb}} \frac{\sin^2 t}{t^2} dt \quad + \Delta T_{OX} \qquad (4.5)$$

$$with\ q^{-1} = \lambda = \sqrt{\frac{\alpha_S}{2\omega}}$$

q^{-1} is the penetration depth λ and b the heater half-width. From Ref. 35, Equation (4.5) indicates that the relative error in substrate thermal conductivity extracted from the linear interpolation of the 3ω data using Equation (4.4) will be in less than 1% error if the substrate thickness is at least five times larger than the penetration depth ($d_S/\lambda > 5$), provided the heater width relative to the penetration depth is small enough (more precisely provided $b/\lambda < 0.2$). Taking the worse case scenario in the case of sample A, b/λ approximates 0.2 at 10,000Hz. Therefore the finite heater width will not lead to errors over 1%. On the other hand, recalling $\lambda/d_S < 5$ for ω<10,000Hz, it is deducted in the case of sample A that the finite substrate thickness represents a substantial source of errors in extracting the thermal conductivity from Equation (4.4).

In case of an adiabatic bottom boundary, it is expected at first sight that the temperature oscillation would shoot up as the penetration depth is reaching the substrate thickness. Following that line of thought, the thermal conductivity would be underestimated. Such an expectation is not true in practice. From Ref. 35, as the penetration depth approaches the substrate thickness, the slope deduced from the derivative of Equation (4.5) versus lnω swings around the slope value determined in the case of a semi-infinite substrate from Equation (4.4). Therefore the slope can be higher or lower than in the case of an ideal semi-infinite substrate depending on the frequency of operation. Relative errors as large as 20% can be made which are reflected on the thermal conductivity.

If Equation (4.4) was applied to sample A, it would bring predictions based on a simplified semi-infinite single layer model that would lead to erroneous thermal conductivity values as demonstrated in the previous paragraphs. To account for the measured 3ω temperature oscillation of sample A in Figure 4.10, the slope of the temperature oscillation ΔT was fit from the slope of the temperature oscillation calculated in a two layer system. The two layers consisted of a 200um film of unknown thermal conductivity on a ~400um substrate. As a result, the conditions of experiment were more faithfully reproduced. But this time ΔT was expressed as a function of film thermal conductivity from finite element analysis instead of analytical expressions. Finite element analysis has the advantage to give predictions when the film thermal conductivity varies as a function of thickness (finite element analysis experiment is explained in Chapter 3). Simply, the temperature oscillation was calculated as a function of film thermal conductivity while heater width, heat capacity, film thickness, substrate thickness were set nearly constant within measurement uncertainties. It was not possible to obtain a fit within less than 5% error if the substrate thermal conductivity was not allowed to vary. This is expected as the penetration depth extends to the transition region between the substrate and the film where the thermal conductivity is expected much lower than in the higher quality part of the film. In other words, a three or four-layer model could be adapted but its complexity prohibits thermal conductivity extraction. Thus the substrate becoming an effective or “pseudo” substrate is a combination of substrate and

transition layers. All in all, the ΔT was fit using a two-layer model with one unknown namely the film thermal conductivity and one parameter namely the pseudo-substrate thermal conductivity.

First the thermal conductivity was assumed constant. A close fit between numerical values and experimental data was possible when the underlying pseudo-substrate had a thermal conductivity of 90 $W \cdot K^{-1} \cdot m^{-1}$. The result of the finite element simulation is plotted in solid line in Figure 4.10. The thermal conductivity was found to be 200 $W \cdot K^{-1} \cdot m^{-1}$ for A2 and 170 $W \cdot K^{-1} \cdot m^{-1}$ for A1. For consistency with subsequent results, the film thermal conductivity was assumed to be logarithmically dependent on sample thickness with the following expression: $K=90+15.5 \ln(10^5 * (z_{GaN}+0.1.10^{-6})$ for A2 and $K=90+11* \ln(10^5 * (z_{GaN}+0.1.10^{-6})$ for A1 with the bottom first 10um set at 90 $W \cdot K^{-1} \cdot m^{-1}$. "$z_{GaN}$" is the height from a point in the GaN layer to the underlying substrate. It turns out that 90 $W \cdot K^{-1} \cdot m^{-1}$ is a value close to the 110 $W \cdot K^{-1} \cdot m^{-1}$ thermal conductivity of micrometer thin film GaN measured in Ref. 1. Corrections brought by assuming a logarithmic dependence of the thermal conductivity were small, within less than a few percents. This can be explained by the fact that most of the thermal conductivity gradient occurs within the first 10um and could account for the substrate thermal conductivity set at 90 $W \cdot K^{-1} \cdot m^{-1}$. All in all, the main source of correction comes from the assumption of finite film thickness and from the thermal conductivity gradient in the bottom part of the gallium nitride layer.

In summary, we could account for the data in Figure 4.10 in two cases: either the thermal conductivity is constant or the thermal conductivity is a logarithmic function of the thickness. Given thickness variations over the sample surface, the average thermal conductivity of sample A is deduced to be ~185 ±20 $W \cdot K^{-1} \cdot m^{-1}$ with a transition region probably around 90 $W \cdot K^{-1} \cdot m^{-1}$.

Sample B (300 K)

The temperature oscillation normalized to power, $\Delta T/P$ is plotted versus frequency ω for sample B in Figure 4.9.

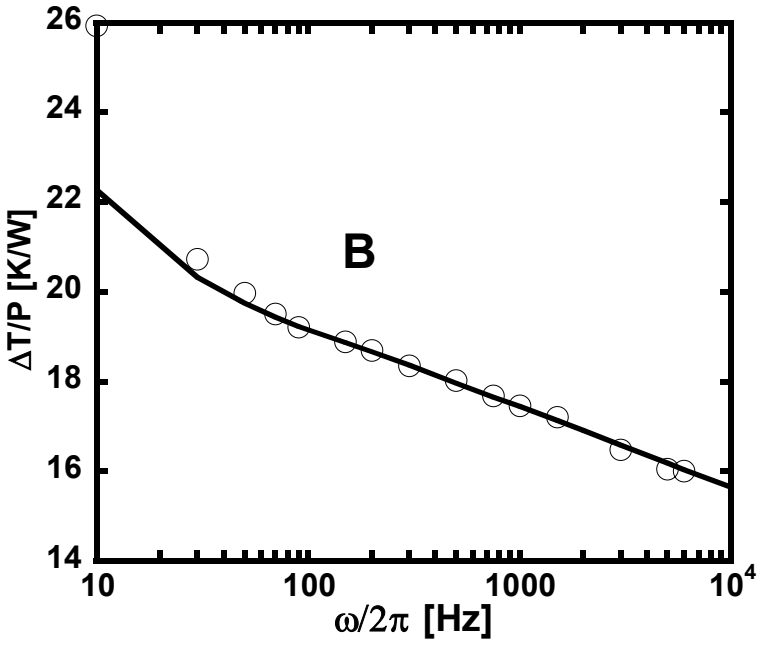

Figure 4.11. 3ω measurements on sample B.

Figure 4.11 depicts the 3ω temperature oscillation in open circles recorded on the 370um bulk sample B. Now sample B is thicker than sample A and at 100Hz $d_S/\lambda \sim 1.6$. Now the penetration depth is confined within the substrate though observable effect can still result form the finite thickness of the sample. Deducing the thermal conductivity from a linear best fit would provide an overestimation of ~5-10%. Once again, numerical calculation was employed to accurately determine the temperature oscillation versus frequency. The best fit is plotted in solid line in Figure 4.11. The best fit of the data over the 100-6000Hz range was obtained for a value of 200 $W \cdot K^{-1} \cdot m^{-1}$ for the film thermal conductivity and 90 $W \cdot K^{-1} \cdot m^{-1}$ for the substrate. This time the backside of sample B has been polished and transition layers removed. The underlying chuck mount is made of a 2mm nickel plate. The thermal conductivity of the nickel plate is 90 $W \cdot K^{-1} \cdot m^{-1}$. In addition, the contact between sample B and the underlying chuck is not intimate unlike the epi layer of sample A on sapphire. Lastly the data in Figure 4.11 is not well fitted at very low frequency. In that regime, the temperature oscillation is sensitive to the bottom contact.

The room temperature thermal conductivity values of sample A, B, C, and D listed in Table 4.1 are summarized in Table 4.4.

Table 4.4. Thermal conductivity at 300K for samples listed in Table 4.1.

Sample	A	B	C	D
K (±10%)	185	200	215	230

Temperature dependence

Finally the thermal conductivity was measured at temperature higher than 370K employing the simple slope method based on Equation (4.4). As the temperature increases, the thermal conductivity drops and the thermal penetration depth decreases, the slope method becomes more applicable. The result is plotted in the figure below.

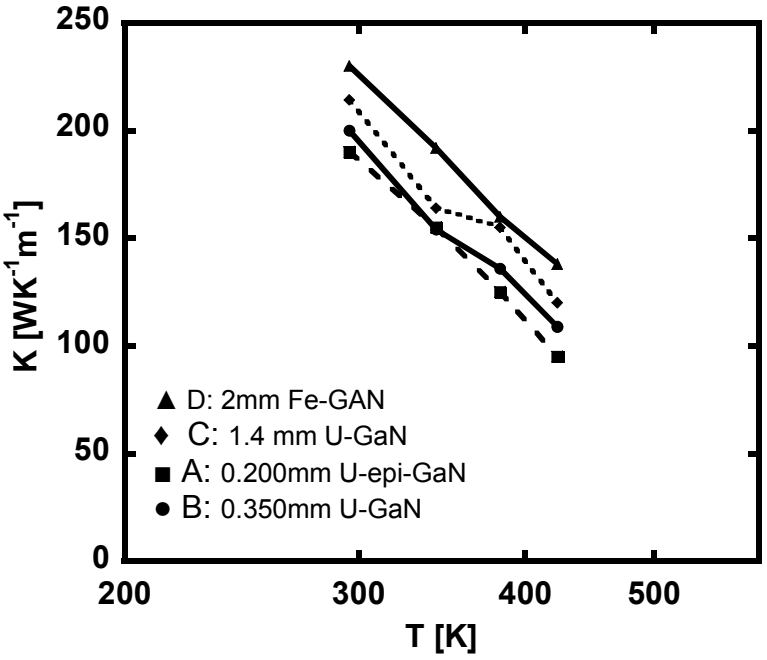

Figure 4.12. Thermal conductivity of gallium nitride versus temperature above 300K.

Even if the thermal conductivity values extracted for the 0.2mm and 0.35mm thick samples at 300K are ignored, Figure 4.12 strongly indicates that the thermal conductivity becomes higher as the sample thickness increases. The two-layer

model for sample A and B was adopted in order to extract room temperature thermal conductivity values as accurate as possible. Thermal conductivity measurements on HVPE gallium nitride samples reveal that:

(i) The thermal conductivity increases with film thickness. Large variations in film thickness from 200um to 2000um (~1000%) yield relatively small variation in thermal conductivity (~25%).

(ii) The thermal conductivity can be extracted for each individual sample by assuming a constant thermal conductivity with thickness (or nearly constant). A logarithm dependence of the thermal conductivity with film thickness is in good agreement with measurements on both thick and thin samples. (On samples C and D, the first top 300um are probed. With $K=90+11*\ln(10^{5}*(z_{GaN}+0.1.10^{-6})$ compatible with the study conducted on sample A, the thermal conductivity becomes nearly constant in the top 500um of 1.4mm sample C and 2mm sample D).

Combining (i) and (i), the thermal conductivity cannot be neither strictly constant with film thickness nor nearly constant with film thickness. However with these assumptions and confirmation with finite element modeling, accurate values can be extracted.

4.4 Strong Evidence of the Dependence of Gallium Nitride Thermal Conductivity on Dislocation Density.

4.4.1 Dislocations in Gallium Nitride

A physical parameter that varies drastically with thickness in gallium nitride grown on non-native substrates is the dislocation density. It has been proved experimentally and theoretically[36,37] that the dislocation density decreases with gallium nitride thickness at least for dislocation densities greater than 10^6 cm^{-2}. Figure 4.13 plots the dislocation density versus thickness. The solid line describes the theoretical model from Ref. 36. Black squares represent experimental values from Ref. 36 while diamonds represents experimental values measured by KYMA technology and NCSU (see Appendix D).

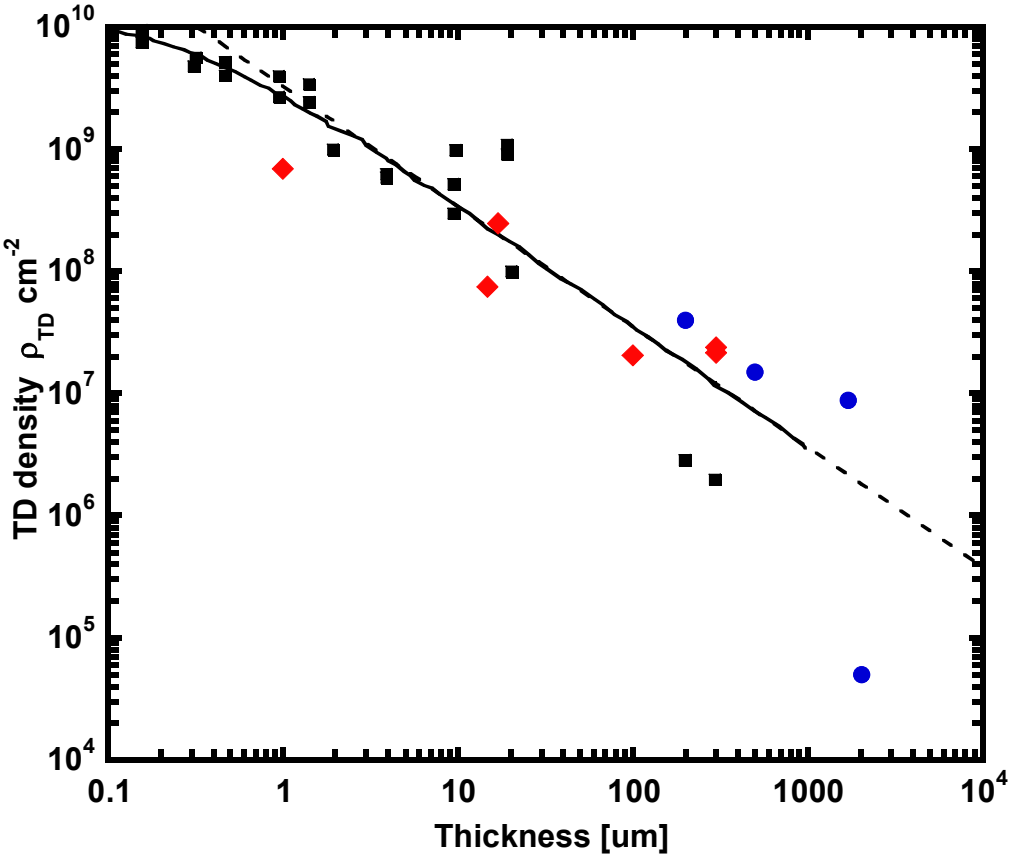

Figure 4.13. Dislocation density versus HVPE gallium nitride film thickness. (—) theoretical model (Ref. 36). (■) experimental values (Ref. 36). (♦) measured values from etch count pits by KYMA Tech. (●) measured values from CL by NCSU. (----) linear interpolation of the theoretical model for thicknesses between 1um and 1000um.

The dashed line in Figure 4.13 illustrates that the dislocation density ρ_D is proportional to the logarithmic of the gallium nitride thickness between 1um and 1000um. An analytical expression for the linear interpolations in dashed line is given by Equation (4.6) below:

$$\log\left(\rho_D\left[cm^{-2}\right]\right) = \log\left(3.27\times10^{-9}\right) - 0.984\cdot\log\left(t\left[\mu m\right]\right) \qquad (4.6)$$

4.4.2 Thermal Conductivity and Dislocation Density

It is possible that the reduction of dislocation density with film thickness expressed by Equation (4.6) may offer a viable explanation for the observed thermal conductivity increase with film thickness in Section 4.3.2. To study the relation between the thermal conductivity and dislocation density, the thermal conductivity values determined at 300K for sample A, B, C, and D in Section 4.3.2 are plotted in diamond in Figure 4.14 versus the corresponding measured dislocation densities in Section 4.2. It is found that the thermal conductivity of gallium nitride is proportional to the logarithmic of the dislocation density until a density of $5\cdot10^6$ cm^{-2} below which the thermal conductivity saturates with dislocation density. The extrapolated logarithmic dependence of thermal conductivity with dislocation density is plotted in dashed line in Figure 4.14. To confirm the validity of these observations, thermal conductivity data taken at 300K from other references was included in Figure 4.14. The agreement is excellent within relative uncertainties between 5 and 10% typical in thermal conductivity measurements[1,9,10] and 20-50% in dislocation densities estimation[5,37]. Again, in this work the thermal conductivity was measured prior to material characterization.

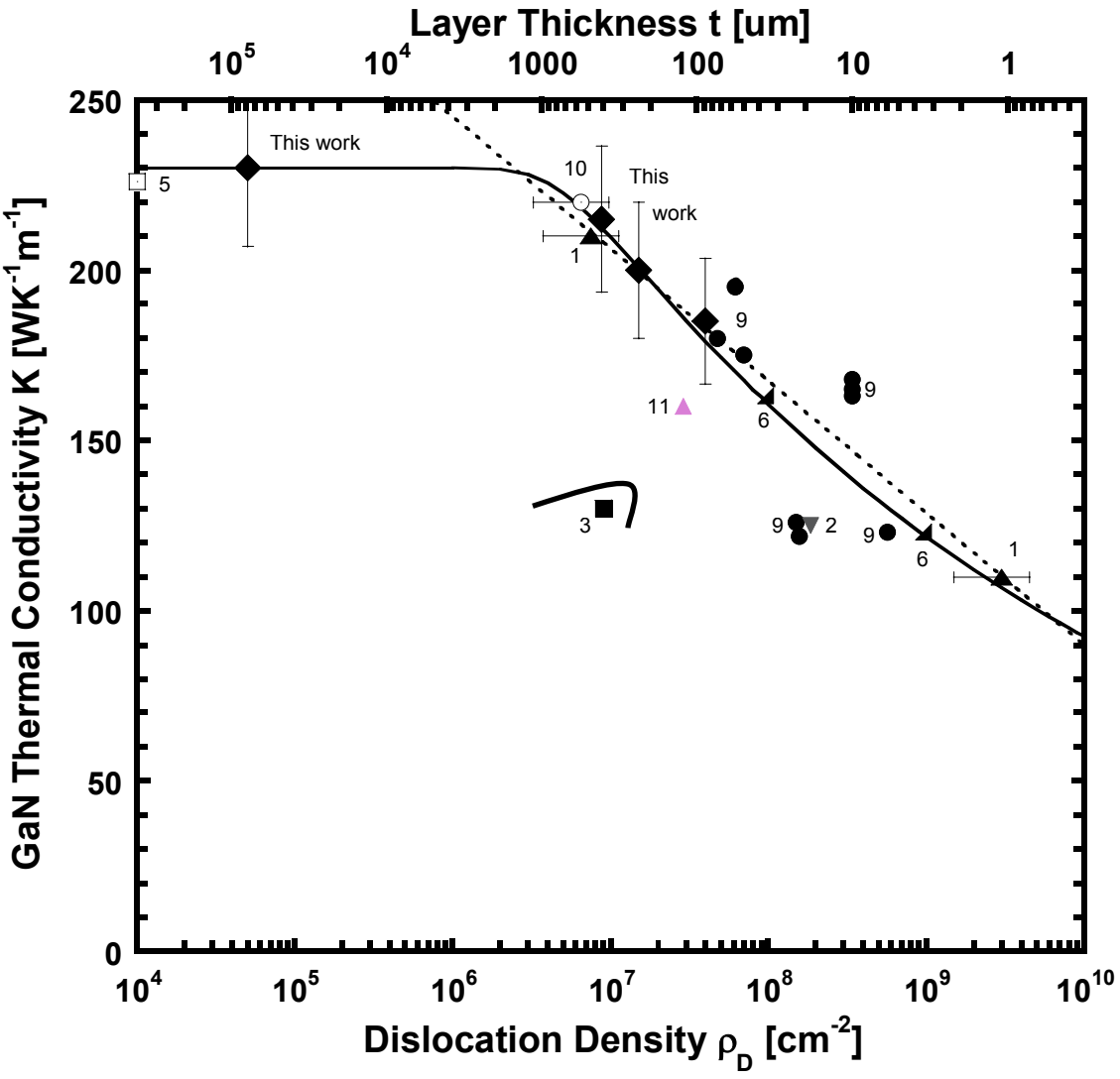

Figure 4.14. Thermal conductivity versus dislocation density values. Diamonds ♦ represent thermal conductivity values measured at 300K by the present author. Associated error bars are typical of measurement uncertainties (10%). All other data points are taken from the literature with each point carefully labeled. References are given in Section 4.7. The solid line was fitted to the data

Taking into account measurement uncertainties, the following empirical relation is determined:

$$K = 230 \bullet \tanh^{0.12}\left(\frac{5 \cdot 10^6}{\rho_D}\right) \qquad (4.7)$$

Equation (4.7) is plotted in Figure 4.14 in solid line. It can be seen that at high dislocation density, the trend is well approximated by a log dependence of the thermal conductivity on dislocation density. At $\rho_D<5\cdot10^{-6}$ cm^{-2}, Equation (4.7) describes a saturation of the thermal conductivity with dislocation density.

Figure 4.13 was constructed by including the highest thermal conductivity values measured at room temperature from other authors who preferentially reported on undoped gallium nitride with a dislocation density accurately known. In strict terms, no studies were satisfactorily found to satisfy all conditions (except perhaps for the present study). Thus it was necessary to compromise to be able to compare this work with other reported results. There are two classes of references on thermal conductivity studies: those that included information on dislocation density and those who only gave information on gallium nitride thicknesses. In the latter case, the thickness had to be given starting from the initial nucleation layer. It was then possible to plot the thermal conductivity versus dislocation density under the assumption Equation (4.6) is valid. References from which the dislocation density can be inferred are: 5, 6, 9 and 10. Thermal conductivity from gallium nitride grown by MOCVD can be included provided the dislocation density can be known. To account for inaccuracy in information on dislocation density in Ref. 1 and Ref. 10, 50% error bars were associated with dislocation densities. The dislocation density on Laterally Epitaxial Overgrown GaN measured in Ref. 1 was taken between $4\cdot10^{-6}$ cm^{-2} and 10^{-7} cm^{-2} from the review in Ref. 37. The highest thermal conductivity value in Ref. 5 corresponds to a dislocation density at some value between 10 and 10^4 cm^{-2}. For sake of clarity in Figure 4.13, the thermal conductivity was plotted at 10^4 cm^{-2}. References that yield information on the thickness are: 2, 3, 9, and 11. Only the thermal conductivities corresponding to sample A1, A2, A3, A4, B1, B2, B3, C1, C2 in Ref. 9 were plotted versus thickness in Figure 4.13 owing to low carrier concentration. Note that Ref. 11 investigates the thermal conductivity of a silicon doped HVPE gallium nitride layer. The first reported thermal conductivity in 1977 was excluded in the data fit analysis of Figure 4.13 because the corresponding data point is far outside the range of interpolation. Actually this suggests that the corresponding gallium nitride layer must have had a large concentration of

dislocations. Indeed the growth conditions and sample preparation in the 1977 article prompt to think the dislocation density would be higher than today's routinely grown HVPE GaN materials. Finally Slack *et al.*[7] report a value of 227 $W \cdot K^{-1} \cdot m^{-1}$ that could not be included in Figure 4.13 simply because of a lack of information on the sample characteristics although the gallium nitride layer is at least 200um after polishing.

4.4.3 Comparison with Previous Theoretical Investigations

The theoretical determination of the thermal conductivity dependence on dislocation density has been performed by Zou *et al.*[15] based on a time-approximation scattering approach. The authors concluded that the thermal conductivity of gallium nitride could be dependent on dislocation density provided the dislocation density was higher than 10^{-10} cm^{-2}. Results on the effect of dislocation density on thermal conductivity calculated by Zou *et al.*[15] are depicted in Figure 4.15.

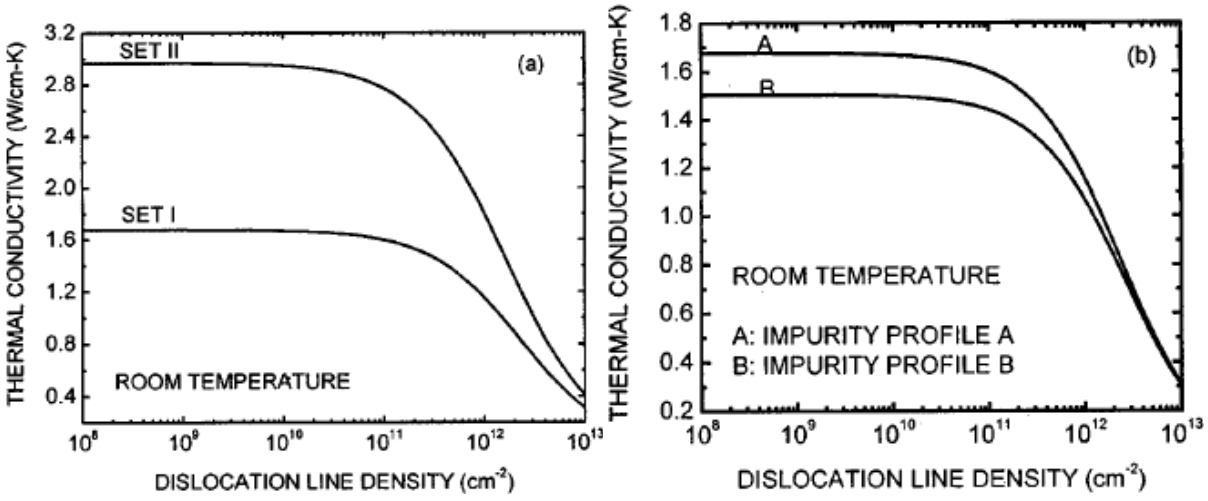

Figure 4.15. Gallium nitride thermal conductivity versus dislocation density reproduced from Ref. 15. The curves are derived from the time relaxation approximation. a) Calculations with two sets of GaN material parameters I and II but with probably impurity profile A. b) Calculations with set I of GaN material parameter but two impurity profiles A and B. Impurity profile A in Ref. 15 is nearly identical to the impurity concentration in undoped material listed in Table 4.2 in this chapter.

It is well established that 10^{-10} cm^{-2} represents a high bound for the dislocation density of gallium nitride as evidenced from Figure 4.13 and supported by Ref. 36. In these conditions, Figure 4.15 implicitly predicts that the gallium nitride

thermal conductivity is independent with dislocation density. Therefore one may conclude from Ref. 15 that the dislocation density has no effects on the thermal conductivity. Indeed most of the attention in Ref. 15 was directed toward the influence of point defects and impurity on thermal conductivity reduction.

Despite an apparent contradiction, it will be shown that the work after Zou *et al.*[15] is in qualitative agreement with the results obtained earlier in Section 4.4.2. First it is worth noting that the average thermal conductivity of gallium nitride taken between set I and Set II at low dislocation density in Figure 4.15a yields 235 $W \cdot K^{-1} \cdot m^{-1}$ while the thermal conductivity was found to be 230 $W \cdot K^{-1} \cdot m^{-1}$ at low dislocation density in this study. But most importantly the trends in Figure 4.15 and Figure 4.13 are very similar in nature if one disregards the scale of the horizontal axis.

To understand the reasons underlying the startling analogy between Figure 4.15 and Figure 4.13, it is necessary to look back in the theory of thermal conductivity derived from a time scattering approach. The authors in Ref. 15 have not derived the expression for the thermal conductivity themselves. Rather they have intelligently plugged in the gallium nitride material parameters in pre-established theoretical works developed in the 50's and 60's by multiple authors including Klemens[38]. However it is well-established that the time scattering approach leads to an underestimation in scattering rates of phonons on dislocations by several orders of magnitude. That subject was the focus of numerous works that are probably best referenced and summarized in 1976 Berman's book[14]. In page 71 of the same book, it can be read that: "A number of experimental studies of the effect of dislocations on the conductivity of non-metallic crystals (see §8.3.4) suggest that the actual scattering is often 10^2 to 10^3 times larger than that calculated for fixed dislocations.". In light of these explanations, the dislocation density value at which the thermal conductivity saturates in Figure 4.15 can be lowered by several orders of magnitude to correct for the flaw of the theory. More precisely, because the phonon relaxation rate is inversely proportional to the dislocation density (Equation (4.8)), an increase of three orders of magnitude on the scattering rate can be translated by an equivalent drop of 3 orders of magnitudes in dislocation density.

$$\frac{1}{\tau_D} \propto \rho_D \tag{4.8}$$

Therefore the saturation of thermal conductivity occurring at 10^{11} cm^{-2} in Ref. 15 will be downshifted by 3 orders of magnitude in dislocation density to reach 10^7 to 10^8 cm^{-2}. In these conditions, qualitative agreement between Figure 4.13 and Figure 4.15 is restored. In reality the thermal conductivity in Figure 4.13 saturates at a dislocation density four to five orders of magnitude lower than in Figure 4.15. Such a discrepancy in dislocation-phonon scattering magnitude could be understood in light of interactions between dislocations. On page 101 of Ref. 14, it can be read that: "It was suggested that the enhanced scattering arose from the association of dislocations". In gallium nitride, the reaction and association of dislocation is an important process during material synthesis that occurs over relatively large film thicknesses compared to cubic systems such as GaAs[36]. This study suggests that gallium nitride represents an adequate candidate to study the effect of dislocation density on thermal conductivity. Multiple authors have devised dedicated experiments to generate dislocations in a control manner in cubic material such as LiF, NaCl, KCl, GaAs in order to study the effect of dislocations in semiconductors[14].

The thermal conductivity will be limited by phonon-dislocation scattering as opposed to intrinsic phonon-phonon scattering for large dislocation density and/or at low temperature[14]. From Figure 4.13 and Equation (4.7), phonon-dislocation scattering in gallium nitride will become non-negligible compared to intrinsic scattering when $\rho_D > 10^7 cm^{-2}$ at room temperature. For increasingly higher dislocation density, Equation (4.8) indicates that the thermal conductivity will become proportional to the dislocation density. The empirical dependence of the thermal conductivity on ρ_D derived in this chapter expressed in Equation (4.7) predicts that the thermal conductivity would be inversely proportional to $\rho_D^{0.12}$ as ρ_D goes to infinity. Agreement with theory can be easily restored by proposing the following semi-empirical relation:

$$K = 230 \bullet \tanh^{m}\left(\frac{5\cdot 10^{6}}{\rho_D}\right)$$
$$with\ m = 0.12 + 0.88\tanh\left(\frac{\rho_D}{10^{12}}\right) \qquad (4.9)$$

Equation (4.9) becomes identical to Equation (4.7) for $\rho_D < 5\cdot 10^{-10}$ cm^{-2}. In the expression of m, the value of 10^{-12} cm^{-2} is arbitrary. Finally, thermal conductivity variations are more pronounced in Figure 4.15 than in Figure 4.13. Between 10^{12} and 10^{13} cm^{-2} dislocation density in Figure 4.15, the thermal conductivity drops by ~77% for material parameter set I and ~66% for set II. The exponent m in Equation (4.9) is smaller than expected for $\rho_D < 5\cdot 10^{10}$ cm^{-2} compared with the theory of Figure 4.15.

4.4.4 Effects of Impurities

Equation (4.7) was fitted to experimental thermal conductivity values measured on gallium nitride having an impurity concentration from 10^{16} to 10^{18} cm^{-3}. Therefore the dependence of thermal conductivity on dislocation density is expected to be higher. Furthermore it ought to be expected that the thermal conductivity will further increase as point defect reduces, if material synthesis permits. From previous works on other semiconductors, there are some indications that the thermal conductivity at room temperature may not be severely affected by a further reduction in point defect such as Iron[39]. Slack *et al.*[7] have addressed some of the effects of oxygen on the gallium nitride thermal conductivity by drawing parallel with AlN but in the meantime the same authors have determined a theoretical value of 227 W·K^{-1}·m^{-1} for gallium nitride at room temperature. The same authors pinpoint the detrimental effect of oxygen and gallium vacancies responsible for thermal conductivity reduction and yellow luminescence apparition at room temperature. We notice that the yellow luminescence of sample D in the catholuminescence spectrum of Figure 4.3 is not observed and that the measured thermal conductivity of sample D corresponds to the theoretical estimation given by the same authors. Overall the

precise magnitude of thermal conductivity reduction with impurity content is not clearly established.

4.4.5 Comparisons Between Gallium Nitride and Diamond

Finally previous studies have already related the variations of thermal conductivity to changing film thicknesses or with a cross-plane gradient in film properties. A parallel can be drawn between thermal conductivity studies on gallium nitride and those on diamond, both materials representing high thermal conductivity non-metallic elements[18]. The former is grown by HVPE on non-native substrate typically sapphire while the latter is synthesized by chemical vapor deposition (CVD) usually on silicon. Diamond and gallium nitride free-standing substrates originate from an early hundreds micron thick epi-layer. The thermal conductivity properties of both diamond and gallium nitride are under investigation[22,40]. Ref. 41 provides a detail discussion on the limitations of the diamond thermal conductivity, which was shown to vary monotonically with film thickness. However, unlike the gallium nitride thermal conductivity, the thermal conductivity dependence on diamond is quadratic with thickness and is caused by the presence of cone-shaped grains, which start out very small and typically increase with increasing film thickness as diamond grows in a columnar structure. The quadratic term is small but non-negligible so that the dependence of diamond thermal conductivity on thickness can be easily approximated by a linear trend for hundreds of micron thick sample. It is worth noting that higher thermal conductivities are observed on unpolished as–grown samples.

4.5 Gallium Nitride Thermal Conductivity Dependence on Temperature

At increasingly higher temperature, the thermal conductivity becomes inversely proportional to the temperature due to the dominance of phonon-phonon umklapp scattering[13,14,16,17]. However a few corrections can be made to the thermal conductivity temperature dependence due to crystal expansion and acoustic-phonon scattering[7,16]. Moreover, the measured thermal conductivity versus temperature below the Debye temperature can provide information about the dominant scattering

mechanism. From Figure 4.12, we find for sample D the following slope ε at constant pressure:

$$\varepsilon = \left(\frac{d \ln \kappa}{d \ln T} \right)_P = 1.43 \qquad (4.10)$$

This slope is characteristics of pure adamantine crystals in the temperature range below the Debye temperature and typically 1.22<ε<1.44[7,16]. Generally ε>1 because the crystal expands on heating[16]. In addition, higher value of ε means higher acoustic-optic phonon interaction[16]. Therefore the parameter ε can indicate the extent to which the acoustic-phonon transport is affected by acoustic-acoustic phonon or acoustic-optic phonon interactions[7,16]. Finally higher ε can also indicate a dominance of phonon-impurity scattering over phonon-phonon scattering[7,16].

Slack *et al.*[7] found an experimental value ε=1.22 from thermal conductivity measurements between 80K and 323K. The authors in Ref. 7 deduced that the thermal conductivity was very likely determined primarily by intrinsic phonon-phonon scattering and not by phonon-impurity scattering although their values was determined from thermal conductivity data measured below room temperature. The reader will notice that the slope value of Slack *et al.*[7] lies in the low range of typical ε values while the value measured here is in the high range. Therefore, one may conclude that phonon-impurity scattering is more important in our case than compared with Slack *et al.*[7] That would indicate that the value of ε for gallium nitride would be smaller than 1.43. It was a 200um thick double-face-polished HVPE gallium nitride free-standing substrate from Samsung that the authors in Ref. 7 characterized.

In general, thermal conductivity temperature dependence measurements are useful to the prediction of device operation. Device heating is responsible for temperature rise in electronic devices. Temperature of operation can easily exceed 150°C. Our data shows that the thermal conductivity of gallium nitride at 150°C is ~50% lower than at room temperature. More precisely, the thermal conductivity of gallium nitride can be expressed as:

$$k(T) = k_0(\rho_D)\left(\frac{T}{300}\right)^{-1.43} \quad (4.11)$$

Where ρ_D is the dislocation density and $k_0(\rho_D)$= 230 $W \cdot K^{-1} \cdot m^{-1}$ for $\rho_D < 10^6$ cm^{-2} at 300K. However it is noteworthy that ε is expected to increase as the dislocation density increases. The data in Figure 4.12 shows that this increase is very probably minor as the variations in extracted values of ε lie within error of uncertainties. Therefore Equation (4.11) provides a fair estimate of the thermal conductivity value beyond room temperature for various dislocation densities.

Thanks to temperature dependent thermal conductivity measurements like ours, device simulators can include the temperature dependence of the gallium nitride thermal conductivity to predict operation of gallium nitride based devices. Reports focusing on the gallium nitride thermal conductivity measured above room temperature like our study are scarce. Ref. 10 investigates the thermal conductivity of gallium nitride above room temperature in agreement with our results.

4.6 Conclusion

By employing the 3ω method, the thermal conductivity of four gallium nitride samples A, B, C and D synthesized by the hydride vapor phase technique was measured between 300K and 350K. Following their alphabetic order, samples A, B, C and D were grown increasingly thicker from ~200um to ~2mm. Samples A, B, C were nominally undoped while sample D was iron doped with a targeted iron concentration of 10^{18} cm^{-3}. Recall that gallium nitride is iron doped at moderate concentration to render the material semi-insulating. Iron was shown to form a deep acceptor level (~0.34eV[25]) below the conduction band. The highest thermal conductivity was found 230 ±15 $W \cdot K^{-1} \cdot m^{-1}$ on iron doped sample D at 300K, which is about 2% higher than the highest reported values discussed in Section 4.1.2. It also was the most accurate measured value in this work probably due to the large thickness of the sample (2 mm) and the temperature of measurements (room temperature).

Out of a total of 16 experimental points, it was clearly found that the thermal conductivity was an increasing monotonic function of gallium nitride thickness. Thermal conductivity values were measured following a routine procedure in the 3ω slope method except for two experimental data points corresponding to namely sample A and B at room temperature. In that particular case, the thermal conductivity was deduced from a two-layer model to account for finite thickness effects. An accurate thermal conductivity value at room temperature could thus be extracted. It was determined that a thermal conductivity dependent on the logarithmic of the thickness was fully compatible with experimental results and were consistent with extracted thermal conductivity assumed constant with layer thickness. This is possible when most of the thermal conductivity gradient occurs in the first 10um of the sample layer. For millimeter thick gallium nitride layer, the 3ω technique is sensitive to the top 500um which is nearly constant assuming a logarithmic dependence of thermal conductivity with thickness. Finite element analysis was employed to analysis the effect of thermal conductivity gradient on the 3ω technique.

In this study, samples were characterized subsequent to thermal conductivity measurements and analysis. Impurity profiles deduced from Secondary Ion Mass Spectroscopy (SIMS) demonstrated the presence of O, H, C, Si in undoped sample with concentration typical of undoped GaN material. From SIMS, the Fe concentration in sample D was measured steady at 10^{18} cm^{-3} over a 2um depth confirming the targeted iron concentration during growth. Electron Paramagnetic Resonance (EPR) conducted by M.E. Zvanut from the University of Alabama at Birmingham confirms an electrical activation of 10^{18} cm^{-3} for Fe^{3+} suggestive of the semi-insulating nature of sample D. Hall effect measurements conducted by William C. Mitchel from AFRL/MLPS labs confirmed the semi-insulating nature of sample D as the resistivity was 10^{8} Ω·cm at 300K. In contrast, the resistivity of undoped samples was measured between 1 to 20 Ω·cm from four-point probe resistance measurements and were consistent with other measurements. The dislocation density was clearly found to decrease with thickness according to catholuminescence imaging. Amazingly, the dislocation density was found to

average $5 \cdot 10^4$ cm^{-2} on sample D with even lower values on some particular areas. Such a dislocation density is ranked by far amongst the lowest achievable densities in HVPE or MOCVD grown gallium nitride and represents perhaps one of the lowest ever reported value on semi-insulating gallium nitride as of today[42]. Further details are given in Appendix D. Room temperature catholuminescence spectra reveal a relative low band edge emission for sample D. No defect peaks can be seen in the spectrum at 550nm. Transmission measurements on sample C and D provide further information on sample qualities.

By plotting the thermal conductivity versus dislocation density, it was found that the thermal conductivity of gallium nitride is approximately linear with the logarithmic of the dislocation density for $\rho_D > 10^7$ cm^{-2} and saturate below $5 \cdot 10^6$ cm^{-2}. Data taken from other references confirmed the trend. By comparing with earlier theoretical work keeping in mind flaw in the theory, it was shown that qualitative agreement can be established between experiment and theory. The thermal conductivity of gallium nitride can be examined according 3 regimes. First, at low dislocation density below $5 \cdot 10^6$ cm^{-2}, the thermal conductivity is constant with dislocation density. At intermediate dislocation density range comprised between $5 \cdot 10^6$ and 10^{10} cm^{-2}, the thermal conductivity varies as the inverse of the logarithmic of the dislocation density. At unrealistically high dislocation density, say beyond 10^{12} cm^{-2}, the thermal conductivity varies as the inverse of the dislocation density. Other thermal conductivity studies on high thermal conductivity semiconductors have established a dependence of thermal conductivity on sample unhomogeneity. For instance, closely related to gallium nitride is CVD diamond on silicon that presents a thermal conductivity quadratic with thickness. Nevertheless, it must be acknowledged that this work has the propensity to underestimate the dependence of the thermal conductivity on dislocation density due to added resistive processes from impurities. It remains that the thermal conductivity of semi-insulating GaN may well stabilized around 230 $W \cdot K^{-1} \cdot m^{-1}$ which can be directly compared to the semi-insulating thermal conductivity of silicon carbide repeatedly measured at 350 $W \cdot K^{-1} \cdot m^{-1}$ by the present author at room temperature (see Chapter 1 and Chapter 2).

The temperature dependence of gallium nitride was found to be ε=1.43 which is slightly higher than the value determined by Slack at 1.22 deduced below room temperature. The temperature dependence is similar to that of silicon carbide (ε ~1.4-1.5). The knowledge of thermal conductivity temperature dependence benefit studies on channel temperature rise in gallium nitride based devices

The results found in this chapter lead to fundamental consequences. This chapter provides further material to discuss on the accuracy of theory relying on time-approximation in the general sense. Moreover the dependence of thermal conductivity with dislocation density is more common to most material than the dependence on cone-shapes grains as in diamond even though they can be related to one another. If the thermal conductivity has not been clearly identified as dependent on the logarithmic of the dislocation density until now, it is maybe partly due to a lack of theoretical understanding on the impact of dislocation density on thermal conductivity.

Overall the results presented in this chapter lead to a better understanding in the nature of key parameters limiting the gallium nitride thermal conductivity during material synthesis.

4.7 References

1 D. I. Florescu, V. M. Asnin, F. H. Pollak, A. M. Jones, J. C. Ramer, M. J. Schurman, and I. Ferguson, "Thermal conductivity of fully and partially coalesced lateral epitaxial overgrown GaN/sapphire (0001) by scanning thermal microscopy," *Applied Physics Letters*, vol. 77, pp. 1464, 2000.

2 W. Liu and A. A. Balandin, "Thermal conduction in $Al_xGa_{1-x}N$ alloys and thin films," *Journal of Applied Physics*, vol. 97, pp. 1-6, 2005.

3 E. K. Sichel and J. I. Pankove, "Thermal-Conductivity of Gan, 25-360k," *Journal of Physics and Chemistry of Solids*, vol. 38, pp. 330-330, 1977.

4 V. M. Asnin, F. H. Pollak, J. Ramer, M. Schurman, and I. Ferguson, "High spatial resolution thermal conductivity of lateral epitaxial overgrown GaN/sapphire (0001) using a scanning thermal microscope," *Applied Physics Letters*, vol. 75, pp. 1240-1242, 1999.

5 A. Jezowski, B. A. Danilchenko, M. Bockowski, I. Grzegory, S. Krukowski, T. Suski, and T. Paszkiewicz, "Thermal conductivity of GaN crystals in 4.2-300 K range," *Solid State Communications*, vol. 128, pp. 69-73, 2003.

6 C. Luo, D. R. Clarke, and J. R. Dryden, "The temperature dependence of the thermal conductivity of single crystal GaN films," *Journal of Electronic Materials*, vol. 30, pp. 138-146, 2001.

7 G. A. Slack, L. J. Schowalter, D. Morelli, and J. A. Freitas Jr., "Some effects of oxygen impurities on AlN and GaN," *BNS 2002, May 18-23 2002*, vol. 246, pp. 287-298, 2002.

8 C. Y. Luo, H. Marchand, D. R. Clarke, and S. P. DenBaars, "Thermal conductivity of lateral epitaxial overgrown GaN films," *Applied Physics Letters*, vol. 75, pp. 4151-4153, 1999.

9 D. I. Florescu, V. M. Asnin, F. H. Pollak, R. J. Molnar, and C. E. C. Wood, "High spatial resolution thermal conductivity and Raman spectroscopy investigation of hydride vapor phase epitaxy grown n-GaN/sapphire(0001): Doping dependence," *Journal of Applied Physics*, vol. 88, pp. 3295-3300, 2000.

10 R. P. Vaudo, G. R. Brandes, J. S. Flynn, X. Xu, M. F. Chriss, C. S. Christos, D. M. Keogh, and F. D. Tamweber, "Synthesis and properties of HVPE nitride substrates," *Proceedings of International Workshop on Nitride Semiconductors, 24-27 Sept. 2000*, pp. 15-18, 2000.

11 M. Kamano, M. Haraguchi, T. Niwaki, M. Fukui, M. Kuwahara, T. Okamoto, and T. Mukai, "Temperature dependence of the thermal conductivity and phonon scattering time of a bulk GaN crystal," *Japanese Journal of Applied Physics Part 1-Regular Papers Short Notes & Review Papers*, vol. 41, pp. 5034-5037, 2002.

12 P. R. W. Touloukian Y.S., Ho C. Y., Klemens P. G., "Thermophysical Properties of Matter," *The TPRC Data Series*, vol. 1,2, 1970.

13 C. M. Bhandari and D. M. Rowe, *Thermal conduction in semiconductors*. New York: Wiley, 1988.

14 R. Berman, *Thermal conduction in solids*. Oxford [Eng.]: Clarendon Press, 1976.

15 J. Zou, D. Kotchetkov, A. A. Balandin, D. I. Florescu, and F. H. Pollak, "Thermal conductivity of GaN films: Effects of impurities and dislocations," *Journal of Applied Physics*, vol. 92, pp. 2534-2539, 2002.

16 G. A. Slack, "Thermal conductivity of nonmetallic crystals.," vol. 34, pp. 1-71, 1979.

17 G. A. Slack, "Nonmetallic Crystals with High Thermal-Conductivity," *Journal of Physics and Chemistry of Solids*, vol. 34, pp. 321-335, 1973.

18 A. Witek, "Some aspects of thermal conductivity of isotopically pure diamond - a comparison with nitrides," *Diamond and Related Materials*, vol. 7, pp. 962-964, 1998.

19 D. Kotchetkov, J. Zou, A. A. Balandin, D. I. Florescu, and F. H. Pollak, "Effect of dislocations on thermal conductivity of GaN layers," *Applied Physics Letters*, vol. 79, pp. 4316-4318, 2001.

20 R. Berman, "Comment on Witek's paper on thermal conductivity of some nitrides," *Diamond and Related Materials*, vol. 8, pp. 2016-2017, 1999.

21 D. I. Florescu, F. H. Pollak, T. Paskova, E. Valcheva, and B. Monemar, "Dislocation/grain boundary effects on the thermal conductivity of hydride vapor phase epitaxy grown GaN/sapphire (0001)," *27th International Symposium on Compound Semiconductors, Oct 2-5 2000*, pp. 467-472, 2000.

22 J. E. Graebner, H. Altmann, N. M. Balzaretti, R. Campbell, H. B. Chae, A. Degiovanni, R. Enck, A. Feldman, D. Fournier, J. Fricke, J. S. Goela, K. J. Gray, Y. Q. Gu, I. Hatta, T. M. Hartnett, R. E. Imhof, R. Kato, P. Koidl, P. K. Kuo, T. K. Lee, D. Maillet, B. Remy, J. P. Roger, D. J. Seong, R. P. Tye, H. Verhoeven, E. Worner, J. E. Yehoda, R. Zachai, and B. Zhang, "Report on a second round robin measurement of the thermal conductivity of CVD diamond," *Diamond and Related Materials*, vol. 7, pp. 1589-1604, 1998.

23 W. J. Moore, J. A. Freitas, G. C. B. Braga, R. J. Molnar, S. K. Lee, K. Y. Lee, and I. J. Song, "Identification of Si and O donors in hydride-vapor-phase epitaxial GaN," *Applied Physics Letters*, vol. 79, pp. 2570-2572, 2001.

24 J. A. Freitas, W. J. Moore, B. V. Shanabrook, G. C. B. Braga, S. K. Lee, S. S. Park, J. Y. Han, and D. D. Koleske, "Donors in hydride-vapor-phase epitaxial GaN," *Journal of Crystal Growth*, vol. 246, pp. 307-314, 2002.

25 R. P. Vaudo, X. P. Xu, A. Salant, J. Malcarne, and G. R. Brandes, "Characteristics of semi-insulating, Fe-doped GaN substrates," *Physica Status Solidi a-Applied Research*, vol. 200, pp. 18-21, 2003.

26 J. I. Pankove, *Optical Processes in semiconductors*. New-York: Dover Publications, Inc, 1971.

27 U. Wahl, A. Vantomme, G. Langouche, J. G. Correia, L. Peralta, and I. Collaboration, "Direct evidence for implanted Fe on substitutional Ga sites in GaN," *Applied Physics Letters*, vol. 78, pp. 3217-3219, 2001.

28 S. Y. Zhang, Q. B. Zhou, and Y. K. Lu, "Reconstruction of thermal properties of inhomogeneous materials from one dimension to two dimensions," *Review of Scientific Instruments*, vol. 74, pp. 363-365, 2003.

29 Q. B. Zhou, Y. K. Lu, S. Y. Zhang, J. C. Cheng, and X. J. Shui, "Two-dimensional reconstruction theory of thermal conductivity profiles based on the thermal wave technique," *Journal of Applied Physics*, vol. 92, pp. 4088-4094, 2002.

30 M. H. Xu, J. C. Cheng, and S. Y. Zhang, "A new method of reconstruction of thermal conductivity-depth profiles from photoacoustic or photothermal measurements," *Journal of Physics D-Applied Physics*, vol. 31, pp. 3154-3159, 1998.

31 M. H. Xu, J. C. Cheng, and S. Y. Zhang, "Reconstruction theory of thermal conductivity depth profiles by the modulated photoreflectance technique," *Journal of Applied Physics*, vol. 84, pp. 675-682, 1998.

32 J. Fivez and J. Thoen, "Thermal Waves in Materials with Linearly Inhomogeneous Thermal-Conductivity," *Journal of Applied Physics*, vol. 75, pp. 7696-7699, 1994.

33 J. Fivez and J. Thoen, "Thermal Waves in Materials with Inhomogeneous Thermal-Conductivity," *Journal De Physique Iv*, vol. 4, pp. 283-286, 1994.

34 C. Glorieux, J. Fivez, and J. Thoen, "Photoacoustic Investigation of the Thermal-Properties of Layered Materials - Calculation of the Forward Signal and Numerical Inversion Procedure," *Journal of Applied Physics*, vol. 73, pp. 684-690, 1993.

35 T. Borca-Tasciuc, A. R. Kumar, and G. Chen, "Data reduction in 3 omega method for thin-film thermal conductivity determination," *Review of Scientific Instruments*, vol. 72, pp. 2139-2147, 2001.

36 S. K. Mathis, A. E. Romanov, L. F. Chen, G. E. Beltz, W. Pompe, and J. S. Speck, "Modeling of threading dislocation reduction in growing GaN layers," *Physica Status Solidi a-Applied Research*, vol. 179, pp. 125-145, 2000.

37 P. Gibart, "Metal organic vapour phase epitaxy of GaN and lateral overgrowth," *Reports on Progress in Physics*, vol. 67, pp. 667-715, 2004.

38 P. G. Klemens, "The Scattering of Low-Frequency Lattice Waves by Static Imperfections," *Proceedings of the Physical Society of London Section A*, vol. 68, pp. 1113-1128, 1955.

39 G. A. Slack, "Thermal-Conductivity of II-VI Compounds and Phonon Scattering by Fe^{2+} Impurities," *Physical Review B*, vol. 6, pp. 3791-&, 1972.

40 R. Berman, "Thermal-Conductivity of Isotopically Enriched Diamonds," *Physical Review B*, vol. 45, pp. 5726-5728, 1992.

41 J. E. Graebner, S. Jin, G. W. Kammlott, J. A. Herb, and C. F. Gardinier, "Unusually high thermal conductivity in diamond films," *Applied Physics Letters*, vol. 77, pp. 1576, 1992.

42 R. P. Vaudo, X. Xu, C. Loria, A. D. Salant, J. S. Flynn, and G. R. Brandes, "GaN boule growth: A pathway to GaN wafers with improved material quality," *Physica Status Solidi a-Applied Research*, vol. 194, pp. 494-497, 2002.

Chapter 5 The Thermal Resistance of AlGaN/GaN HFET

5.1 Overview

5.1.1 Self-heating Effects

High power high frequency devices suffer from self-heating as evidenced by numerous studies that are probably best referenced and summarized in Ref. 1, 2, 3, and 4. Self-heating affects device reliability, device performance and device non-linearity. For instance, as the device temperature increases, electromigration causes metallization failures. Current non-uniformity can create hot spots and burn-out. Gradual degradation of contact resistance worsens as device temperature becomes higher. Another example concerns device performance that is altered by a drop in transconductance at increasing temperature due to a falling saturation velocity. Thermal runaway processes (thermal instabilities) limit both reliability and device operation. For instance semi-insulating layers can become conductive as the temperature increases causing burn-out. In heterojunction bipolar transistors, non-uniform temperature distribution may entail a rise in middle finger current density feeding back heat generation and temperature rise. Consequently, as device parameters vary with temperature, non-linearities are inherently introduced via non-zero temperature coefficient and temperature dependent thermal conductivity. These non-linearities cause a variety of undesirable effects including harmonic generation, distortion, gain reduction, etc.

As device parameters change due to self-heating depending on RF power level, circuit performance will depend on RF power level via temperature rise. For

instance, conditions for implementing an efficient matching network will vary depending on device temperature during dynamic operation. Therefore it is crucial to account for self-heating in microwave circuit design. This short overview on adverse effects of self-heating is not meant to be exhaustive. More details can be found in Ref. 1, 2, 3 and 4. Rather, this paragraph illustrates the importance of predicting and controlling device self-heating, which turn to be especially important in GaN RF devices[5-7].

5.1.2 Status in Thermal Modeling.

The lack of thermal modeling in microwave circuit designs is widely acknowledged[1,2,4,8-11]. According to Ref. 4 Chapter 9, there exists two approaches in thermal modeling of power amplifiers. One approach consists of considering a self-heating model in which the effect of the temperature rise is cross-coupled with electrical characteristics of the device (electrothermal model)[10]. Although the self-heating analysis has been part of the device model, it is possible to make it part of simulator. Active research is currently in progress to efficiently include appropriate thermal model into powerful simulators like harmonic-balance[9]. The other approach is thermal scaling in which the user estimates the temperature of the device and enters it as model parameter. It is the second approach that will be discussed in this thesis. In that framework, the problem of predicting the device temperature can quickly become very complex. The trade-off lies between model complexity and accuracy in prediction. Establishing such a trade-off in device temperature estimate is one of the objectives pursued in this chapter. Here, the strategy consists of considering a full three dimensional analytical model to be subsequently simplified mathematically. The end goal is to express accurate closed-form design expressions for thermal resistances. This approach is not conventional. What has been often done by other workers is to either develop intractable analytical or numerical models of increasingly higher complexity or to oversimplify complex device physics resulting in a complex mathematical formalism[12]. To illustrate these statements, a brief overview on previous works is now given.

A variety of thermal models were implemented in the 1970's. Several approaches emerged. Thermal device modeling derived from analogies with electrical models[13] or the heat equation solved from numerical or analytical method[1, 14-17]. Throughout the 80's, reports tend to indicate that thermal models derived from electrical analogies[18] were of most practical interest although a few authors made novel contribution to the determination of thermal resistance[1,2,19-22]. Perhaps the relatively low magnitude of power density achieved in the 80's did not require extensive analysis. In the 1990's, the significance of solving the heat equation directly was acknowledged[19,20,23-25] compared with methods based on numerical calculations[26,27] or electrical analogies[18]. It must be remarked that technological progresses had been impressive, resulting in a steady increase of power density. For instance GaAs HEMT had gained in maturity since its inception in 1979[2]. Since then, thermal modeling has for the most part become more and more complex as the power density increased[4,10,11,28]. As acknowledged by Darwish *et al.*[8] in a 2005 publication, there is a lack of closed-form expression for FET thermal resistances with excellent accuracy and limited complexity.

Partly due to a lack of knowledge in GaN thermal parameters, the potential in GaN HEMT thermal performances have remained overlooked despite an increasing number of studies on the topic[7,29-31]. Simplified modeling of HEMT thermal resistance will enable the ability to compare the AlGaN/GaN HEMT grown on silicon carbide with performance of AlGaN/GaN HEMT grown on gallium nitride substrate.

In this chapter, a compact closed-form analytical model is presented to predict the device temperature and the thermal resistance of multifinger HEMT structures. The accuracy of the model is verified against finite element analysis. Gallium nitride thermal parameters are used in numerical applications. A key point is to compare the thermal performance of gallium nitride HEMT grown on SiC with the thermal performance of homoepitixially grown GaN HEMT. Section 5.2 analyzes the trade-offs in FET thermal design using the analytical modeling presented in Appendix A. Finally Section 5.3 addresses a comparative study on the performance of AlGaN/GaN HEMT grown on SiC and GaN.

5.2 Trade-off in Thermal Design

5.2.1 Definitions

Higher power can be achieved by increasing device width. The power density is expressed per unit length, typically W/mm. Typically a power device is laid out using adjacent cells. In brief, cells permit to increase the packing density, reduce failures by reducing the current density. In theory, failing fingers do not prohibit device operation although they will reduce performance[1]. An elementary multifinger gallium arsenide field effect transistor is shown in Figure 5.1 below. The long dimension of the finger is called the width and the total length of the device is called the periphery. The narrow dimension of the gate is called the length.

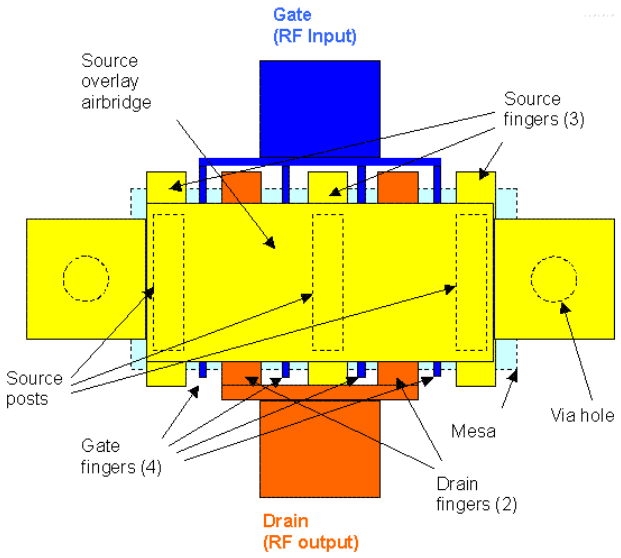

Figure 5.1. Typical multifinger FET structure. For sake of simplicity, neither return path nor bias circuit are shown.

A common approach in conventional thermal models is based upon the concept of thermal resistance. The thermal resistance R from the active region of a HEMT can be defined as the ratio between the power dissipated P_{dis} in the active region and the temperature difference between the active region (T) and the heat sink (T_0).

$$R = \frac{T - T_0}{P_{dis}} \tag{5.1}$$

T_0 is usually the ambient temperature. Because the concentration of holes is negligible in FET or HEMT, heat generation originates from joule heating[2]. In these conditions, P_{dis} is given by $P_{dc}+P_{in}-P_{out}$ with $P_{dc}=V_{dc}I_{dc}$, P_{in} the input RF power. Since $P_{out}=\eta_{eff}\ P_{dc}$ where η_{eff} is the power added efficiency, $P_{dis}=P_{dc}-(G_p-1)P_{in} = P_{dc}\cdot(1-\eta_{eff}\cdot(1-1/\ G_p)) \sim P_{dc}\cdot(1-\eta_{eff})$ where G_p is the power gain in the linear regime. As expected, the dissipated power will decrease with increasing RF input power. The thermal resistance R is expressed in mK/W with P_{dis} in W or if P_{dis} in W/mm, then R is expressed in K·mm/W. Increasing power added efficiency reduces dissipated power but increases design complexity[4,7]. Therefore there is an acute interest to reduce self-heating at the device level.

The thermal treatment of semiconductor devices is non-linear by essence. The thermal conductivity of semiconductor is often found to have the following dependence on temperature[2,30]:

$$k(T) = k(T_0)\left(\frac{T}{T_0}\right)^{-\lambda},\ T_0 = 300K \tag{5.2}$$

In Chapter 4, It was established that the temperature dependence for gaN is $\lambda_{GaN}=1.43$ whereas for SiC λ_{SiC} can reliably taken equal to λ_{GaN}[30]. Given the temperature dependence of the thermal conductivity, it is shown in Appendix B that the temperature varies quadraticly with power and thermal resistance.

$$T = T_0 + PR + P^2\frac{\lambda R^2}{2T_0} \tag{5.3}$$

R is the thermal resistance at 300K. Equation (5.1) becomes less accurate for T > 600-700 K. Now comes an important point: the thermal resistance R at 300K is sufficient to characterize device temperature rise when the thermal conductivity is dependent on temperature. With a room temperature thermal resistance of 22 W·mm/K, the non-linearity in channel temperature with power density becomes observable as shown in Figure 5.2.

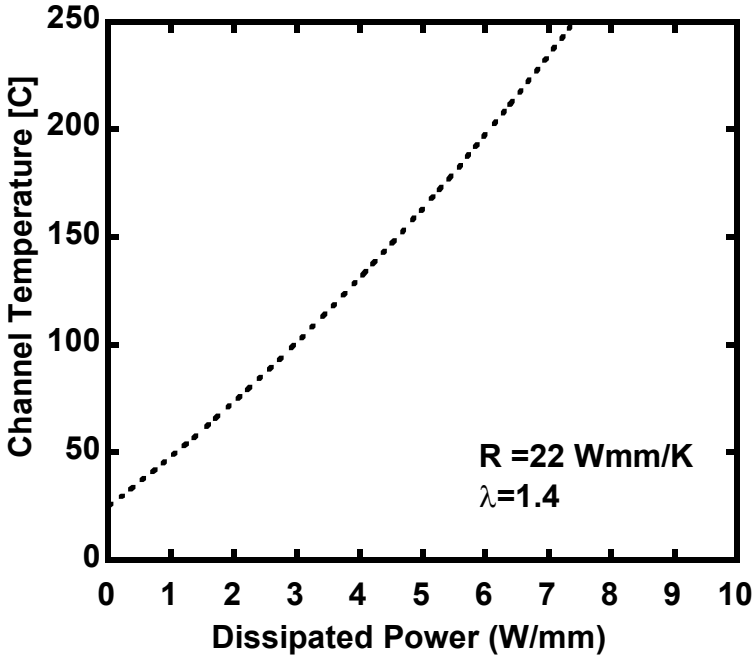

Figure 5.2. Channel temperature rise versus dissipated power. The resistance is 22 K·mm/W., λ=1.4, and T_0 = 25 °C. A close fit to the experimental data of Ref. 31 is obtained by adopting 22 K·mm/W.

Figure 5.2 faithfully reproduces the channel temperature measured over a central finger of a 8-finger AlGaN/GaN SiC HEMT transistor operating in DC mode in Ref. 31. A value of 22 W·mm/K is typical of AlGaN/GaN HEMT SiC transistor. Furthermore, Equation (3.1) and Figure 5.2 illustrate that channel temperature estimations are easily in error by several percents. For instance, an uncertainty of 0.1 in λ (λ~1.4-1.5) results in a relative error of 5% in channel temperature, which leads to an error of 10°C at 7 W/mm in Figure 5.2.

The determination of the thermal resistance relies on several assumptions. Figure 5.3 depicts a cross-sectional view of a device considered in our analysis.

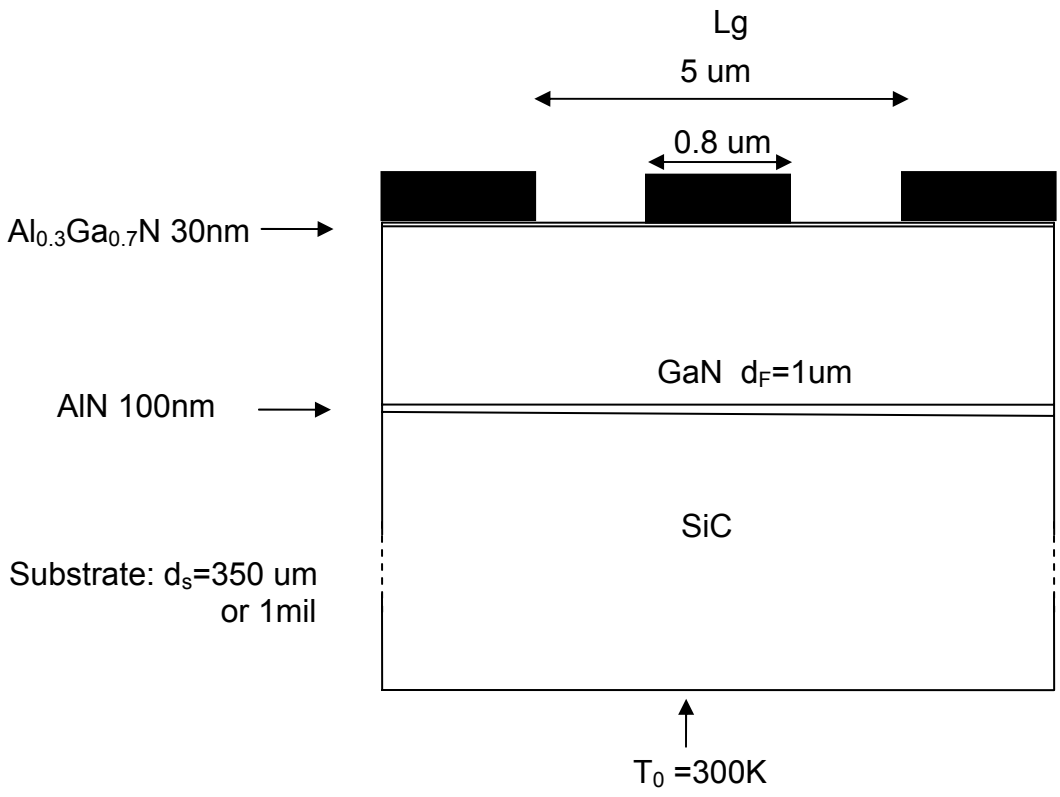

Figure 5.3. Cross-sectional schematic of simplified HEMT on silicon carbide. The gate is drawn rectangular directly on top of the AlGaN layer for sake of simplicity.

Assumptions are listed by order of importance below:

(1) The dissipated power generates a time-independent uniform constant heat flux due to joule heating in a sheet region under the gate or from the source edge to drain edge contact at the AlGaN/GaN interface (two possibilities). All dissipated power diffuses into the layer underneath.

(2) The substrate makes a perfect thermal contact on a perfect heat sink (isothermal boundary condition).

(3) The 1um thin film gallium nitride on SiC has thermal conductivity estimated in the upper bound at 110 $W \cdot K^{-1} \cdot m^{-1}$. The room temperature thermal conductivity of semi-insulating silicon carbide is 350 $W \cdot K^{-1} \cdot m^{-1}$. The room temperature of semi-insulating gallium nitride is 230 $W \cdot K^{-1} \cdot m^{-1}$. The GaN layer grown on GaN substrate has the same thermal

conductivity value. The thermal conductivity is independent of thickness.

(4) Heat diffuses one-dimensionally in the 100nm AlN buffer layer.

(5) The temperature dependence on thermal conductivity is assumed the same for gallium nitride, silicon carbide and any other layers (λ=cst).

(6) The device is exposed to air at room temperature and is unpackaged and tested with RF probes or DC probes.

(7) The temperature gradient normal to the top surface is neglected in the metal layer and in any layers above the metal. The effect due to the presence of the AlGaN layer is neglected. The effect of losses from top layers are briefly discussed in Appendix C. Effects from metal vias are neglected.

These assumptions are typical in present-day thermal resistance studies[7,8,30-32]. The first assumption (1) deserves more attention. The heat source width noted 2b may not necessarily be equal to the gate length L_g. Previous studies showed the heat source was indeed located under the gate due to a gradient in electrical field[2,26] (V_{ds}>0). In this study, the heat source will be set to some values between the gate length and the source-to-drain spacing. It is not rare to observe measurements of the channel temperature in DC operating conditions (see Ref. 31). In that case gate voltage and power added efficiency can be set at zero (Vg=0). As already discussed, the channel temperature depends on power added efficiency under RF condition. It can be useful to keep in mind that additional effects might come to play under RF condition.

The present model gives predictions including the following elements:

- Multifingers have a finite width and a non-zero gate length.
- The active layer, buffer layer and substrate are included.
- The thermal conductivity is temperature dependent.

In contrast with few other authors[8,30,32], our analysis will incorporate the effect of buffer layers.

The definition of the device temperature is somewhat arbitrary. Should it be the average temperature ΔT over the heat source width or should it be the temperature T at an arbitrary position in the channel? Electrical measurements of the channel temperature usually average the channel temperature out[1,2]. Infra-red cameras employed to measure device temperature have a resolution of 1um about the channel length[1]. In addition, temperature values used in the expression of the device current correspond to an average temperature[1,2]. In contrast, the emergence of hot spots should be examined by considering the temperature at a single point. In this work, both the average channel temperature and the temperature at the center gate will be considered. However for sake of simplicity, more emphasis is put on the average channel temperature ΔT.

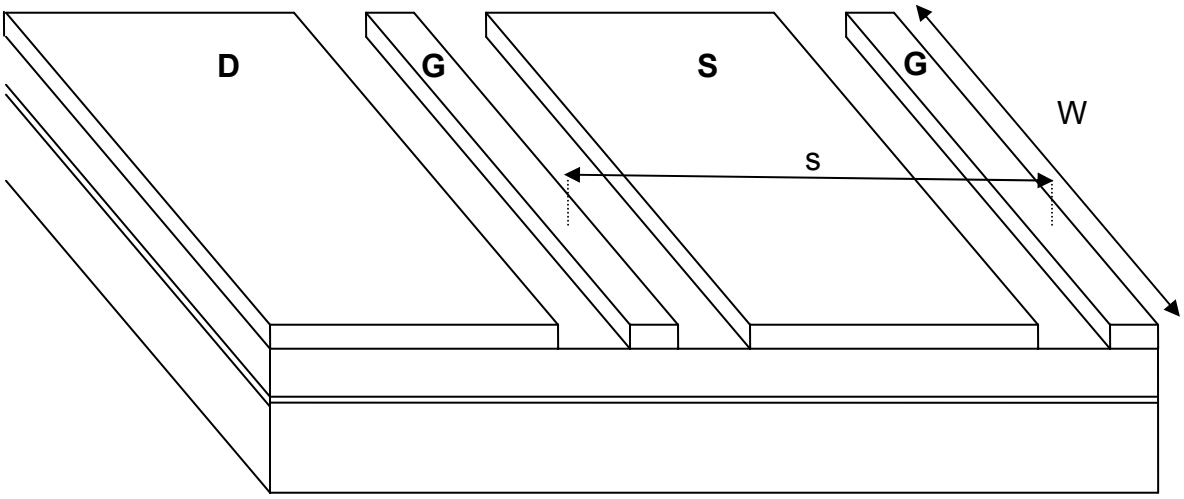

Figure 5.4. Simplified multifinger structure considered in this analysis.

Typical parameters for a mutlifinger GaN HEMT in the 2-4 Ghz band are given below[31].

Gate-gate spacing: s=25 μm

Gate length: L=0.8 μm (half-width: b=0.4 μm)

Gatewidth: W =250 μm

Substrate thickness: d_S=350 μm

GaN layer: d_F=1um

Dissipated power : 0 to 10 W/mm

Number of gate finger: 8

A few elementary electrical design rules will suffice to examine the thermal properties of the multifinger HEMT in a simplified approach. First the channel length is set by speed and gain consideration, the finger width by power. Gate width is limited by parasitics such as the gate resistance that reduce f_{max}. The device periphery, width and lateral dimension can be limited by phase change. Small drain-to-source spacing can cause electromigration to occur. As the frequency of operation increases, the periphery and gate width will have tendency to decrease. The number of finger may correspondingly increase although the device must be excited uniformly while parasitics must be reduced. These considerations trade-off with thermal design.

5.2.2 Single Finger on Substrate (Long Gate Width)

Consider a single gate HEMT on a bare substrate with in-plane thermal conductivity K_{Sx} and out-of-plane thermal conductivity K_{Sy}. The average substrate thermal conductivity is $K_S = \sqrt{k_{Sx}k_{Sy}}$. The anisotropy factor is $K_{Sxy}= \sqrt{\frac{k_{Sx}}{k_{Sy}}}$. The average thermal resistance taken over the length of a long single finger is:

$$R_S = \frac{1}{\pi\ k_S}\left[\ln(\beta_S)+1.0484\right],\ \beta_S > 5$$
$$\beta_S = \sqrt{\frac{k_{Sx}}{k_{Sy}}}\frac{d_S}{b} \qquad (5.4)$$

The full derivation of the following expression is found in Appendix A. Again, d_S is the substrate thickness, and b is the heat source half-width equal to the gate half-width. If the resistance is proportional to the temperature at a given point halfway underneath the gate, the constant 1.0484 must be substituted by the constant 1.241. Equation (5.4) represents an excellent approximation of Equation A.14a in Appendix A. For instance Equation (5.4) is within 0.2% error with equation A.14 at β_S=875, 0.4% error at β_S=60, and 1.4% in error at β_S=5. A thin 1 mil thick substrate and a very large 10um gate length gives β_S=5. Therefore Equation (5.4) is of complete practical use. Moreover Equation (5.4) takes into account anisotropy of the substrate. The thermal resistance increases with increasing substrate thickness, decreasing with gate length.

5.2.3 Multifinger on Substrate

The temperature profile of 8-finger HEMT was calculated along a line perpendicular to the gate fingers using Equation A.9. The device was assumed to be located on a bare silicon carbide substrate (K=350 $W \cdot K^{-1} \cdot m^{-1}$). The result is plotted in Figure 5.5(a) and compared to measurements and numerical simulation depicted in Figure 5.5(b) taken from Ref. 31. Excellent qualitative agreement is observed between Figure 5.5(b) and Figure 5.5(a). The temperature is the highest in the middle part of the central finger, and slowly diminishes toward device edges.

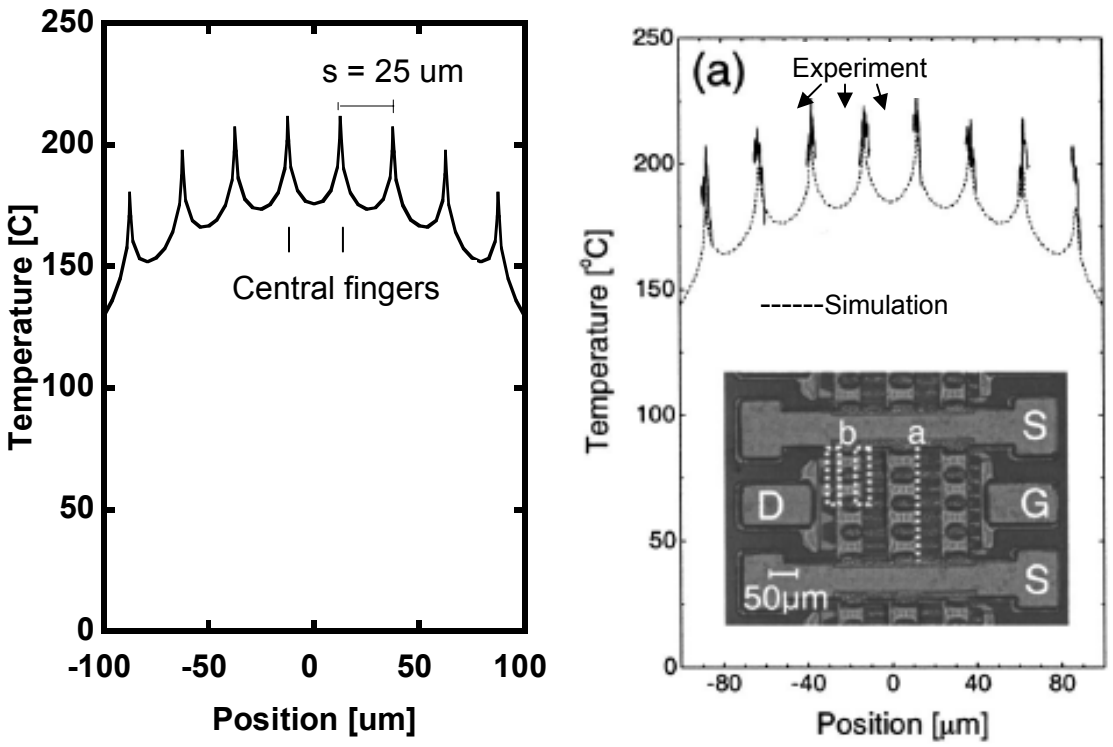

Figure 5.5. Temperature versus position along a line perpendicular to finger width. a) Equation A.9 (bare SiC, K=350 W·K^{-1}·m^{-1}). b) Ref. 31: experiment and simulation (K_{SiC}=350 W·K^{-1}·m^{-1}). P=6.7 W/mm in both figures.

Placing one extra finger next to a single isolated finger will add a thermal resistance. If the spacing between the two fingers is s_q, the thermal resistance induced by the second finger becomes, as shown in Appendix A:

$$R = \frac{1}{\pi \ k_S}\left[\ln(\beta_S) - \ln\left(\frac{\pi}{4}\frac{s_q}{b}\right)\right] \tag{5.5}$$

Equation (5.5) is valid if the spacing between two fingers is smaller than the substrate thickness or larger than the gate half-width. This is actually the case for practical device. If the gate-to-gate spacing is larger than the substrate thickness d_S, the thermal heating produced by the second heater on the first finger is negligible. Therefore increasing the number of finger indefinitely with constant gate-to-gate spacing should not have any practical effects. Reversely, if two fingers overlap, the thermal resistance double as if the power density doubled. Reducing the substrate thickness from 350um to 1mil will decrease the effect of thermal heating generated

by the second heater. The extra resistance due the presence of a second finger can become zero if the gate width is sufficiently small and the gate-to-gate spacing is sufficiently large. These observations become all the more accurate that the gate length becomes smaller compared with the substrate thickness. A rigorous illustration is given in Figure 5.6. Remember that a 1um gate on a 350um substrate corresponds to β_S=175.

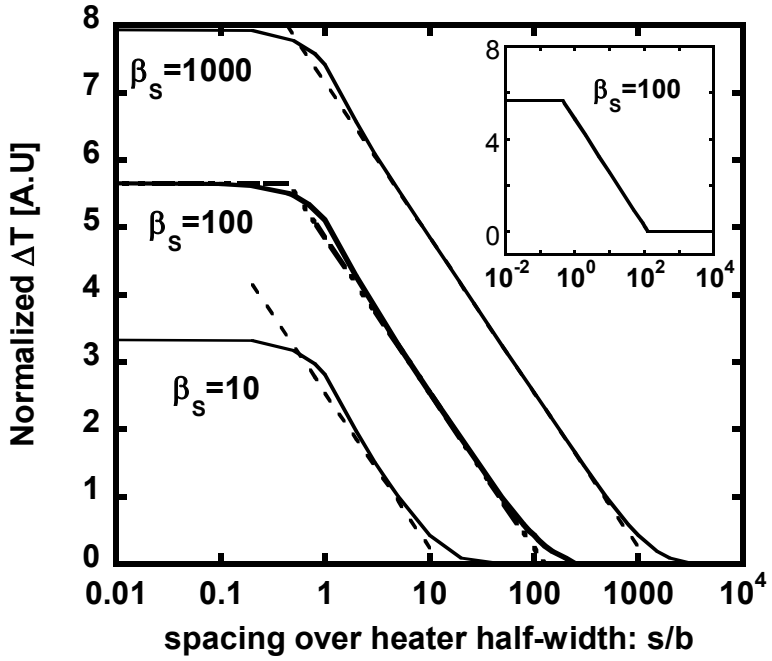

Figure 5.6. Illustration of the temperature rise produced by a second heater placed adjacent to an initial finger. The vertical axis corresponds to the temperature rise normalized to $1/(\pi k_s)$. The horizontal axis represents the ratio of the gate-to-gate spacing s over gate half-width b. Equation (5.5) is plotted in solid line . Figure 5.6 is taken from Appendix A.

The two-finger case can easily be extended to an odd number of p=2r+1 fingers. The average thermal resistance of the central finger becomes:

$$R_{Sm} = \frac{1}{\pi\sqrt{k_{Sx}k_{Sy}}}\left[\ln\left(\frac{4^{2r}\left(\sqrt{k_{Sxy}}\right)^{2r+1} d_S^{2r+1}}{\pi^{2r} r!^2\, s^{2r} b}\right) + 1.048\right] \qquad (5.6)$$

In Appendix A, it is demonstrated that the expression for the thermal resistance for an even number of p=2r fingers is almost identical. The resistance at

the center part of the central finger (as opposed to the average channel resistance) is described by Equation (5.6) provided the constant 1.048 is substituted by 1.241. Equation (5.6) is valid provided the distance between the edge finger to the central finger is smaller than the substrate thickness: $(r+1)\cdot s<d_S$. The temperature rise can be easily plotted against the number of fingers (Figure 5.7). If the number of fingers exceeds the substrate thickness-to-spacing ratio $r>d_S/s$, the channel temperature of the middle finger saturates and becomes independent of the number of fingers.

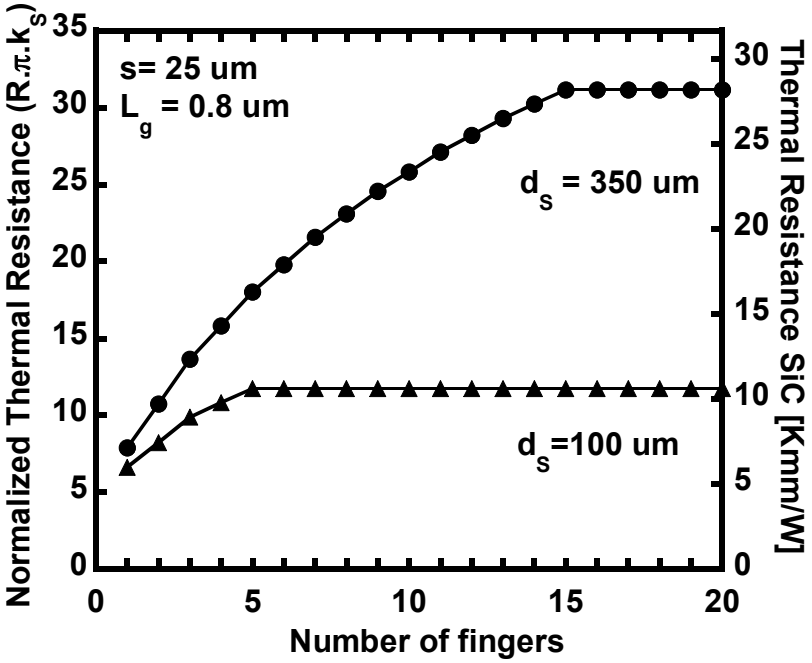

Figure 5.7. Thermal resistance of central finger as a function of finger number. The difference between the average resistance and the resistance at the middle part of the central finger is not visible on this graph.

As the substrate thickness increases, the saturation will be delayed to a higher number of fingers. Increasing the gate-to-gate spacing has nearly the same effect as decreasing the substrate thickness. Interestingly, similar conclusions are drawn in Ref. 7 from a numerical approach. Ref. 7 predicts a temperature saturation beyond 10-12 fingers with a 40um gate-to-gate pitch! However while in Ref. 7 numerical analysis of a fairly complex structure is considered, this work provides deep insights into the parameters governing the thermal resistance dependence on the number of finger.

5.2.4 Multifinger on a Multilayer Film.

This section presents an expression for the thermal resistance of the HEMT device shown in Figure 5.3. Following the same approach as in Chapter 3, the total junction temperature is decomposed into a substrate temperature rise with no film and a film temperature rise: $\Delta T_{F+S}=\Delta T_S+\Delta T_F$. The expressions for ΔT_S and ΔT_F are given in Chapter 3 Equation (3.22). Temperature is easily converted into thermal resistance as follows:

$$R_T = R_{Sm} \times \left[\Delta_F + 1\right] \tag{5.7}$$

R_{Sm} is the thermal resistance of the central finger in a multifinger or single finger structure on a bare substrate. The subscript "sm" stands for "substrate multifinger". The product $\Delta_F R_{Sm}$ represents an effective film thermal resistance R_F while Δ_F is the relative increase in thermal resistance due to the film. Δ_F is given as:

$$\Delta_F = \varepsilon F\ \beta_F\left(\frac{k_S}{k_F}-\frac{k_F}{k_S}\right)+\varepsilon G\left(\frac{R_{buff}}{b/k_S}\right)$$

$$\begin{cases} \varepsilon = \dfrac{1}{2\ R_{Sm}\ \sqrt{k_{Sx}k_{Sy}}}, \\ \beta_F = \sqrt{\dfrac{k_{Sx}}{k_{Sy}}}\,\dfrac{d_F}{b} \\ F = \dfrac{1}{\left(1+0.38\beta_F+\dfrac{\beta_F}{1+0.8\beta_F}\dfrac{k_F}{k_S}\right)} \\ G = \dfrac{1}{\left(1+\beta_F^{1.2}+\left(1.57\beta_F+3.51\cdot 10^{-3}\right)\dfrac{k_F}{k_S}\right)} \end{cases} \tag{5.8}$$

K_S is the substrate thermal resistance, K_F is the film thermal resistance, b the heat source half-width (gate half-width) and R_{buff} is the buffer layer thermal resistance expressed in $K\cdot m^2\cdot W^{-1}$. It is important to note that the effective film thermal resitance $\Delta_F R_{Sm}$ is independent of substrate thickness d_S and gate pitch s.

This property has important consequences in thermal design and will be discussed in more details.

In the particular case of a single finger structure, Equation (5.8) is unchanged except for ε that takes the value:

$$\varepsilon = \frac{\pi/2}{\left[\ln\left(\beta_S\right)+1.05\right]} \tag{5.9}$$

The expression for Δ_F in Equation (5.8) above assumes that the thermal resistance is spatially averaged over the channel length. In the case of thermal resistance at a single point located in the middle part of the central gate, the expression for Δ_F will differ from Equation (5.8) by a slight change in constant values.

The specificity of this model lies in the fact the thermal resistance is expressed as the sum and product of the substrate thermal resistance and an apparent film thermal resistance. Therefore the effect from the substrate and adjacent gates are decoupled from the thermal effects induced by the film and buffer layer. Moreover if the thermal conductivity dependence on temperature is assumed constant in the GaN buffer, AlN layer and SiC substrate, Δ_F is independent of temperature. All temperature dependence is expressed in R_{Sm}.

In order to borrow mathematical expressions developed in Chapter 3, a few subtle approximations were made. First, the substrate bottom surface was assumed adiabatic in the derivation of Δ_F but remained isothermal in the determination of the substrate thermal resistance R_{Sm}. This approximation becomes valid when the substrate thickness-to-gate length ratio is larger than one and substrate-to-film thickness ratio is elevated. This is easily the case in practice. Second the buffer layer is treated as an interfacial boundary resistance. Third, the effect of adjacent heaters on the expression of Δ_F is negligible. The accuracy of the model will be compared to finite element simulation in Section 5.3

Effect of the film thickness, gate with, film thermal conductivity, and buffer layer on the thermal resistance

Equation (5.8) shows that the thermal resistance is greatly altered depending on the film-to-substrate thermal conductivity ratio. A temperature drop of a relatively high magnitude can develop across thermally insulating layers. The thermal resistance is also greatly affected by the thermal resistance of the buffer layer. The thermal resistance will decrease linearly with film thickness-to-gate length aspect ratio β_F. As the film thickness increases, heat spreading becomes more severe in the film and the thermal resistance increases sensibly. For sake of simplicity, numerical values will not be given here. Rather the reader is referred to Section 5.3.

Effect of substrate thickness and number of fingers

The temperature rise due to the presence of the film is independent of the number of finger. Therefore in order to reduce the effect of a thermally insulating layer, it may be judicious to increase the number of fingers. The reduction in thermal resistance at lower substrate thickness may be limited by the film-to-substrate thermal conductivity ratio. This can be easily understood. As the substrate is thinner, the thermal contribution from the film becomes of a greater contribution because the film-to-substrate thickness ratio increases. It is interesting to note that observations of a similar nature were made in a 2003 study on the power handling of AlGaN/GaN HEMT from simulation experiment[33].

5.2.5 Small Width Device

From Appendix A, Figure A.6, finite dimension in gate width W reduces device temperature. The associated reduction in thermal resistance depends on both the substrate thickness-to-gate width ratio (β_{Sz}) and substrate thickness-to-gate length ratio (β_{Sx}).

An accurate approximate expression was derived in Appendix A to capture effects of the finite gate width on the average channel temperature. The thermal resistance R_{3D} at the center part of the central finger is easily inferred.

$$R_{3D} = R_{2D} \bullet \tanh^{0.15}\left(\sqrt{\frac{k_{Sy}}{k_{Sz}}}\frac{W}{2d_S}\right) \tag{5.10}$$

R_{2D} is the thermal resistance determined in a two dimensional analysis. K_{Sz} is the substrate thermal conductivity along a direction parallel to a gate finger.

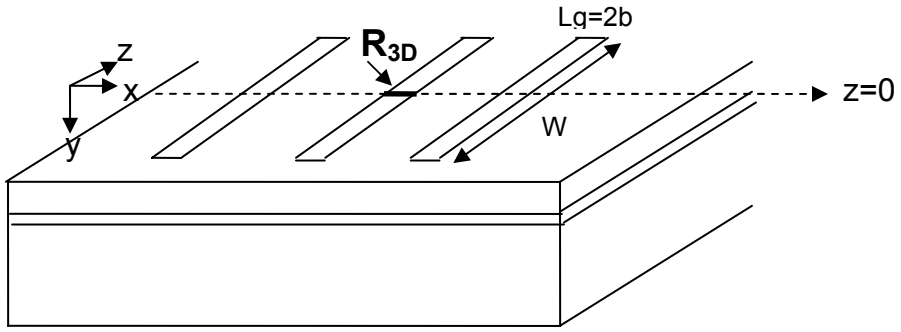

Figure 5.8. R_{3D} is the thermal resistance averaged over the channel of the central finger half-way between gate extremety widthwise.

The film thermal conductivity K_{Fz} along z is assumed identical to the film thermal conductivity along K_{Fx} (K_{Fz}=K_{Fx}). In HEMT structures, geometrical parameters range for W>0.2 d_S, L_g<5um and d_S>25um. In these conditions, It is established in Appendix A that Equation (5.10) is at most within less than 7% error. Effects due to finite gate width becomes more pronounced as the substrate thickness becomes comparable to the half-gate width,

The cooling at the gate extremity widthwise is not negligible. For instance, a 250um wide gate on a 350um thick substrate causes a ~15% reduction in thermal resistance using Equation (5.10). Kuball *et al.*[31] finds a ~15-18% reduction in thermal resistance from numerical calculation adopting similar simplifying assumptions and device parameters as ours. Equation (5.10) shows that thermal resistance drop due to finite gate width becomes more pronounced as the substrate thickness becomes comparable to the half-gate width. Equation (5.10) decouples thermal effects widthwise from two-dimensional effects in a plane perpendicular to the gate width.

5.3 Comparative Study between the Thermal resistance of GaN/SiC HEMT and GaN/GaN HEMT.

In this section, the average thermal resistance taken over the central finger width is estimated in a single-finger and 8-finger GaN HEMT based on the model presented above. The thermal resistance is calculated for an AlGaN/GaN SiC HEMT and an homoepitaxially grown GaN HEMT. The same approximations are kept constant throughout the study (same geometry, same thermal property, same boundary conditions, etc…). In addition simulation of the heat flow is carried out and compared with analytical results. The cooling effect from the finite width is not included since the heat flow is analyzed in a plane perpendicular to gate width. Room temperature thermal conductivity of GaN and Silicon carbide were measured in Chapters 1 and 4. The temperature dependence of silicon carbide is taken equal to the temperature dependence of gallium nitride measured in Chapter 4[30].

Table 5.1. Thermal parameter employed in the thermal resistance evaluation of GaN HEMT. R_{buff} is the thermal resistance of the AlN buffer layer

K_{GaN} $W\cdot K^{-1}\cdot m^{-1}$	K_{SiC} $W\cdot K^{-1}\cdot m^{-1}$	K_F $W\cdot K^{-1}\cdot m^{-1}$	R_{buff} $m^2\cdot K\cdot W^{-1}$	λ
230	350	110	0	1.4
			10^{-8} (K_{AlN} =10 $W\cdot K^{-1}\cdot m^{-1}$)	
			10^{-9} (K_{AlN} = 50 $W\cdot K^{-1}\cdot m^{-1}$)	

In order to consider the effects of the buffer layer on thermal resistance, the thermal resistance of AlN must be known. A few studies have indicated that the AlN thermal conductivity ranged between 1 $W\cdot K^{-1}\cdot m^{-1}$ and 50 $W\cdot K^{-1}\cdot m^{-1}$ for films thickness between a few hundreds of nanometers to a few microns[34-37]. Lambropoulos *et al.*[34] have shown that microstructural defects can be detrimental to thin AlN film thermal conductivity properties. Fair agreement was found between

theoretical and experimental values and measurements[34]. Morkoç emphasizes the microstructural characteristics in AlN buffer layers[38]. All in all, there are strong indications that the thermal conductivity of AlN buffer layer is between 10 to 100% lower than bulk values[34-37]. As a result, the thermal resistance of AlN buffer layers will be 10^{-8} $m^2 \cdot K \cdot W^{-1}$ and 2.10^{-9} $m^2 \cdot K \cdot W^{-1}$ for a thermal conductivity of 10 $W \cdot K^{-1} \cdot m^{-1}$ and 50 $W \cdot K^{-1} \cdot m^{-1}$ respectively. For comparison, the equivalent thermal boundary resistance of a 1um GaN layer is 9.10^{-9} $m^2 \cdot K \cdot W^{-1}$ nearly the same as the AlN thermal resistance.

Thermal resistances are calculated for a single-finger having a 0.8um gate length. For a 8-finger structure, gate length is either 0.8um or 5um. Geometrical parameters used in this study have been listed in Section 5.2.1. The gate pitch is 25um. The substrate thickness is 350um by default but was sometimes set a 25um (~1mil). Resistance calculations are presented in 3 tables. The last column of each table corresponds to the thermal resistance of HEMT grown on GaN substrates while the second last column gives the thermal resistance values for a GaN/SiC HEMT. The gate length is constant in each table. Results obtained from simulation are displayed in parentheses besides analytical values. Parameters used in each table are summarized as follows:

- Table 5.1: Lg=0.8um, 1-finger 25um spacing, ds= 350um or 1 mil, substrate: SiC or GaN.
- Table 5.3: Lg =0.8um, 8-finger, 25um spacing, ds=350um or 1 mil, substrate: SiC or GaN.
- Table 5.4: Lg=5um, 8-finger, 25um spacing, ds= 350um or 1 mil, substrate: SiC or GaN.

Unless specified the substrate thickness is 350um. The cooling effect from the finite width is not included as it does not impact the present comparative study.

5.3.1 Single Finger

The thermal resistance for a single finger device is given in Table 5.1.

Table 5.1. Thermal resistance estimation of a single finger HEMT. c =calculated; s = simulated. L_g=2b=0.8um. Bold characters: substrate thickness d_S=350um; Italic characters: d_S=25um (1mil). Film thickness = 1um.

Film	Buffer	Multilayer	HEMT on SiC	HEMT on GaN
K_F	R_{buff} [$m^2 \cdot K \cdot W^{-1}$]	Δ_F	R_{SiC+F} [°C·mm/W] 25°C	R_{GaN} [°C·mm/W] 25°C
0	0	0	**d_S=350um 7.12 (c) 7.12 (s)**	**d_S=351um 10.83 (c) 10.83 (s)**
110	0	0.64	**11.74 (c) 11.39 (s)**	**10.83 (c) 10.83 (s)**
110	10^{-8}	1	**14.13 (c)**	**10.83 (c)**
110	2.10^{-9}	0.95	**12.22 (c)**	**10.83 (c)**
110	0	0.98	*d_S =25 um 9.34 (c) 9.0 (s)*	*d_S =26um 7.23 (c) 7.23 (s)*

The thermal resistance of a single finger AlGaN/GaN HEMT grown on SiC silicon carbide HEMT is found to be higher that the thermal resistance of AlGaN/GaN HEMT grown on GaN. If the buffer layer is including in the analysis, the thermal resistance of HEMT grown on SiC becomes even higher. The origin for this discrepancy can be clearly identified. From the simple model in Equation (5.7), the relative increase in thermal resistance originates from the presence of the thin film that cause a relative increase of 0.64/(0.64+1)=40% with no buffer layers. Analytical predictions are verified through finite element simulation. Figure 5.9 illustrates a two-dimensional cross-sectional view of a single-finger structure. The temperature Ts is

calculated in the middle part of the gate region while the temperature Tint is deducted at the interface GaN/SiC 1um below the center of the gate.

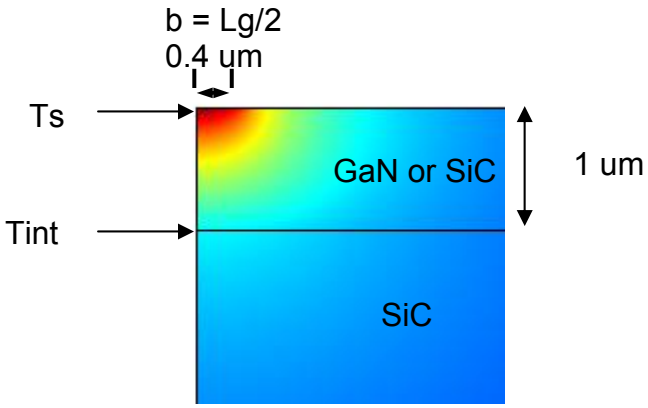

Figure 5.9. Cross-sectional schematic temperature distribution under the gate.

Results are summarized in Table 5.2 below.

Table 5.2. Simulated temperature values under the gate.

	GaN/SiC	bare SiC	δT
Ts	119.3°C	72.92°C	46.38°C
Tint	59.11°C	55.27°C	3.84°C
Ts-Tint	60.19°C	17.65°C	42.54°C

The difference of surface temperature between a heat source on GaN/SiC and bare SiC is 119.3°C-72.92°C= 46.38°C. The difference of temperature across the layer Ts-Tint for the GaN/SiC device is 119.3°C-59.11°C= 60.19°C. The difference of temperature Ts-Tint across the top 1um layer of a bare SiC substrate is only 72.92°C-55.27°C= 17.65°C. As 60.19°C-17.65°C= 42.54°C, the temperature rise develops entirely across the thin layer.

Simulation confirms an increase of 40 % in channel temperature due to the presence of a 1um GaN film. Yet, more can be said. The parameters responsible for temperature rise can be clearly identified. Equation (5.8) is key to thermal engineering. Ignoring the buffer layer, the film-to-substrate thermal conductivity ratio

is 350/110= 3.18 and the film thickness to heater half-width ratio β_F is 1/0.4= 2.5. Therefore the film-to-substrate ratio plays a leading role in the magnitude of the thermal resistance. The film-to-substrate thermal conductivity is perhaps even more important than β_F. The thermal conductivity of the GaN layer is of utmost importance, probably almost as important as the thermal conductivity of the substrate. Table 5.1 gives an excellent illustration. It would take a substrate with a thermal conductivity of 419 $W \cdot K^{-1} \cdot m^{-1}$ to achieve higher thermal resistance than that obtained on GaN substrate. Moreover decreasing the silicon carbide substrate thickness aggravates the situation compared with GaN from Table 5.1. Simulation results have illustrated the accuracy of the model presently developed.

5.4 Multifinger

The previous section examined the device temperature rise for a device in a single-finger. The influence of multifingers on thermal resistance is analyzed. Again, simulation results were compared with analytical predictions. A typical cross-sectional view of an isothermal profile in a half 8-finger structure is shown in Figure 5.10 below.

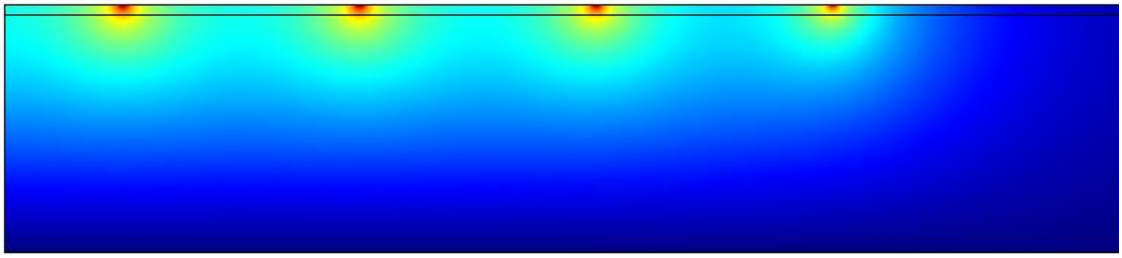

Figure 5.10. Cross-sectional view of temperature solution in a half structure of a 8-finger HEMT.

Thermal resistance values were computed for Lg=0.4um and the result is shown in the table below. In the multifinger case, thermal resistance is lower with HEMT on SiC even when low thermally insulating buffer layer is included. This can be understood from Equation (5.7). The product $R_{sm}\Delta_F$ is independent of the number of fingers whereas R_{sm} does dependent strongly the finger number. Physicaly, heat spreading occurs mostly in the substrate but represent a minor part in the

multilayers. Note that R_{sm} becomes independent of the number of fingers at large gate pitch or at elevated finger number as illustrated in Figure 5.6. It would take only two fingers with a gate pitch of 68um for the thermal resistance of a structure on GaN/SiC to be equivalent to the thermal resistance of a structure on GaN substrate, keeping the gate length at 0.8um and substrate thickness at 350um. For 2 fingers or more with a gate-to-gate spacing smaller than 68um, the thermal performance in the case of a SiC substrate should be higher than the thermal performance of a HEMT on a GaN substrate.

Table 5.3 . Thermal resistance estimation in a 8 finger HEMT. L_g=2b=0.8um. c=calculated. s= simulated. Bold characters: substrate thickness d_S=350um. Italic characters: d_S=25um (~1mil). Fim thickness = 1um.

Film	Buffer	Multilayer	HEMT on SiC	HEMT on GaN
K_F	R_{buff} [$m^2 \cdot K \cdot W^{-1}$]	Δ_F	**R_{SiC+F} [°C·mm/W] 25°C**	**R_{GaN} [°C·mm/W] 25°C**
0	0	0	**d_S=350um 20.6 (c) 21 (s)**	**d_S=351um 31.36 (c) 31.95 (s)**
110	0	0.233	**25.53 (c) 25.26 (s)**	**31.36 (c) 31.95 (s)**
110	10^{-8}	0.356	**28.06 (c)**	**31.36 (c)**
110	2.10^{-9}	0.257	**26.02 (c)**	**31.36 (c)**
110	0	0.9	*d_S =25um 9.78 (c) 9.98 (s)*	*d_S =26um 8.0 (c) 8.81 (s)*

It remains that the thermal resistance of GaN/GaN HEMT is approaching the thermal resistance of GaN/SiC HEMT made on thinner substrate and with mutilayer of lower thermal conductivity.

Finally the thermal resistance was determined in the case of large gate length: L_g=5 um.

Table 5.4. Thermal resistance estimation in an 8-finger HEMT. The gate length is now 5um (b=2.5um). c = calculated. s = simulated. Bold characters: substrate thickness d_S=350um. Italic characters: d_S=24um (~ 1mil). Fim thickness= 1um.

Film	Buffer	Multilayer	HEMT on SiC	HEMT on GaN
K_F	R_{buff} [$m^2 \cdot K \cdot W^{-1}$]	Δ_F	**R_{SiC+F} [°C·mm/W] 25°C**	**R_{GaN} [°C·mm/W] 25°C**
0	0	0	**d_S=350um 18.94 (c) 19.3 (s)**	**d_S=351um 28.82 (c) 29.4 (s)**
110	0	0.074	**20.34 (c) 20.06 (s)**	**28.82 (c) 29.4 (s)**
110	10^{-8}	0.313	**24.87 (c)**	**28.82 (c)**
110	$2 \cdot 10^{-9}$	0.096	**20.75 (c)**	**28.82 (c)**
110	0	0.377	*d_S = 25um 4.8 (c) 5.39 (s)*	*d_S = 26um 5.47 (c) 6.29 (s)*

As the gate length increases, the dissipation performance of AlGaN/GaN SiC HEMT becomes clearly superior to that of homoepitaxially grown GaN HEMT. This is simply because the film thickness-to-heater half-width ratio drops. A question must be asked: why is the thermal resistance of GaN/GaN HEMT only 15% higher than that of GaN/SiC HEMT at a substrate thickness of 1 mil? Simply because at constant gate length, the thermal resistance (=$R_{sm}\Delta_F$) of the film is independent of substrate thickness as Equation (5.8) proves.

In modern technology gate length are becoming increasingly shorter. Table 5.3 is more representative of the thermal performance of AlGaN/GaN SiC HEMT than Table 5.4.

5.5 Conclusion

An analytical model has been developed to capture governing parameters impacting the thermal design of AlGaN/GaN HEMT devices. The present model has been borrowed from state-of-the art developments in thermal engineering. Upon further refinements, this model has been brought to the field of device thermal modeling. An important feature of the model is to be able to treat the effect of buffer layers analytically. Buffer layers represent an important characteristic of GaN-based technologies as GaN is grown on non native substrates. The impact of gate length, substrate thickness, gate pitch, gate width, film thickness, buffer layer and film thermal conductivities on thermal performance can be examined separately in these models. The complete mathematical development is addressed in Appendix A and Chapter 3. The model is accurate within a few percent compared with numerical simulations calculated for heat source to substrate thickness ratios greater than 10.

Thanks to the characterization of the gallium nitride thermal conductivity in Chapter 4, it is possible to compare the thermal performance of AlGaN/GaN HEMT grown on SiC with the performance of AlGaN/GaN HEMT grown on gallium nitride. Single finger GaN/GaN HEMTs are more thermally advantageous compared to GaN/SiC HEMT. A significant part in discrepancy is accounted for by the contribution of the film-to-substrate thermal conductivity ratio. Multifinger HEMTs formed on SiC are expected to present higher thermal performance than multifinger HEMT formed on GaN substrates. This is because the thermal resistance is sensitive to heat spreading in the substrate. At short gate length and thin substrate, thermal performances of GaN/GaN HEMTs are expected to improve. Finally the presence of buffer layer between the gallium nitride layer and the silicon carbide substrate causes observable increase in thermal resistance.

5.6 References

1 J. V. DiLorenzo and D. D. Khandelwal, *GaAs FET principles and technology*. Dedham, Mass.: Artech House, 1982.

2 R. Anholt, *Electrical and thermal characterization of MESFETs, HEMTs, and HBTs*. Boston: Artech House, 1995.

3 R. Remsburg, *Thermal design of electronic equipment*. Boca Raton, Fla.: CRC Press, 2001.

4 S. A. Maas, *Nonlinear microwave and RF Circuits*, 2nd ed. Boston: Artech House, 2003.

5 C. Lee, L. Witkowski, M. Muir, H. Q. Tserng, P. Saunier, H. Wang, J. Yang, and M. A. Khan, "Reliability evaluation of AlGaN/GaN HEMTs grown on SiC substrate," *High Performance Devices, 2002. Proceedings. IEEE Lester Eastman Conference on*, pp. 436-442, 2002.

6 H. Kim, V. Tilak, B. M. Green, H.-y. Cha, J. A. Smart, J. R. Shealy, and L. F. Eastman, "Degradation characteristics of AlGaN-GaN high electron mobility transistors," *Reliability Physics Symposium, 2001. Proceedings. 39th Annual. 2001 IEEE International*, pp. 214-218, 2001.

7 S. Nuttinck, B. K. Wagner, B. Banerjee, S. Venkataraman, E. Gebara, J. Laskar, and H. M. Hariis, "Thermal analysis of AlGaN-GaN power HFETs," *Ieee Transactions on Microwave Theory and Techniques*, vol. 51, pp. 2445-2452, 2003.

8 A. M. Darwish, A. J. Bayba, and H. A. Hung, "Accurate determination of thermal resistance of FETs," *Ieee Transactions on Microwave Theory and Techniques*, vol. 53, pp. 306-313, 2005.

9 W. Batty, C. E. Christoffersen, A. J. Panks, S. David, C. M. Snowden, and M. B. Steer, "Electrothermal CAD of power devices and circuits with fully physical time-dependent compact thermal modeling of complex nonlinear 3-d systems," *Components and Packaging Technologies, IEEE Transactions on [see also Components, Packaging and Manufacturing Technology, Part A: Packaging Technologies, IEEE Transactions on]*, vol. 24, pp. 566-590, 2001.

10 V. d'Allesandro and N. Rinaldi, "A critical review of thermal models for electro-thermal simulation," *Solid-State Electronics*, vol. 46, pp. 487-496, 2002.

11 M. Pesare, A. Giorgio, and G. A. Perri, "An analytical method for the thermal layout optimization of multilayer structure solid-state devices," *Solid-State Electronics*, vol. 45, pp. 511-517, 2001.

12 F. N. Masana, "A closed form solution of junction to substrate thermal resistance in semiconductor chips," *Ieee Transactions on Components Packaging and Manufacturing Technology Part A*, vol. 19, pp. 539-545, 1996.

13 H. F. Cooke, "FETs and bipolars differ when the going gets hot," *Microwaves*, pp. 55, 1978.

14 R. David, "Computerized Thermal Analysis of Hybrid Circuits," *Parts, Hybrids, and Packaging, IEEE Transactions on*, vol. 13, pp. 283-290, 1977.

15 R. C. Joy and E. S. Schlig, "Thermal properties of very fast transistors," *Electron Devices, IEEE Transactions on*, vol. 17, pp. 586-594, 1970.

16 A. G. Kokkas, "Thermal analysis of multiple-layer structures," *Electron Devices, IEEE Transactions on*, vol. 21, pp. 674-681, 1974.

17 Y. C. Wang and M. Bahrami, " Investigation of thermal resistance in single- and multiple-cell GaAs MESFETs." vol. 47, pp. 147-153, 1979.

18 H. F. Cooke, "Precise technique finds FETs thermal resistance," *Microwaves & RF*, pp. 85-87, August 1986.

19 C. C. Lee, Y. J. Min, and A. L. Palisoc, "A general integration algorithm for the inverse Fourier transform of four-layer infinite plate structures," *Components, Hybrids, and Manufacturing Technology, IEEE Transactions on [see also IEEE Trans. on Components, Packaging, and Manufacturing Technology, Part A, B, C]*, vol. 12, pp. 710-716, 1989.

20 D. H. Smith, "Predicting operating temperatures for GaAs ICs," presented at Gallium Arsenide Integrated Circuit (GaAs IC) Symposium, 1991. Technical Digest 1991., 13th Annual, 1991.

21 D. H. Smith, A. Fraser, and J. O'Neil, "Measurement and prediction of operating temperatures for GaAs ICs," *IEEE SEMI-THERM symp.*, Dec. 1986, Paper A5.

22 G. Ghione, P. Golzio, and C. U. Naldi, "Self-consistent thermal modelling of GaAs MEFET's: a comparative analysis of power device mountings," *Alta Frequenza*, vol. 57, pp. 311-319, 1988.

23 D. E. Dawson, "Thermal modeling, measurements and design considerations of GaAs microwave devices," presented at Gallium Arsenide Integrated Circuit (GaAs IC) Symposium, 1994. Technical Digest 1994., 16th Annual, 1994.

24 J. Albers, "An exact solution of the steady-state surface temperature for a general multilayer structure," presented at Semiconductor Thermal Measurement and Management Symposium, 1994. SEMI-THERM X., Proceedings of 1994 IEEE/CPMT 10th, 1994.

25 A. L. Palisoc, Y. J. Min, and C. C. Lee, "Thermal properties of five-layer infinite plate structures with embedded heat sources," *Journal of Applied Physics*, vol. 65, pp. 4438-4444, 1989.

26 P. W. Webb and I. A. D. Russell, "Thermal resistance of gallium-arsenide field-effect transistors," *Circuits, Devices and Systems, IEE Proceedings G*, vol. 136, pp. 229-234, 1989.

27 P. W. Webb, "Thermal modeling of power gallium arsenide microwave integrated circuits," *IEEE Transactions on Electron Devices*, vol. 40, pp. 867-877, 1993.

28 D. J. Walkey, D. Celo, T. J. Smy, and R. K. Surridge, "A thermal design methodology for multifinger bipolar transistor structures," *Electron Devices, IEEE Transactions on*, vol. 49, pp. 1375-1383, 2002.

29 A. M. Darwish, A. J. Bayba, and H. A. Hung, "Thermal resistance calculation of AlGaN-GaN devices," *Ieee Transactions on Microwave Theory and Techniques*, vol. 52, pp. 2611-2620, 2004.

30 J. C. Freeman, "Channel temperature model for microwave AlGaN/GaN power HEMTs on SiC and sapphire," presented at 2004 IEEE MITT-S

International Microwave Symposium Digest, Jun 6-11 2004, Fort Worth, TX, United States, 2004.

31 M. Kuball, S. Rajasingam, A. Sarua, M. J. Uren, T. Martin, B. T. Hughes, K. P. Hilton, and R. S. Balmer, "Measurement of temperature distribution in multifinger AlGaN/GaN heterostructure field-effect transistors using micro-Raman spectroscopy," *Applied Physics Letters*, vol. 82, pp. 124-126, 2003.

32 J. Park, M. W. Shin, and C. C. Lee, "Thermal modeling and measurement of GaN-based HFET devices," *Ieee Electron Device Letters*, vol. 24, pp. 424-426, 2003.

33 R. Dietrich, A. Wieszt, A. Vescan, H. Leier, R. Stenzel, and W. Klix, "Power handling limits and degradation of large area AlGaN/GaN RF-HEMTs," *Solid-State Electronics*, vol. 47, pp. 123-125, 2003.

34 J. C. Lambropoulos, S. D. Jacobs, S. J. Burns, L. Shaw-Klein, and S.-S. Hwang, "Thermal conductivity of thin films. Measurement and microstructural effects," presented at Winter Annual Meeting of the American Society of Mechanical Engineers, Dec 1-6 1991, Atlanta, GA, USA, 1991.

35 P. K. Kuo, G. W. Auner, and Z. L. Wu, "Microstructure and Thermal-Conductivity of Epitaxial Aln Thin-Films," *Thin Solid Films*, vol. 253, pp. 223-227, 1994.

36 Y. Zhao, C. Zhu, S. Wang, J. Z. Tian, D. J. Yang, C. K. Chen, H. Cheng, and P. Hing, "Pulsed photothermal reflectance measurement of the thermal conductivity of sputtered aluminum nitride thin films," *Journal of Applied Physics*, vol. 96, pp. 4563-4568, 2004.

37 A. Jacquot, B. Lenoir, A. Dauscher, P. Verardi, F. Craciun, M. Stolzer, M. Gartner, and M. Dinescu, "Optical and thermal characterization of AlN thin films deposited by pulsed laser deposition," *Applied Surface Science*, vol. 186, pp. 507-512, 2002.

38 H. Morkoç, *Nitride semiconductors and devices*. Berlin ; New York: Springer, 1999.

Chapter 6 Summary and Conclusions

The thermal properties of gallium nitride and gallium nitride based heterojunction field effect transistors (HFET) devices were investigated in order to identify major limitations in heat transfer. As a result, the potential of the 3ω differential technique to characterize the thermal conductivity of thin film GaN grown on sapphire or silicon was theoretically investigated. The thermal conductivity of hundreds of micrometers thick gallium nitride grown by hydride vapor phase epitaxy was measured using the 3ω slope method from 300K to 450K. Material properties including defect density were characterized and compared with previously measured thermal conductivity values. The heat model developed in this study along with experimental gallium nitride thermal parameters represented a starting point for the thermal modeling of GaN based Heterostructure Field Effect Transistors (HFET) devices.

6.1 Summary

6.1.1 Thin Film Thermal Conductivity Characterization Using the 3ω Method

The potential to characterize the thermal conductivity of thin films for a single film-on-substrate system using the differential 3ω method was theoretically addressed when the film-to-substrate thermal conductivity ratio (k_F/k_S) was higher than one and when an interfacial boundary resistance existed between film and substrate. It was demonstrated that a thin thermally insulating buffer layer can be modeled by an interfacial boundary resistance. The impact of frequency affecting thermal conductivity extraction was also examined.

By expressing the general solution of the temperature oscillation for a multilayer stack, the expression for the temperature oscillation on a single film-on-substrate system with thermal boundary resistance was deduced based on the concept of an apparent film thermal conductivity K_{1D}. In the situation of low thermal conductivity films, the thermal boundary resistance measured from routine procedures must be modified by a correction factor. For arbitrary values of film-to-substrate thermal conductivity ratios, the expression for the temperature oscillation was simplified so that the impact of governing parameters on the apparent thermal conductivity could be examined. The film effective resistance K_{1D} was found to be quadratic with the film-to-substrate thermal conductivity ratio depending on the film thickness-to-heater width aspect ratio and the interfacial resistance. The film effective resistance K_{1D} will take positive, infinite, or negative values depending on the film-to-substrate thermal conductivity ratio. It is worth noting that a change of sign in the effective film thermal conductivity as defined in Chapter 3 is peculiar to multi-dimensional time-independent heat conduction problems in contrast with one-dimensional static cases.

At film-to-substrate thermal conductivity ratios higher than unity such as GaN/Sapphire, the 3ω differential technique was found weakly sensitive on geometrical parameters such as film thickness and heater width, which would make experiments difficult to implement. The situation worsened dramatically when a thermally insulating buffer layer was introduced between film and substrate. Therefore in the regime of film-to-substrate thermal conductivity higher than unity, thermal parameter extraction is error prone compared to measurements on films where the thermal conductivity is much lower than the substrate thermal conductivity.

6.1.2 Thermal Conductivity of Gallium Nitride.

The thermal conductivity of undoped and iron doped hydride vapor phase epitaxy grown gallium nitride samples was measured from 300K to 450K using the 3ω slope method. The highest thermal conductivity value was measured at room temperature at 230 $W \cdot K^{-1} \cdot m^{-1}$ on a 2mm thick iron doped specimen. A resistivity of

$2 \cdot 10^8$ Ω·cm was measured of the same iron doped sample by hall measurements confirming the semi-insulating properties of this sample. Thermal conductivity values were measured following a routine procedure in the 3ω slope method except for two experimental data points at room temperature. In that particular case, the thermal conductivity was accurately deduced from a two-layer model to account for finite thickness effects in a finite element simulation approach. Overall, the thermal conductivity was monotonically increasing with gallium nitride thickness. It was established that thermal conductivity dependent on the logarithmic of the thickness was fully compatible with experimental results and were consistent with the case of extracted thermal conductivity assumed constant with layer thickness.

Material properties were characterized using a variety of techniques including secondary ion mass spectroscopy, cathodoluminescence, atomic force microscopy, Nomarski images, photospectrometry, four-point probes, hall measurements (conducted by William C. Mitchel from AFRL/MLPS laboratories), and Electron Paramagnetic Resonance (EPR) (conducted by M.E. Zvanut from the University of Alabama at Birmingham). The undoped material presented concentration of impurities typical of undoped gallium nitride reported in the literature. Dislocation density was found to be accurately given from cathodoluminescence imaging while etch pit count was found to underestimate the dislocation density. The reduction in dislocation density was found to follow the model developed by previous authors down to 10^6 cm^{-2}. On a 2mm thick iron doped sample, the average dislocation density was observed as low $5 \cdot 10^{-4}$ cm^{-2} over several millimeter areas. Therefore the reduction in dislocation density with film thickness can be more efficient than accepted theoretical model would predict. From this standpoint, this work illustrates that hydride vapor phase epitaxy represents a genuine attractive and promising technique for the commercialization of gallium nitride substrate.

By plotting the thermal conductivity against the dislocation density, the thermal conductivity was found to be strongly dependent on the logarithmic of the dislocation density for densities as low as a $5 \cdot 10^{-6}$ cm^{-2}. Below, the thermal conductivity saturated with dislocation density. By comparing with previous experimental work, the thermal conductivity dependence on dislocation density was

confirmed. Previous theoretical work based on a time approximation approach showed good qualitative agreements. By correcting for flaws in the theory of the relaxation time theory, fair quantitative agreement between theoretical expectation and measurements was found.

Finally temperature dependent measurements beyond room temperature indicated that the thermal conductivity decreased inversely proportional to $T^{-1.43}$ similar to the thermal conductivity temperature dependence of gallium phosphide or silicon carbide.

6.1.3 The Thermal Resistance of HFETs.

An expression for the thermal resistance of multifinger field effect transistor was analytically derived. The latter model was employed in a comparative study between the thermal performance of AlGaN/GaN SiC multifinger HEMT and the thermal performance of homoepitaxially grown AlGaN/GaN multifinger HEMT.

First a three-dimensional analytical model was developed to capture the governing parameters underlying thermal design of AlGaN/GaN HEMT devices. The present model was borrowed from state-of-the art developments in thermal engineering. Upon further refinements, this model was brought to the field of device thermal modeling. The model analytically accounted for the effect of buffer layers on thermal resistance. This is an important feature as gallium nitride is grown on non native substrates with buffer layers. The impact of gate length, substrate thickness, gate pitch, gate width, film thickness, buffer layer and film thermal conductivities on thermal performance can be examined separately in these models. The complete mathematical development is addressed in Appendix A and Chapter 3. The model is accurate within a few percents from simulation for heat source to substrate thickness ratios superior to 10.

Thanks to the characterization of the gallium nitride thermal conductivity presented in Chapter 4, it was possible to compare the thermal performance of AlGaN/GaN HEMT grown on SiC with the performance of AlGaN/GaN HEMT grown on gallium nitride. Establishing the dependence of thermal conductivity with film thickness and dislocation densities represented factors essential to the success of

the study. It was determined that single finger AlGaN/GaN/GaN HEMTs are thermally more advantageous than AlGaN/GaN/SiC HEMT. A significant part in discrepancy is accounted for by the film-to-substrate thermal conductivity ratio less than unity and nearly 0.3. It would take a thermal conductivity of 420 $W \cdot K^{-1} \cdot m^{-1}$ for silicon carbide to give a thermal advantage to single finger AlGaN/GaN/SiC HEMT over AlGaN/GaN/GaN HEMT with the parameters used in Chapter 5. Nonetheless, multifinger HEMTs formed on SiC substrates presented higher thermal performance than multifinger HEMT formed on GaN substrates. This was because the thermal resistance was strongly dependent on heat spreading in the substrate as the number of fingers increase. For instance, the thermal resistance of AlGaN/GaN/SiC HEMT became lower than that of AlGaN/GaN/GaN HEMTs for a two finger device with a gate-to-gate spacing lower than 68um assuming the same device parameters as in Chapter 5. However, at short gate length and thin substrate, the thermal resistance of GaN/GaN HEMTs was expected to improve and even catch up with the thermal resistance of AlGaN/GaN HEMT grown on thin SiC substrates. Finally the presence of buffer layer between the gallium nitride layer and the silicon carbide substrate can cause substantial increase in thermal resistance. Therefore reduction of the thermal resistance of the GaN layer on silicon carbide by growing high quality GaN with lateral epitaxial overgrowth or pendeo-epitaxy techniques would be a challenging task as the overall device thermal resistance decrease even further due to the presence of thermally insulating buffer layers such as SiO_2 or voids.

6.2 Future Directions

While this work has addressed some of the issues related to the thermal characterization and modeling of gallium nitride material and device, there is still a number of topics to be examined.

Though this work has established the strong dependence of the gallium nitride thermal conductivity on dislocation density, it is expected that point defects would impact the thermal conductivity of gallium nitride. The precise effect of oxygen, silicon, carbon, hydrogen, iron and gallium vacancies remains unclear. Furthermore, characterization of the thermal conductivity temperature dependence

in temperature range above 600K would complete the thermal property characterization of gallium nitride.

This work has revealed the importance to clarify the relationship between thickness and dislocation density for hydride vapor phase epitaxy grown gallium nitride having dislocation densities well below 10^{-6} cm^{-2}. Further studies would be necessary to narrow the origin of mechanisms underlying the effective reduction in dislocation density.

Theoretical predictions in the thermal properties of AlGaN/GaN HEMT grown on gallium nitride substrate would need to be experimentally compared with thermal performance of AlGaN/GaN HEMT formed on semi-insulating gallium nitride substrate.

Appendix A

3-Dimensional Solution of the Thermal Diffusion Equation for Periodic and Time-Independent Adjacent Strip Heat Sources Deposited on a Stratified Medium

A.1 Presentation

The purpose of this appendix is to calculate the temperature field T(X,y=0) at any location on the top surface of the multilayer system. The solution is sought for both time-independent and sinusoidal time varying heat sources. The ultimate goal is to express the average temperature ΔT_{q0} taken over the heater width of an arbitrary heater labeled q_0. The solution will be applied to the simplified situation of equally spaced heaters of identical width delivering identical power per unit length.

Consider a number of p infinitely long metal heater strips deposited parallel to one another on a n-layer system as shown in Figure A.1 below.

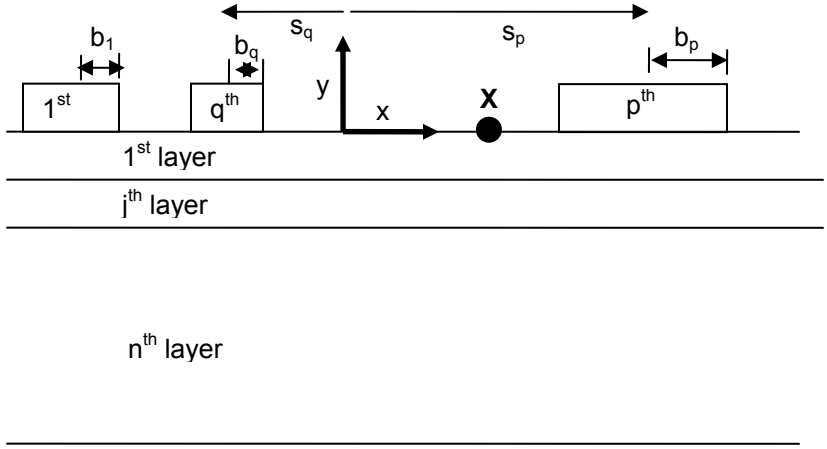

Figure A.1. Schematic of parallel wires deposited on a multilayer stack.

Given the linearity of the problem described in detail below, the solution is known beforehand via the principle of superposition applied to the case of a single heater. However, the superposition of the temperature T(X,0) deduced from a single heater can be applied to the multi-heater situation provided the distance between the point X and the heat source is conserved during superposition and provided each heater keeps a different width and heating power. In this appendix, full treatment of

the thermal diffusion equation will be presented. The principle of superposition can be applied to check the validity of the results. The next paragraph provides further details on the situation depicted in Figure A.1.

As introduced earlier, p is the total number of heaters. The subscript q corresponds to the q^{th} heater starting from the left. The q^{th} strip source with half-width b_q is laterally centered at a distance s_q from the origin of the horizontal axis and delivers a power per unit length P_{lq} in the underlying stratified medium. Each metal strip heater is infinitely thin. The subscript j corresponds to the j^{th} layer starting from the top. The j^{th} layer has a cross plane thermal conductivity k_{yj}, an in-plane thermal conductivity k_{xj}, a cross-plane diffusivity α_{yj}, and a thickness d_j. In other words, each layer is homogeneous. Besides, in each layer one of the principal axes of the thermal conductivity tensor is perpendicular to the film plane with zero off-diagonal. The thermal boundary resistance between the j^{th} layer and $j\text{-}1^{th}$ layer is noted $R_{j-1,j} \geq 0$. The n^{th} layer is better referred to as the substrate. Each heat source varies sinusoidally with time and delivers heat uniformly at the same angular frequency ω over the heater width:

$$Q_q = \frac{P_{lq}}{2b_q}\mathrm{Re}\left\{e^{i\omega t}\right\} \quad \omega \geq 0 \tag{A.1}$$

At ω=0, each metal heater will deliver a heat flux independent with time. In these conditions, the thermal diffusion equation becomes:

$$k_{xyj}\frac{\partial^2 T}{\partial x^2} + \frac{\partial^2 T}{\partial y^2} - \frac{i2\omega}{\alpha_{yj}}T = 0 \quad with\ k_{xyj} = \sqrt{\frac{k_{xj}}{k_{yj}}} \tag{A.2}$$

Assuming that the top surface of the stratified system is adiabatic between heaters, the boundary condition at the top of the first layer in the horizontal plane bears on the heat flux Q_p delivered by p heaters:

$$Q_p = k_{y1}\left|\frac{\partial T}{\partial y}\right|_{y=0} = \sum_{q=1}^{p}\frac{P_{lq}}{2b_q}RECT_q\left(x - s_q\right) \tag{A.3}$$

The function $RECT_q(x)$ is unity for $|x|<b_q$ and zero otherwise. If the substrate is semi-infinite, the temperature is imposed to vanish at an infinite distance from heat sources. If the substrate is finite, the boundary condition at the bottom surface can

be isothermal or adiabatic. The time-independent solution corresponds to an angular frequency ω strictly zero provided an isothermal boundary condition is set at the bottom surface of the substrate.

A.2 Resolution in the Two-Dimensional Case

Amongst possible methods of resolution, the Green function, the Fourier transform or the separation of variable can be conveniently adopted. The method of separation of variable (in the spectral domain) has the advantage to indicate the adequate basis in the Hilbert space forming a solution of the aforementioned problem. However the Cartesian symmetry here is clear and the Fourier transform is preferentially adopted over the separation of variable.

$$\widetilde{T} = F[T] = \frac{1}{\sqrt{2\pi}} \int_{-\infty}^{+\infty} T e^{itx} dx \tag{A.4}$$

The heat equation becomes one-dimensional in the Fourier space:

$$\frac{\partial^2 \widetilde{T}}{\partial y^2} - \left(k_{xyj}\, t^2 + \frac{i2\omega}{\alpha_{yj}} \right) \widetilde{T} = 0 \tag{A.5}$$

The Fourier transform of the boundary condition at the top surface of the multilayer system is deduced from basic Fourier transform properties:

$$\widetilde{Q}_p = k_{y1} \left| \frac{\partial \widetilde{T}}{\partial y} \right|_{y=0} = \frac{1}{\sqrt{2\pi}} \sum_{q=1}^{p} P_{lq} e^{its_q} \frac{\sin\left(tb_q\right)}{tb_q} \tag{A.6}$$

Fourier transforms of boundary condition at the bottom surface of the substrate are trivial. The solution for the on-dimensional Equation (A.5) is sought at y=0. For a stratified medium, the solution to Equation (A.5) can be elegantly expressed in a recursive relationship following the one-dimensional algorithm in Ref. 1. Intermediate steps of calculation can be found in Ref. 2 and Ref. 3

$$\widetilde{T}(y=0)=\frac{\widetilde{Q}_p}{k_{y1}/b_q}\frac{M_{q,1}}{N_{q,1}}$$

with

$$\begin{cases} M_{q,j-1}=\dfrac{M_{q,j}+N_{q,j}\rho_{q,j}+\dfrac{k_{yj}N_{q,j}}{k_{yj-1}N_{q,j-1}}\tanh\left(\varphi_{q,j-1}\right)}{\dfrac{k_{yj}N_{q,j}}{k_{yj-1}N_{q,j-1}}+\left(M_{q,j}+N_{q,j}\rho_{q,j}\right)\tanh\left(\varphi_{q,j-1}\right)}, \quad j=2..n \\ N_{q,j}=\left(k_{xyj}\left(b_q t\right)^2+i\frac{2\omega}{\alpha_{yj}}b_q^2\right)^{1/2},\ \varphi_{q,j}=N_{q,j}\frac{d_j}{b_q},\ k_{xyj}=k_{xj}/k_{yj} \\ \text{with}\ \rho_{q,j}=\dfrac{R_{j-1\,j}}{b_q/k_{yj}} \\ M_{q,n}=\tanh^{\nu}\left(\varphi_{q,n}\right) \quad \nu=\begin{vmatrix} 1 & \text{Isothermal backside or } \omega=0 \\ 0 & \text{Semi - infinite backside} \\ -1 & \text{Adiabatic backside} \end{vmatrix} \end{cases} \tag{A.7}$$

The temperature T(x,y=0) in the top plane between heaters and the stratified medium is easily deduced from the inverse Fourier transform.

$$T(x,y=0)=F^{-1}\left[\widetilde{T}\right]=\frac{1}{\sqrt{2\pi}}\int_{-\infty}^{+\infty}\widetilde{T}e^{-itx}dt \tag{A.8}$$

Noting the inversion symmetry of this particular Fourier transform t→(-)t, it comes:

$$T(x,y=0)=\frac{1}{\pi k_{y1}}\sum_{q=1}^{p}P_{lq}\int_0^{\infty}\frac{M_{q,1}}{N_{q,1}}\frac{\sin u}{u}\cos\left[\frac{s_q-x}{b_q}u\right]du \tag{A.9}$$

The change of variable $tb_q \rightarrow u$ has taken place between Equation (A.8) and Equation (A.9). As expected, the temperature field is real at ω=0 and the dependency of the temperature on the position x is independent of the angular frequency ω≥0. Thus the average temperature at the interface between a given heater, say q_0, and the underlying medium can be carried out by averaging over the

corresponding heater width $2b_{q0}$. The heater q_0 is distant from the origin with a spacing s_{q0} as depicted in Figure A.2.

$$\Delta T_{q0} = \frac{1}{\sqrt{2\pi}} \frac{1}{2b_{q0}} \int_{-\infty}^{+\infty} \tilde{T} \int_{-b_{q0}+s_{q0}}^{b_{q0}+s_{q0}} e^{itx} dx dt \qquad \text{(A.10)}$$

In these conditions, it comes:

$$\Delta T_{q0} = \frac{1}{\pi k_{y1}} \sum_{q=1}^{p} P_{lq} \int_{0}^{\infty} \frac{M_{q,1}}{N_{q,1}} \frac{\sin tb_q}{tb_q} \frac{\sin(tb_{q0})}{tb_{q0}} \cos\left[(s_q - s_{q0})t\right] b_q dt \qquad \text{(A.11)}$$

ΔT_{q0} represents the temperature oscillation amplitude at the $q0^{th}$ heater due to the presence of a number p of sinusoidally periodic heat sources. In case of a time independent heat source $\omega=0$, ΔT_{q0} represents a time-independent temperature rise. Considering a single wire p=1 and $s_q=s_{q0}=0$, Equation (A.11) is the expression for the temperature oscillation of a single wire given in Chapters 2 and 3.

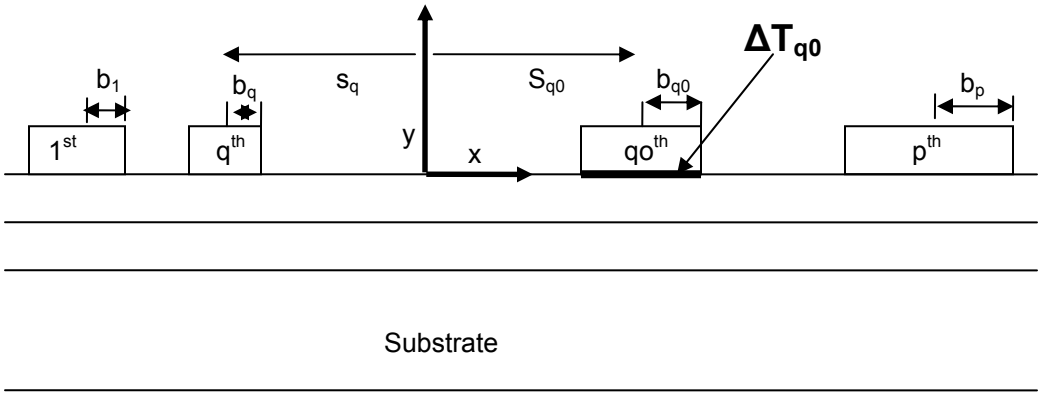

Figure A.2. ΔT_{q0} is the average temperature at the $q0^{th}$ heater caused by the presence of all heat sources including the $q0^{th}$ source itself.

A.3 Identical Strip Sources

In the case of equally spaced heat sources with spacing s and with identical width 2b and identical power per unit length P_l, the expression for the average temperature ΔT taken at the $q0^{th}$ heat source simplifies:

$$\Delta T_{q0} = \frac{P_l}{\pi k_{y1}} \int_0^{\infty} \frac{M_1}{N_1} \frac{\sin^2 u}{u^2} \left[\sum_{q=1}^{p} \cos\left((q - q_0) \frac{s}{b} u \right) \right] du \qquad \text{(A.12)}$$

The change of variable tb→u has taken place between Equation (A.11) and Equation (A.12). If s=0 for all p sources, the solution describes the temperature rise corresponding to a single strip but with a p-fold increase in power per unit length. For an odd number p=2q0-1 of equally spaced strip sources centered about the heater strip q0, the temperature oscillation of the q0th strip source is:

$$\Delta T_{q0} = \frac{P_l}{\pi k_{y1}} \int_0^{\infty} \frac{M_1}{N_1} \frac{\sin^2 u}{u^2} \left[\sum_{q=0}^{\frac{p-1}{2}} 2 \cos\left(q \frac{s}{b} u \right) \right] du \qquad \text{(A.13)}$$

Figure A.3 illustrates the situation corresponding to Equation (A.13) in the particular case of p=3 strips.

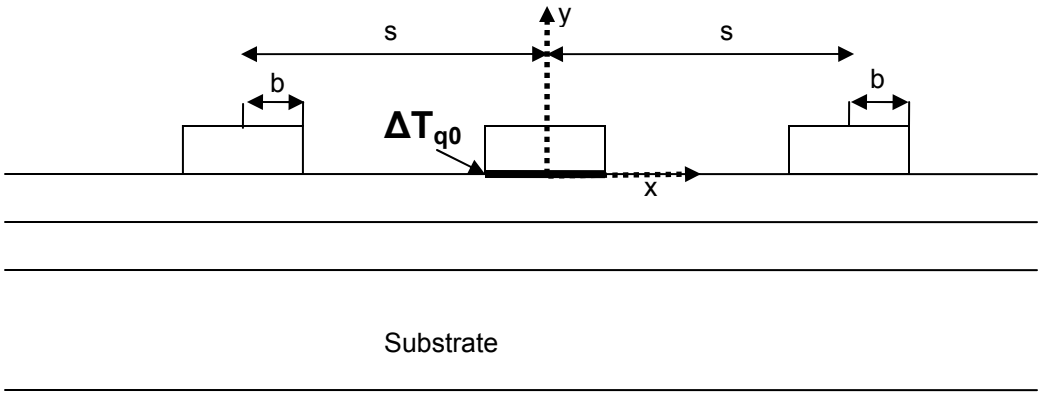

Figure A.3. Schematic cross-section for an odd number of identical strip sources on a multilayer stack. The average temperature ΔT_{q0} is taken for the middle heater. In this particular case, p=3 and q0=2.

In the case of time independent identical strip heaters deposited on a bare anisotropic substrate, one can define the substrate to heater half-width ratio: $\beta_S = (k_{Sxy})^{1/2} d_S/b$ (k_{Sxy} is the substrate anisotropy factor). Further simplifications can be carried out for β_S>3 and s/b ratios smaller than β_S but higher than 1.

$$\int_0^{\infty} \frac{\tanh(\beta_S u)}{u} \frac{\sin^2 u}{u^2} du \underset{\beta_S \to \infty}{=} \ln(\beta_S) + 1.0484\ldots \qquad (a)$$
$$\int_0^{\infty} \frac{\tanh(\beta_S u)}{u} \frac{\sin^2 u}{u^2} \cos\left(\frac{s_q}{b} u\right) du \underset{\beta_S \to \infty}{=} \ln(\beta_S) - \ln\left(\frac{\pi}{4} \frac{s_q}{b}\right) \qquad (b) \qquad \text{(A.14)}$$

A justification can be given now. Let first consider the first expression (A.14a). Equation (A.14a) can be integrated in three blocks: from zero to $1/\beta_s$, then from $1/\beta_s$ to one and finally from one to infinity: $\int_0^{1/\beta_S} f(u)du + \int_{1/\beta_S}^{1} f(u)du + \int_1^{\infty} f(u)du$ where f(u) is the integrand in Equation (A.14a). The first integral $\int_0^{1/\beta_S} f(u)du$ gives $\int_0^1 \frac{\tanh(u)}{u} du = 0.90967$ after a change of variable and in the limit of infinite β_S because $\sin^2 u/u^2$ becomes strictly unity. The last integral $\int_1^{\infty} f(u)du$ becomes $\int_1^{\infty} \frac{\sin^2 u}{u^3} du = 0.3857$ because now $\tanh(\beta_S u)$ can be set strictly unity in the limit of infinite β_S. The determination of $\int_{1/\beta_S}^{1} f(u)du$ is a little more delicate. First the terms $\tanh(\beta_S u)$ and $\sin^2 u/u^2$ are both almost unity so that the integrand f(u) is almost du/u. More precisely $\int_{1/\beta_S}^{1} f(u)du = \int_{1/\beta_S}^{1} \frac{du}{u}$ + $\int_{1/\beta_S}^{1} \frac{\tanh(\beta_S u)\sin^2 u - u^2}{u^3} du$ and in the limit of infinite β_S, $\int_{1/\beta_S}^{1} \frac{\tanh(\beta_S u)\sin^2 u - u^2}{u^3} du$ = -0.24696. Hence The expression (A.14a) is easily inferred. The simplification in Equation (A.14a) is less than 1% error for β_S>3 and describe a situation corresponding to a strip source on a thick substrate. For thin substrates corresponding to small β_S, it is easy to show that the left part of Equation (A.14a) reduces to $\beta_S \frac{\pi}{2}$ with less than 1% error if β_S<0.04. This is in agreement with one-dimensional Fourier's law as expected for a single wire on a very thin substrate with isothermal bottom boundary condition. It is straightforward to check that the temperature rise is $\Delta T = d_S/k_{Sy} * (P/2bl)$.

The determination of Equation (A.14b) follows the same approach. First it is assumed that $\beta_S >> \lambda = s_q/b >> 1$. The integral is decomposed into $\int_0^{1/\beta_S} g(u)du + \int_{1/\beta_S}^{1/\lambda} g(u)du + \int_{1/\lambda}^{1} g(u)du + \int_{1}^{\infty} g(u)du$ where g(u) is the integrand in Equation (A.14b). Similarly to the previous case, $\int_0^{1/\beta_S} g(u)du$ gives $\int_0^1 \frac{\tanh(u)}{u}du = 0.90967$. From the variable change $\lambda x = u$, $\int_{1/\beta_S}^{1/\lambda} g(u)du = \int_{\lambda/\beta_S}^{1} \frac{dx}{x} + \int_{1/\alpha}^{1} \frac{\tanh(\alpha x)\cos(x)-1}{x}dx$ as the term $\sin^2 u/u^2$ becomes 1 as λ goes to infinity. In the last expression, $\alpha = \beta_S/\lambda$ goes to infinity. When α is infinite, $\int_{1/\alpha}^{1} \frac{\tanh(\alpha x)\cos(x)-1}{x}dx$ =-0.3307 so that $\int_{1/\beta_S}^{1/\lambda} g(u)du = \ln\left(\frac{\beta_S}{\lambda}\right) - 0.3307$. For the same reasons as previously explained and via adequate variable change, the third integration $\int_{1/\lambda}^{1} g(u)du = \int_{1}^{\infty} \frac{\cos(u)}{u}du$ =-0.3374 when λ is infinity. It does not take too much effort to demonstrate that the last integration $\int_{\lambda}^{\infty} g(u)du$ goes to zero as λ goes to infinity. By noting that $\ln(4/\pi) = 0.24156$, Equation (A.14b) is easily derived and is plotted in Figure A.4 below.

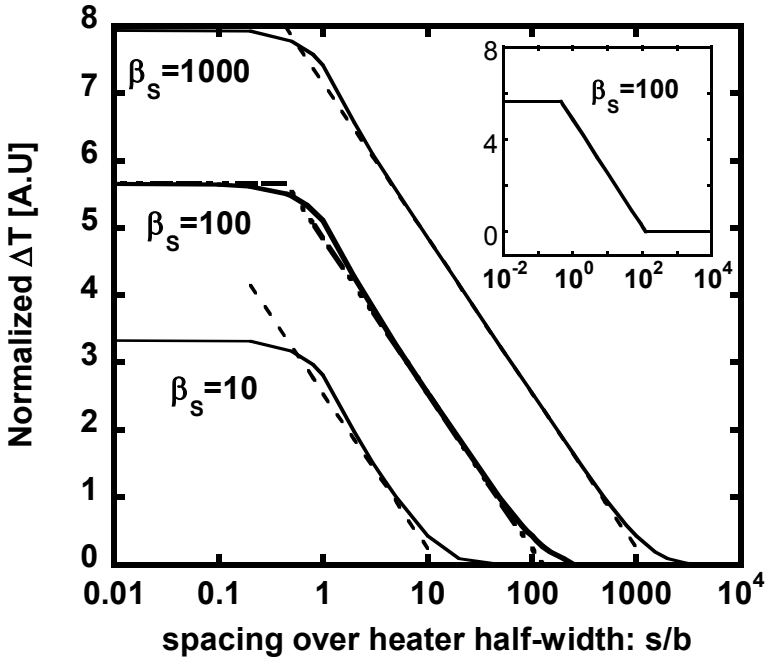

Figure A.4. Equation (A.14b) is plotted versus s/b for different β_S ratios. The solid line represents the left part of Equation (A.14b) while the dotted lines plot the approximated expression on the right hand part of (A.14b). The inset shows that the average temperature rise at a heater q_0 (induced by another heater q distant s from the heater q_0) can be approximated by simple expressions for three different ranges of s/b ratios.

Equation (A.14b) is within less than1% error if $3<s/b<0.3\ \beta_S$ with $\beta_S>25$. If Equation (A.14b) is to be within less than 5 % error, then the condition becomes: $1<s/b<\beta_S/2$ with $\beta_S\geq 10$. For a spacing-to-substrate thickness ratio higher than unity ($s/d_S>1$), thermal coupling becomes negligible and the temperature rise decreases exponentially with the s/b ratio. While for s/b <1, ie for overlapping heat sources, the temperature rise varies linearly with the s/b ratio.

The temperature T(x=0, y=0) at the center of the heater q_0 can be deduced from the expression of ΔT by substituting $\frac{\sin^2 u}{u^2} \rightarrow \frac{\sin u}{u}$ in Equation (A.14). The constant 1.0484 must be substituted by 1.24156 in Equation (A.14a).

Considering an even number 2r of heaters with r≥1 deposited on an anisotropic substrate, It is easy to show from Equation (A.14) that the temperature rise of the center heater q_0=r or q_0=r+1 is:

$$\Delta T_{q0} = \frac{P_l}{\pi\sqrt{k_{Sx}k_{Sy}}}\left[\ln\left(\frac{4^{2r-1}\left(\sqrt{k_{Sxy}}\right)^{2r} d_F^{2r}}{\pi^{2r-1} r!\, r-1!\, s^{2r-1} b}\right)+1.048\right] \quad \text{(A.15)}$$

For an odd number of heaters 2r+1 r≥1, the temperature rise of the center heater q_0=r+1 is given as:

$$\Delta T_{q0} = \frac{P_l}{\pi\sqrt{k_{Sx}k_{Sy}}}\left[\ln\left(\frac{4^{2r}\left(\sqrt{k_{Sxy}}\right)^{2r+1} d_F^{2r+1}}{\pi^{2r} r^2!\, s^{2r} b}\right)+1.048\right] \quad \text{(A.16)}$$

These formulas are valid within the framework of conditions discussed previously.

A.4 3-Dimensional Resolution

The solution follows the same methodology as in the two-dimensional case, the Fourier transform is taken over the rectangular heat source shown in Figure A.5. It is assumed for simplicity that all heaters are centered at z=0.

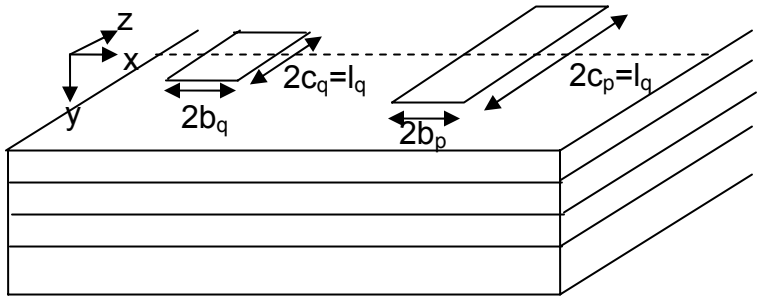

Figure A.5. Three dimensional Rectangular heat source.

The problem is quickly restated. The heat flux is uniformly generated over each rectangle area with a power P_q typically expressed in Watt:

$$Q_q = \frac{P_q}{2b_q 2c_q}\mathrm{Re}\left\{e^{i\omega t}\right\} \quad \omega \geq 0 \quad \text{(A.17)}$$

At ω=0, each metal heater will deliver a heat flux independent with time. In these conditions, the thermal diffusion equation becomes:

$$k_{xyj}\frac{\partial^2 T}{\partial x^2}+k_{xyj}\frac{\partial^2 T}{\partial z^2}+\frac{\partial^2 T}{\partial y^2}-\frac{i2\omega}{\alpha_{yj}}T=0 \quad with\ k_{xyj}=\sqrt{\frac{k_{xj}}{k_{yj}}},\ k_{xyj}=\sqrt{\frac{k_{zj}}{k_{yj}}} \tag{A.18}$$

Assuming that the top surface of the stratified system is adiabatic between heaters, the boundary condition at the top of the first layer in the horizontal plane bears on the heat flux Q_p delivered by p heaters:

$$Q_p=k_{y1}\left|\frac{\partial T}{\partial y}\right|_{y=0}=\sum_{q=1}^{p}\frac{P_q}{2b_q 2c_q}RECT_q\left(x-s_{xq},z\right) \tag{A.19}$$

The function $RECT_q(x,z)$ is unity for $|x|<b_q$ and $|z|<c$, zero otherwise. The two-dimensional Fourier transform is:

$$\widetilde{T}=F\left[T\right]=\frac{1}{2\pi}\int_{-\infty-\infty}^{+\infty+\infty}Te^{it_x x}e^{it_z z}dxdz \tag{A.20}$$

The heat equation becomes one-dimensional in the Fourier space:

$$\frac{\partial^2\widetilde{T}}{\partial y^2}-\left(k_{xyj}\,t_x{}^2+k_{xzj}\,t_z{}^2+\frac{i2\omega}{\alpha_{yj}}\right)\widetilde{T}=0 \tag{A.21}$$

The Fourier transform of the boundary condition at the top surface of the multilayer system is deduced from basic Fourier transform properties:

$$\widetilde{Q}_p=k_{y1}\left|\frac{\partial\widetilde{T}}{\partial y}\right|_{y=0}=\frac{1}{2\pi}\sum_{q=1}^{p}P_q e^{its_q}\,\frac{\sin\left(t_x b_q\right)}{t_x b_q}\frac{\sin\left(t_z c_q\right)}{t_z c_q} \tag{A.22}$$

Noticing the symmetrical role played by the heater width and heater length, the geometric means of the heater width and length is defined as $a_q=(b_q c_q)^{1/2}$. Thus the solution of the aforementioned problem is easily expressed.

$$T\left(x,z,y=0\right)=\frac{1}{\pi^2 k_{y1}}\sum_{q=1}^{p}\frac{P_q}{a_q}\int_0^\infty\int_0^\infty\frac{M_{q,1}}{N_{q,1}}\frac{\sin u_x}{u_x}\frac{\sin u_z}{u_z}\cos\left[\frac{s_{xq}-x}{b_q}u_x\right]\cos\left[\frac{z}{c_q}u_z\right]du_x du_z \tag{A.23}$$

The change of variable $b_q t_x = u_x$ and $t_y = u_y / c_q$ has occurred. Finally in Equation (3.1) the following substitutions must take place $N_{q,j} = \left(k_{xyj} \left(\frac{a_q}{b_q} u_x \right)^2 + k_{zyj} \left(\frac{a_q}{c_q} u_z \right)^2 + i \frac{2\omega}{\alpha_{yj}} a_q^{\,2} \right)^{1/2}$ while b_q must be substituted by a_q in the other terms of Equation (3.1). In the case of a very long rectangular heat source compared to its width $c_q >> b_q$, Equation (A.23) reduces to (A.9) because $\int_0^\infty \frac{\sin u_z}{u_z} du_z = \frac{\pi}{2}$ and $P_{lq} = P_q / 2b_q$.

It has been assumed in this section that the sources were centered at z=0. It does not take much effort to generalize to the case of (p,m) heat sources on the y=0 plane. By applying the translation transform $z \rightarrow z - s_{zk}$, where $1 \le k \le m$ and by adding an additional sigma symbol and appropriate notation, the solution is easily deduced. For heat source with arbitrary geometry, the Fourier transform of the source geometry can be taken directly or the source can be decomposed into small rectangles. In the special case of heat source with circular symmetry, the Hankel transform is used instead of the Fourier transform. In addition, Equation (3.1) can be generalized in the case of a heat source buried into a multilayer stack[1]. If layers are finite size in the direction parallel to the substrate with for instance adiabatic boundary on the side, the solution can be typically expressed as a Fourier series[1].

In our situation, we are interested in simple formulations. For instance a particular case concerns the temperature average taken at a heater q_0 induced by identical parallel heaters with a length is much greater than the width. In that case, it may be more convenient to express M_1/N_1 as a function of b or b/c only.

$$\Delta T_{q0} = \frac{P/2c}{\pi k_{y1}} \int_0^\infty \frac{2}{\pi} \int_0^\infty \frac{M_1}{N_1} \times \frac{\sin^2 u_x}{u_x^2} \frac{\sin^2 u_z}{u_z^2} \sum_{q=1}^{p} \cos\left[\frac{\left(s_q - s_{q0} \right)}{b} u_x \right] du_x du_z \qquad \text{(A.24)}$$

With $N_{q,j}=\left(k_{xyj}u_x{}^2+k_{zyj}\left(\frac{b}{c}u_z\right)^2+i\frac{2\omega}{\alpha_{yj}}b^2\right)^{1/2}$ and M_1 an explicit function of b and $N_{q,j}$ only.

In time-independent steady state for a single wire on a anisotropic bare substrate with isothermal boundary condition on the back side, the temperature field on the y=0 plane is given by the simplified formula:

$$T(x,z,y=0)=\frac{P/2c}{\pi\sqrt{k_{Sx}k_{Sy}}}\int_0^\infty\frac{2}{\pi}\int_0^\infty\frac{\tanh\left(\sqrt{\beta_{Sx}^2u_x{}^2+\beta_{Sz}^2u_z{}^2}\right)}{\sqrt{u_x{}^2+k_{Szx}\left(\frac{b}{c}u_z\right)^2}}\times \frac{\sin u_x}{u_x}\frac{\sin u_z}{u_z}\sum_{q=1}^{p}\cos\left[\frac{(s_q-x)}{b}u_x\right]\cos\left[\frac{z}{c}u_z\right]du_xdu_z \qquad \text{(A.25)}$$

$K_{Szx}=K_{Sz}/K_{Sx}$ and $\beta_{Sx}=d_S/b(K_{Sx}/K_{Sy})^{1/2}$ and $\beta_{Sz}=d_S/c(K_{Sz}/K_{Sy})^{1/2}$. In the case of a very long rectangular heat source compared to its width c>>b and compared to the substrate thickness ($c>>d_S$), Equation (A.24) reduces to equation (A.12).

Equation (A.25) averaged over the heater width 2b must retrieve Equation (A.14a) in the limit c goes to infinity. Equation (A.25) averaged over 2b at y=0 is plotted in Figure A.6 against β_{Sz} after normalization with $\frac{P/2c}{\pi\sqrt{k_{Sx}k_{Sy}}}$.

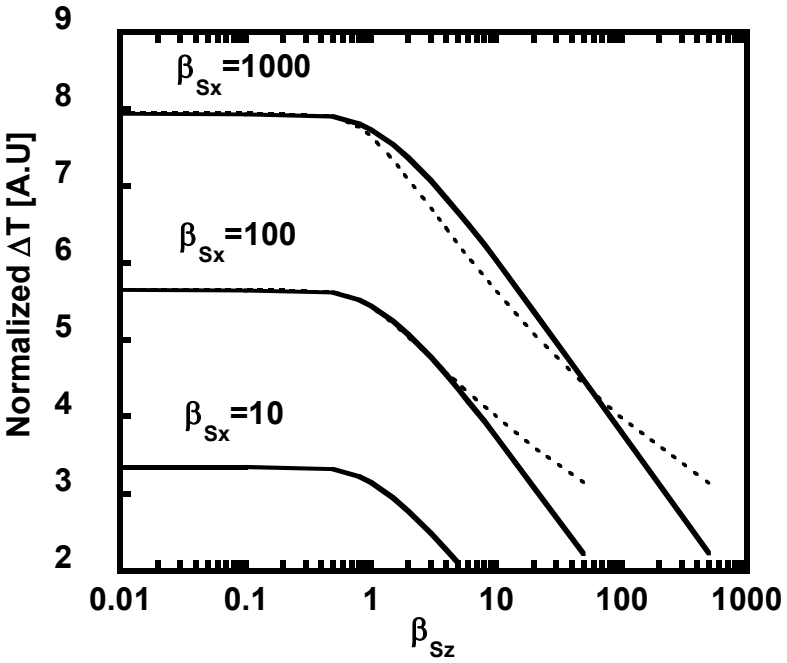

Figure A.6. Normalized average temperature versus substrate thickness to heater half-length. In solid line is the analytical expression. The dashed line represented an approximated solution near $\beta_{Sz} = 1$.

The solid line in Figure A.6 can be approximated within less than 7% error by the following expression for $\beta_{Sz}<10$ and $100<\beta_{Sx}<1000$.

ΔT_{2D} is the average channel temperature rise calculated in a two-dimensional model.

$$\Delta T = \Delta T_{2D} \tanh^{0.15}\left(1/\beta_{Sz}\right) \tag{A.26}$$

A.5 References

1 A. Feldman, "Algorithm for solutions of the thermal diffusion equation in a stratified medium with a modulated heating source," *High Temperatures-High Pressures*, vol. 31, pp. 293-298, 1999.

2 T. Borca-Tasciuc, A. R. Kumar, and G. Chen, "Data reduction in 3 omega method for thin-film thermal conductivity determination," *Review of Scientific Instruments*, vol. 72, pp. 2139-2147, 2001.

3 J. H. Kim, A. Feldman, and D. Novotny, "Application of the three omega thermal conductivity measurement method to a film on a substrate of finite thickness," *Journal of Applied Physics*, vol. 86, pp. 3959-3963, 1999.

Appendix B Solution for Temperature Dependent Thermal Conductivity

B.1 Presentation

The solution of the non-linear heat equation due to temperature dependent thermal conductivity k(T) can be solved using the Kirchhoff's transformation[1]. From the homogoneous non-linear heat equation,

$$\nabla \bullet k\nabla T = 0 \tag{B.1}$$

one can define an apparent temperature

$$k(T_0)\nabla^2\theta = 0 \tag{B.2}$$

where θ relates to the thermal conductivity as:

$$\theta = T_0 + \frac{1}{k(T_0)} + \int_{T_0}^{T} k(T)dT \tag{B.3}$$

Θ and T have the same heat flux and temperature boundary condition. Therefore given θ known, all is necessary to know is the solution of the heat equation at constant temperature. Typically $\Theta = P \cdot R(T_0)$ where P is the dissipated power and R_0 is the thermal resistance at constant temperature, usually the ambient temperature (300K). We may now proceed to the determination of θ

For semiconductor at or beyond 300K, it is fair to assume a relation of the type:

$$k(T) = k(T_0)\left(\frac{T}{T_0}\right)^{-\lambda}, \lambda \; real \tag{B.4}$$

Typically λ=1 to 1.5 for semiconductor material. Given the previous derivations, θ can be expressed as a function of T.

$$T = T_0\left[(1-\lambda)\frac{(\theta - T_0)}{T_0} + 1\right]^{\frac{1}{1-\lambda}}, \quad \lambda \neq 1$$
$$T = T_0 \exp\left(\frac{(\theta - T_0)}{T_0}\right), \quad \lambda = 1 \qquad \text{(B.5)}$$

Typically in semiconductor devices operated at room temperature, it is fair to assume in most cases that the temperature Θ-T_0=P.R(T_0) is lower than T_0, ie the temperature rise must be lower than 600K if the reference temperature is 300K. In that case, Equation (B.5) leads to a non-linear quadratic dependence of the temperature on the dissipated power:

$$T = T_0 + PR + P^2\frac{\lambda R^2}{2T_0} \quad \lambda \; real \qquad \text{(B.6)}$$

It can be seen from the above expression that the device temperature rise T increases with higher values of λ. If λ=0, the thermal conductivity is independent of temperature and the temperature rise is linear with power.

An important point that must be discussed concerns the applicability of the Kirchhoff's transformation. The latter can be applied to piecewise inhomogeneous thermal conductivity such as a multilayer stack provided the ratio of thermal conductivity is temperature independent[2]. In case of semiconductor, it is easily the case.

B.2 References

1 W. B. Joyce, "Thermal Resistance of Heat Sinks with Temperature-Dependent Conductivity," *Solid-State Electronics*, vol. 18, pp. 321-322, 1975.

2 F. Bonani and G. Ghione, "On the Application of the Kirchhoff Transformation to the Steady-State Thermal-Analysis of Semiconductor-Devices with Temperature-Dependent and Piecewise Inhomogeneous Thermal-Conductivity," *Solid-State Electronics*, vol. 38, pp. 1409-1412, 1995.

Appendix C Estimation of Surface Heat Losses

C.1 Presentation

In this appendix, heat loss from the top surface of a multi-finger HEMT will be estimated in the case of an unpackaged structure exposed to air and tested from the top with probes. Such a structure is shown in the Figure 1 of Ref. 1. Heat loss arises from radiation losses and heat conduction through the top metal layers. Already the main result can be announced: top surface heat losses represent a minor contribution, if not negligible, compared to heat conduction in the substrate. This is because of the relative small dimensions of the HEMT structure (~200um x 200um), the small thickness of the metal layers, and a limited channel temperature rise compared to the absolute room temperature (300K).

C.2 Heat Loss by Radiation.

The power loss is estimated from:

$$P_{loss} = \varepsilon\sigma A\left(T^4 - T_0^4\right) \qquad \text{(C.1)}$$

σ=5.6703·10^{-8} W·m^{-2}·K^{-4}, A is the emitting area, $\varepsilon \leq 1$ is the emissivity (ε~1). The total length of a height-finger HFET with a 25um gate-to-gate spacing is 200um. Assuming an upper range of temperature at ~600K radiating over an overestimated length of 600um length (3 times the HFET length) and 250um width, Equation (C.1) yields a P_{loss}= 4·10^{-3} W/mm which is 2500 times lower than a typical achievable[2] input power density of 10 W/mm. This estimate is small because the channel temperature is actually not very high compared to the absolute room temperature and the area of radiation is relatively small. Note that In case of temperature rise smaller in magnitude than room temperature (300K), Equation (C.1) becomes a linear function with temperature following $P_{loss}= G(T-T_0)$ with $G= 4\varepsilon\sigma AT_0^3$

As the thermal conductivity of air (~0.025 W·K^{-1}·m^{-1}) is 50 times lower than the thermal conductivity of a typical insulating passivation layer such as silicon

nitride or SiO_2, heat does not diffuse normal to the top of the sample. The top surface on the metal layer can be assumed adiabatic.

Note that channel temperature measurements employing infra-red detectors for instance rely on the measurement of the radiation, ie the electromagnetic spectrum. The temperature is deduced provided the emissivity is known. Those techniques are therefore optical methods by essence. Webb provides deeper insight into the challenges of device thermal imaging[4].

C.3 Heat Loss by Conduction

Since the top surface of the metal layer is adiabatic as shown in the previous section, the heat could only significantly diffuse laterally in the metal layer outward from the center of the device to the surrounding periphery and to the needle probes. It is assumed here that heat flows in a thin rectangular metal sheet around the device area set at constant channel temperature. Also assuming that the metal pads represent a perfect heat sink, the heat loss can be expressed as:

$$P_{loss} = G\left(T - T_0\right) \tag{C.2}$$

This time G is the thermal conductance estimated as $G=k_m/W*L*t_m$ where k_m~100 $W\cdot K^{-1}\cdot m^{-1}$ is the metal thermal conductivity, L is the metal length and W the metal width. In the best case scenario, W is small while t_m and L are large.

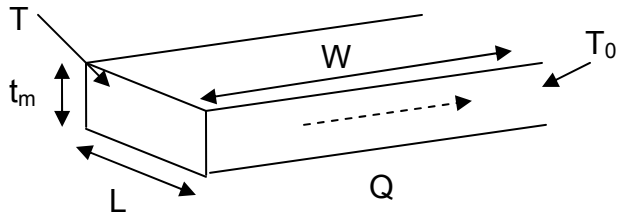

Figure C.1. Metal layer characteristics

The metal thickness layer can be approximately to be 1 um. From Figure 1 in Ref. 1, heat can be assumed to dissipate around the device in four rectangular sheets of W=~10um x L=~50um in a best case scenario always. In that situation, G

=2 mW/K. With a channel temperature of 600K, the total power loss is overestimated to 3% of the total power assuming an input power of 10W/mm from a 250um wide eight-finger HFET device. Therefore in the best case scenario, heat losses due to the presence of the metal layer represent a few percent of the total dissipated power. Basically, the thermal conductance of the metal layer is small because the metal thickness is thin. Based on a numerical approach, Webb has studied the effect of surface metallization to shown that they can make an observable contribution to the reduction of thermal resistance[3]. He concluded that that the lateral heat flow would increase in significance as the width of the gate fingers decrease. Such an observation is in agreement with our predictions.

C.4 References

1 M. Kuball, S. Rajasingam, A. Sarua, M. J. Uren, T. Martin, B. T. Hughes, K. P. Hilton, and R. S. Balmer, "Measurement of temperature distribution in multifinger AlGaN/GaN heterostructure field-effect transistors using micro-Raman spectroscopy," *Applied Physics Letters*, vol. 82, pp. 124-126, 2003.

2 K. K. Chu, P. C. Chao, M. T. Pizzella, R. Actis, D. E. Meharry, K. B. Nichols, R. P. Vaudo, X. Xu, J. S. Flynn, J. Dion, and G. R. Brandes, "9.4-W/mm power density AlGaN-GaN HEMTs on free-standing GaN substrates," *Electron Device Letters, IEEE*, vol. 25, pp. 596-598, 2004.

3 P. W. Webb, "Thermal modeling of power gallium arsenide microwave integrated circuits," *IEEE Transactions on Electron Devices*, vol. 40, pp. 867-877, 1993.

4 P. W. Webb, "Thermal imaging of electronic devices with low surface emissivity.," *IEE proceedings*, vol. 138, pp. 390, 1991.

Appendix D Defect Density Characterization

D.1 Introduction

This appendix addresses the characterization of defect density in gallium nitride, and more precisely the characterization of dislocation density of sample A, B, C, D listed in Table D.1 corresponding to Table 4.1 in Chapter 4. To this effect, etch pit count (EPC) from atomic force microscopy scans and pantochromatic catholuminescence (CL) imaging have been carried out. The relation between the presence of subsurface defects and surface morphology was complemented by Nomarski optical microcraphs and secondary electron microscopy images.

Table D.1. Samples were grown by hydride vapor phase epitaxy (Identical Table 4.1). Dislocation densities were taken from catholuminescence imaging.

Sample ID	Doping	GaN layer	Initial Thickness [um]	Final Thickness [um]	Resistivity [Ω·cm]	Dislocations at surface [cm^{-2}]
A	U	epi	~250	200±70	1-20	$4 \cdot 10^{7}$
B	U	bulk	~700	370±20	1-20	$1.5 \cdot 10^{7}$
C	U	bulk	1700	1400±50	1-20	$8.8 \cdot 10^{6}$
D	Fe	bulk	2000	2000±50	$2 \cdot 10^{8}$	$5 \cdot 10^{4}$

It is known that catholuminescence can detect the presence of non-radiative recombination centers[1]. In gallium nitride, dislocations appear as dark spots on catholuminescence images because dislocations act as non-radiative recombination centers[2,3]. It was shown that there is a close one-to-one correspondence between

the presence of dark spots on CL images and dislocations on gallium nitride epitaxial films by cross checking with other techniques[2-5]. CL imaging has the advantage of reduced sample preparation and large scan areas but is limited to the characterization of dislocation density below 10^8 to $5 \cdot 10^8$ cm^{-2}. At high dislocation density, plane view or cross sectional view transmission electron microscopy (TEM) can be considered. In fact, the TEM technique is extremely valuable to characterize the nature of dislocations (mixed, edge, screw) present in gallium nitride as well as dislocation reduction mechanisms. Atomic force microscopy scans can also be utilized for the characterization of high density dislocation provided the surface remains atomically smooth[2,4].

In semiconductors, It is well known that non-radiative defects evidenced from the presence of dark areas in catholuminescence imaging[1-3] will match the emergence of defects during etching experiment[1-3]. In the case of gallium nitride, anisotropy etching occurs in the vicinity of a dislocation termination to leaves pits behind that can be subsequently characterized by AFM scans[2-5]. However Hong *et al.*[6] illustrated that pits do not systematically form at a dislocation termination. It was showed from TEM experiment that preferential etch occur due to nanopipes (open-core srew dislocations). Several other authors are debating the experimental interpretations of the latter study; for instance, it is argued that TEM preparation induces the formation of dislocation[4]. Nevertheless, etch pit count is routinely performed in the gallium nitride community to characterize the dislocation density[2,3,5]. Etch pits can be hexagonal on Ga-Polar surface of gallium nitride or circular on N polar surface of gallium Nitride[3]. It is noteworthy that, depending on etching conditions, photo-assisted etching (PEC) results in the formation of whiskers, unlike pits, mainly because light recombine at dislocation thereby slowing down the etch rate[3]. Among the various solutions to etch gallium nitride are hot phosphoric acid (H_3PO_4), mixed H_3PO_4 / H_2SO_4, and molten potassium hydroxide (KOH).

In this work, etching experiment was conducted as follows: Sample A and B were dipped in a 200°C phosphoric acid (HPO_3) bath for 15 mn altogether, while sample C and D were left 200°C HPO_3 bath for 30 mn. The samples were laid down

face up in a Teflon basket placed in a Pyrex beaker. The experimental calibration concerning etch rate, etchant volume, temperature stability, etc was achieved by monitoring the emergence of tiny pits from both optical micrograph and AFM scans on small dummy pieces diced from sample A and B. Great care on reproducible etching conditions must be adopted as the density and size of defects can vary significantly depending on varying experimental conditions. It was found from AFM scans that large micrometer size pits appeared on sample B much faster than on sample A after 1 minute dip in hot acid only. On each sample listed in Table D.1, catholuminescence imaging and optical micrograph were taken before and after etching. No appreciable variations in the density of dark spots were seen during CL imaging before or after etching.

D.2 Catholuminescence Prior to Etching (Sample A, B, C, D).

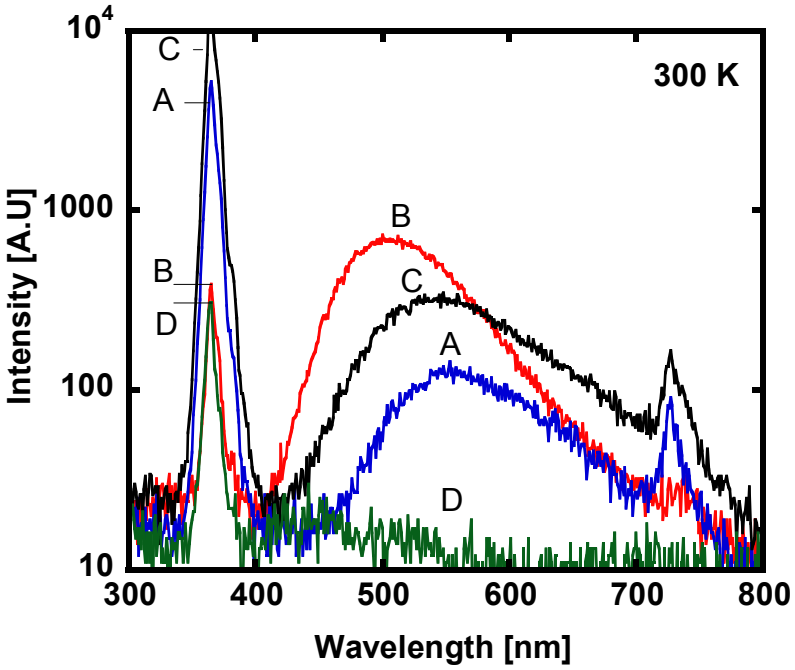

Figure D.1. Catholuminescence spectrum at 300K for sample A, B, C (undoped) and D (iron doped). The peak at 730nm is the second order diffraction of the band edge emission. The defect peak is absent for sample D or lies within the noise level. The probe current was 0.1nA for samples A, B, C and 3nA for sample D.

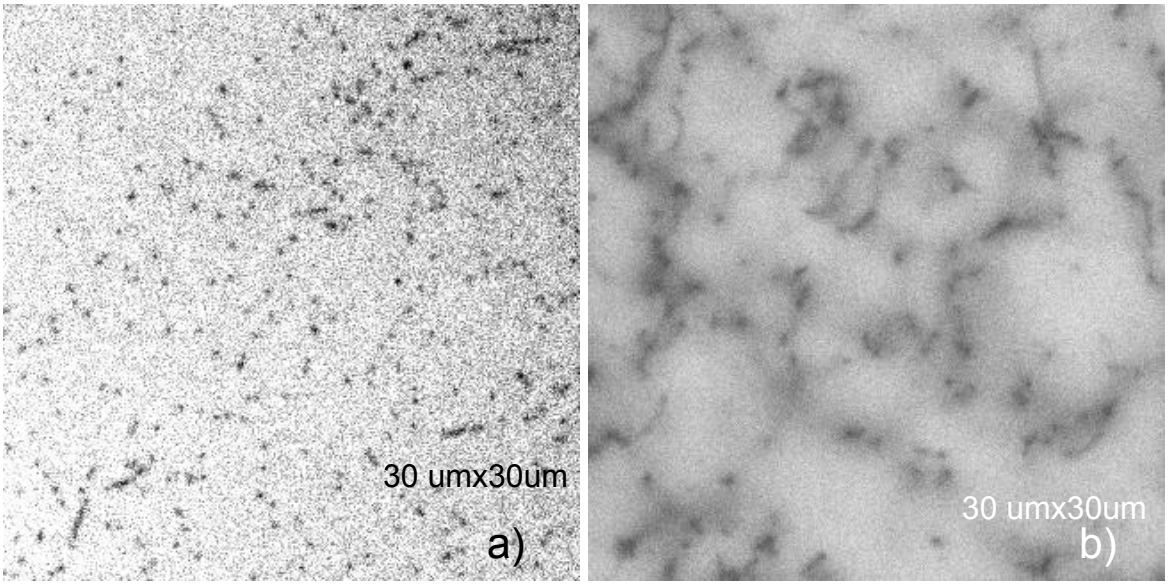

Figure D.2. 30x30um^2 catholuminescence imaging prior to etching for a) Sample A and b) Sample B. The probe current was 10^{-10}A.

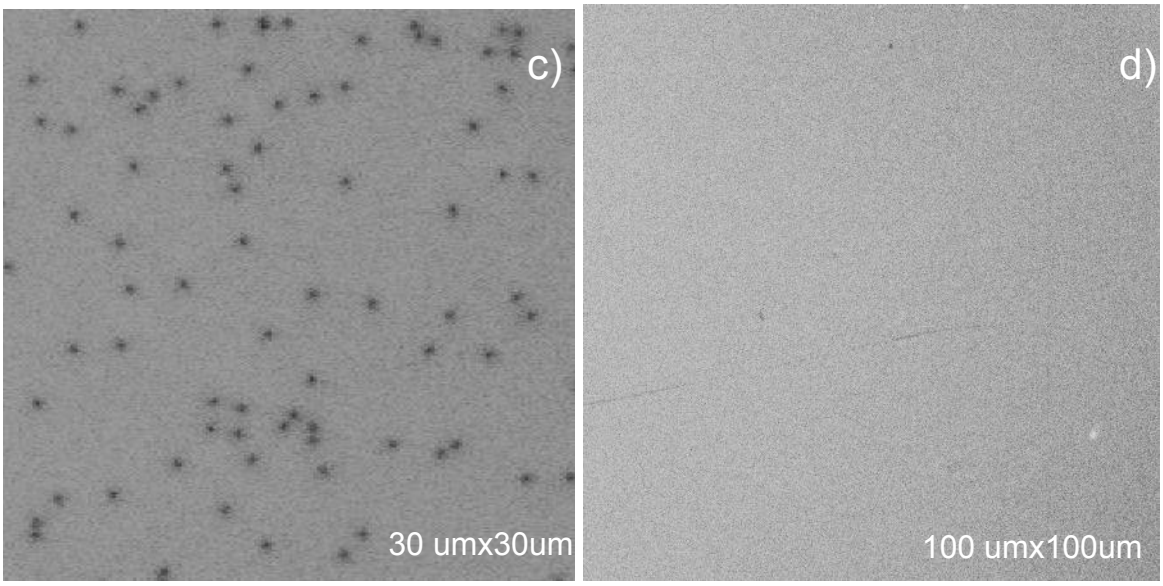

Figure D.3 Catholuminescence imaging prior to etching for c) Sample C and d) Sample D. The probe current was 10^{-10}A.

D.3 Micrograph Before Etching (Samples C, D).

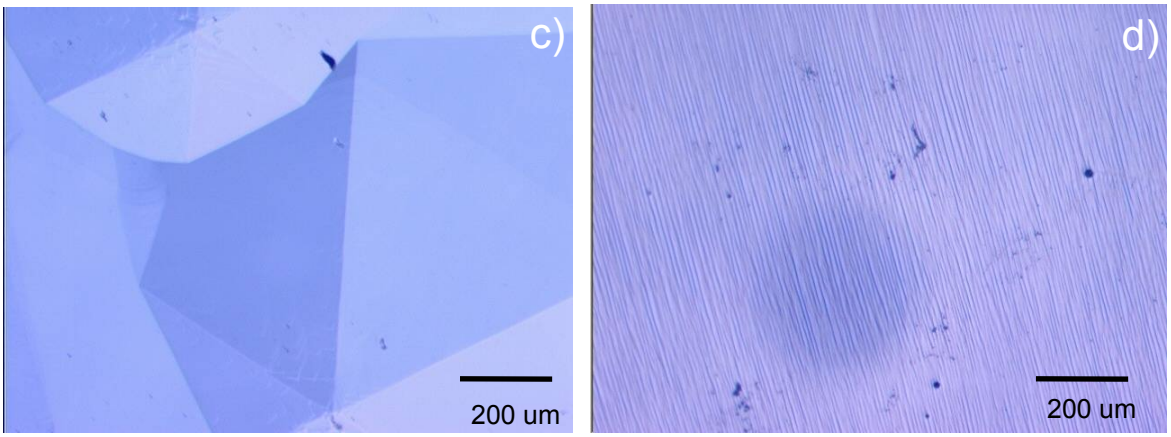

Figure D.4. Micrograph of the gallium nitride surface morphology for c) Sample C and d) Sample D. Note the presence of large hillocks for sample C while striations are clearly visible for sample D. These morphologies are typical of HVPE grown gallium nitride surfaces[7].

D.4 Micrograph After Etching (Samples A, B, C, D)

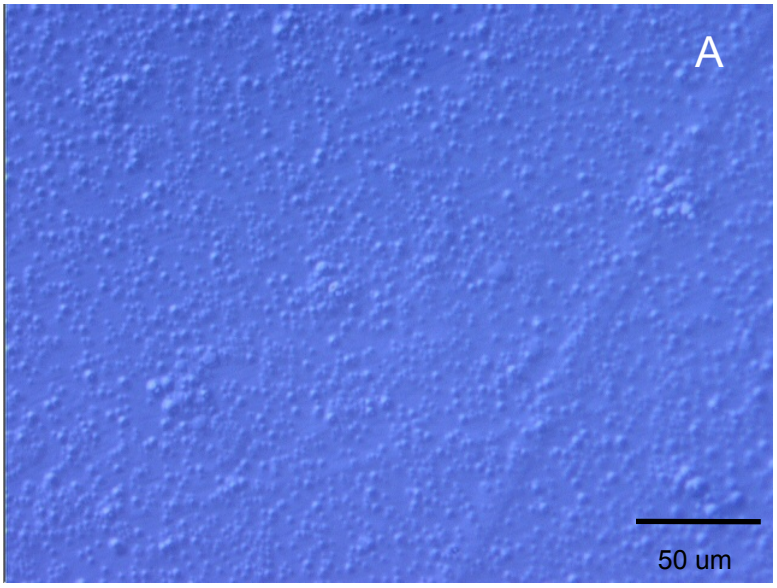

Figure D.5. Typical micrograph of the surface of sample A after a 15mn 200°C phosphoric bath. It seems that pits cover the surface sample uniformly with a relative homogeneous size. Atomic force microscopy (AFM) images will complement the micrographs for analysis at submicron dimensions. AFM will actually show that pit sizes vary unhomogeneously.

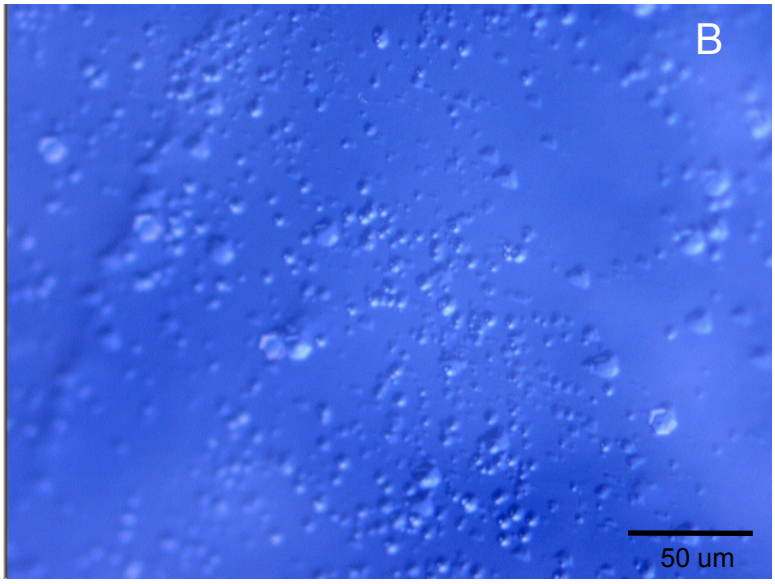

Figure D.6. Typical micrograph at the surface of sample B after a 15mn 200°C phosphoric bath. Pits cover the sample surface non-uniformly with a strong variation in pit size.

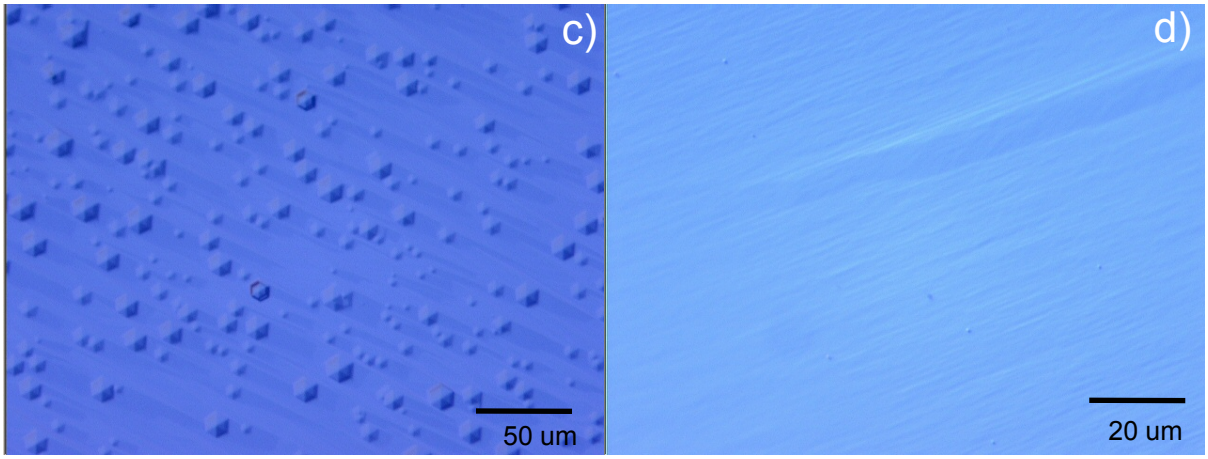

Figure D.7. Micrograph of c) Sample C and d) Sample D after a 30mn 200°C phosphoric acid dip (same bath). For sample C, the distribution of pits is homogeneous but pit sizes are large and mostly hexagonal. Pits can be counted from optical microscopy while AFM images will confirm the absence of nanoscopic pits. Almost no pits can be seen at the optical microscope on sample D over millimeter large area as illustrated in the particular case of the left figure d). Figure D.7 part (d) is a magnification of subsequent Figure D.11 part (iv) where the longitudinal feature can be seen 200um from the white arrow.

D.5 AFM After Etching (Sample A, B, C, D)

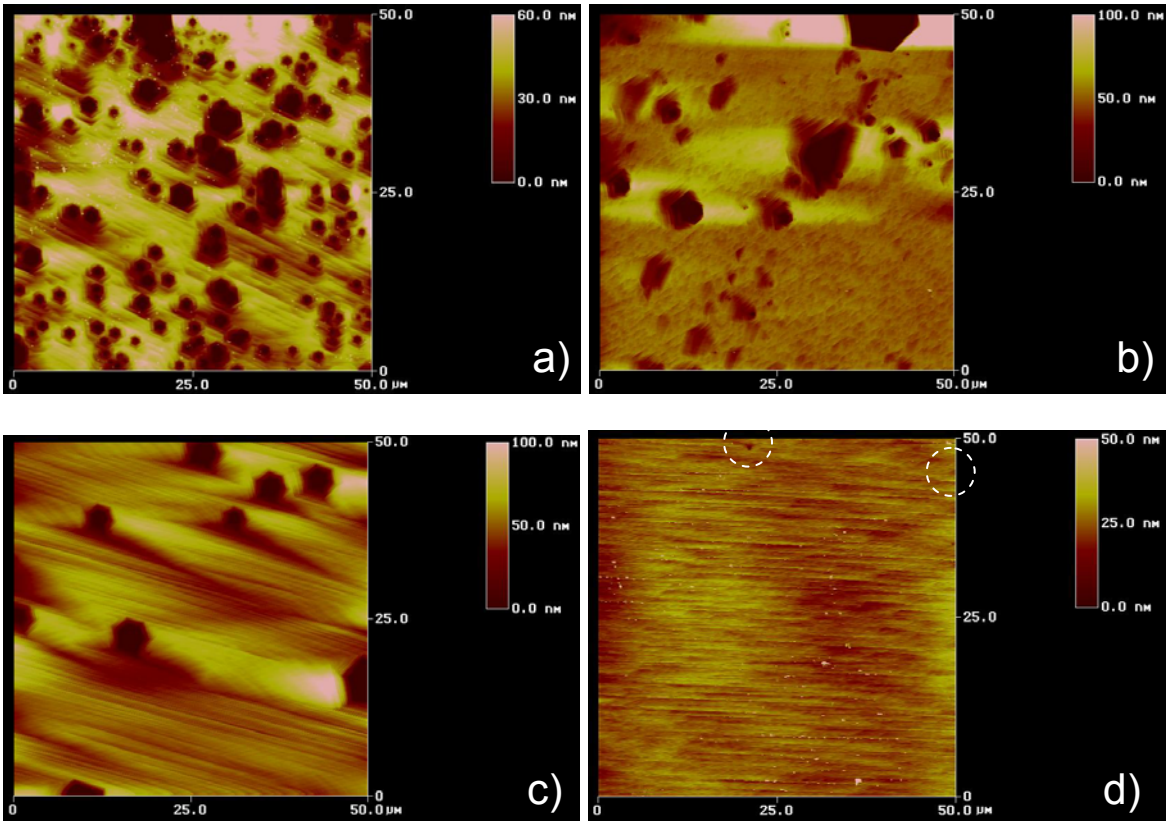

Figure D.8. Random 50X50um^2 AFM scans on a) Sample A, b) Sample B, c) Sample C, d) Sample D. Same etching conditions as in Section A4. Both tens of micron and submicron pits are visible in a), whereas only large hexagonal pits are seen for c) sample C.

D.6 Sample C

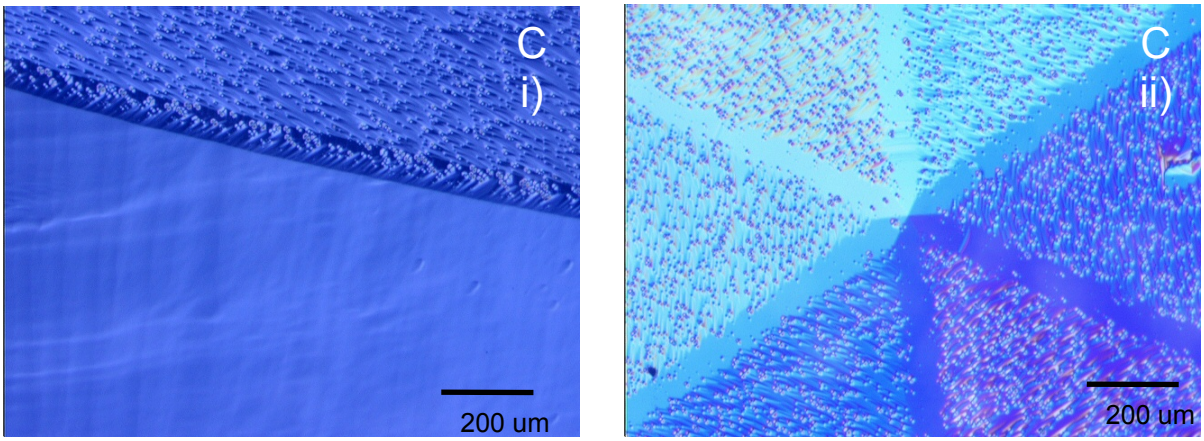

Figure D.9. Peculiarity: i) At a boundary on sample C. Near-dislocation areas are not etched at same rate (if any). ii) Micrograph on hillock. Same etching conditions as in Section D.4.

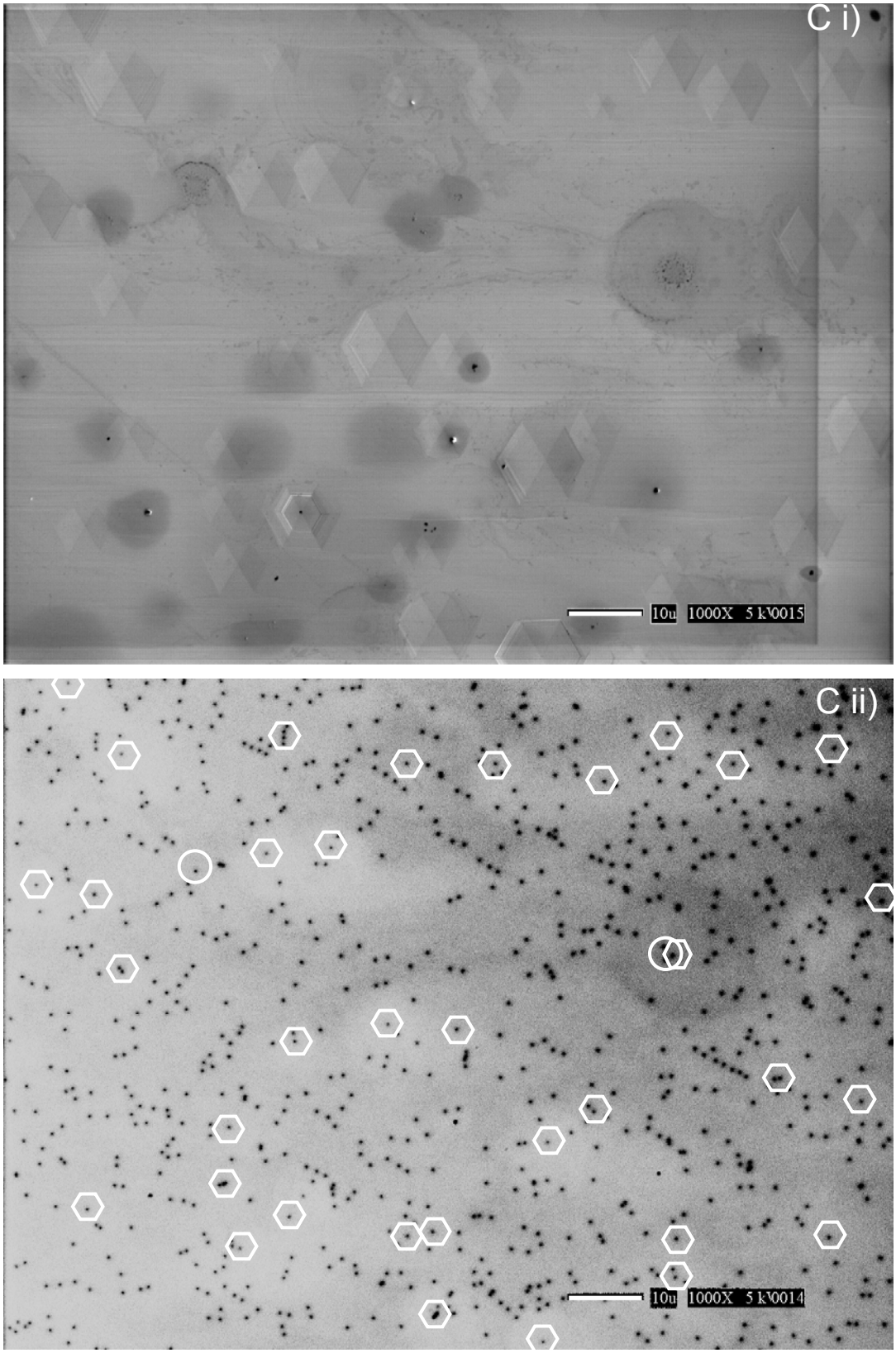

Figure D.10. i) SEM ii) CL imaging at exact same location (10^{-10} A). Hexagons and circles in i) are representatively drawn at a matched dark spot in ii). Dark lines in i) are SEM artifacts.

D.7 Sample D

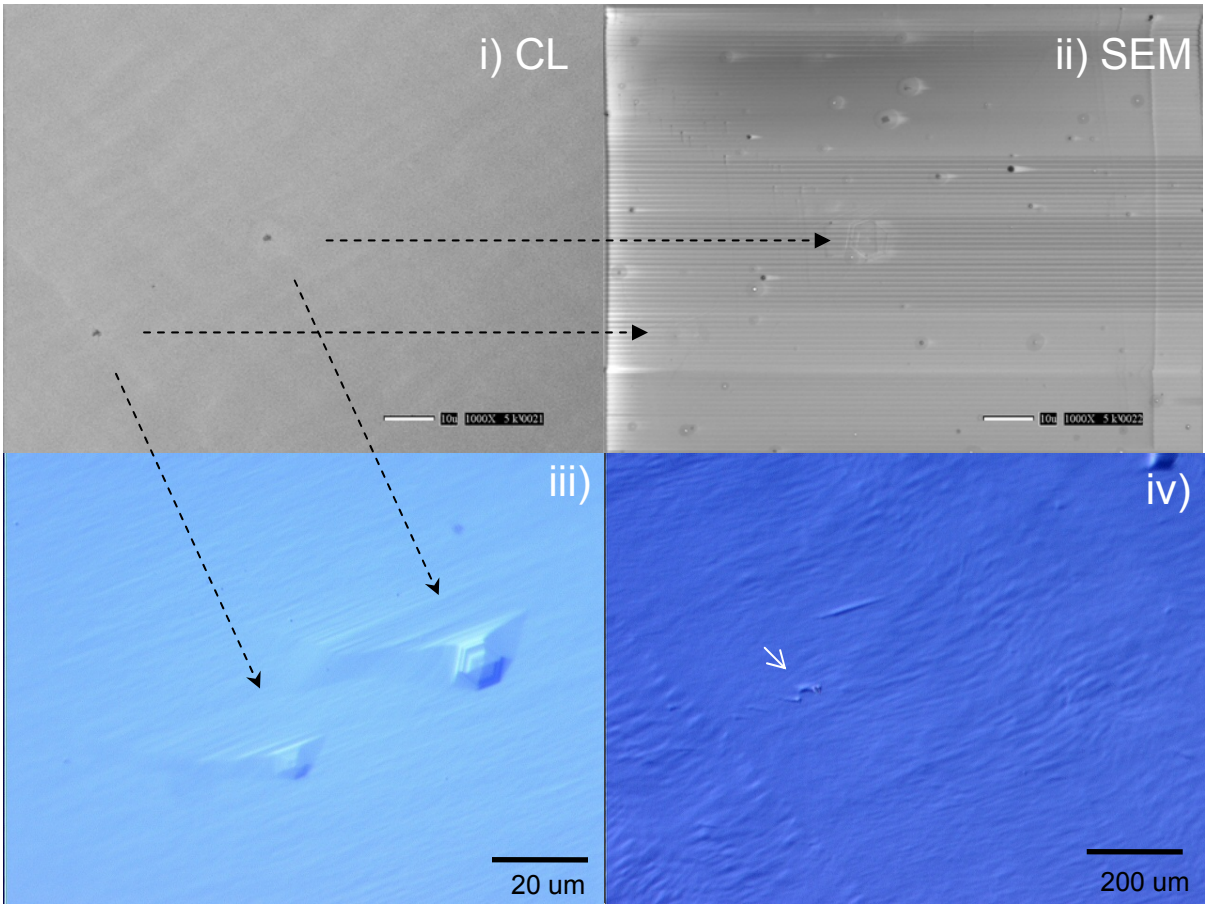

Figure D.11. Comparison between CL (10^{-10}A), SEM, and micrographs taken at the same location on sample D

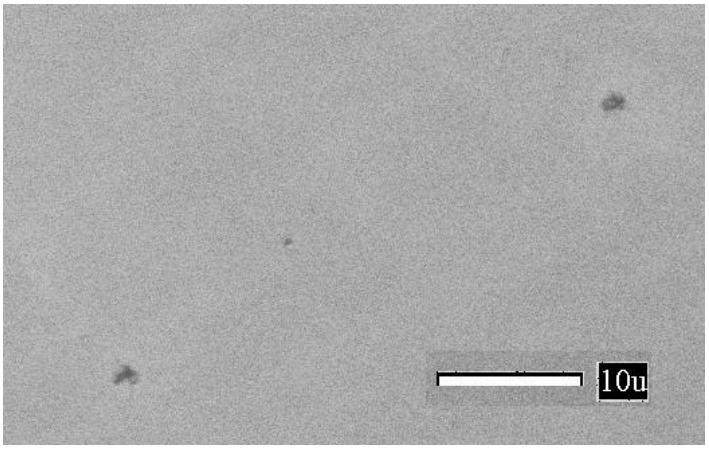

Figure D.12. Enlargement of Figure D.11 part (i) suggesting that large pits are formed at a cluster of dislocations and that reaction between dislocation may be efficient in sample D.

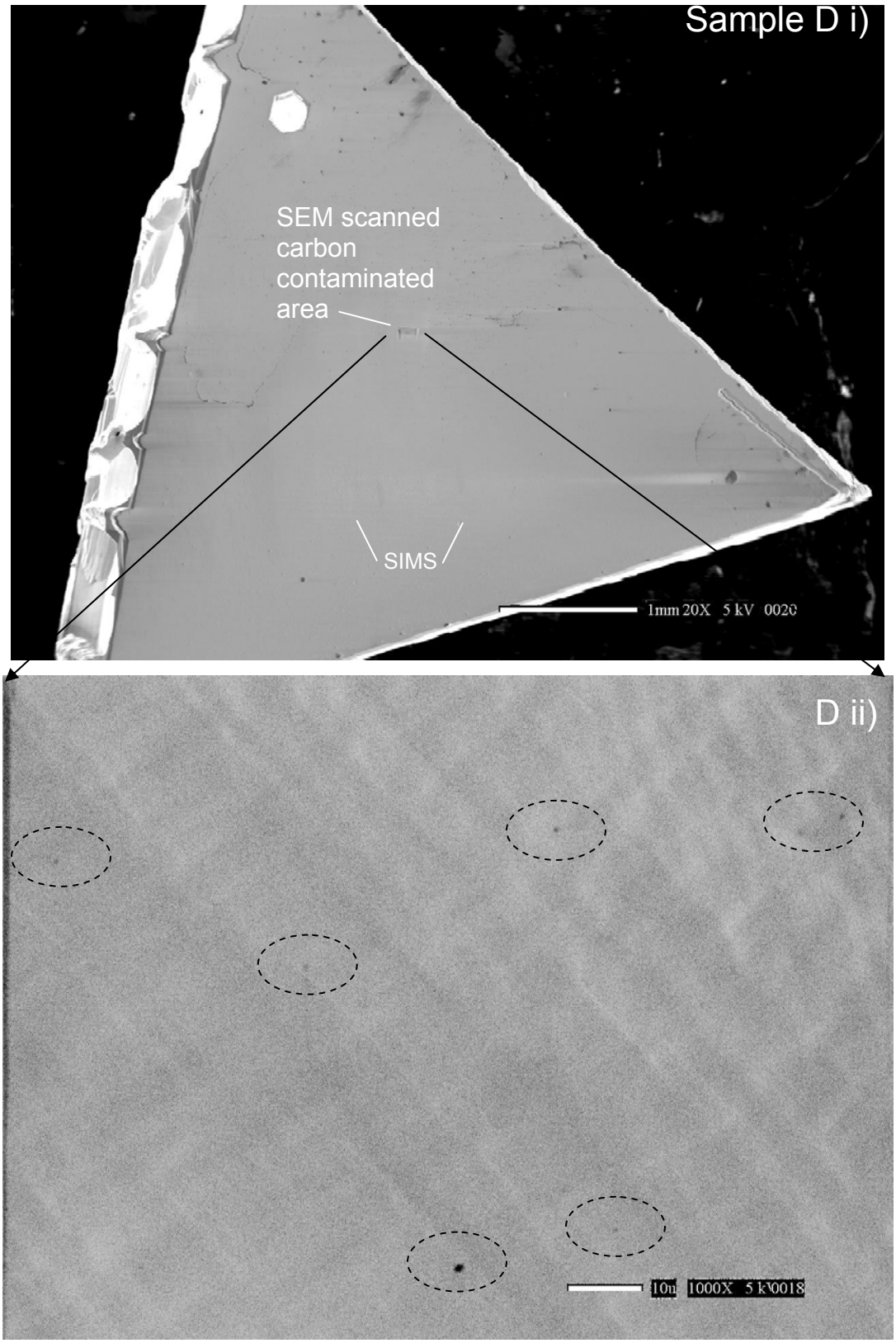

Figure D.13. i) SEM and ii) CL imaging on semi-insulating sample D after 30mn etching (probe current: 3.10^{-9} A).

D.8 Conclusion

The dislocation density was estimated from two different techniques: atomic force microscopy following etch pit (EPC) and from catholuminescence imaging (CL). The result is summarized in Figure D.14 below.

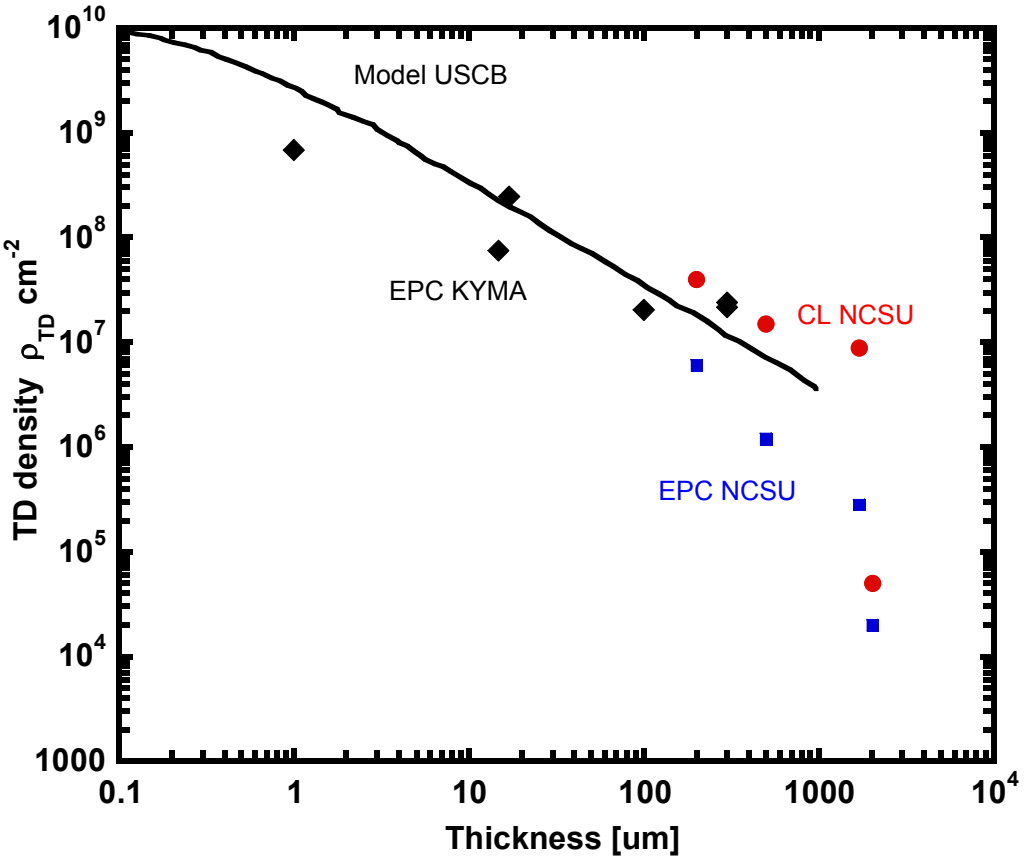

Figure D.14.Dislocation density versus thickness. ♦: KYMA technology ECP, ● KYMA-NCSU CL, ■ NCSU ECP. The solid line describes the model in Ref. 8 and reproduced in Ref. 7.

In this study, It is found that etch pit count (EPC) underestimates the dislocation density especially at dislocation density higher than 10^6 cm^{-2}. At short etching time (~1mn), the pit density was low, typically 2 or 3 pits were found per 50umx50um area on sample A or B. Moreover the difficulty in conducting high resolution AFM scans was exacerbated due to the elevated surface roughness of thick HVPE acid-etched gallium nitride samples (~100nm deep pits). For long etching time, pits increase in size until coalescing. In that case, it is clear that etch pit count will underestimate the defect density. An intermediate situation was found

when sample A and B were etched for 15mn in 200°C phosphoric acid while sample C and D (with lower defect densities) were etched for 30 mn in 200°C phosphoric acid. Figure D.10 demonstrates that defects estimated from CL imaging outnumber defects estimated from etch pits from secondary electron scanning microscopy (SEM). Although plane-view images show most defects hexagonal, it is possible that circular defects formed. Indeed two circular defects in Figure D.10.i can be matched to at least two dislocations in Figure D.10.ii. At present, aside the dislocation density discrepancy, there is no explanation for the difference in kinetics from defect to defect and sample to sample although samples A, B, C, and D did not present an as-grown surface throughout the defect characterization experiment. For thermal conductivity characterization purposes, the samples had previously been coated with a 100nm oxide layer subsequently removed in buffer oxide etchant (BOE).

At low dislocation density, microscope inspection following a generous hot acid overetch can lead to a satisfactory dislocation density characterization procedure although Figure D.11 clearly illustrates that such a method will tend to underestimate the dislocation density; pits may simply not always form as demonstrated in Figure D.11 and Figure D.12, or adjacent dislocations may not be counted due to coalescing pits forming during large overetching necessary for optical inspection. Overall, the most reliable dislocation density measurement is found to be deduced from catholuminescence imaging though it might present a propensity to overestimate the dislocation density[1].

The low dislocation density of ~$5 \cdot 10^4$ cm^{-2} on sample D has been confirmed to a high level of confidence over a 1mm square area and redundantly observed over several square centimeter areas. It is easy to find 100umx100um sites with dislocation densities of ~$1 \cdot 10^4$ cm^{-2} while some other regions can have as much as ~$1 \cdot 10^5$ cm^{-2} dislocation density. The dislocation density corresponding to sample D in Figure D.14 departs significantly from the model in Ref. 8 plotted in solid line in Figure D.14. Such a departure cannot be ascribed to measurement uncertainties alone. In the case of sample C, pits are associated with narrow dark spots (Figure D.10). However In the case of sample D, extended dark spots mostly centered on hexagonal etch pits were observed repeatedly (Figure D.12 and Figure D13). Higher

magnification CL imaging taken at slightly improved resolution was suggestive of the presence of dislocation clustering, probably reacting. Unfortunately SEM beam current induced charging prohibited image recording.

Other authors[9] have focused on the formation of HVPE gallium nitride grown with a low dislocation density from 10^4 to 10^6 cm^{-2}. Large departure was observed from the model of Ref. 8 where an extensive treatment on the theory underlying dislocation density reduction is provided. The authors in Ref. 8 showed that edge dislocation is poorly efficient in fusion or annihilation processes compared to mixed dislocations. It is not impossible that the initial growth conditions underlying the formation of sample D have favored the formation of a high content of mixed dislocations whereas a higher content of edge dislocation would have been formed for sample C, accounting for the difference in observed dislocation clustering. Furthermore the effect of a high content of iron impurities on dislocation density has not been included in the model of Ref. 8. For comparison, the presence of point defects such as tellurium in gallium arsenide was shown to strongly influence the phonon-dislocation interaction[10]. Additional characterization will certainly benefit any studies on dislocation density reduction at low dislocation density content.

D.9 References

1 J. I. Pankove, *Optical Processes in semiconductors*. New-York: Dover Publications, Inc, 1971.

2 S. J. Rosner, E. C. Carr, M. J. Ludowise, G. Girolami, and H. I. Erikson, "Correlation of cathodoluminescence inhomogeneity with microstructural defects in epitaxial GaN grown by metalorganic chemical-vapor deposition," *Applied Physics Letters*, vol. 70, pp. 420-422, 1997.

3 D. Zhuang and J. H. Edgar, "Wet etching of GaN, AlN, and SiC: A review," *Materials Science and Engineering R: Reports*, vol. 48, pp. 46, 2005.

4 P. Visconti, K. M. Jones, M. A. Reshchikov, R. Cingolani, H. Morkoc, and R. J. Molnar, "Dislocation density in GaN determined by photoelectrochemical and hot-wet etching," *Applied Physics Letters*, vol. 77, pp. 3532-3534, 2000.

5 K. Lee and K. Auh, "Dislocation Density of GaN Grown by Hydride Vapor Phase Epitaxy," *MRS Internet J. Nitride Semicond.*, vol. 6, 2001.

6 S. K. Hong, Y. Yao, B. J. Kim, S. Y. Yoon, and T. I. Kim, *Applied Physics Letters*, vol. 77, pp. 82, 2000.

7 P. Gibart, "Metal organic vapour phase epitaxy of GaN and lateral overgrowth," *Reports on Progress in Physics*, vol. 67, pp. 667-715, 2004.

8 S. K. Mathis, A. E. Romanov, L. F. Chen, G. E. Beltz, W. Pompe, and J. S. Speck, "Modeling of threading dislocation reduction in growing GaN layers," *Physica Status Solidi a-Applied Research*, vol. 179, pp. 125, 2000.

9 R. P. Vaudo, X. Xu, C. Loria, A. D. Salant, J. S. Flynn, and G. R. Brandes, "GaN boule growth: A pathway to GaN wafers with improved material quality," *Physica Status Solidi a-Applied Research*, vol. 194, pp. 494-497, 2002.

10 J. Jouglar, P. L. Vuillermoz, and A. Laugier, "Influence of Nonstoichiometry on Phonon-Dislocation Interactions in Gaas-Te," *Journal of Solid State Chemistry*, vol. 20, pp. 227-232, 1977.